Chair of Surface and Interface Physics (E20)
TUM School of Natural Science
Technical University of Munich

Technische Universität München

PhD Thesis

Title of the Thesis:

Non-Metallic Surface Preparation and Chemistry: Molecular Depositions and Reactions

Author:	Rostami, Mohammadreza
Address:	James-Franck-Strasse 1 D-85748 Garching (Germany) Room 204 Physics Department II
Matriculation Number:	03777122
Supervisor:	Prof. Dr. Johannes Barth Prof. Dr. Lifeng Chi
Begin:	01. October 2020
End:	31. December 2024

TECHNISCHE UNIVERSITÄT MÜNCHEN

TUM School of Natural Sciences

Non-Metallic Surface Preparation and Chemistry: Molecular Depositions and Reactions

Mohammadreza Rostami

Vollständiger Abdruck der von der TUM School of Natural Sciences der Technischen Universität München zur Erlangung eines Doktors der Naturwissenschaften (Dr. rer. nat.) genehmigten Dissertation.

Vorsitz: Prof. Dr. Martin Zacharias

Prüfende der Dissertation:

1. Prof. Dr. Johannes Barth
2. Prof. Dr. Xinliang Feng

Die Dissertation wurde am 25.11.2024 bei der Technischen Universität München eingereicht und durch die TUM School of Natural Sciences am 10.12.2024 angenommen.

Acknowledgment

I extend my deepest gratitude to all those who have supported my doctoral research and contributed to this project. First and foremost, I express my sincere appreciation to my supervisors, Prof. Dr. Johannes V. Barth, Prof. Dr. Lifeng Chi, and Prof. Dr. Martin Stutzmann, for offering me this PhD position, providing invaluable guidance, access to state-of-the-art instruments, vibrant laboratory environments, unwavering support, and stimulating scientific discussions. It has been an honor to work at the E20 laboratories at TUM, an opportunity graciously provided by Prof. Johannes V. Barth. The support from Prof. Dr. Lifeng Chi during my travels to China and in conducting my research there was particularly significant.

I am profoundly grateful to Prof. Dr. Peter Feulner and Dr. Biao Yang for their technical assistance in the PSD and JT-STM laboratories at E20, as well as for their guidance and insightful scientific discussions. Their doors were always open whenever I had questions or encountered challenges, for which I am deeply thankful. I also extend my thanks to Peter for developing several useful programs, including the one for analyzing TPXPS data. I am especially appreciative to them and my supervisors, Prof. Barth, Prof. Chi, and Prof. Stutzmann, for their meticulous revisions, corrections, and enhancements of my drafts and manuscripts. Additionally, I thank Dr. Francesco Allegretti for his valuable scientific discussions and guidance during the early stages of my PhD project. My thanks also go to Karl Eberle, Dr. Felix Haag, and Fabian Strunk for their technical support and maintenance efforts in the E20 laboratories. I would also like to extend my sincere appreciation to Viktoria Blaschek, the secretary of E20, for her invaluable administrative support.

I am thankful to Dr. Sifan You and Minchong Sheng for the scientific discussions and technical support provided at the Institute of Functional Nano & Soft Materials (FUNSOM), Joint International Research Laboratory of Carbon-Based Functional Materials and Devices, Soochow University, Suzhou, P. R. China.

My gratitude extends to Prof. Dr. Bing Wang, Prof. Dr. Shijing Tan, and Dr. Xiaochuan Ma for the enriching scientific discussions on the TiO_2 projects, as well as for their technical and personal support at the CAS Center for Excellence in Quantum Information and Quantum Physics (QIQP) (Nano and Femto Research Group (NFRG)) at the University of Science and Technology of China (USTC) in Hefei, Anhui, China. I also acknowledge the technical assistance provided by Jin Zhou and Huimin Xu during my project in Hefei.

I wish to thank the simulation team at Turkish Accelerator and Radiation Laboratory (TARLA), Graduate School of Natural and Applied Sciences at Ankara University, Department of Physics Engineering of Faculty of Engineering at Ankara University, and Department of Physics of Adnan Menderes University in Aydin in Turkey, including Prof. Dr. Ethem Aktürk, Prof. Dr. Çağıl Kaderoğlu, Prof. Dr. Handan Olgar, Mahsa Seyedmohammadzadeh, and Pinar Kaya Fizmuh, for their complementary density functional theory calculations and scientific discussions related to the Cu_2N projects which is used by their permissions.

My thanks also go to Prof. Dr. Mathias O. Senge from the Institute for Advanced Study (TUM-IAS), Technical University of Munich, for providing the CBCP and porphyrin molecules used in this work. I appreciate Prof. Dr. Long Chen for providing me with the TBN molecules. I am grateful to Michał Boćkowski (Institute of High-Pressure Physics, Polish Academy of Sciences, Warsaw, Poland) for supplying the ammonothermal GaN sample for our experiments.

Additionally, I extend my gratitude to all my colleagues and members of E20 at TUM, CAS at USTC, and FUNSOM at Soochow University for their support and contributions, which fostered a vibrant and stimulating atmosphere throughout my PhD program.

I acknowledge financial support from the Institute for Advanced Study (IAS), Technische Universität München (funded by the German Excellence Initiative), the German Excellence Strategy (e-conversion Cluster of Excellence EXC2089/1-390776260), FUNSOM at Soochow university (the Collaborative Innovation Center of Suzhou Nano Science & Technology, the Suzhou Key Laboratory of Surface and Interface Intelligent Matter (Grant SZS2022011), and the 111 Project), and CAS QIQP (NFRG) at USTC.

Finally, my most heartfelt thanks go to my family for their unwavering support throughout my life and studies.

Abstract

Wide band gap semiconductor single crystals and insulating thin films are emerging as promising alternatives to metallic substrates in surface science, offering a means to prevent the quenching of electronic and optical excitations in surface-bound atoms, molecules, and nanoarchitectures. In this thesis, we explore the potential of GaN and TiO_2 single crystals, as well as Cu_2N thin films, for these applications. The efficacy of these substrates for on-surface reactions and subsequent electronic spectroscopy analyses is thoroughly examined in the following chapters.

Gallium nitride (GaN), a wide bandgap semiconductor with absorption and emission in the ultraviolet/visible range, is proposed as an alternative to metallic surfaces for assembling organic molecular structures aiming at optoelectronic applications. However, the formation of a persistent surface oxide layer in air considerably limits the use of GaN for well-defined interfaces. In Chapter 3, we have investigated, characterized and processed n-type free-standing c-plane hexagonal wurtzite GaN crystals grown by hydride vapor phase epitaxy and ammonothermal growth methods. Surface cleaning and full removal of the oxide layer on GaN surfaces could be reproducibly achieved via sputtering and annealing cycles, as evidenced by X-ray photoelectron spectroscopy and low-energy electron diffraction. Scanning tunneling microscopy, however, indicated substantial roughening of the GaN surface and the formation of unwanted Ga-rich islands and clusters. Although ammonia (NH_3) and bromine (Br) treatments compensated the N/Ga atoms ratio reduced by sputtering, the surface morphology remained rough, exhibiting randomly shaped and distributed hillocks. In addition, we studied the effect of electron bombardment on the surface quality of GaN during NH_3 annealing, on-surface debromination and polymerization of 1,3,5-tris(4-bromophenyl) benzene on GaN and the removal of Ga atoms by Br atoms during the desorption.

Copper nitride (Cu_2N) thin films represent a metallic yet stable buffer layer in ultra-high vacuum, bearing promise for decoupling functional structures from a metallic copper substrate. Although a preparation protocol based on nitrogen ion bombardment has been previously applied for in-situ deposition of Cu_2N monolayers on Cu surfaces, the reduced domain size limits its application potential. In Chapter 4, we have grown extended Cu_2N monolayer films on a Cu (111) surfaces by ammonia-mediated post-annealing of ultrathin copper oxide films. The structure and properties of Cu_2N and copper oxide monolayers were characterized by scanning tunneling microscopy and low-energy electron diffraction. The exchange of nitrogen with oxygen elements in the respective Cu_2N and copper oxide layers on Cu (111) surfaces was revealed by X-ray photoelectron spectroscopy. This oxidation-reduction two-step strategy provides a promising new approach to fabricate Cu_2N buffer layers on which we studied molecular depositions and assemblies and confirmed their decoupling effect by tunneling spectroscopy and DFT calculations.

Ullmann coupling stands out as one of the most efficient, controllable, and predictable surface-assisted aryl-aryl coupling reactions, extensively employed for fabricating poly(para-phenylene) (PPP) wires, also referred to as the narrowest n-armchair graphene nanoribbons (nAGNRs, n = 3). These nanostructures are pivotal for next-generation electronic applications due to their precisely adjustable band gap. In Chapter 5, we demonstrated the capability of Ullmann coupling of 5,15-(di-4-bromophenyl)porphyrin ($(BrP)_2P$) and 4,4”-dibromo-p-terphenyl (DBTP) molecules and the formation of PPP wires on Cu_2N, highlighting its role as a metallic thin film with the decoupling potential, making this an unparalleled substrate for surface science techniques and the investigation of electronic and optical excitations and properties of on-surface atoms, molecules, and nanoarchitectures. Tunneling spectroscopies revealed an enlargement of the HOMO-LUMO gap of the decoupled $(BrP)_2P$ molecules and PPP wires on Cu_2N compared to Cu (111) islands, indicating crucial potential for fundamental understanding and transformative insights into the electronic and optical phenomena within the surface.

While the metallic nature of copper nitride (Cu_2N) thin films provides a suitable platform for surface science techniques such as scanning tunneling microscopy and spectroscopy, the decoupling effect of this two-dimensional material holds critical promise for preventing the

quenching of optical and electronic excitations or quasiparticles in adsorbed atoms, molecules, and nanoarchitectures from the underlying substrate. In Chapter 6, we developed a novel replacement method for fabricating Cu_2N thin films on Cu (100) by iterative cycles of oxidation and nitridation under ultra-high vacuum conditions, with an adjustable coverage and patch size distribution controlled by the number of cycles and the surface temperature. Hereby the O atoms in a $\left(2\sqrt{2} \times \sqrt{2}\right)R45°$ CuO-superstructure are replaced by N atoms from NH_3 on the CuO surface at 675 K, forming a $\left(\sqrt{2} \times \sqrt{2}\right)R45°$ Cu_2N structure, with N atoms residing at hollow sites of the Cu (100) surface atomic layer. This nanostructure comprises a square unit cell with a lattice parameter of approximately 0.4 nm. The appearance of highly intense and regular confinement states in the conduction band of Cu_2N patches on Cu (100), quenched at the point defects, is intriguing for further investigation of electronic and optical excitations and quasiparticles couplings. Due to the high stability of the Cu_2N surface, the adsorption enthalpy on surrounding Cu stripes and islands is significantly more favorable than on Cu_2N patches, as monitored by dominant molecular adsorption and assembly on Cu stripes rather than on the Cu_2N surface. In addition, the enlargement of the HOMO-LUMO gap value indicated the decoupling of on-surface pentacene and diaminophenyl-porphyrin molecules from the Cu (100) substrate by the Cu_2N layer.

In addition, in Chapter 7, we studied the influence of light and Fe adatoms on the debromination of 4,4”-dibromo-*p*-terphenyl precursors affording poly(*para*-phenylene (PPP as the narrowest GNR) wires through the Ullmann coupling reaction on a rutile TiO_2(110) surface, which we studied by scanning tunneling microscopy and X-ray photoemission. The temperature threshold for bromine bond cleavage and desorption is reduced upon exposure to UV light (240-395 nm wavelength), but the reaction yield could not be improved. However, in the presence of codeposited iron adatoms, precursor debromination occurred even at 77 K, allowing for Ullmann coupling and PPP wire formation at 300-400 K, i.e., markedly lower temperatures compared to the conditions without Fe adatoms. Furthermore, scanning tunneling spectroscopy data reveal that adsorbed PPP wires feature a HOMO-LUMO gap of ≈ 3.1 eV.

Although on-surface synthesis provides promising strategies to successfully construct various nAGNRs, the use of metal surfaces as substrate cannot avoid the quenching of electronic and optical excitations, thus preventing the study on intrinsic electronic structures and resulting in contradictory reports in the case of HOMO-LUMO gap of 5AGNRs. In Chapter 8, we prepared 5AGNRs on semiconducting rutile TiO_2 (110) and anatase TiO_2 (101) surfaces using photocatalysis of surface-assisted Ullmann coupling of 1,4,5,8-tetrabromonaphthalene (TBN) molecules. Although annealing monolayers or multilayers on both rutile and anatase TiO_2 favored the TBN debromination on these surfaces, as indicated by X-ray photoelectron spectroscopy, rarely C-C coupling and the formation of 5AGNRs were observed in the scanning tunneling microscopy images. On the other hand, irradiation of the surface by violet or UV light could drastically enhance the formation of 5AGNRs. Light with a shorter wavelength in the UV range (265 nm) causes more extensive debromination on this inert surface compared to near-violet light (377 nm). Furthermore, STS revealed a HOMO-LUMO gap of about 2.1 eV for 5AGNRs, exhibiting their semiconducting nature.

Keywords

Titanium dioxide, Graphene nanoribbons, Hexagonal wurtzite gallium nitride, Surface science, X-ray photoelectron spectroscopy, Scanning tunneling microscopy, Copper nitride, on-surface synthesis

Contents

List of Abbreviations

0D	Zero-Dimensional
1D	One-Dimensional
2D	Two-Dimensional
3D	Three-Dimensional
DFT	Density Functional Theory
LEED	Low Energy Electron Diffraction
OMBE	Organic Molecular Beam Evaporator
HVPE	Hydride Vapor-Phase Epitaxy
AMMONO	Ammonothermal
MBE	Organic Molecular Beam Epitaxy
ARPES	Angle-Resolved Photoemission Spectroscopy
PSD	Photo-Stimulated Desorption
STM	Scanning Tunneling Microscope/Microscopy
TPD	Temperature-Programmed Desorption
UHV	Ultra-High Vacuum
XPS	X-ray Photoelectron Spectroscopy
TPXPS	Temperature-Programmed XPS
DOS	Density of States
LDOS	Local Density of States
STS	Scanning Tunneling Spectroscopy
LUMO	Lowest unoccupied molecular orbital
HOMO	Highest occupied molecular orbital
nAGNRs	n-Armchair Graphene Nanoribbons
JT-STM	Joule-Thomson STM
LN_2	Liquid Nitrogen
LHe	Liquid Helium
dI/dV	Differential Conductance
TBB	1,3,5-Tris(4-Bromophenyl)Benzene
DBTP	4,4”-Dibromo-P-Terphenyl
DAPPor	Diaminophenyl-Porphyrins
$(BrP)_2P$	5,15-(di-4-bromophenyl)porphyrin
PPP	Poly(Para-Phenylene)
AP	Appendix
PDOS	Projected Density of States

PBAND	Projected Band Structure
BS	Band Structure
FFT	Fast Fourier transform
L	Langmuir
CBCP	Bicyclo[1.1.1]Pentane-1,3-Dicarboxylic acid
TPA	Terephthalic Acid

Chapter 1

Introduction

The objective of this thesis was to develop and investigate new materials to study electronic properties, such as electronic transport, optical absorption, and excited state imaging, in highly ordered molecular monolayers, polymeric organic wires, and sheet structures [1-7]. Nanostructures were examined on the surfaces of wide bandgap semiconductors, particularly gallium nitride (GaN) [8-13] and titanium dioxide (TiO_2) [14-17], and decoupling thin films like copper nitride (Cu_2N) [18-24]. These innovative heterostructures were fabricated through directed molecular assembly and on-surface synthesis [1-7]. This project integrated advanced interfacial molecular engineering on metal surfaces under ultra-high vacuum (UHV) conditions [1-7] with expertise in the growth and preparation of wide bandgap semiconductor substrates [8-12, 14-17] and decoupling layers [18-24]. Novel nanoscale lateral structuring techniques were developed to achieve unprecedented complexity and thoroughly explore the properties of these structures, which are promising for organic electronics and other rapidly advancing technologies [25-34]. The preparation and molecular-level characterization of highly ordered molecular assemblies and polymeric nanostructures on different substrates under UHV conditions, utilizing scanning tunneling microscopy (STM), ST spectroscopy (STS), low energy electron diffraction (LEED), temperature-programmed desorption (TPD), and x-ray photoelectron spectroscopy (XPS), is a rapidly growing field. It opens novel avenues for atomically precise fabrication of functional interfaces and heterosystems [35-38], enhanced by recent advances in covalent interfacial architectures [39-42]. A notable example is the implementation of low-energy electron irradiation on long alkene molecules deposited on an Au (110) surface, controlling and inducing structural changes followed by thermo-activated polymerization. STM monitored the corresponding detailed packing structures [43].

However, metallic substrates are unsuitable for investigating the electronic and optical properties of molecular nanosystems, such as lateral electronic transport, photoluminescence, or STM imaging of optically excited states, because the metallic substrate quenches or short-circuits the properties of interest [1-7, 35, 44]. An elegant solution is to use wide bandgap semiconductors such as GaN [8-12], TiO_2 [14-17], or diamond [45-48] as the substrate or to employ a decoupling film like Cu_2N [18-24] on a metallic surface. These wide band gap semiconductors are transparent to light up to the far UV spectral range. They can be substitutionally doped to control their electrical conductivity, making them suitable for STM imaging or other surface science techniques [8-12]. This enables the partial transfer of self-assembly strategies to non-metallic substrates, such as graphene monolayers on diamond [46]. Molecular self-assembly is a versatile nanofabrication technique that achieves atomic precision, paving the way for molecule-based electronic components and devices. For example, supramolecular bi-component network architectures on an all-carbon sp^2-sp^3 transparent platform have been reported, with an optimized fabrication procedure providing clear evidence for a photoactive molecular sheet structure [45]. The substrate consists of a hydrogenated diamond decorated with a monolayer graphene sheet. The bilayer assembly of a

melamine−naphthalenetetracarboxylic diimide supramolecular network, exhibiting a nanoporous honeycomb structure, was initially explored via STM at the solution-highly oriented pyrolytic graphite interface [45-48]. This research opens a new field that offers unexplored optoelectronic properties and functionalities and focuses on ordered super-molecular assemblies and covalent nanostructures on established wide bandgap semiconductor substrates. Below, we will briefly introduce the different chapters of this thesis.

GaN has garnered significant attention in optical and electronic research and devices due to its notable properties, including bandgap tunability, dopability, and transparency to light up to the UV spectral range [8-12]. GaN-based devices [25-27, 34] have been extensively studied [9, 49, 50]. As an alternative to metallic surfaces, GaN is a potential candidate for hosting epilayers or (self-)assembled molecular structures, preventing the strong quenching of electronic excitations [1-7]. Therefore, controlling the surface and interface processes of GaN thin films and single crystals is critical for advancing GaN-based devices, as many applications employ heterostructures comprising thin films of various materials on the GaN surface [9, 51-55]. Upon exposure to air, the surface of wz/zb GaN forms an approximately 1 nm thin gallium oxide film [9]. This oxide layer significantly limits surface science research, preventing direct access to the pristine GaN surface. Therefore, removing the topmost oxide layer using different cleaning methods is crucial for assessing the intrinsic properties of the GaN surface [9, 51, 56-60]. In Chapter 3, we investigated free-standing silicon (Si)-, germanium (Ge)-, and oxygen (O)-doped C-plane wurtzite (wz) GaN surfaces for potential applications in surface science. We investigated the influence of sputtering, annealing, ammonia (NH_3), electron bombardment, and bromine (Br) desorption on the nitrogen (N) to gallium (Ga) atomic ratio near the surface and surface roughness.

Copper nitride thin films have versatile potential applications, such as microelectronic semiconductor materials [23, 61], lithium and sodium-ion batteries [62], and materials for maskless laser writing [18, 24]. These thin films exhibit promising physical properties [18, 63], low cost [18, 63, 64], non-toxicity [18, 21], high optical absorption coefficients in the solar spectrum [65], and high stability [18, 22, 66, 67]. Various mechanisms for the fabrication of copper nitride thin films have been reported [18, 23, 64, 68, 69]. Due to the low reactivity of copper and nitrogen, replacement methods have been the most common method for preparing copper nitride in the past [18, 70, 71]. This approach prepared cuprous oxides using the solution-based Russell's method, converted into copper nitride under NH_3 dosage [70-75]. In Chapters 4-6, we investigated the fabrication and properties of the Cu_2N decoupling layer on Cu (111) and Cu (100) surfaces. We developed a new fabrication method in UHV, replacing O atoms in copper oxide with N atoms from NH_3 gas during the surface annealing. The decoupling effect of these films, as well as on-surface molecular adsorption, assembly, and reactions such as Ullmann coupling, were investigated.

TiO_2 is the most extensively studied metal oxide in surface science [14-17]. It is used for various applications, including solar cells, corrosion protection, catalysis, bioimplants, memristors, and gas sensors [14, 76-80]. Anatase [14, 81-87] and rutile [14, 88-95] TiO_2 are introduced for on-surface synthesis of one-dimensional (1D) or two-dimensional (2D) structures to avoid hybridization of the electron density of the epilayer molecules and structures with the substrate, unlike metallic substrates [1-7, 35, 88, 96, 97]. The rutile TiO_2 (110) surface is the most stable surface of this crystal [14, 98]. Rutile TiO_2, as a semiconducting oxide, is a well-known substrate for on-surface reactions and Ullmann coupling, prohibiting the quenching of electronic excitations required for reliable optical and electronic measurements [88-93]. Ullmann coupling provides a convenient method for producing conjugated polymers on this surface [88]. The efficiency of covalent coupling of aryl halides on reduced rutile TiO_2 significantly depends on the density of hydroxyls on the surface [88]. In chapters 7-8, we investigated the surface-assisted Ullmann coupling and the formation of n-armchair graphene nanoribbons (nAGNRs) on TiO_2 surfaces. We studied the catalytic effect of light and Fe ad-atoms on debromination reactions and C-C coupling.

Chapter 2

Principles of Experimental Methods

In this section, we describe the various techniques and equipment related to this thesis. The experimental setups are located in the laboratories at the Chair of Surface and Interface Physics (E20) at the Technical University of Munich (TUM) in Garching, Germany, and at the CAS Center for Excellence in Quantum Information and Quantum Physics at the University of Science and Technology of China (USTC) in Hefei, Anhui, China. These experiments were conducted in different UHV chambers equipped with various techniques, including STM, Scanning Tunneling Spectroscopy (STS), XPS, Temperature-Programmed XPS (TPXPS), LEED, and TPD. The reduced number of electrons scattered by gases in UHV makes it an essential requirement for spectroscopies and microscopies. Additionally, lower gas pressure leads to fewer surface reactions and oxidation, resulting in a cleaner surface, which is necessary for surface science [99-101].

2.1. X-ray Photoelectron Spectroscopy

XPS is a common spectroscopic technique for surface analysis based on the photoelectric effect, electron-surface interactions, and the influence of an element surrounding on its electrons binding energy [102-104]. In XPS, X-ray photons excite electrons from the core levels of atoms in solids into the vacuum, providing information about the electronic properties and structure of the materials with elemental, chemical state, and surface sensitivity. When a photon with energy $\hbar\omega$ excites an electron with a binding energy E_b, the electron adsorbs the entire energy of the photon and moves to an unoccupied state above the vacuum level. Therefore, the incident photon emits a photoelectron into the vacuum with a kinetic energy described by Equation 2.1. $\hbar$, ω, E_b, and E_{kin} are Planck's constant, photon frequency, electron binding energy, and ejected electron kinetic energy, respectively. A hemispherical electron energy analyzer (HEEA) collects and detects the ejected electrons, as shown in Fig. 2.1 [100].

$$\hbar\omega - E_B = E_{kin} \qquad \text{Equation 2.1.}$$

For solids, binding energy (E_b) is calculated based on the Fermi level rather than the vacuum level, as shown in Fig. 2.1. Therefore, Equation 2.2 describes the kinetic energy of an emitted electron from a solid surface. ϕ_ω is the work function of the materials, which is the minimum required energy to eject an electron from the solid surface to the vacuum [100].

$$\hbar\omega - E_b - \phi_\omega = E_{kin} \qquad \text{Equation 2.2}$$

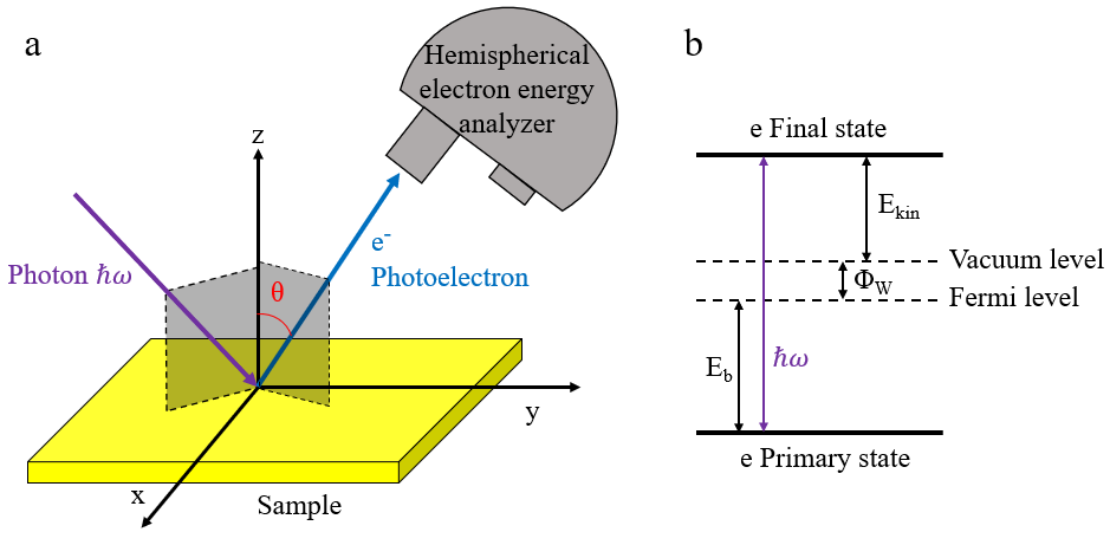

Fig. 2.1. Schematic views of (a) a photoelectron emission and HEEA setup and (b) the relation between the binding and kinetic energies of an electron and its Fermi and vacuum levels.

At a specific incident photon energy, spectra of the number of emitted photoelectrons versus the kinetic energy or binding energy, as defined by equation 2.2, can be plotted. This spectrum identifies the binding energies of electrons in the core levels of each element. Since no two elements have the same set of binding energies, XPS spectra serve as fingerprints for different elements. All elements are recognizable by XPS, except hydrogen and helium due to the absence of core level electrons in these atoms. Furthermore, various chemical environments lead to shifts in the XPS peaks, known as chemical shift. For example, higher positive oxidation states shift the peaks to higher binding energies. This shift is due to the presence of stronger coulomb interactions with the ion core as a result of a valence electron loss from chemical bonding. The shape and width of XPS peaks depend on various parameters, such as instrumental variations. For example, the line shape and width of the incident X-ray line used to excite the electrons, and the HEEA pass energy and resolution influence the obtained full-width at half maximum (FWHM). Broadening effects, such as the lifetime of core holes, thermal effects of intramolecular vibration modes (phonons), excitation of electron-hole pairs around the fermi level (many-body effect), and shake-up satellites, can affect the obtained spectral peaks. Thus, the corresponding FWHM is larger for electrons in inner shells and for atoms with larger atomic numbers. The total FWHM is calculated by taking the square root of the quadratic sum of the FWHM values caused by each effect. Besides that, core-level line splitting can be monitored due to spin-orbit coupling effects, which result from the interaction between an unpaired spin and orbital angular momentum [100].

The mean free path of electrons (λ_e) is the average distance an electron can travel within a material without experiencing inelastic collision, scattering, or energy loss. Since primarily electrons that do not lose energy are important in XPS, the mean free path of electrons is a critical parameter. Electron spectroscopies, including XPS, are surface-sensitive due to the short mean free path of electrons in solids and the strong interaction between the solid surfaces and electrons. In a grazing emission geometry, an incident photoelectron beam is emitted onto the sample at an angle of θ from the surface normal. Therefore, in this case, the sampling depth is $3\lambda_e \cos\theta$ and the measurement becomes more surface-sensitive [100, 105].

Assuming that the excitation of an electron above the vacuum level does not affect the energy state of other core electrons, we obtain the binding energy of the electrons using Koopman's theorem, as shown in Equation 2.3. In this equation, $E_B(\upsilon)$, $E_f(N-1)$, $E_i(N)$, and ε_υ represent the binding energy of an electron, the energy of the ground state of an atom with N electrons, the energy of the final state of an atom with N-1 electrons, and the energy of an electron in state υ below the vacuum level, respectively. However, in reality, the emission of a core electron influences the energy state of other core electrons. After the removal of a

photoelectron, the other core electrons rearrange and relax due to the formation of a positive hole in a core-level of the atom. Consequently, Koopman's binding energy is higher than the observed binding energy, leading to a shift in the measured binding energies around 10-20eV [100].

$$E_B(v) = E_f(N-1) - E_i(N) = -\varepsilon_v \qquad \text{Equation 2.3.}$$

The final relaxed electrons system after photoemission possesses less kinetic energy. Photoemission leads to the excitation of a bonded electron to higher unoccupied levels, causing satellite peaks to shift to higher binding energies. As shown in Fig. 2.2, shake-up and shake-off satellites arises from the excitation of an additional valence electron from an occupied state to an unoccupied bonding level and above the vacuum level, respectively. Additionally, as shown in Fig. 2.3, plasmon loss satellites result from the excitation of quantized plasma, so-called collective oscillations of the free electron gas relative to the cation cores. These satellites are shifted to higher binding energies by values $n\hbar\omega_p + m\hbar\omega_s$ compared to the elastic line. In this equation, n and m are integers, and $\hbar\omega_p$ and $\hbar\omega_s$ represent the surface and bulk plasmon energies, respectively [100].

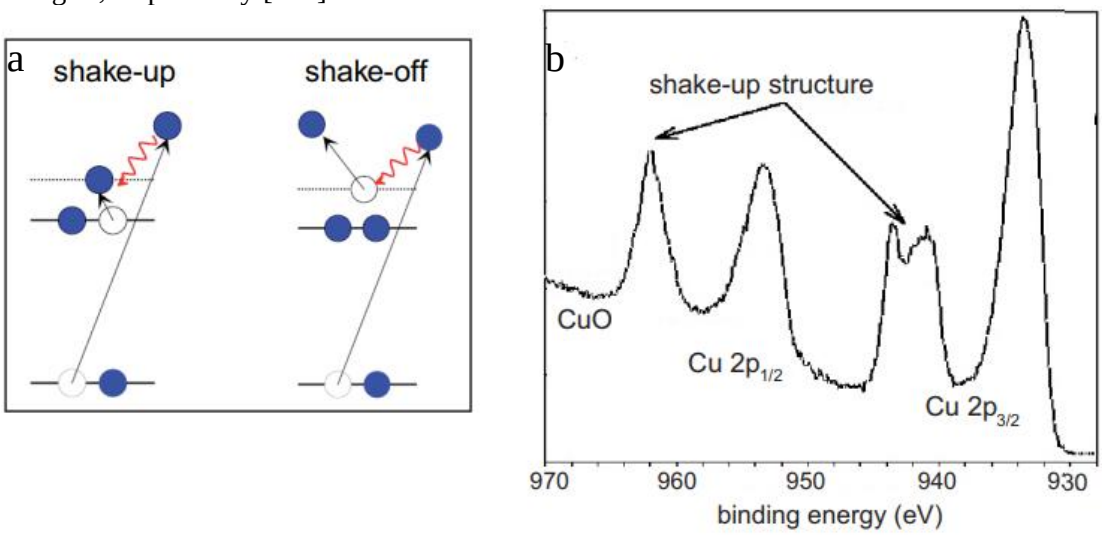

Fig. 2.2. Schematic view of the shake-up and shake-off transitions in an element. This image is sourced from reference [106]. (b) A shift in the Cu 2p peaks of copper oxide due to shake-up loss. This image is sourced from reference [106] and adapted from reference [107].

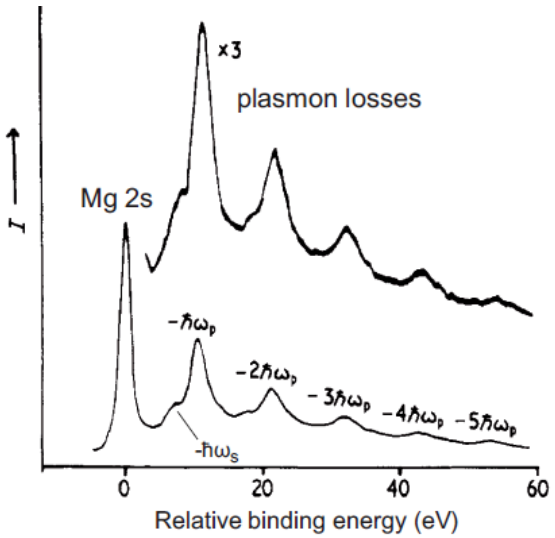

Fig. 2.3. Narrow region Mg 2s core-level XP spectrum, depicting satellites due to plasmon losses. This image is sourced from reference [106] and adapted from reference [108].

There are two distinct de-excitation mechanisms for an excited electron. This electron can decay from a higher energy level to a lower energy level by emitting a photon with energy equal to the difference in binding energies of these two levels. This mechanism is known as fluorescence. Another mechanism is known as Auger electron emission, in which an electron from an outer shell decays to fill a hole in an inner shell, and the energy is transferred to another electron in the outer shell, causing its emission. Core level lines and Auger lines can be distinguished from each other in the spectrum. By changing the photon energy, the kinetic energy of Auger line remains fixed, while it changes linearly for core level lines according to Equation 2.2. Furthermore, secondary electrons produced by inelastic scattering contribute to the presence of a featureless and step like background on which all photoemission features are superimposed [100, 108, 109]. Resultant XPS peaks can be fitted using Voigt, Gaussian, and Lorentzian line shapes for further analysis. Metal photoelectron peak fitting exhibits more Lorentzian character than Gaussian character. In addition, conducting materials exhibit an exponential tail due to conduction band interactions, which can be fitted using a Voigt function [110]. Moreover, there is no well-established method for background subtraction in XPS data analysis. One reason is that the background of a mixed material can differ from the mixture of the background of the related pure materials, even when using the same XPS equipment. To treat and analyze the background of the Fe 2p spectrum, either the Shirley or the parametric Tougaard method can be used [110, 111]. The Tougaard background reduction method is based on the contribution of inelastically scattered electrons losing some amount of energy [102, 107, 110]. For quantitative analysis of the ratio of two different atoms in detected molecules or structures in XPS spectra, we compare ratio of the corresponding intensities divided by their sensitivity factor. In this context, when fitting a core-level electron in XPS peaks, the contributions of different possible bonds such as C-C, C-N, C-H, and C-H_3 must be considered [103].

In XPS, the HEEA analyzes the energy of emitted electrons by dispersing them according to their kinetic energy. As shown in Fig. 2.4, electrons are focused by an electrostatic lens and enter the HEEA at S point. A potential difference (ΔV) is applied between the inner and outer spheres. This potential difference bends the path of electrons according to their kinetic energy. Only electrons with a specific kinetic energy, called the pass energy (5-50 eV for XPS measurements), can reach the detector at F point. The lower the pass energy, the higher the resolution of the energy analysis. For XPS measurements, we set a constant pass energy (E_P) to achieve a specific resolution [112]. Furthermore, by recording the XPS spectra of a core-level electron during precise heating of the surface at a constant rate, a TPXPS profile can be acquired, and each XPS spectrum for a given temperature can be plotted.

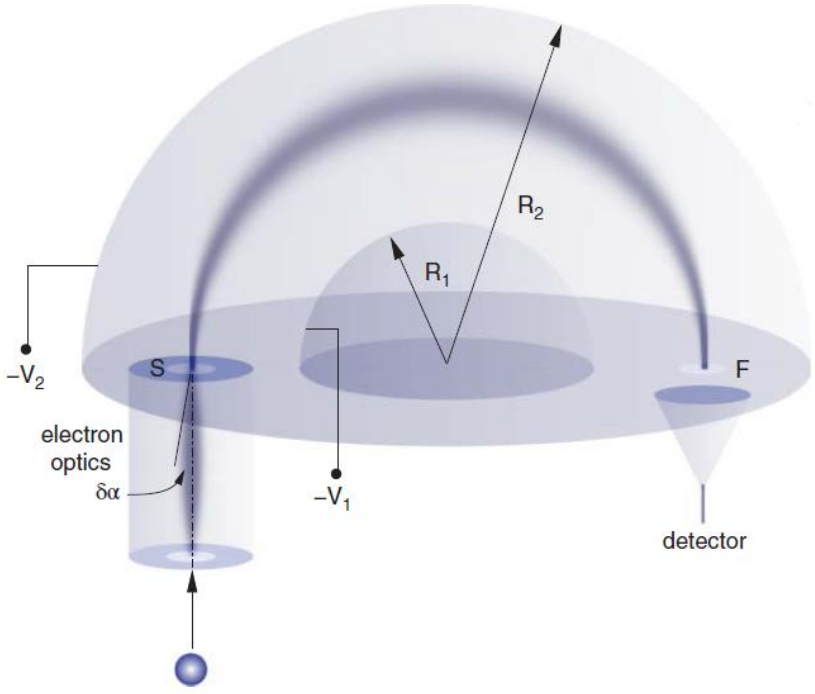

Fig. 2.4. Schematic view of HEEA having two hemispheres at negative potentials. This figure has been taken from the reference [112].

2.2. Temperature-Programmed Desorption

In the TPD technique, a mass spectrometer monitors the desorption of molecules from the surface as it is heated at a constant rate, providing insight into desorption behavior and the interactions and bonds between molecules, molecular fragments, and the surface. As illustrated in Fig. 2.5, in the mass spectrometer, molecules and atoms are ionized by electron bombardment from a hot filament directed toward a positive grid and are then filtered based on their mass-to charge ratio (m/e). The positively ionized gas is accelerated by a field axis (FA) potential between four parallel rods, which create a quadrupole electric field that filters the cations. The resulting output is a plot of quadrupole mass spectrometer (QMS) intensity versus heating temperature. The quadrupole electric field is generated by applying an AC voltage with a DC offset. Two positively charged rods filter the lighter masses by causing them to collide with the rods due to large oscillation induced by the AC voltage. Conversely, two negatively biased rods destabilize the heavier masses. The AC field mainly focuses ions, while the DC field defocuses them. Consequently, the AC/DC ratio determines the resolution of the measurement [113-116].

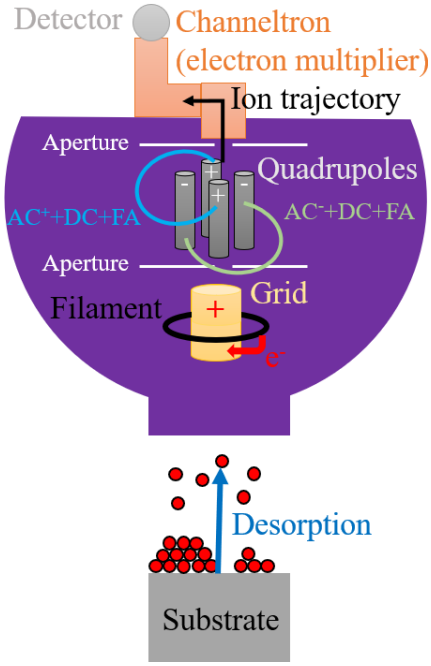

Fig. 2.5. Schematic representation of a simplified TPD setup.

By accounting for the initial temperature and the constant heating rate, the relation between time and temperature can be determined to measure molecular desorption at various surface temperatures. The desorption rate follows an Arrhenius-type behavior, as described by the Polanyi-Wigner equation in Equation 2.4. Here, n, ν_x, x, E_{des}, k_B, , β, and T represent the concentration of desorbing species on the surface, the frequency factor, the order of desorption, the activation energy, the Boltzmann constant, the linear heating rate, and the surface temperature, respectively [113, 116].

$$-\frac{dn}{dT} = \frac{\nu_x n^x}{\beta} e^{-\frac{E_{des}}{k_B T}} \qquad \text{Equation 2.4.}$$

When $x = 0$, zero-order desorption occurs, which is typically observed in thick multilayers. Since the multilayer is considered unlimited in this scenario, desorption is independent of the particle concentration (n) and coverage. In first-order desorption, each desorbed particle in the gas phase corresponds to one adsorbed particle. This implies that molecules do not dissociate

during adsorption or desorption [113, 116-119]. When $x = 1$, the desorption rate is directly proportional to n. Consequently, maximum desorption occurs at the same temperature for varying coverages [116, 117]. In second-order desorption, molecules dissociate upon adsorption and reassociate during desorption [113, 116, 117, 120].
Key concepts related to TPD include physisorption and chemisorption. As anticipated, in the absence of chemical bonds, the adsorption energy for physisorption is significantly lower than chemisorption. Therefore, during TPD, physiosorbed compounds desorb at lower temperatures compared to chemisorbed specifies. Examples of physiosorbed species include multilayer adsorption on various surfaces and the physisorption of rare gases on metal surfaces at sufficiently low temperatures [116, 121-123].

2.3. Low-Energy Electron Diffraction

The LEED technique utilizes low-energy electrons primarily for the analysis of 2D atomic structure of the surface, as well as the extended order, symmetry, and periodicity of adsorbed molecular layers relative to the substrate surface [100, 116, 124]. At typical electron energies used in LEED (20-300 eV), the de Broglie wavelength of electrons ranges from 1 to 2 Å, comparable to the interatomic distances in crystalline structures [100]. The mean free path of low-energy electrons is short enough, on the order of a few atomic layers, ensuring that most elastic collisions occur near the surface [100]. In Equation 2.5, λ, h, m, and E denote the de Broglie wavelength of electrons, Planck's constant, electron mass, and the kinetic energy of photoelectrons, respectively [100]:

$$\lambda = \frac{h}{\sqrt{2mE}}, \lambda[\text{Å}] = \sqrt{\frac{150}{E(eV)}} \qquad \text{Equation 2.5.}$$

Constructive interference occurs when diffraction satisfies the Laue condition for elastic scattering, as shown in Equation 2.6, where k, k_0, and G represent the wavevector of the scattered electron beam, the wavevector of the incident electron beam, and the vector of the periodic reciprocal lattice [100, 116]:

$$k - k_0 = G \qquad \text{Equation 2.6.}$$

As shown in Fig. 2.6, the experimental setup of LEED consists of an electron gun that produces a collimated low-energy electron beam to bombard the sample, which is mounted on a holder, and a hemispherical fluorescent screen to monitor the diffraction pattern. The sample is centered on the curvature of the screen and aligned with its four sets of grids. The electron gun consists of a cathode filament, equipped with a Wehnelt cylinder, held at a negative potential, and an electrostatic lens. The last aperture of the lens, the sample, and the first grid are held at ground potential. Consequently, the cathode emits electrons toward the sample surface. Electrons are accelerated through the gun, propagated, and scattered from the sample surface. The second and third grids are held at a negative potential, preventing inelastically scattered electrons from passing through. The larger the potential difference (ΔV) between the cathode and the second and third grids, the more intense LEED patterns and background become. Thus, ΔV is adjusted to optimize the contrast between the diffraction spots and the background. The fourth grid, held at potential, accelerates the diffracted electrons that pass through the retarding grids to high energy for detection on the fluorescent screen [100].

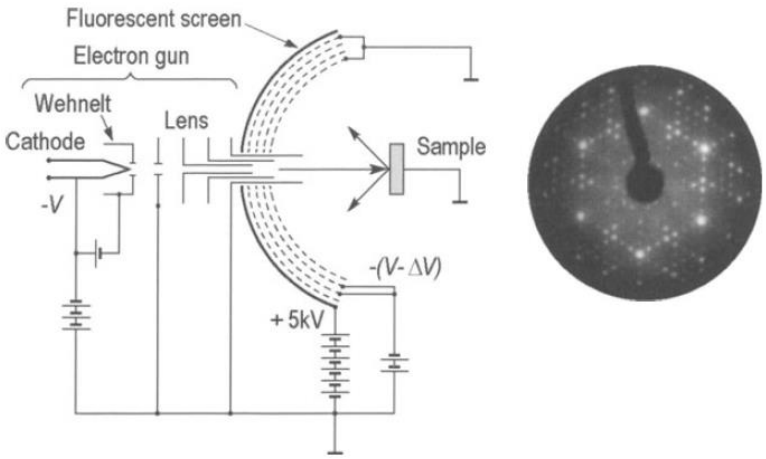

Fig. 2.6. Schematic of a LEED experimental setup and the corresponding LEED pattern of a Si(111)7×7 surface. This image is sourced from reference [100].

The diffraction pattern observed in LEED provides a view of the surface reciprocal lattice, as predicted by the Ewald sphere. The radius of the Ewald sphere is proportional to the inverse of the electron wavelength [100]. A sharp and bright LEED pattern with low background intensity indicates a well-ordered crystalline surface structure. An increase in surface defects and imperfections, along with a decrease in surface crystallinity, leads to the broadening of diffraction spots. Additionally, these factors reduce the sharpness and brightness of the diffraction pattern and decrease the contrast between the LEED spots and the background [100]. Two notations are commonly used to describe the surface crystalline structure: matrix and Wood's notation. Matrix notation displays the basic translational vectors of the surface structure (superstructure) in relation to those of the substrate crystal. Wood's notation describes the superstructure in terms of the substrate plane on which it is formed, the ratio of translational vectors between the substrate and superstructure, and the rotation angle of the superstructure relative to the substrate axes, as shown below [100]. A matrix notation of $\begin{bmatrix} G_{11} & G_{12} \\ G_{21} & G_{22} \end{bmatrix}$ represents the correlation between the superstructure and the substrate, as illustrated in Equation 2.7, where a_s and b_s are the basic translational vectors of the superstructures, and a and b are those of the substrate [100].

$$a_s = G_{11}a + G_{12}b, b_s = G_{21}a + G_{22}b \qquad \text{Equation 2.7.}$$

Besides that, Wood's notation is utilized to describe the structure of the superstructure on the surface. If the superstructure forms on the substrate X on the (hkl) plane. If the vectors of the superstructure are defined as $|a_s| = m|a|$ and $|b_s| = n|b|$, and it is rotated by an angle φ relative to the main plane [100], and the adsorbate inducing the superstructure is Y, then Wood's notation is given as shown in Equation 2.8:

$$X(hkl)m \times n - R\varphi - Y \qquad \text{Equation 2.8.}$$

If no adsorbate induces the superstructure and the rotation angle is 0°, the terms $-R\varphi - Y$ are omitted from Equation 2.8.

To better understand atomic positions in the surface structure, a plot of intensity versus primary electron energy, known as the IV curve, is highly useful. In the LEED technique, the IV curve can be measured using a TV camera or by directly measuring the beam current with a movable Faraday cup [100]. To check the consistency between experimental and calculated IV curves, a criterion called R-factor (reliability factor) is used. The R-factor takes into account various parameters of consistency, such as the shape of the curve, the presence and position of maxima and minima, background intensity, and other features. An R-factor below 0.2 indicates good agreement between experimental and calculated IV curve. An R-factor of 0.5 indicates a poor agreement between IV curves [100].

2.4. Scanning Tunneling Microscopy

STM, pioneered by Binnig and Rohrer at IBM Zurich in 1981-1982 [125], is a non-destructive surface investigation technique that leverages the tunneling current between a probe tip and a conductive surface. STM can be operated under diverse conditions, including ambient, UHV, and liquid environments. STM is incompatible with insulating materials, as electronic states are absent at the energy levels accessible by the applied sample bias. STM offers atomic resolution microscopy (Å), making it a powerful tool for surface science by providing detailed information on surface topography and the distribution of electronic states [125-128]. This technique typically employs atomically sharp tips, usually made of metals such as tungsten (W), platinum-iridium (Pt-Ir), and gold (Au). Tip preparation methods vary and include grinding, etching, cleavage, as well as in situ steps like annealing, evaporation, and soft crashing [100].
STM operates primarily in two modes: constant height and constant current, where the tunneling current and height profile are measured, respectively. The distance between the tip and the conducting sample typically ranges from 4 to 10 Å, with an applied bias voltage spanning a few millivolts to several volts. The distance between the tip and the surface is precisely controlled by a piezo scanner, as illustrated in Fig. 2.7. The tunneling current can be calculated using the Schrödinger equation, as defined in Equations 2.9 and 2.10. In these equations, $\hbar, m, z, \psi, V, E, I_t, C, d,$ and V_0 denote Planck's constant divided by 2π, electron mass, distance from the zero point, wavefunction, potential energy, electron energy, tunneling current, a constant, the distance between the tip and the sample, and the potential barrier, respectively. In metals, E corresponds to the Fermi energy (E_F), while V equals the vacuum energy (E_{vac}). Therefore, the work function (Φ) of the metal, defined as the difference between the vacuum and Fermi energies ($V_0 - E = E_{vac} - E_F = \Phi$), plays a critical role [126, 129-131].

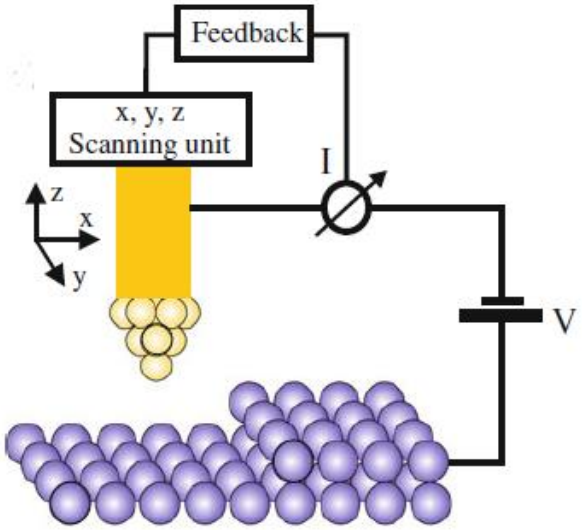

Fig. 2.7. Schematic of STM operation based on tunneling current between a conducting tip and surface under an applied bias voltage. V and I (I_t) represent the tunneling bias and current, respectively. The distance between the tip and surface (d) ranges from 4 to 10 Å. The yellow rectangle indicates the piezo scanner. Image sourced from reference [126].

$$-\frac{\hbar}{2m}\frac{d^2\psi}{dz^2} + V\psi = E\psi \qquad \text{Equation 2.9.}$$

$$I_t = C.\exp(-2\kappa d) = C.\exp(-2\frac{\sqrt{2m(V_0-E)}}{\hbar}d) \qquad \text{Equation 2.10.}$$

The direction of the tunneling current depends on the applied bias voltage, considering the band alignment and Fermi levels for the tip and the sample, as depicted in Fig. 2.8. A negative sample bias raises the sample's Fermi level relative to the tip, causing the tunneling current to flow from the sample to the tip, and in vice versa. Consequently, positive and negative sample biases allow the probing of surface's empty and filled states, corresponding to the highest occupied

molecular orbitals (HOMOs) and lowest unoccupied molecular orbitals (LUMOs) of the sample [126].

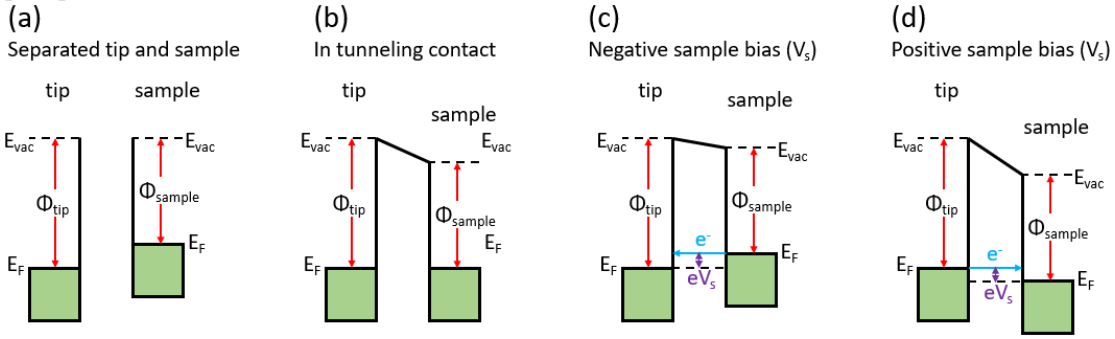

Fig. 2.8. Schematic representations of Fermi levels and band alignment of a tip and a sample under an applied bias voltage. (a) The tip and sample are separated, maintaining the same vacuum level. (b) In tunneling contact, the Fermi levels of the tip and sample align. (c) Tunneling current flows from the filled states of the sample to the empty states of the tip under a negative sample bias. (d) Under a positive sample bias, tunneling current flows from the filled states of the tip to the empty states of the sample.

During STM operation, the tip's position is precisely controlled and adjusted by a piezoelectric material. The actuator elements finely adjust the tip position in response to the voltage applied to their electrodes. The tip is brought close to the surface until a suitable tip-sample distance is achieved for tunneling current generation. The tip then scans the surface line by line, collecting tunneling current and apparent height data for constant height and constant current modes, respectively as shown in Fig. 2.9. As the tip-sample distance decreases, the tunneling current increases. A 0.1 Å decrease in the tip-sample distance can result in a 20% increase in tunneling current. Thus, the tunneling current serves as a precise parameter for determining and adjusting the tip-sample distance. In constant current mode, a feedback loop adjusts the tip height to maintain a constant tunneling current, preventing the tip from crashing into the sample. This allows the topography image to be obtained by monitoring changes in the tip's z-axis position. On the other hand, in constant height mode, the average distance between the tip and the sample surface is maintained without a feedback loop. Here, the tunneling current is continuously monitored and measured. The apparent height, inferred from the tunneling current, can be influenced by electrical effects. For example, two atoms of the same height on the surface may appear differently when measured by the same tip. In an STM image, the more conductive atom, located at the same height as the other atom, will appear higher at a constant tunneling current [126].

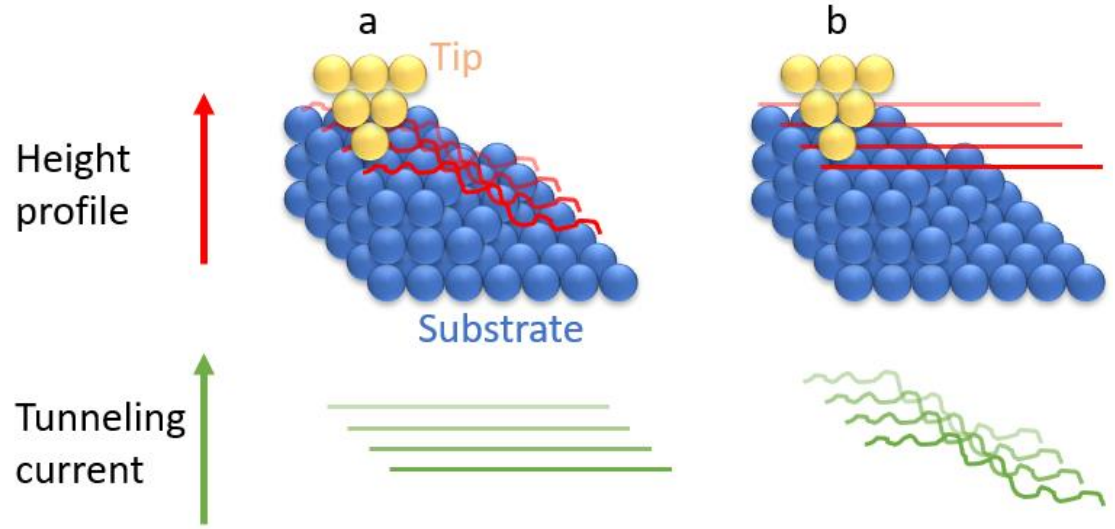

Fig. 2.9. Schematic of STM operation and measurement in (a) constant current and (b) constant height modes. Variations in the tunneling current and tip height relative to the sample along the scanning axis are represented by green and red lines, respectively.

STM has numerous applications, including investigating the atomic structure and electronic properties of single crystal surfaces [132], studying on-surface reactions [35, 133], and analyzing nanoarchitectures formed through techniques such as self-assembly [35, 134, 135] and nanofabrication [133, 136]. Additionally, STM can track particle movement and diffusion on surfaces [137], and monitor the growth of 2D materials, such as boron nitride (BN) monolayers, using various techniques on metallic single crystalline substrates [138].

2.4.1 Scanning tunneling spectroscopy

STS determines the density of states (DOS) of the sample by measuring variation in the tunneling current as a function of bias voltage across the tunneling junction. During an STS measurement, the tip height remains constant, while dI/dV measures the conductance and local DOS (LDOS), thereby revealing the HOMOs, LUMOs, and band gap of a specific surface location as the bias voltage is varied [100, 126]. DOS represents the number of electronic states within the sample in the energy range of E to $E + dE$. The number of states within the energy range from E_1 to E_2 can be calculated according to the Equation 2.11, considering $\rho(E)$ is the distributional function [139]:

$$N(E_1, E_2) = \int_{E_1}^{E_2} \rho(E) dE \qquad \text{Equation 2.11}$$

The LDOS is illustrated using Equation 2.12, considering $\psi_n(r)$ and δ are the probability of the particle at a specific position (r) and the Dirac delta function, respectively [139]:

$$LDOS = \rho(E, r) = |\psi_n(r)|^2 \delta(E - E_n) \qquad \text{Equation 2.12}$$

Beyond point spectroscopy, spatial mapping of the electronic structure in a specific surface region can also be achieved. Spectroscopic imaging can be performed by scanning a surface feature at a constant current using a specific voltage, thereby mapping the LDOS across different pixels [126].

2.5. Instrumentation, data acquisition, and analysis

2.5.1 The Spectroscopy-Based Chambers

We conducted XPS measurements detailed in this thesis using two custom-built UHV chambers at E20 laboratories: The Photo-Stimulated Desorption (PSD) and Electron Spectroscopy for Chemical Analysis (ESCA) chambers, depicted in Fig. 2.1a and 2.1b, respectively. UHV conditions were achieved through a three-stage pumping process, beginning with primary pumping down to 10^{-3} mbar, followed by turbomolecular pumping to a pressure range of 10^{-8}-10^{-9} mbar. The chambers were then baked to reach a final pressure of 10^{-10}-10^{-11} mbar, which was maintained by an ion pump. These chambers were equipped with panchromatic Kα radiation sources from Mg and Al anodes, and feature SPECS Phoibos 100 CCD HEEAs for XPS. XPS measurements were performed using the SpecsLab2 software (version 2.74-r24090). In addition, SPECS LEED instruments are integrated into these chambers. The sample temperature can be controlled from 77 K, using liquid nitrogen (LN_2), to over 1200 K, using heating filaments situated below the supporting plate. Temperature measurements are precisely managed a K-type thermocouple affixed to the sample, and controlled by a proportional-integral-derivative (PID) controller (Schlichting Physikalische Instrumente HS 130), ensuring accurate temperature regulation essential for TPXPS and TPD experiments. For TPD measurements, a SPECS mass spectrometer is attached to the chamber to monitor desorbing masses during controlled heating. The manipulator provides rotational movement along the z-axis and translational movement along the x-, y-, and z-axes. These chambers are equipped with multiple ports, allowing the attachment of various instruments, including costume-built metal evaporators, molecular evaporators such as organic molecular beam evaporators (OMBEs), gas

dosing systems, and light emitting diodes (LEDs). Detailed images of the chambers interiors and further information about the experimental setups are available in the experimental sections of different chapters and in the appendix.

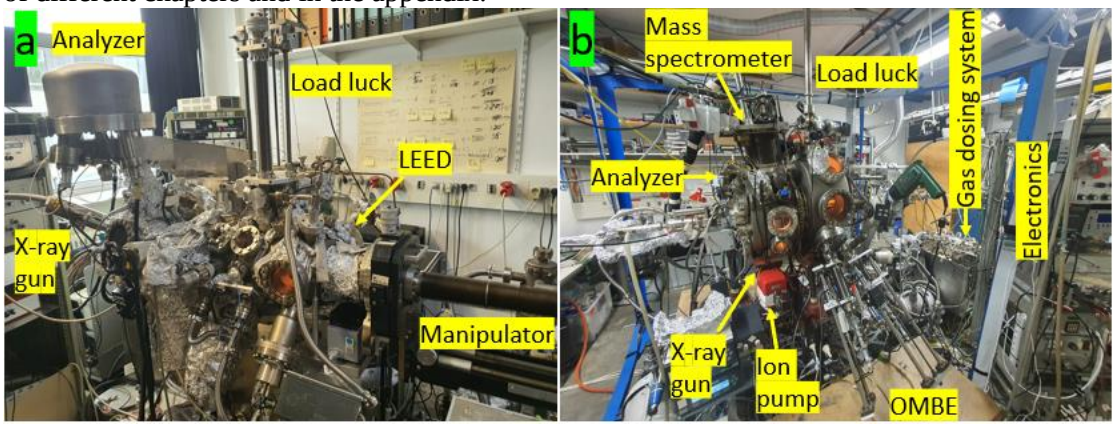

Fig. 2.10. Photographs of (a) ESCA and (b) PSD chambers.

2.5.2 Scanning Tunneling Microscopy Chambers

We carried out STM measurements in two distinct chambers: a commercial SPECS Joule-Thomson (JT)-STM [140] chamber at E20, TUM School of Natural Science and an Omicron low-temperate chamber at the CAS Center for Excellence in Quantum Information and Quantum Physics at USTC in Hefei, Anhui, China. The JT-STM chamber operates at temperatures of LN_2 (77 K), liquid He (LHe) (4 K), and JT-cooler (1.2 K), while the Omicron chamber operates only down to LN_2 temperature. Both setups consist of separate STM and preparation chambers, divided by a shutter. STM head, connected to the cryostat, is housed in the STM chambers, alongside sample parking stages. The preparation chambers are equipped with an ion sputtering gun, dosing valves, metal evaporators, and molecular evaporators, such as OMBEs. Additionally, load lucks are attached to the preparation chambers to facilitate sample loading and unloading. The JT-STM chamber is also outfitted with a SPECS LEED instrument mounted separately on the chamber. A manipulator allows for precise samples positioning for sputtering, annealing, molecular deposition, gas dosing, and transfer. To minimize external vibrations and noises, the chambers are mounted on four damping legs, which result in a floating instrument with reduced noise levels. Noises from the cooling system, particularly from the LN_2 and LHe outlets, is mitigated by hanging the STM head an eddy current damping spring. Furthermore, the entire instrument is grounded to eliminate electrical noise. Most STM data for this project were collected in constant current mode unless otherwise specified. The sample bias serves as the reference for mentioned bias voltages. STS data were acquired using a digital lock-in amplifier on the JT-STM instrument, with the bias voltage modulated by an AC voltage of 1 kHz frequency and 10 mV amplitude. Additional photographs of the chamber interiors can be found in the appendix.

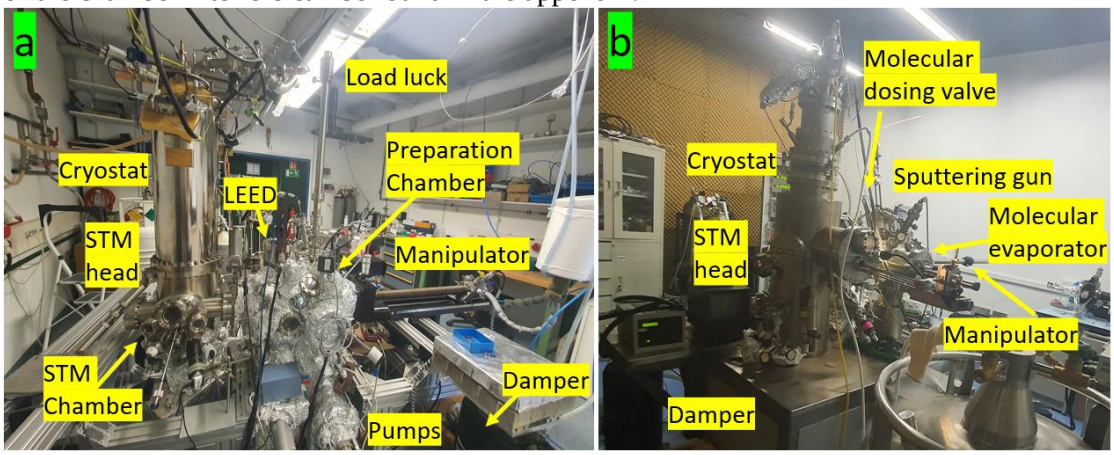

Fig. 2.11. Photographs of (a) JT-STM and (b) Omicron STM chambers.

Details on samples preparations, substrates, molecules, and specific experimental procedures are provided in the experimental sections of each chapter.

2.5.3 DFT Calculations

All the DFT calculations in this thesis have been done at Türkiye, Turkish Accelerator and Radiation Laboratory (TARLA) (Çağıl Kaderoğlu, Cagil.Kaderoglu@eng.ankara.edu.tr), Graduate School of Natural and Applied Sciences, Ankara University, 06110, Ankara, Türkiye (Pınar Kaya and Mahsa Seyedmohammadzadeh), Department of Physics Engineering, Faculty of Engineering, Ankara University, 06100 Ankara, 06830 Ankara, Türkiye (Handan Olgar), and Department of Physics, Adnan Menderes University, 09100, Aydin, Türkiye (Ethem Aktür, ethem.akturk@adu.edu.tr) and used by their permissions. The first principle plane wave calculations in Vienna *ab-initio* Simulation Package (VASP) program including Projector-Augmented Wave (PAW) calculations were utilized to obtain the results [141].

Chapter 3

Influencing the Surface Quality of Free-Standing Wurtzite Gallium Nitride in Ultra-High Vacuum: Stoichiometry Control by Ammonia and Bromine Adsorption

This chapter delves into the Influencing the surface quality of free-standing wurtzite gallium nitride in ultra-high vacuum: stoichiometry control by ammonia and bromine adsorption, including content that has been published in the following paper:
Rostami, M., Yang, B., Haag, F., Allegretti, F., Chi, L., Stutzmann, M. and Barth, J.V., 2024. Influencing the surface quality of free-standing wurtzite gallium nitride in ultra-high vacuum: Stoichiometry control by ammonia and bromine adsorption. Applied Surface Science, 674, p.160880. https://doi.org/10.1016/j.apsusc.2024.160880 [142].

3.1. Contributions

Mohammadreza Rostami: Experiments, Data Analysis, Writing, Review & Editing, Model drawing. Biao Yang: Experiments, Review & Editing. Francesco Allegretti: Experiment Discussion, Review & Editing. Lifeng Chi: Review & Editing, Supervision. Martin Stutzmann: Review & Editing, Supervision. Johannes V. Barth: Review & Editing, Supervision.

3.2. Introduction

In the last few decades, gallium nitride (GaN) as a wide bandgap semiconductor has attracted much attention in optical and electronic research and devices. This is due to its interesting properties, including bandgap tunability, dopability, and transparency to light up to the UV spectral range [8-12], which may foster advanced technological applications. GaN-based light-emitting diodes [25-27, 34], transistors [28-30], energy production [31-33], and catalyzers [57, 143-146] have been vastly investigated in, both, the stable hexagonal wurtzite (wz) [9, 49, 50] and the metastable cubic zincblende (zb) crystalline structures [147, 148]. In addition, as an alternative to metallic surfaces, GaN is a potential candidate for hosting epilayers or (self-)assembled molecular structures to avoid strong quenching of the electronic excitations [1-7]. Consequently, wide bandgap semiconductors such as GaN are promising alternatives as solid substrates for investigation of electronic properties of adlayers [9, 45, 46, 59, 149-151]. In this context, the control of the surface and interface processes of GaN thin films as well as single crystals is crucial for the development of GaN-based devices, since in many applications, heterostructures comprising thin films of various materials on the surface of GaN are employed [9, 51-55].

As soon as exposure to air occurs, the surface of wz/zb GaN is subjected to the formation of a ≈ 1 nm thin gallium oxide film [9]. This oxide layer is a major limitation for surface science research, preventing direct access to the pristine GaN surface. Therefore, to assess the intrinsic properties of the GaN surface, the removal of the topmost oxide layer by different cleaning methods is of crucial importance [9, 51, 56-60]. One major strategy to prevent the formation of the oxide layer on the GaN surface relies on the in-situ growth by molecular beam epitaxy (MBE) of GaN layers under UHV conditions [9, 56, 152-155]. For instance, Smith et al. [60] studied the surface reconstruction of GaN $(000\bar{1})$ films for the first time by STM and reflection high-energy electron diffraction (RHEED). They grew a 200nm thick GaN $(000\bar{1})$-terminated film on a sapphire (0001) substrate in a UHV chamber and reported four dominant surface reconstructions [60]. This underlines the importance of investigating the surface cleaning of GaN and the resulting GaN surface quality. In addition, cleaving a free-standing GaN sample in UHV for cross-sectional STM of the m-plane surface was reported by Banfi and coworkers [156]. On the other hand, the removal of the oxide layer on GaN single-crystalline surfaces by different cleaning methods was also investigated, employing high temperature annealing, ion sputtering and wet etching (Br_2) [9, 51, 52, 56, 57, 157, 158], on the metal-organic vapor phase epitaxy (MOVPE) [51] and metal-organic chemical vapor deposition (MOCVD) grown GaN [52]. However, none of the reported methods was completely successful, since surface quality, roughness, surface termination, stoichiometry, decomposition, reactivity and dopant segregation pose severe limitations to the surface cleaning process [9, 51, 52, 56, 57, 157, 158].

In the present work, hydride vapor phase epitaxy (HVPE) and ammonothermal (AMMONO) GaN crystals were investigated due to their smoother surface and smaller threading dislocation density compared to MOVPE GaN [159-179]. Refined surface cleaning methods were applied to O/Si/Ge-doped free-standing gallium (Ga) and nitrogen (N) polar c-plane wz GaN [180], with the aim to study the surface quality after removal of the oxide layer. Furthermore, the effect of ammonia (NH_3) annealing together with electron bombardment and the influence of bromine (Br) atoms desorption on the recovery of the preferential removal of N atoms during sputtering as well as the resulting surface roughness were investigated. The potential application of the resulting oxide-free surfaces as a template for surface-assisted Ullmann coupling reactions via debromination of 1,3,5-tris(4-bromophenyl)benzene (TBB) and 4,4″-dibromo-p-terphenyl (DBTP) was investigated (Fig. 10A.1, in the Appendix (AP)) [1-3].

3.3. Experiments

10 mm × 10.5 mm HVPE (AP, Table 10A.2) Si/Ge-doped and 10 mm × 10 mm epi-ready AMMONO (see the AP, Table 10A.3) O-doped n-type free-standing c-plane wz GaN samples

(Fig. 3.1a) were provided from MSE Supplies LLC company (US) and the Institute of High-Pressure Physics of the Polish Academy of Sciences (IHPP PAS; Warsaw, Poland), respectively. These samples have a ≈ 1 nm-thick natural oxide layer on the GaN surface. The properties of the Si and Ge-doped samples are nominally the same [9]. We characterized the Ga and N polar samples by XPS (photon lines: Mg $K_\alpha \approx 1253.6$ eV and Al $K_\alpha \approx 1486.6$ eV), LEED, and STM, after cleaning the samples by multiple cycles of Ar^+ or Ne^+-sputtering (1 keV, 10 minutes, I_{ion} ≈ 20 μA, ≈ 0.012 C) and annealing (950 K, 20 minutes). XPS and LEED measurements were performed in home-built UHV chambers. Due to the large thermal conductivity of doped GaN, a K-type (Nickel-Chromium / Nickel-Alumel) thermocouple was attached to the molybdenum plate supporting the GaN samples. The base pressure of the chambers employed was below 2×10^{-10} mbar.

In a commercial JT-STM (SPECS GmbH) chamber, conversely, the annealing temperature was measured via a pyrometer calibrated by a thermocouple. The base pressure of the preparation and principal STM chamber was 1.1×10^{-10} mbar and 8.5×10^{-11} mbar, respectively. The STM scans were acquired at liquid nitrogen (77 K) and close to liquid helium (He) (4.6 K) temperatures.

The TBB and DBTP powders were supplied by Sigma Aldrich (97%) and Shanghai Aladdin Bio-Chem Technology, respectively, and loaded into a quartz crucible of home-built OMBE. After surface cleaning, TBB and DBTP molecules were deposited on the Ge and Si-doped HVPE and O-doped AMMONO GaN surfaces, with the GaN substrates held at 100 or 300 K, respectively. The deposited molecular films were characterized by XPS and LEED. Subsequently, the samples were heated at certain rates (mostly 1 K/s) and annealed at different temperatures to study the onset of TBB debromination on the GaN surfaces by XPS and TPD (Fig. 3.1b).

We heated the sample from the back via radiation and bombardment with electrons emitted from a W filament, and dosed NH_3 gas at the same time or separately (AP, Fig. 10A.1). We investigated different processes by various combinations of Ne^+ (20 minutes, $I_{ion} \approx 23$ μA, 0.0276 C, $E_{ion} = 1$ keV) or Ar^+ (30 min, $I_{ion} \approx 5.8$ μA, 0.010 C, $E_{ion} = 1$ keV) sputtering, annealing (≈ 950 K), electron bombardment (electron energy = 220 eV/1000 eV, emission current = 1.5 mA), and NH_3 dosing ($P_{chamber} \approx 3 \times 10^{-8}$ - 1.3×10^{-6} mbar) (AP, Table 10A.1). The effects of these treatments (Fig. 3.1b) on the surfaces of GaN (0001) and (000$\bar{1}$) are discussed in Section 3.5.

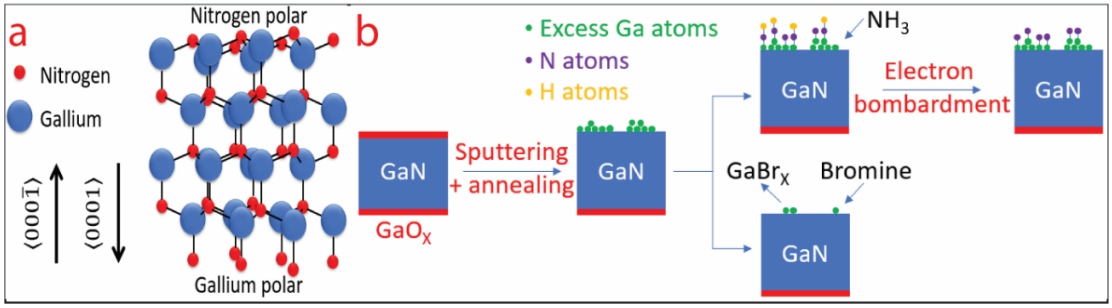

Fig. 3.1. a) Schematic view of the polar c-plane wurtzite GaN faces and b) our strategy for compensation of preferential removal of nitrogen.

3.4. Results and Discussion

3.4.1 HVPE GaN Surface Cleaning

Sputtering and annealing cycles have been developed to efficiently remove the oxide layer at the GaN surface. To this purpose, the optimum annealing temperature must be high enough to decompose the oxide layer and below the decomposition temperature of GaN in the UHV chamber (see the AP, Fig. 10A.2-AA.4). The cleanliness of the HVPE Si-doped free-standing GaN surface was investigated by XPS. The sample was O and C-free after the sputtering and

annealing cycles (see the AP, Fig. 10A.3), the amount of oxygen and carbon contamination being below the detection limit. On the other hand, the GaN surface cleaning changes the surface stoichiometry due to the preferential removal of the lighter atoms (N) by sputtering and annealing (see the AP, Fig. 10A.2-AA.4). The associated change of stoichiometry affects the surface morphology and leads to undesired changes in the surface roughness [9, 51, 54, 56, 181, 182].

Fig. 3.2 shows LEED patterns and STM images of the HVPE Si and Ge-doped free-standing GaN (0001) and $(000\bar{1})$ samples after cleaning. Fig. 3.2a shows the sharp (1×1) LEED pattern of Si-doped free-standing GaN (0001) after 7 sputtering (≈0.007-0.013C) and annealing (< 950 K) cycles, showing the good single-crystalline quality of the hexagonal wz GaN crystal. Fig. 3.2b shows an STM image of Si-doped GaN (0001) after these cleaning cycles. By annealing to higher temperatures, the oxide layer was also removed, but the surface became even rougher, made of randomly sized and shaped hillocks (roughness exceeding 0.75 nm), and with no atomically flat domains.

Prior to the formation of the oxide layer, the Si-doped GaN (0001) surface is nominally Ga polar with lattice constant ≈0.32 nm (Fig. 3.1a) [9, 53, 152, 154]. Preferential removal of N during sputtering and annealing leads to the presence of a Ga-richer surface. In addition, bombardment of the surface by ions forms defects and damaged areas that can not be sufficiently repaired by annealing. Moreover, due to the high mobility of Ga at high annealing temperatures, the Ga atoms rearrange and form unwanted clusters, crystallites, hillocks or facets. These large Ga-rich clusters and crystallites under which the sub-surface crystalline layer of GaN is buried increase the surface roughness significantly. A similar phenomenon is also observed for the N polar Ge-doped GaN $(000\bar{1})$ surface (Fig. 3.2c, see the AP, Fig. 10A.3).

In Fig. 3.2c, the HVPE Ge-doped free-standing GaN $(000\bar{1})$ sample was cleaned by 7 cycles of sputtering (≈ 0.020 C) and annealing (<950 K for 20-60 minutes). Due to the similar properties of Ge and Si-doped samples at small concentrations of dopants, we observed similar LEED and STM results for these samples (see the AP, Fig. 10A.3). Before cleaning the surface, the rms-roughness of the samples was less than 0.2nm. As shown in Fig. 3.2c, the surface became rougher and larger crystallites and hillocks formed (rms-roughness exceeding 0.79 nm). Therefore, although the surface oxide layer is removed and the surface is cleaned, no atomically flat region appears at the surface. Fig. 3.2d displays the size distribution of a disc radius, equivalent to the features projected area in the STM images shown in Fig. 3.2b and c. Same as for the previous STM image, in spite of the different image sizes, most of the features have sizes between 0-7.0 nm. The average features sizes in these two STM images are similar (≈4.5 nm for Fig. 3.2b and ≈4.1 nm for Fig. 3.2c), proving the similar behavior of (0001) and $(000\bar{1})$ GaN surfaces upon sputtering and annealing. More STM data are discussed in the AP, Fig. 10A.5 and AA.6. Based on previous studies, the most common surface reconstruction of GaN (0001) is a (2×2) reconstruction [9]. LEED patterns combined with the STM results indicate that the (1×1) LEED pattern comes from the crystalline bulk layers below the larger nanoclusters formed on the surface. This is also consistent with the reported inelastic mean free path (IMFP) of the electrons through GaN (IMFP ≈ 0.5 nm for E_{kin} ≈ 60 eV[52]).

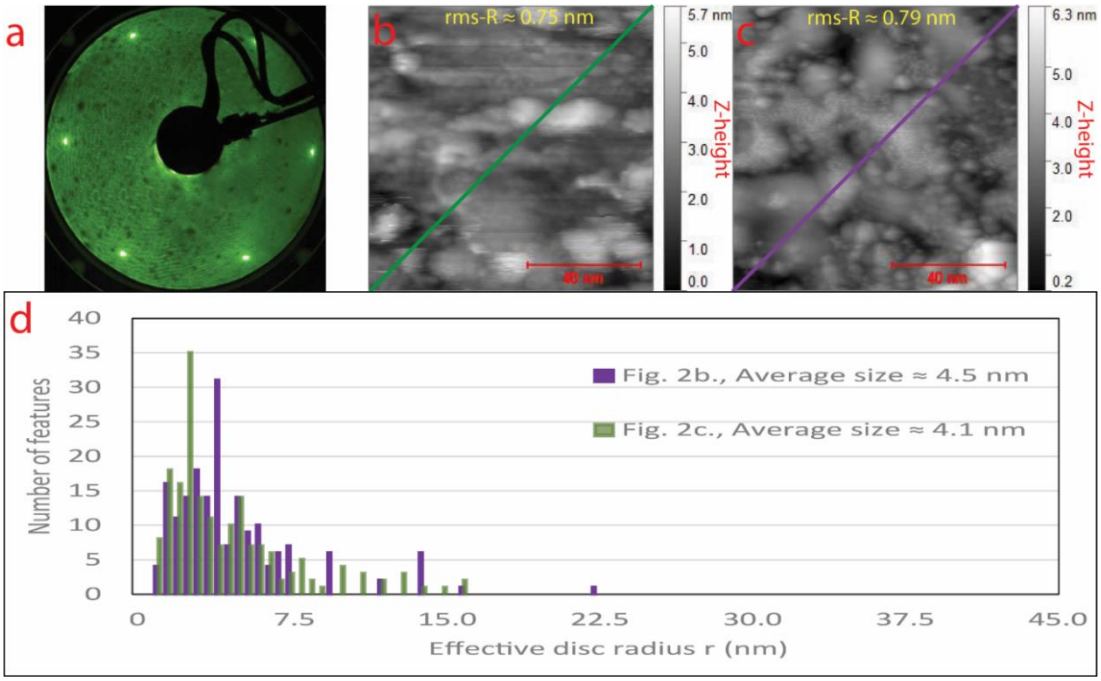

Fig. 3.2. (a) (1×1) LEED pattern (electron energy: 63 eV) of cleaned HVPE Si-doped free-standing GaN (0001). (b) STM image of HVPE Si-doped free-standing GaN (0001) after cleaning by seven cycles of sputtering and annealing up to 950 K; 100 nm × 100 nm, V_s=-4.00 V, I_t=100 pA, rms-roughness=0.75 nm. STM acquisition temperature: 4.6 K. (c) STM image of HVPE Ge-doped GaN $(000\bar{1})$ after nine cleaning cycles of sputtering and annealing up to 950 K; 100 nm × 100 nm, V_s = -4.00 V, I_t = 100 pA, rms-roughness = 0.79 nm. STM acquisition temperature: 77 K. (d) Histogram of disc radii, equivalent to the features projected area in Fig. 3.2b and c. The effective disk radius r is chosen to reproduce the area of the observed features as $A = \pi \times r^2$. Features smaller than a pixel are neglected to reduce noise contribution in the calculations. The analyses were performed by the Gwyddion software [183].

3.4.2 Ammonia Annealing of the GaN Surfaces

As mentioned above, sputtering and annealing of GaN lead to the preferential removal of N and enrichment of Ga atoms, with the consequence of roughening and faceting on the surface. To overcome this problem, we annealed GaN samples in the presence of NH_3 gas, which is a reactive precursor for the growth of GaN by the CVD, MOVPE and AMMONO methods [159-179]. We investigated the influence of annealing in the presence of NH_3 in the UHV chamber by comparing the ratio of N 1s and Ga 2p XPS intensities after each step of sputtering and annealing (Fig. 3.3a and c, see also the AP, Fig. 10A.4). The ratios of the XPS peak area of N 1s (excluding ammonia-related components, see Fig. 10A.4) to Ga 2p were calculated and plotted in Fig. 3.3b and d for normal and grazing angle (70°) emission XPS using Mg Kα radiation (1253.6 eV). The grazing angle measurements are more surface-sensitive. In Fig. 3.3b and d, by dividing the ratio of N 1s to Ga 2p peak areas by the ratio of the N 1s to Ga 2p photoionization cross-sections [184] and IMFPs [185] and calibrating the transfer function of the XPS hemispherical analyzer for different kinetic energies ($\propto \frac{1}{\sqrt{E_K}}$) [186], the stoichiometric ratio of the atoms is estimated. As observed in both graphs, the ratio of N atoms compared to Ga atoms is mostly reduced due to preferential removal of the lighter atoms (N) by sputtering. Annealing the GaN $(000\bar{1})$ surface in the presence of NH_3 reestablishes a larger proportion of N atoms compared to the UHV annealed surface. NH_3 molecules were dissociated on the surface of GaN providing a source of N atoms. Primarily, NH_3 molecules are expected to be adsorbed on the gallium-rich surface as N-H_x products and to form Ga-N-H_x bonds, hindering the formation of desired Ga-N bonds and the network in the deeper areas of the crystal. We

used electron bombardment to break the N-H bonds on the surface and enhance the chance of the formation of Ga-N bonds. However, the other obstacle to the formation of "perfect" GaN nitride layers is that after the adsorption of the first layer of nitrogen on the surface, there are not enough mobile gallium atoms on the top to form the next Ga-N stoichiometric layer. If the temperature is sufficiently high, gallium atoms can be very mobile so as to rearrange in a new morphology on the surface. This is, in turn, limited by the decomposition temperature that would lead to the decomposition of the GaN substrate below. Therefore, a compromise is necessary to achieve a surface of good quality. To this end, we annealed the sample, at the same time as dosing NH_3, to the highest possible temperature at which the crystal does not decompose of about 950 K (decomposition temperature: ≈1050 K). Fig. 3.3b reveals that the annealing in the presence of NH_3 combined with electron bombardment ($I_{emission}$ = 1.0-1.5 mA, electron energy = 220 eV) increases the ratio of N atoms compared to Ga atoms over the sampling depth more efficiently than in the absence of electron bombardment. On the other hand, Fig. 3.3d displays that NH_3 annealing without electron bombardment increases the surface N/Ga ratio more pronouncedly. These results suggest that electron bombardment helps to form Ga-N bonds in the bulk, while without electron bombardment the Ga-N bonds are more linked to surface adsorption and dissociation. Since the Ga-rich clusters are rough and extended vertically, the formation of Ga-N bonds in deeper regions is more desirable to increase the probability of rearrangement of the Ga-rich rough clusters on the surface and the surface smoothening. In addition, an electron bombardment in the absence of NH_3 several hours later than the NH_3 annealing, when most of the NH_3 gas is already pumped out of the chamber, leads not only to the removal of N-H (see Fig. 3.3), but also to Ga-N bond breaking and subsequent N removal. Therefore, electron bombardment has a detrimental effect on the surface, as soon as no remnant NH_3 is present in the chamber, although it has a positive effect on the surface and bulk/subsurface when NH_3 is present. More details are given in the AP, Fig. 10A.4 and AA.7-AA.9.

In Fig. 3.3a and c, we also observe that after NH_3 annealing (blue curves), a significant shoulder appears due to N-H bonds in the N 1s XPS narrow scan region. The formation of these N-H bonds on the surface reduces the formation of the GaN layer on the clean surface [187]. On the other hand, after electron bombardment of the NH_3 annealed sample (red curves), there is no or very little N-H shoulder. In this case, electron bombardment was started several hours after NH_3 annealing, when the pressure due to the presence of remnant NH_3 on the chamber walls had decayed. When the electron bombardment was done right after NH_3 annealing and there was remnant NH_3 close to the surface of the GaN sample (black curves), the small N-H shoulder was still observed, reduced significantly. Therefore, Fig. 3.3a and c confirm that the electron bombardment reduced the amount of N-H bonds on the surface. On the flip side, based on Fig. 3.3b and d, this procedure also removed some Ga-N bonds in the bulk and on the surface and reduced the ratio of N atoms to Ga atoms in the absence of the NH_3 gas. More details are displayed in the AP, Fig. 10A.8-AA.10.

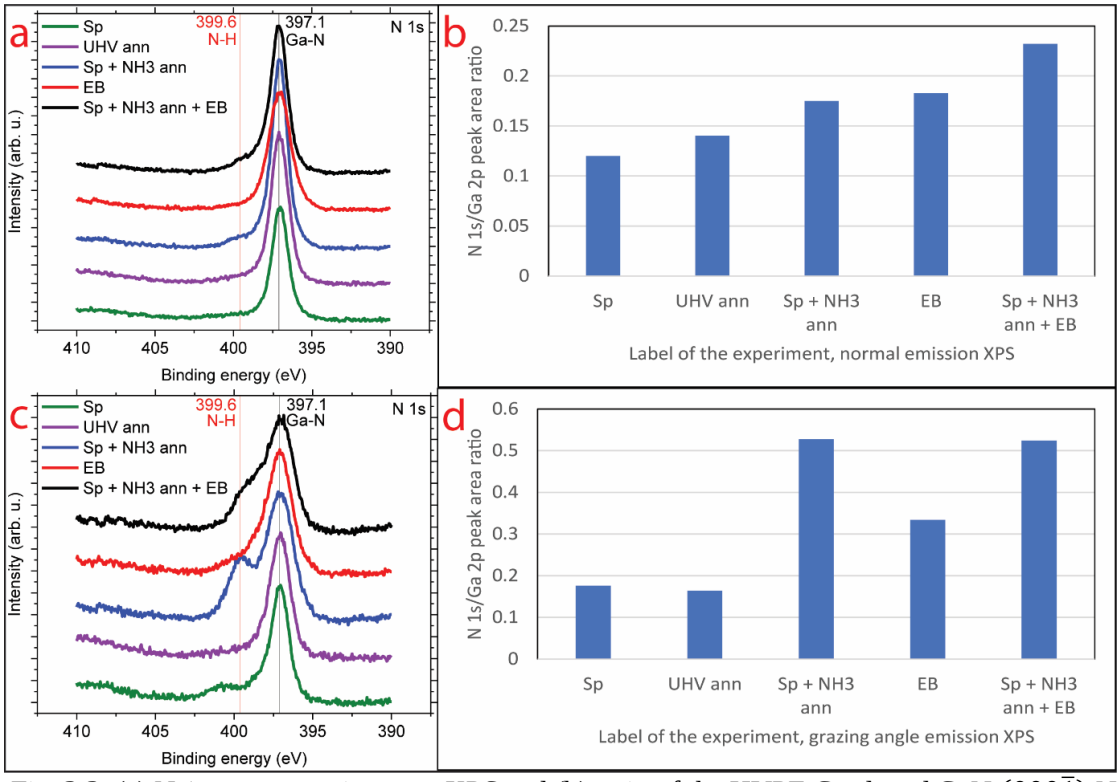

Fig. 3.3. (a) N 1s narrow region scan XPS and (b) ratio of the HVPE Ge-doped GaN $(000\bar{1})$ N 1s/ Ga 2p peak area at normal emission for XPS with Mg Kα radiation, before or after annealing at 950 K for 20 minutes in the presence of NH_3 with and without electron bombardment. (c) Grazing angle emission narrow region scan XPS for HVPE Ge-doped GaN $(000\bar{1})$ N 1s by Mg Kα radiation after various experiments and (d) their corresponding N 1s/ Ga 2p peak area ratio. The peak areas were divided by photoionization cross-sections and IMFPs and multiplied by the square root of the kinetic energies for calibrating the transfer function of the XPS hemispherical analyzer. The abbreviations Sp, UHV, ann, NH3, and EB refer to sputtering, ultra-high vacuum, annealing, NH_3 exposure and electron bombardment, respectively.

Fig. 3.4a shows different regions of the HVPE Ge-doped GaN $(000\bar{1})$ surface after sputtering, NH_3 annealing with electron bombardment. Although upon NH_3 annealing smoother areas were observed compared to UHV annealing, still rougher regions of the same sample appeared as well (Fig. 3.4b) As shown in Fig. 3.4d and e, the number of the smaller features and hillocks in Fig. 3.4b are less than in Fig. 3.4a. On the other hand, the average of the feature size in Fig. 3.4b (≈6.0 nm) is larger than for Fig. 3.4a (≈3.9 nm). Fig. 3.4c demonstrates that NH_3 annealing of the AMMONO GaN sample without sputtering and electron bombardment leads to a much smoother surface with smaller average feature size. However, this surface was still not atomically smooth enough to image adsorbed DBTP molecules by STM (see the AP, Fig. 10A.13). This implies that NH_3 annealing does not sufficiently improve the surface morphology, and the desired atomically flat surface necessary for model surface studies cannot be achieved by this approach. Furthermore, electron bombardment did not change the surface rms-roughness significantly. These results are compatible with Fig. 3.3 and Fig. 10A.9. The N 1s/Ga 2p ratio was found to increase in the bulk/subsurface and decrease on the surface by increasing the electron bombardment energy (see the AP, Fig. 10A.11 and AA.12). In fact, sputtering leads to preferential removal of nitrogen and permanent surface damage. Upon annealing without NH_3, Ga atoms tend to aggregate into unwanted islands, clusters, and hillocks. NH_3 annealing is expected to favor the growth of new GaN layers on the surface. Since the layers below are rough, the epilayers on the top follow the underlying morphology and become rough. Thermally-induced mobility increase of Ga atoms could promote their rearrangement and the formation of a flatter surface. However, the surface did not become smoother and no evidence of an atomically flat surface was found (see the AP, Fig. 10A.11-AA.13). By increasing the

NH_3 annealing temperature close to the GaN decomposition temperature, the probability of decomposition of rough clusters and hillocks on the surface and at the same time of formation of new flat GaN layers increases. However, we observed that in the presence of NH_3 gas in the chamber, the decomposition temperature of GaN increases (see the AP, Fig. 10A.2 and AA.11). Hence, no strategy was found that could lead to an atomically flat surface by NH_3 annealing, though in general NH_3 annealing improved the rms-roughness locally in small areas. Consequently, we were not able to image the TBB and DBTF molecules on the GaN surface for further investigation of the polymerization of these molecules on the surface (Fig. 10A.12).

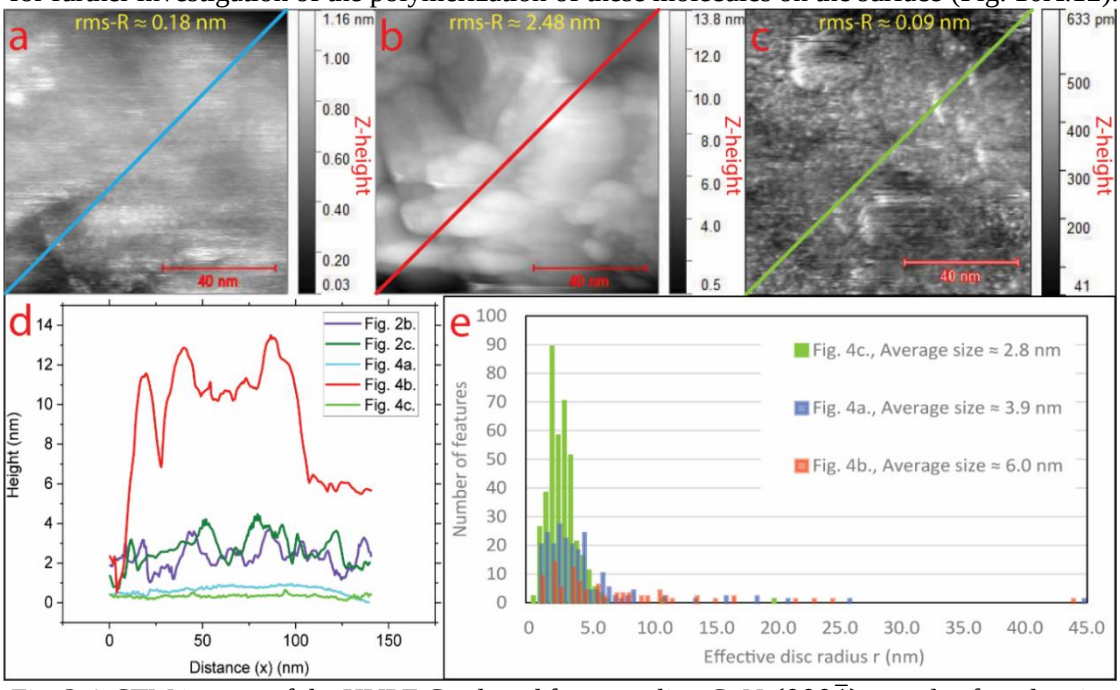

Fig. 3.4. STM images of the HVPE Ge-doped free-standing GaN $(000\bar{1})$ sample after cleaning by five cycles of sputtering (0.010 C) and NH_3 annealing up to 923 K together with electron bombardment ($I_{emission}$ = 1.5 mA); (a) 100 nm × 100 nm, V_s = -3.00 V, I_t = 1 nA, rms-roughness = 0.18 nm. (b) another area of the same sample; 100 nm × 100 nm, V_s = -3.00 V, I_t = 100 pA, rms-roughness = 2.48 nm. The STM measurements in (a) and (b) were performed at 4.6 K. (c) STM image of the AMMONO GaN (0001) sample after cleaning by four cycles of NH_3 annealing up to 950 K without sputtering and electron bombardment (77 K). 100 nm × 100 nm, V_s = -1.00 V, I_t = 100 pA, rms-roughness = 0.09 nm. (d) Comparison of the height profiles through the diagonal of the STM images shown in Fig. 3.4a, b and c, Fig. 2b, and Fig. 2c. The lowest point of each STM image is considered the zero height for that image. (e) A disc radius, equivalent to the features projected area (nm) in (a), (b) and (c). The effective disk radius r is chosen to reproduce the area of the observed features as $A = \pi \times r^2$. Features smaller than a pixel were neglected to reduce noise in the calculations. The calculations were done by the Gwyddion software.

3.4.3 TBB Deposition on the Cleaned HVPE GaN Surface

To assess the potential of the free-standing HVPE GaN surface, we deposited TBB on this surface at the sample temperature of ≈ 77 K by thermal evaporation (AP, Fig. 10A.14 and AA.15). On-surface debromination of TBB is an intermediate step for Ullmann coupling reactions routinely observed on metallic single-crystal surfaces [1-3]. After deposition of TBB on GaN held at ≈ 77 K, the ability of GaN substrate to promote TBB debromination upon annealing at elevated temperatures was monitored by XPS. Fig. 3.5a shows the narrow-scan XPS spectra of the Br 3d core level region before (black curve) and after annealing at different temperatures. By annealing the sample below 200 K, no significant changes were observed. The debromination started slightly at 200 K and more significantly above 300 K, where the

corresponding shoulder at 69.3 eV (the red curve in Fig. 3.5a, see the AP, Fig. 10A.14) increased by the annealing temperature enhancement. Annealing the sample at 400 K for 10 minutes was sufficient to ensure the occurrence of the debromination process. However due to the surface complexity, some molecules remained stably on the surface, including C-Br bonds. After debromination, the Br 3d core level peak binding energy shifted to smaller values (from 71.65 eV to 71.1 and 69.3 eV), with the Br-C bonds breaking and bromine atoms being adsorbed on the surface to likely form Ga-Br bonds. Due to the increased electron density for the bromine atoms upon bonding to Ga atoms on the surface, the binding energy of the Br 3d core level electrons decreases [102]. This observation supports the conclusion of a Ga-rich surface. Furthermore, in addition to some degree of molecular desorption, in Fig. 3.5b, zoomed-in C 1s core level spectra after deposition of TBB on HVPE GaN $(000\bar{1})$ before and after annealing at 400K confirm the interpretation of Fig. 3.5a. As seen, the C 1s peak binding energy decreases after annealing at 400 K upon debromination due to a higher electron density for carbon atoms. The broadening of Br 3d peaks is due to a weak C-Br shoulder in the TBB spectrum before annealing, at larger binding energies, whereas it vanishes at 400 K. Thus, the GaN substrate catalyzes the debromination of TBB. While debromination on the GaN surface starts at about 200 K, it occurs at 300-600 K for TBB on gold, silver and copper surfaces [1-3, 188]. Furthermore, Fig. 3.5c reveals that by increasing the coverage and the multilayer thickness, the Br 3d XPS peak total area corresponding to the heating to 400 K increases. These area values are normalized to the Br 3d peak area corresponding to 15 layers of TBB on GaN. Although our TPD results revealed the multilayer desorption at temperatures below 400 K, XPS results show the lack of bromine atom saturation on the GaN surface for below 15 layers of TBB deposition (see the AP, Fig. 10A.16). In addition, by increasing the coverage, the Br 3d peak binding energy shift due to debromination after heating to 400 K becomes smaller compared to the TBB deposition, while we expect a larger shift for the thicker multilayers (see the AP, Fig. 10A.14). Therefore, the Br 3d binding energy after heating to 400 K stays at higher values for larger coverages, which could be a sign of an increase in the Br-to-Ga atomic ratio on the surface.

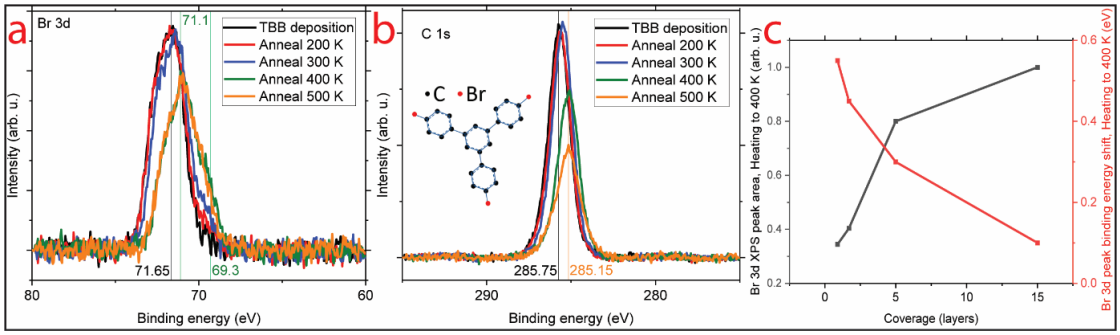

Fig. 3.5. Zoomed-in XP spectra of (a) Br 3d (coverage ≈ 0.9 monolayer (ML)) and (b) C 1s (coverage ≈ 0.9 ML) regions after deposition of TBB on HVPE Ge-doped GaN $(000\bar{1})$ and their evolution upon annealing (inset schematic structure of a TBB molecule). (c) The Br 3d peak area after debromination by heating to 400 K and bonding some bromine atoms to the Ga atoms on the HVPE Ge-doped GaN $(000\bar{1})$ surface, normalized by the Br 3d peak area corresponding to 15 layers of TBB on GaN versus the deposited TBB coverage. In addition, the peak binding energy shift of the Br 3d XPS narrow region scan after heating to 400 K versus the TBB coverage (see AP, Fig. 10A.14).

Fig. 3.6a shows the TPD of bromine isotopes (81 amu is similar to 79 amu) and benzene ring (75 amu) of ≈ 0.8 and ≈ 0.4 monolayers of TBB molecules deposited on Ge-doped HVPE GaN $(000\bar{1})$. The TBB desorption peak for the ≈ 0.8 submonolayer coverage is around 378 K. For bromine isotopes also a broad peak in the range of 400-900 K is observed which corresponds to the desorption of bromine atoms that were detached from TBB and bonded to surface atoms. Therefore, bromine atoms in the multilayer desorb at around 378 K together with the TBB multilayer itself, observed as a mass spectrometry fragmentation of the parent mass (543 amu), and bromine atoms bonded to the GaN surface desorb gradually from the surface at 450-850 K,

which is compatible with our XPS observations. Interesting results were observed for the TPD of ≈ 0.4 monolayer TBB deposition on GaN. As seen, there is no desorption peak related to the benzene rings while bromine atoms still desorb at higher temperatures. This implies that the TBB molecules debrominated on the surface and the molecular backbone remains adsorbed on it, even at much higher temperatures, hinting at the polymerization of debrominated TBB radicals on the surface of Ge-doped HVPE GaN $(000\bar{1})$, the well-known Ullmann coupling reaction.

Fig. 3.6b and Fig. 3.6c show the TPD of clean GaN compared to GaN with TBB sub-monolayer and the ratio of a bromine isotope of 79 amu to two different Gallium isotopes of 69 amu and 71 amu, respectively. The combination of these results with Fig. 3.5 indicates that after debromination, Br atoms strongly bond to Ga and H atoms ($mass_{HBr}$ = 80 and 82 amu) at the surface. Ga atoms are larger than Br atoms, therefore Br can bond to Ga from a one-to-one up to a three-to-one ratio [189-201]. In addition to the different Br-to-Ga atomic ratio on the surface and the formation of HBr products desorbing at different temperatures, another reason for a broad Br TPD peak and the desorption tail at higher temperatures, increasing with coverage, could be due to the surface roughness and the presence of clusters and hillocks of different sizes. Therefore, bonding to the Ga site on different parts of the hillocks involves different binding energies for Br atoms. Therefore, they desorb at a wide temperature range and, by increasing the coverage, more Br atoms can chemically bond to Ga atoms on the surface.

Fig. 3.6b shows that at higher temperatures up to 900 K, Br and Ga atoms bonded to each other desorb at the same time. Since there is no Ga desorption for the clean surface and Ga-Ga (138 kJ/mol [202-205]) bond dissociation energy is smaller than Ga-Br (444 kJ/mol [202, 205, 206]) and Ga-N (195 kJ/mol [207, 208]), it is inferred that Br atoms do not desorb singly, but as $GaBr_X$ products removing the excess Ga atoms of the surface. Notably, the ratio of Br atoms to Ga atoms changes upon varying the TBB coverage at the surface (Fig. 3.6c). This finding is also promising for the preferential removal of Ga atoms by deposition of Br atoms on the surface, in the effort to compensate for the preferential removal of N atoms by sputtering and annealing and to etch the Ga-rich islands (see the AP, Fig. 10A.16).

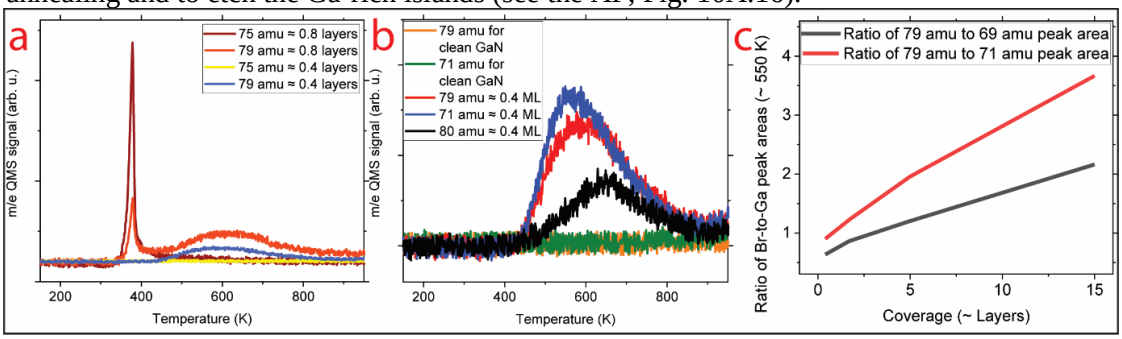

Fig. 3.6. TPD spectra of (a) TBB molecule fragments (75 and 79 amu corresponding to a benzene ring and a bromine isotope, respectively) dosed on Ge-doped HVPE GaN $(000\bar{1})$. (b) TPD spectra of Ga (71 amu), Br (79 amu) and HBr (80 amu) for clean GaN and a TBB submonolayer on Ge-doped HVPE GaN $(000\bar{1})$. (c) The ratio of Ga-to-Br TPD peak areas at temperatures higher than 470 K.

3.5. Conclusions

Our XPS results confirm the chemical cleaning of the surfaces of GaN $(0001)/(000\bar{1})$ samples, completely removing the natural oxide layer on the surface by sputtering and annealing at 950 K in UHV. However, STM experiments reveal that the surface becomes rough after cleaning, and unwanted clusters, hillocks and crystallites of different size form on it. This is partially due to the appearance of permanent surface damage and the preferential removal of N atoms by sputtering and the rearrangement of mobile Ga atoms at high temperatures to form clusters and crystallites that roughen the surface. After sputtering and UHV annealing, a (1×1)

LEED pattern is observed, originating from the crystalline sub-surface layers. Furthermore, the GaN surfaces were annealed at 950 K in the presence of NH_3 gas. This procedure increased the ratio of N-to-Ga atoms, whereby electron bombardment of the surface appears to increase the number of N atoms in the bulk. This observation is promising for enhancing the surface quality of GaN (0001) under UHV conditions. However, STM proved that, while some smoother regions could be observed after NH_3 annealing, the surface is not yet atomically flat to image TBB and DBTP molecules deposited on this surface. In addition, on these rough sputtered and annealed GaN surfaces, the debromination reaction can be catalyzed. The separated Br atoms can selectively remove Ga atoms from the surface to aid to overcome the problem of the preferential removal of N atoms and to favor surface smoothening. Therefore, as a further outlook, we envision the on-surface etching of Ga-rich hillocks using pure Br atoms or Br_2 molecules as a potential surface treatment to improve and smoothen the GaN surface in UHV.

Chapter 4

Post-synthesis of Cu_2N Monolayers on Cu (111) from Copper Oxide Films and Their Decoupling Effects

This chapter explores the post-synthesis of Cu_2N monolayers on Cu (111) from copper oxide films and their decoupling effects. It includes content that is currently being prepared for submission, with permission from Rostami, M., Kaderoğlu, C., Yang, B., Seyedmohammadzadeh, M., Kaya, P., Olgar, H., Aktürk, E., Senge, M.O., Chi, L., and Barth, J.V., 2024.

4.1. Contributions

Mohammadreza Rostami: Experiments, data analysis, writing, review & editing, experiment discussion, model drawing. Çağıl Kaderoğlu: DFT calculations. Biao Yang: Experiments, Experiment discussion, review & editing, supervision. Mahsa Seyedmohammadzadeh: Density Functional Theory (DFT) calculations. Pinar Kaya Fizmuh: DFT calculations. Handan Olgar: DFT calculations. Ethem Aktürk: DFT calculations. Peter Fuelner: Experiment discussion, review & editing. Mathias O. Senge: Synthesis of molecules. Lifeng Chi: Review & editing, supervision. Johannes V. Barth: Review & editing, supervision.

4.2. Introduction

Copper nitride thin films are materials of interest for versatile applications in optical information storage devices [18-24], microelectronic semiconductor materials like a resistive switch [61], magnetic tunnel junction barrier [23], lithium and sodium-ion batteries [62], materials for maskless laser writing [18, 24], metal-based catalysts [64], new energy materials [18, 65, 209-211], and quantum corrals [210, 212-214]. These thin films have promising physical properties [18, 63], low cost [18, 63, 64], nontoxicity [18, 21], high optical absorption coefficients in the solar spectrum [65], and high stability [18, 22, 66, 67]. Different mechanisms for the fabrication of copper nitride thin films have been reported, including chemical methods

[18, 64], molecular beam epitaxy (MBE) [18, 23, 68], atomic layer deposition [211], reactive pulsed laser deposition in nitrogen (N) gas [24], chemical vapor deposition [67, 215], magnetron-sputtering single-crystal epitaxy [18, 216-218], plasma immersion ion implementation on a $TaN/SiO_2/Si$ substrate [61], and N sputtering of a copper surface to produce either Cu_2N [210, 212, 219-229] or Cu_3N thin films [18, 217, 230-232]. Because of the low reactivity of copper and nitrogen, the most common method of copper nitride preparation in the past has been replacement methods [18]. For example, Cu_3N powders were produced by the replacement of fluorine (F) atoms in CuF_2 [18] or oxygen (O) atoms in CuO or Cu_2O with N atoms upon annealing in the presence of dried ammonia (NH_3) at about 250-280 ˚C in a low vacuum [70, 71]. In this case, cuprous oxides were prepared by the solution-based Russell's method [70-75]. The production of Cu_3N by annealing of a Cu surface in the presence of NH_3 at about 900-1000 ˚C was also reported [70, 233-235].

Cu_3N growth under NH_3:H_2 gas dosing reveals reproducible band structures, while Cu_3N grown by reactive sputtering in N_2 gas at 300 K (10^{-2} mbar) shows a different band structure due to a smeared density of states, poor crystal quality and a high defect density [236]. The copper nitride lattice constant (≈ 0.3385 - 0.382 nm) varies significantly depending on the preparation method [18, 70, 215, 237]. This leads to changes in copper nitride conductivity ranging from an insulator to a conductor [18, 61]. Some research introduced copper nitride (Cu_XN, $1 \leq X \leq 3$) thin films as insulators, observing a band gap larger than 4 eV by scanning tunneling spectroscopy (STS) [18, 61, 219, 220, 224, 230], and as semiconductors with a reported band gap of 1.4-2 eV by ultra-fast pump-probe spectroscopy [23, 65, 231, 236]. In addition, Cu or N-poor conditions result in Cu and N vacancies, producing p-type and n-type copper nitride thin films, respectively, which increase the conductivity of these thin films [18, 61]. On the other hand, the Cu_3N bandgap increases to 2.25-2.48 eV in strained regions [231, 236, 238]. However, Cu_3N acts as an insulating layer in both the absence and presence of H atoms in the system [23]. By contrast, Cu_4N has been reported as a metal [61]. Surprisingly, recent DFT calculations have described copper nitride monolayers (MLs) as semimetals [238]. Conversely, recent research considers Cu_2N as metallic thin films based on DFT calculations, which include first-principles calculations and tight-binding (TB) model analysis and experiments including angle-resolved photoemission spectroscopy (ARPES) [62, 68]. The metallic nature is due to hole pockets near the fermi level, derived from its checkerboard lattice (a 2D line-graph lattice) and a hole-like band at each M point of Cu_2N [68]. This research suggests the reason for these contradictory results is that STS detects the band gap at the Γ point of the Brillouin zone (BZ), whereas ARPES reveals that the valence (VB) and conduction bands (CB) of Cu_2N thin films overlap at the M point of the BZ [62, 68, 239]. However, ultra-fast pump-probe spectroscopy reveals the presence of M and R direct band gaps, proving that Cu_3N is a defect-tolerant semiconductor, with defect states close to CB and VB [236].

Despite the metallic behavior revealed by ARPES, copper nitride thin films (Cu_2N) provide a crucial decoupling effect due to high stability and low interaction with the on-surface molecules, as confirmed by phonon simulations and LEED experiments [23, 68]. Therefore, copper nitride thin films are promising for preventing the quenching of electronic excitations of epilayers and 2D structures on the surface [219, 224, 225, 230]. Copper nitride possesses strong potential for controlling the coupling between adsorbates and the substrate surface electron density, as well as reducing electron transfer between a molecule and the substrate [35, 219, 224, 225, 230]. This decoupling effect facilitates the measurement and imaging of the atomic-scale spins excitations and interactions in magnetic structures [224], as well as the molecular orbitals and vibronic states, by enhancing the lifetime of transient molecular charge states [230].

Fabrication protocols for Cu_2N in UHV, such as copper evaporation in the presence of N gas [69] and sputtering a copper surface with N atoms while annealing [210, 212, 219-229], with characterization by XPS, STM, and STS suffer from limited sub-monolayer coverage and lack of an extended defect-free single or double layers [210, 212, 218-220, 224, 225, 227, 228]. The Cu (100) c(2×2)-N submonolayers formed on Cu surfaces have been reported as commensurate superstructures, with coverage controlled by annealing temperature and duration [210, 217, 220, 228]. However, a Cu_2N monolayer is not stable on Cu (111) above 700 K [229]. Besides that, a limited number of STM investigations of molecular depositions on copper nitride have been

reported, including the deposition of tetraphenylporphyrin on a Cu_3N monolayer [230, 240] and azobenzene on a Cu_2N monolayer [241], and their decoupling from the Cu substrate [230, 240, 241]. The less nitridated a surface, the smaller the molecular adsorption enthalpy on the Cu_2N sub-monolayer; however, on a heavily nitridated surface, the molecular adsorption on Cu_2N is weaker and limited [221, 225]. In this work, we developed a new replacement method for the fabrication of Cu_2N on Cu (111) by exchanging O atoms in the oxygenated substrate [242-244] with N atoms. Since our technique does not involve sputtering or any preparation that dissociates the post-synthesized Cu_2N layer, such as annealing above 700 K, repeating cycles of our replacement method induce Cu_2N film formations on Cu (111). In addition, we investigated Cu_2N properties, atomic structure, molecular depositions on this surface, and its decoupling effect using STM, STS, XPS, LEED, and DFT calculations. We thus present a multi-technique investigation to better understand the nature, structure, and properties of Cu_2N thin film, considering the contradictory reports about the system electronic properties. In addition, we studied the molecular deposition of diaminophenyl-porphyrins (DAPPor) and their assembly on Cu_2N, for which there are limited investigations and reports in the literature.

4.3. Experimental

Sample preparation: The single crystal Cu (111) surface was cleaned by multiple cycles of Ar^+ or Ne^+-sputtering (≈ 1 keV, 30 minutes, $I_{ion} \approx 7.5$ μA, ≈ 0.014 C) and annealing (≈ 700 K, 30 minutes). Cu_2N submonolayers were fabricated by repeating cycles of oxidation by dosing 60 L oxygen gas at the surface temperature of ≈ 600 K followed by dosing 180 L NH_3 at the surface temperature of ≈ 625 K. We heated the sample from the back using radiation and bombardment with electrons emitted from a W filament, and dosed O_2 or NH_3 gas simultaneously.
Characterization: We characterized the Cu (111), Cu_2N and, molecules by XPS (photon line: Mg $K_\alpha \approx 1253.6$ eV), LEED, and STM, after cleaning the samples in home-built UHV chambers. In the XPS chamber, a K-type (Nickel-Chromium/Nickel-Alumel) thermocouple was attached to the molybdenum plate supporting the Cu (111) sample. The base pressure of the employed chambers was below 2×10^{-10} mbar. The XPS acquisition temperature was at liquid nitrogen (77 K). In a commercial JT-STM (SPECS GmbH) chamber, the thermocouple was directly attached to the surface. The base pressure of the preparation and principal STM chambers was 1.1×10^{-10} mbar and 8.5×10^{-11} mbar, respectively. The STM and STS acquisition temperatures were liquid nitrogen (77 K) and liquid He (4.6 K).
Molecular deposition: The DAPPor powder was provided by Mathias O. Senge's group and loaded into a quartz crucible of home-built OMBE. DAPPor molecules were deposited on the clean Cu_2N/Cu (111) surface at room temperature. The deposited molecular films were characterized utilizing STM and STS. Subsequently, the molecular assemblies at room temperature by STM and the decoupling effect of Cu_2N films by STS on molecules on Cu_2N and Cu (111) were studied.
Softwares: The structural models and their freestanding optimizations were done using ChemDraw software [245]. In addition, the STM images analyses were done using the Gwyddion software [183].
DFT calculations: DFT calculations and simulations were conducted to further investigate the atomic structure and electronic properties of our Cu_2N submonolayer.

4.4. Results and Discussion

Nitrogen gas under normal conditions does not interact with the Cu surface [228]. Therefore, we developed a new method for fabricating 2D Cu_2N on Cu (111) surface by replacing O atoms in copper oxide with N atoms through NH_3 annealing at 625 K, confirmed by XPS, LEED, STM, and STS. In this method, no destructive techniques like sputtering are used for Cu_2N production. Therefore, by repeating the oxidation and nitridation cycles, the Cu_2N film

formation is enhanced. In addition, we investigated the band gap and decoupling effect of this Cu_2N layer using STS and the corresponding on-surface molecular assemblies utilizing STM.

4.4.1 Growth

Fig. 4.1a shows three different superstructures of oxygenated Cu (111) imaged by STM after dosing 60 L O_2 at the Cu (111) surface held at 600 K in UHV. Tow high-order superstructures observed in Fig. 4.1a are known as "44" and "29" Cu_2O reconstructions [236, 246]. The third observed phase is amorphous, different from "5-7" Cu_3O_2 [246]. The prevailing phase on this surface was "44". Wood's notation as $\sqrt{13}R46.1° \times 7R21.8°$ and $\sqrt{73}R5.8° \times \sqrt{21}R - 10.9°$ correspond to "29" and "44" superstructures, which are 29 and 44 times larger than the (1 × 1) unit cell, respectively [247]. Fig. 4.1b and 4.1c display zoomed-in STM images of two islands with different superstructures after dosing 18 L NH_3 at 625 K on the copper oxide surface. Fig. 4.1 c reveals that by dosing 18 L of NH_3 gas at the surface temperature of 625 K, reduction of the O/Cu (111) phases happens, initiated by transferring into islands with the $(\sqrt{3} \times \sqrt{3})R30°$ superstructure [248], consisting of a combination of an oxide and a nitride (see the AP, Fig. 10B.1 and 10B.2). The $(\sqrt{3} \times \sqrt{3})R30°$ superstructure of copper oxide can be formed by the removal of one-third of outermost oxygen atoms on the Cu (111) surface [248]. The reduction of Cu (111) oxides by gases starts at defect sites and defect boundaries [246]. In Fig. 4.1d, STM displays the surface after 30 minutes of annealing at 625 K with a 180 L NH3 gas dosage in UHV. The surface reconstructed at a higher NH_3 pressure, and as evidenced in Fig. 4.1e and 4.1f by enlargement of the N 1s and the vanishing of the O 1s XPS peaks, a pure copper nitride submonolayer formed. The Cu_2N submonolayer possesses distorted features elongated in different directions, forming islands surrounded by other Cu_2N islands with different elongation directions and bare copper patches. Lu et al. [61] reported a peak containing three different components of N 1s XP spectra at binding energies of 397.4 eV, 395 eV, and 396.8 eV, speculated to correspond to Cu_3N, Cu_4N, and an unclear origin, respectively [61]. We observe three separate peaks at different stages of our fabrication method at ≈ 400.3 eV, ≈ 397.3 eV, ≈ 396.9 eV, and 394 eV, corresponding to O-N-H, O-N-Cu, Cu_2N, and physiosorbed NH_3 on Cu (111), respectively. Because O is more electronegative than N, bonding O to N results in the O 1s and N 1s peak binding energy shifts to lower and higher binding energies, respectively. Additionally, a higher ratio of N to Cu then a larger degree of Cu oxidation lead to a higher electron density around N atoms and a shift of the N 1s binding energy to lower values. Fig. 4.1e and 4.1f indicate that by dosing 60 L O_2 at 600 K, a sharp O 1s peak arises. Annealing the copper oxide sample at 625 K with 18 L NH_3 dosage reduced the O 1s peak, and several caused small N 1s peaks. Then, by annealing with 180 L NH_3 dosage, the Cu_2N-related N 1s peak dominated, and the O 1s peak vanished. This provides a solid proof for replacement of O atoms in copper oxide by N atoms from NH_3. Therefore, the most important parameter that can significantly change the lattice constant, structure, and properties of copper nitride is nitrogen partial pressure (r) [18]. The higher the N concentration, the greater the distortion of the copper nitride structure [221]. Furthermore, Fig. 4.1g shows LEED patterns of copper nitride submonolayer on Cu (111). The brightest spots belong to the Cu (111) substrate in a hexagonal symmetry of the (1×1) Cu (111) surface reconstruction. Between the Cu (111) related LEED spots, a highly ordered LEED pattern with an oblique symmetry is observed. This LEED pattern is the same as that reported in the literature and its simulations for a deposition of atomic nitrogen on the surface of Cu (111) [68, 210, 221]. This pattern belongs to a Cu (100) c(2×2)-N superstructure, in which the top surface atomic layer of Cu (111) reconstructed to Cu (100), and N atoms are placed in the hollow sites [68, 210, 221]. A LEED spot of the Cu (111) substrate and the unit mesh of the Cu_2N overlayer are shown by a red arrow and a white dashed square, respectively.

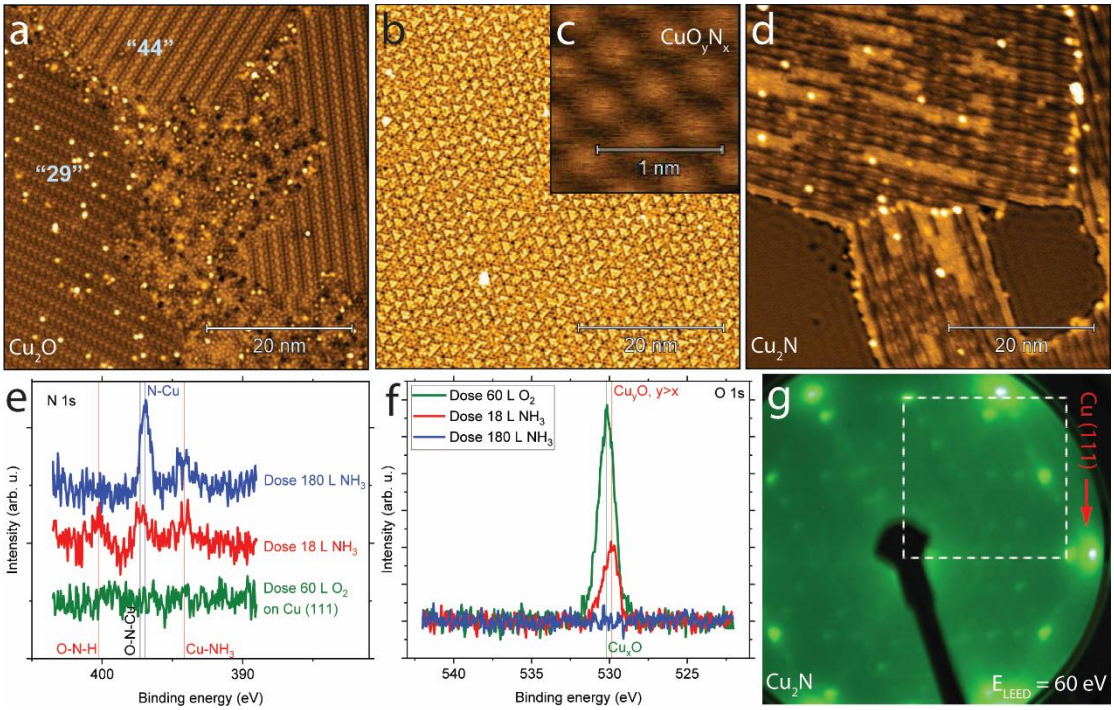

Fig. 4.1. (a) STM image of copper oxide on Cu (111) after dosing 60 L O_2 in UHV; The distance between the brightest and darkest points (Z-height) = 0.16 nm, V_s = 1.00 V, I_t = 100 pA, rms-R = 0.01 nm. (b) STM image of the intermediate CuO_yN_x layer on Cu (111) after dosing 18 L NH_3 in UHV; Z-height = 0.09 nm, V_s = 0.50 V, I_t = 100 pA, rms-R = 0.01 nm. (c) STM image of a different region of the intermediate CuO_yN_x on Cu (111) after dosing 18 L NH_3 in UHV; Z-height = 0.09 nm, V_s = 0.02 V, I_t = 1 nA, rms-R = 0.01 nm. (d) STM image of Cu_2N on Cu (111) after dosing 180 L NH_3 in UHV; Z-height = 0.20 nm, V_s = -0.10 V, I_t = 1 nA, rms-R = 0.02 nm. STM acquisition temperature: 4.6 K. Zoomed-in XPS spectra of (e) N 1s and (f) O 1s (coverage ≈ 0.5 ML). (g) LEED pattern (electron energy: 60 eV) of a Cu_2N submonolayer on Cu (111). The unit mesh of the Cu(100)–c(2 × 2)N overlayer, comprising three domains with orientations offset by 60° and 120° relative to each other on the Cu(111) substrate, is outlined by dashed white lines.

4.4.2 Structural Analyses

Fig. 4.2 depicts an atomic resolution STM image and the corresponding atomic structural model of the Cu_2N sub-monolayer. Fig. 4.2a shows and overview STM image of a Cu_2N island next to a Cu (111) island measured at bias voltage of 1V. Atomic resolution of the distorted Cu_2N film elongated in a parallel line shape features are visible in this large-scale image. The border of the Cu_2N and Cu (111) islands is brighter than other regions which could be due to charge confinement in the border, corrugation of the structures close to border due to a large lattice mismatch, and accumulation of the excess Cu atoms due to the larger density of the Cu (111) surface compared to Cu (100). Fig. 4.2b presents the fast Fourier transform (FFT) of the Cu_2N domain shown in Fig. 4.2a, calculated using WSxM software. Given that three distinct domains of Cu_2N on this surface exhibit the same structure but with orientation offsets of 60° and 120°, combining this FFT pattern with two additional, similarly rotated patterns produces a reasonable match with the Cu(100)–c(2 × 2)N LEED pattern shown in Fig. 4.1g. Fig. 4.2c shows that Cu_2N on Cu (111) has square-like features elongated in parallel rows, with one- or two-unit cells in width, distorted and strained significantly due to the lattice mismatch with the substrate. The green square in Fig. 4.2c shows a proposed unit cell for the distorted Cu_2N on Cu (111). This unit cell parameter (≈ 0.54 nm) is differs from the bulk Cu_3N shown in Fig. 4.2d and reported Cu_2N on Cu (100) [18]. Fig. 4.2d displays the three-dimensional (3D) unit cell of the bulk Cu_3N in which red and yellow spheres represent the Cu and N atoms, respectively. The

lattice parameter is 0.3817 nm. A face of this 3D unit cell of Cu_3N is the same as the 2D unit cell of Cu_2N. Fig. 4.2e indicates the proposed structural model of the Cu_2N on Cu (111), where the blue, green and red circles represent Cu atoms in Cu (111), Cu atoms in Cu (100) and N atoms. The structure is the same as the reported pseudo-(100) structure, having many misalignments due to lattice mismatch of Cu (111) surface and copper nitride in Cu <110> direction [210, 212, 220]. This means the packing density of the copper surface has changed compared to the bulk [228], and the top atomic layer of Cu (111) reconstructed to Cu (100). Then N atoms lie between the Cu atoms in the hollow sites, forming covalent bonds with copper atoms [210, 219], as an incommensurate superstructure or a $(25\times7\sqrt{3})$ commensurate reconstruction [228, 229, 241]. This is compatible with the LEED pattern in Fig. 4.1e and reported LEED simulations [210, 221, 229]. The long-range corrugation in Fig. 4.2c comes from $(25\times7\sqrt{3})$ super unit cells, similar to the Cu (100) – c (2 × 2) N structure [210, 212, 220, 229]. Fig. 4.2e indicates that considering the lattice parameter of copper nitride, the diagonal of the unit cell is about 0.54 nm. Therefore, either the square-like features of Cu_2N on Cu (111), shown by the green square in Fig. 4.2c, are equivalent to the Cu_2N unit cell diagonal on Cu (100), or an enlarged unit cell parameter of Cu_2N on Cu (111) due to the significant distortion caused by the lattice mismatch of Cu_2N and Cu (111).

Fig. 4.2f shows the DFT simulations of the atomic structure of Cu(100)–c(2 × 2)N on a Cu(111) substrate, which becomes cracked after relaxation on the surface due to the significant lattice mismatch. This cracking results in the formation of linear elongations within the Cu_2N structure, matching the shape and density of the features observed in the experimental results. The distortion of the Cu–N bonds due to this cracking could explain the increase in the unit cell parameter of Cu_2N from 0.38 nm in bulk to approximately 0.54 nm in this 2D structure on Cu (111). The periodic features observed in the STM simulations, in Fig. 4.2g and Fig. 10B.3-4 (the AP), provide the best fit among our models for the elongations seen in the experimental STM images. However, the elongations in the STM images appear more bent and distorted, with a clearer periodicity of a unit cell parameter of 0.54 nm, which slightly differs from the simulated case. Furthermore, the growth direction of the elongations in the cracked Cu_2N model on Cu (111) is preferentially in the higher symmetry direction, compatible with the experimental results, considering the step edges of Cu (111). In the following sections, we will also compare our results with other proposed models.

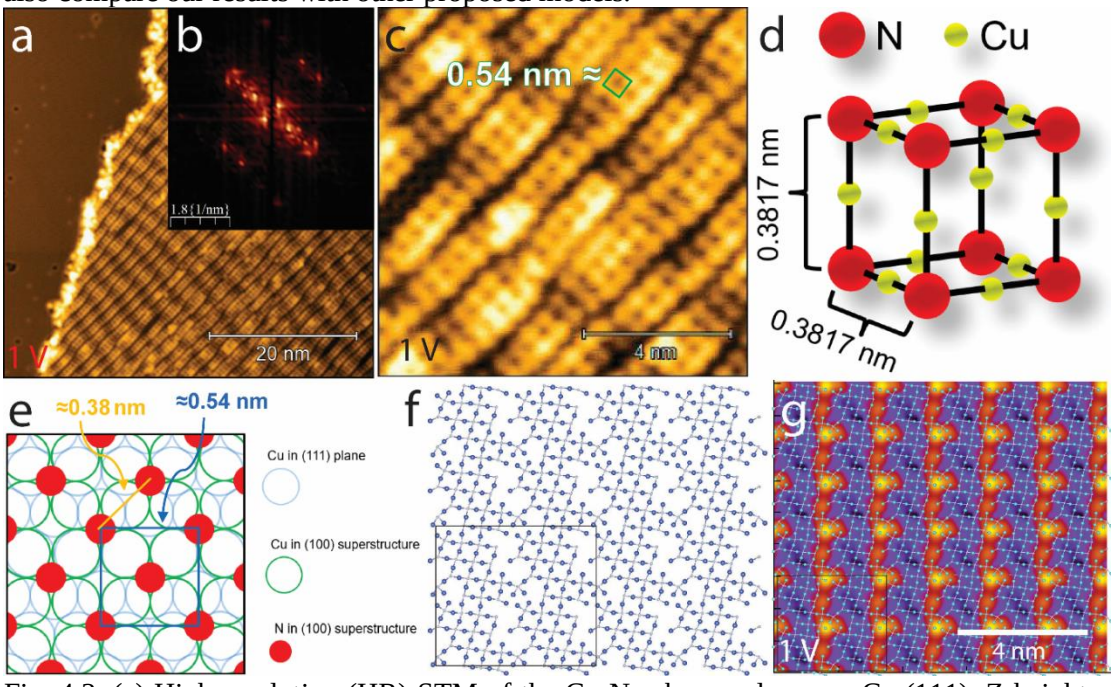

Fig. 4.2. (a) High resolution (HR)-STM of the Cu_2N sub-monolayer on Cu (111); Z-height = 0.16 nm, Vs = 1 V, It = 100 pA, rms-R = 0.02 nm. (b) FFT of the Cu_2N domain displayed in (a), calculated using WSxM software. (c) High resolution (HR)-STM of the Cu_2N sub-monolayer on Cu (111); Z-height = 0.08 nm, V_s = 1 V, I_t = 1 nA, rms-R = 0.01 nm. (d) A

schematic of the bulk Cu_3N cubic anti-ReO_3 structure. (e) A schematic of the Cu (100) c(2x2)-N thin film on Cu (111) (Cu_2N). (f) DFT simulation of the atomic structure of relaxed Cu (100) – c (2 × 2) N on a Cu (111) substrate, and (g) the corresponding STM simulation. The black square represents four unit cells of the proposed structure. Blue and white spheres represent the Cu and N atoms, respectively. STM and STS acquisition temperature: 4.6 K.

Topographical features, the surface morphology, and electronic properties of the Cu_2N layer on Cu (111) were investigated more comprehensively by varying the bias voltage of STM. Fig. 4.3 presents the bias-dependent STM images of Cu_2N on Cu (111) (see the AP, Fig. 10B.1). Fig. 4.3a, b, and c correspond to the bias voltages of 0.1 V, -1 V and 4 V, respectively. Darker spots correspond to the lower height or smaller density of states. Fig. 4.3a displays darker features for the Cu_2N surface, as most of electrons were not excited from the tip to the surface at a bias voltage of 0.1 V. The Cu (111) area in the image, which is surrounded normally by Cu_2N in a larger scale, shows oscillating features due to the formation of standing waves patterns of the electron density in these metallic islands called quantum corrals (QCs) as previously reported in the literature [210, 214]. The formation of QCs in Cu (111) islands surrounded by Cu_2N at lower bias voltages indicates the localized electronic states close to the Fermi level [210, 214]. Fig. 4.3b exhibits a flat darker Cu (111) patch and slightly brighter Cu_2N features at the bias voltage of -1 V compared to Fig. 4.3a at the bias voltage of 0.1 V. Furthermore, Fig. 4.3c shows a very bright Cu_2N layer and an extremely dark Cu (111) surface at the bias voltage of 4 V. This figure shows square like regular periodic features of Cu_2N which could be due to the periodic potential of Cu_2N arising from iterative placements of N atoms in the hollow sites of Cu (111) surface reconstructed to Cu (100) at the top atomic layer of the surface.
Two additional atomic structural models were proposed in Figs. 4.3d-i. In Fig. 4.3d, a Cu (100) – c (2 × 2) N island has been modeled, embedded within the top atomic layer of Cu (111). The corresponding DFT simulations of STM images of this model at bias voltages of -1 V and 4 V are shown in Figs. 4.3e and f, respectively. These STM simulations indicate that the Cu_2N island appears darker than surrounding Cu (111) surface at -1 V, while this contrast is reversed at the bias voltage of 4 V, where the islands appear brighter. This change in the electronic states between these two bias voltages, however, is not consistent with our experimental STM results (see the AP, Fig. 10B.5). On the other hand, Fig. 4.3g presents an alternative structural atomic model where a Cu (100) – c (2 × 2) N island is located on the top of the Cu (111) surface. The corresponding STM simulations at bias voltages of -1 V and 4 V have been displayed in Figs. 4.3h and i, respectively. In both cases, the Cu_2N island appears brighter than the surrounding Cu (111) surface. In Fig. 4.3h, darker features within the Cu_2N island can be observed in the STM image, likely a combination of both height and electronic state effects. By contrast, in Fig. 4.3i, the Cu_2N island is significantly brighter, displaying a periodic feature dominated by electronic states due to the excitation of states above the CB (see the AP, Fig. 10B.6). This makes the model shown in Fig. 4.3g more consistent with our experimental STM results, supporting it as the expected structural model for the Cu_2N islands formed on the Cu (111) surface.

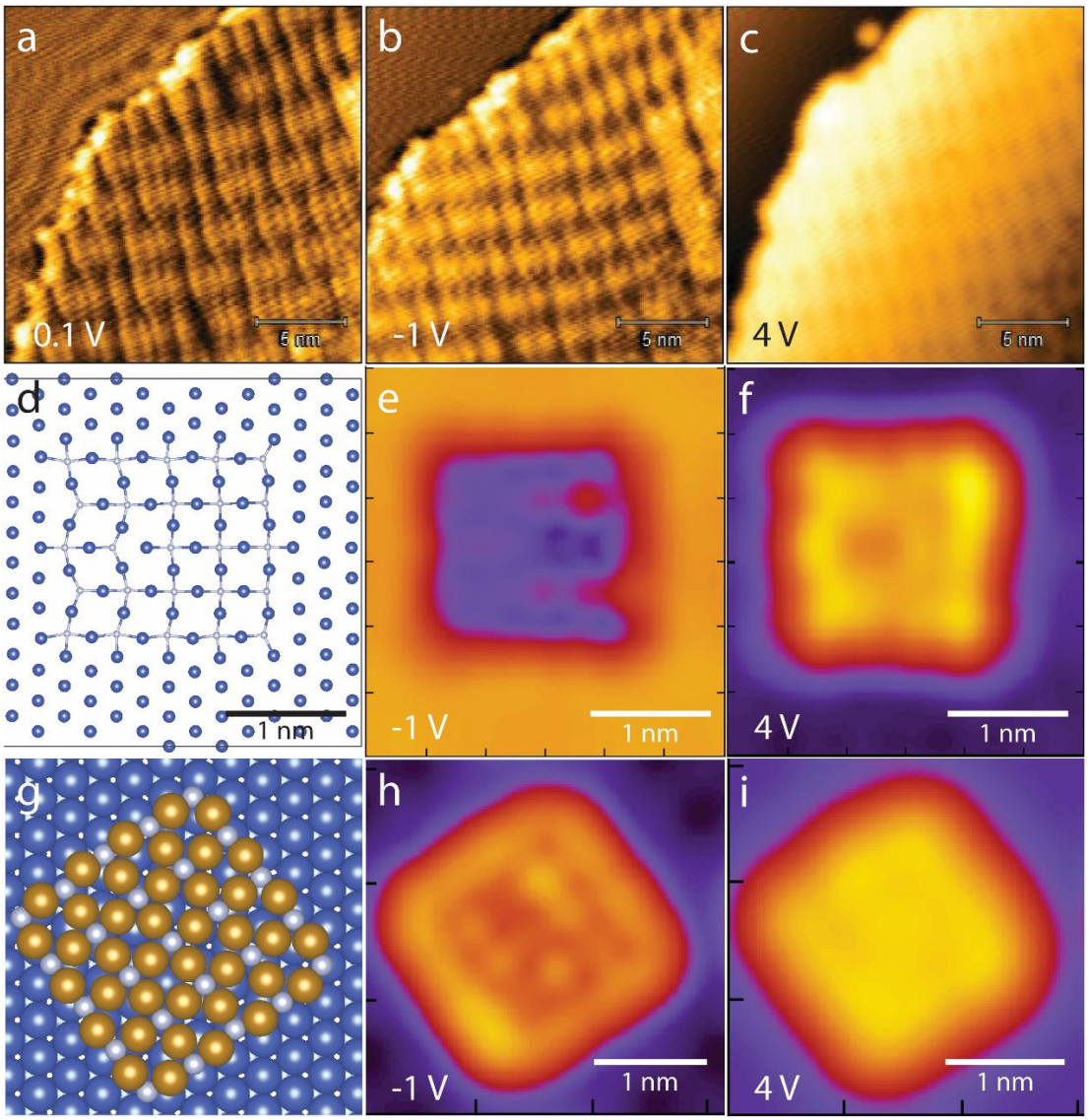

Fig. 4.3. Bias-dependent STM measurements of Cu_2N sub-monolayers on Cu (111) after four cycles of dosing with 10^{-6} mbar O_2 and 10^{-7} mbar NH_3 in UHV; (a) STM image with Z-height = 0.09 nm, V_s = 0.1 V, I_t = 1 nA, rms-R = 0.01 nm. (b) STM image with Z-height = 0.11 nm, V_s = -1 V, I_t = 100 pA, rms-R = 0.01 nm. (c) STM image with Z-height = 0.44 nm, V_s = 4 V, I_t = 1 nA, rms-R = 0.10 nm. STM acquisition temperature: 4.6 K. (d) Structural atomic model of a Cu (100) – c (2 × 2) N island embedded within the top atomic layer of Cu (111) surface. (e, f) DFT simulations of STM images for the structural model in Fig. 4.3d at bias voltages of -1 V and 4 V, respectively. (g) Structural atomic model of a Cu (100) – c (2 × 2) N island positioned on top of the Cu (111) surface. (h, i) DFT simulations of STM images for the model in Fig. 4.3g at bias voltages of -1 V and 4 V, respectively.

To tackle the contradictory reports about the electronic conductance of Cu_2N, the band gap of the Cu_2N sub-monolayer on Cu (111) was measured by STS, as shown in Fig. 4.4a. The STS measurements were calibrated on a clean Cu (111) surface. There is a CB with a high density of states at a bias voltage of 1.8 V. The far smaller VB at a bias voltage of -2 V results in a band gap of 3.8 V, which is categorized as a wide-band gap semiconductor. Our STS results reveal a large band gap for Cu_2N that is comparable with the literature, though STS is dominated by information related to the Γ point of the BZ, and M point-related information remains elusive [219, 224, 230]. On the other hand, reported (ARPES) measurements and new DFT calculations show an overlap of the CB and VB at the M point of the BZ, indicating a metallic behavior of Cu_2N checkerboard films [62, 68].

Consequently, in Figs. 4.3a-c, at positive bias voltages, CB electrons or the lowest unoccupied molecular orbital (LUMO) activate and at negative bias voltages VB electrons and the highest occupied molecular orbital (HOMO) were studied, enabling energy-resolved electronic structure mapping of the surface. Fig. 4.3a, depicting an STM image below the CB, shows height-dominant Cu_2N features, indicating the distortion of the elongated features due to lattice mismatch of the epilayer and the underlying substrate. At the bias voltage of -1 V below the VB in Fig. 4.3b, a brighter contrast of Cu_2N features suggests that some VB electrons are transferred to the tip, which could be due to some interband states at the distorted, strained, or defected parts of the Cu_2N film. Fig. 4.3c exhibits the large conductivity of the Cu_2N films at the bias voltage of 4 V above its CB. At the bias voltage of 2 V (see the AP, Fig. 10B.1m), in contrast to the Fig. 4.3c, a distorted feature is observed rather than the iterative electronic potential, as it remains closer to the CB position compared to Fig. 4.3c. Consequently, the crucial change in states at bias voltages above 2 V causes the Cu_2N submonolayer to appear significantly brighter, while the Cu (111) substrate surface becomes notably darker. This occurs due to the high density of states in Cu_2N, which are excited by a bias voltage of 2 V or higher. Therefore, this observation confirms the presence of the Cu_2N CB below 2 V with a high density of states in this region.

DFT simulations and calculations of the projected DOS (PDOS) (Fig. 4.4b) and the projected band structure (PBAND) of a Cu_2N ML slice consisting of three atoms (Fig. 4.4c and d) reveal the metallic nature of relaxed Cu_2N films on Cu (111). The band structure, achieved using the Heyd-Scuseria-Ernzerhof hybrid functional (HSE) approach, indicates that the CB and VB of Cu_2N overlap at the M point of the BZ. On the other hand, a significant band gap of over 5 eV is observed at Γ point. The overlap only at a single point implies the complicated characteristic of the Cu_2N monolayer. However, in the strained regions, and in spin polarized simulations (see the AP, Fig. 10B.7), the band gap expands, reaching values typical of semiconductors. Phonon simulations and LEED experiments indicated the high stability of Cu_2N, suggesting minimal interaction with the molecules and atoms on the surface, which is desirable for decoupling the electronic excitations of on-surface structures and molecules from the substrate [62, 68]. STM simulations of Cu_2N without H bonds on Cu (111) across various bias voltages are more compatible with the experimental STM data. Moreover, the STS simulations at the Γ point of the BZ are fairly close to our experimental STS measurements depending on the simulation approaches, confirming the suggested structural model, properties, and nature of our Cu_2N films.

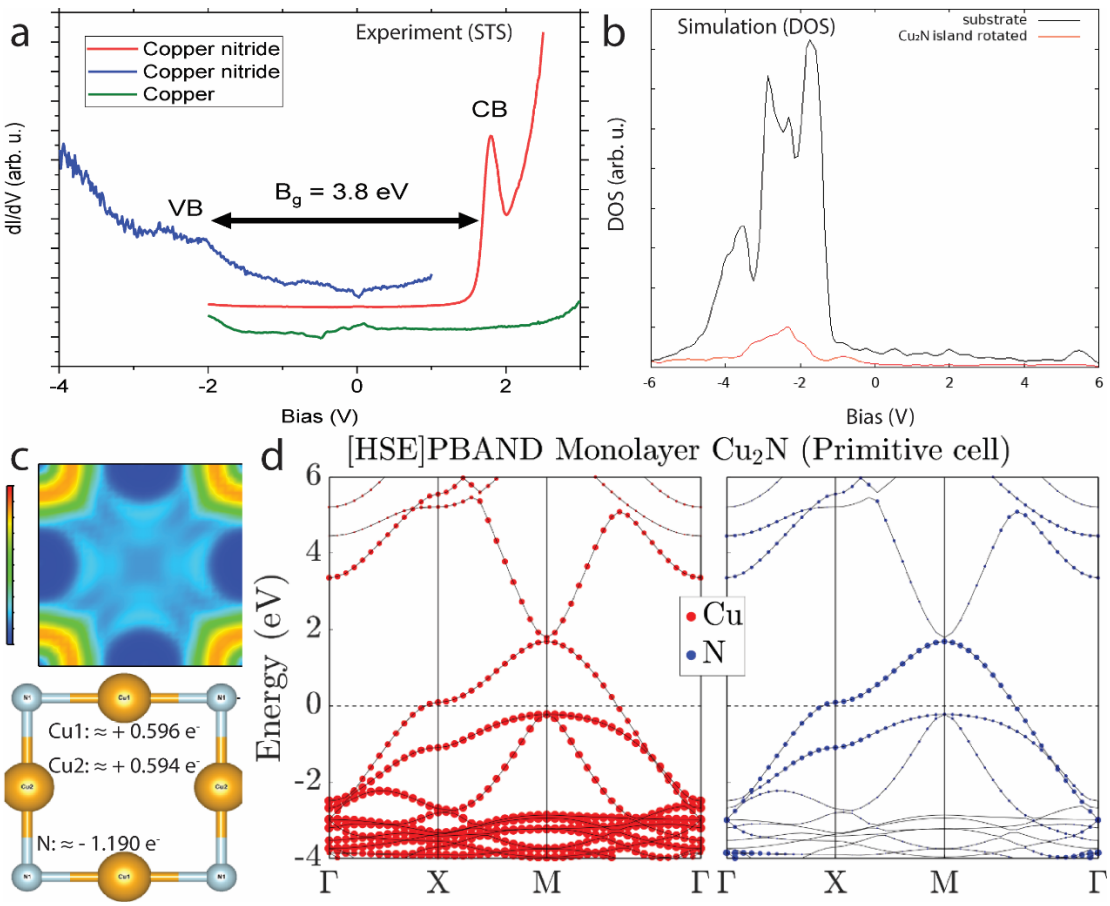

Fig. 4.4. (a) STS of the Cu_2N layer on Cu (111), calibrated on a clean Cu (111) surface. STM and STS acquisition temperature: 4.6 K. (b) DFT Simulation of DOS of Cu_2N islands on Cu (111) substrate corresponding to Fig. 4.3g, and Cu (111) substrate versus the applied bias voltages, simulating the STS measurements. (c) DFT simulation of the electron localization function on atoms on a Cu_2N ML slice confirming the Cu-N covalent bonds and the corresponding atomic model including three atoms (2 Cu and 1 N atoms). (d) DFT simulation of the PBAND of the Cu_2N monolayer shown in Fig. 4.4c, using the HSE approach.

We observed that Cu_2N is stable in UHV below 700 K, while heating a Cu_2N monolayer above 700 K leads to its desorption [229]. On Cu (100), the growth of an extended copper nitride monolayer in UHV was not successful due to a significant lattice mismatch [210, 212, 219-221, 224, 225, 227]. Cu_2N islands on Cu (111) have three preferential growth directions, resulting in intersections at borders, leaving bare copper islands in between, containing a reported QC effect [210, 212-214]. By repeating our replacement methods, the coverage of the extended Cu_2N submonolayer can be adjusted. Fig. 4.5a and 4.5b display the Cu_2N submonolayers after one and six cycles of oxidation followed by ammonia annealing, resulting in approximately 30% and 90% of Cu_2N coverage on Cu (111), respectively. In Fig. 4.5a, the red and blue arrows highlight the Cu_2N and Cu (111) islands, respectively, where, on average, the Cu (111) islands are vaster than the Cu_2N islands.

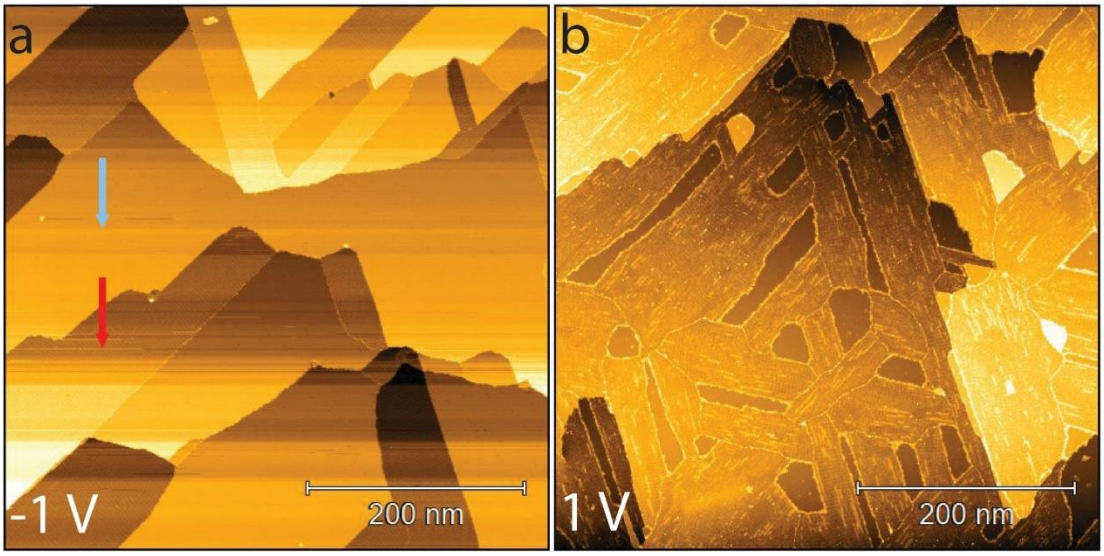

Fig. 4.5. STM measurements of Cu_2N sub-monolayers on Cu (111) after (a) 1 and (b) 6 cycles of dosing with 10^{-6} mbar O_2 and 10^{-7} mbar NH_3 in UHV, resulting in coverage of ≈ 30% and ≈ 90%, respectively. STM parameters are as follows; (a) Z-height = 0.79 nm, V_s = -1 V, I_t = 100 pA, rms-R = 0.11 nm. (b) Z-height = 0.74 nm, V_s = 1 V, I_t = 100 pA, rms-R = 0.01 nm. STM acquisition temperature: 4.6 K.

4.4.3 Molecular Deposition

Fig. 4.6 shows the deposited DAPPor molecules on Cu_2N and Cu (111) islands. Due to the high chemical and dynamic stabilities of the Cu_2N layer, proven by LEED experiments and phonon simulations, respectively [68, 225], there is a very low probability that this film interacts and hybridizes with adsorbates, reducing adsorption probability on this surface and efficiently decoupling the epilayer molecules [68, 225]. As a result, the majority of molecules are adsorbed on the Cu areas, and a minority of molecules can be found on Cu_2N [241]. Fig. 4.6a display the coexistence of both single (blue arrows) and double layers (white arrows) of DAPPor on Cu (111) islands, but a very low coverage of DAAPor (red arrows) on, Cu_2N below 10%. Varying the bias voltage from -0.5 V to -2 V changed the state of the porphyrin layers in STM images (see the AP, Fig. 10B.9a) due to the presence of a HOMO between these two values. In Fig. 4.6a, at bias voltage of -2 V, below the HOMO of these DAPPor molecules, the double layer appearance changed to triangular like features, where the horizontal sides of the triangle represent the porphin macrocycle and the vertical sides represent the amine-phenyl chains. In the single layer DAAPor, the porphin macrocycles appeared as larger spheres, with the amine-phenyl chains placed at about 10° from the vertical direction and four pyrroles at the sides of the porphins emerged as dot- or smaller spheres-like features. Considering the sharp and straight step edges of the Cu (111) surface, the vertical direction in these STM images forms an angle of ≈30˚ with the $[\bar{1}\bar{1}2]$ crystallographic direction [249]. By increasing the bias voltage to -0.5 V (see the AP, Fig. 10B.9a), for both single and double layers, macrocycle porphins are seen as circle-like features, linearly assembled with the adjacent molecules from the amines side with the angle of 10° compared to the vertical direction. Fig. 4.6b is a zoomed-in STM image of the assembly of unreacted DAPPor molecules on a Cu_2N island. Single unreacted DAPPor molecules tend to assemble either parallel or perpendicular to the elongations of Cu_2N. Although the assembly of some DAPPor molecules on Cu_2N is dominant, high-resolution STM images of individual DAPPor molecules reveal four pyrrole rings that appear brighter at a bias voltage of 0.5 V (see the AP, Fig. 10B.9b and 10B.9c). DAPPor molecules on Cu_2N fit the free-standing relaxed gaseous model very well. Fig. 4.6c presents a high-resolution STM image of DAPPor molecules in a molecular monolayer on a Cu (111) island. The proposed structural model based on the observed bias-dependent STM images is exhibited (see the AP, Fig. 10B.9). Based on our model in Fig. 4.6c for the single layer of DAPPor on Cu (111), we speculate that

the overlap of the density of states of hydrogen atoms from the benzene rings and a neighboring pyrrole constructively interferes, making four bright sphere-like features around the DAPPor molecules in the STM images. The DAPPor model looks distorted from the free-standing equilibrium shape. This confirms the significant interaction of the molecule with the Cu (111) surface, while there is limited interaction of the molecule with the Cu_2N surface, similar to free-standing gaseous molecules optimized by the ChemDraw software. Fig. 4.6d shows the STS of clean Au (111) (black), DAPPor on Cu_2N (red), and DAPPor on Cu (111) (blue). The HOMO-LUMO gap values of DAPPor on Cu (111) and Cu_2N were equal to $\approx$ 0.9 eV and $\approx$ 2.4 eV, respectively. These results indicate that, based on our STS measurements, the Cu_2N layer decoupled the DAPPor molecules from the copper substrate due to a reduction in the hybridization of the porphyrin C atoms with the substrate atoms [225, 230]. This is evidenced by the enlarged STS HOMO-LUMO gap and the distance between the highest occupied molecular orbital (HOMO) and LUMO of a DAPPor molecule on Cu_2N compared to on Cu (111), calibrated by a clean Au (111) STS. In addition, DFT simulations revealed an increase in the HOMO-LUMO gap of DAPPor molecules on Cu_2N islands (Fig. 4.6f) compared to Cu (111) islands (Fig. 4.6e), confirming the decoupling effect of the Cu_2N layer. However, the simulated HOMO-LUMO gap for these molecules in both cases are smaller than the experimental STS measurements (see the AP, Fig. 10B.9).

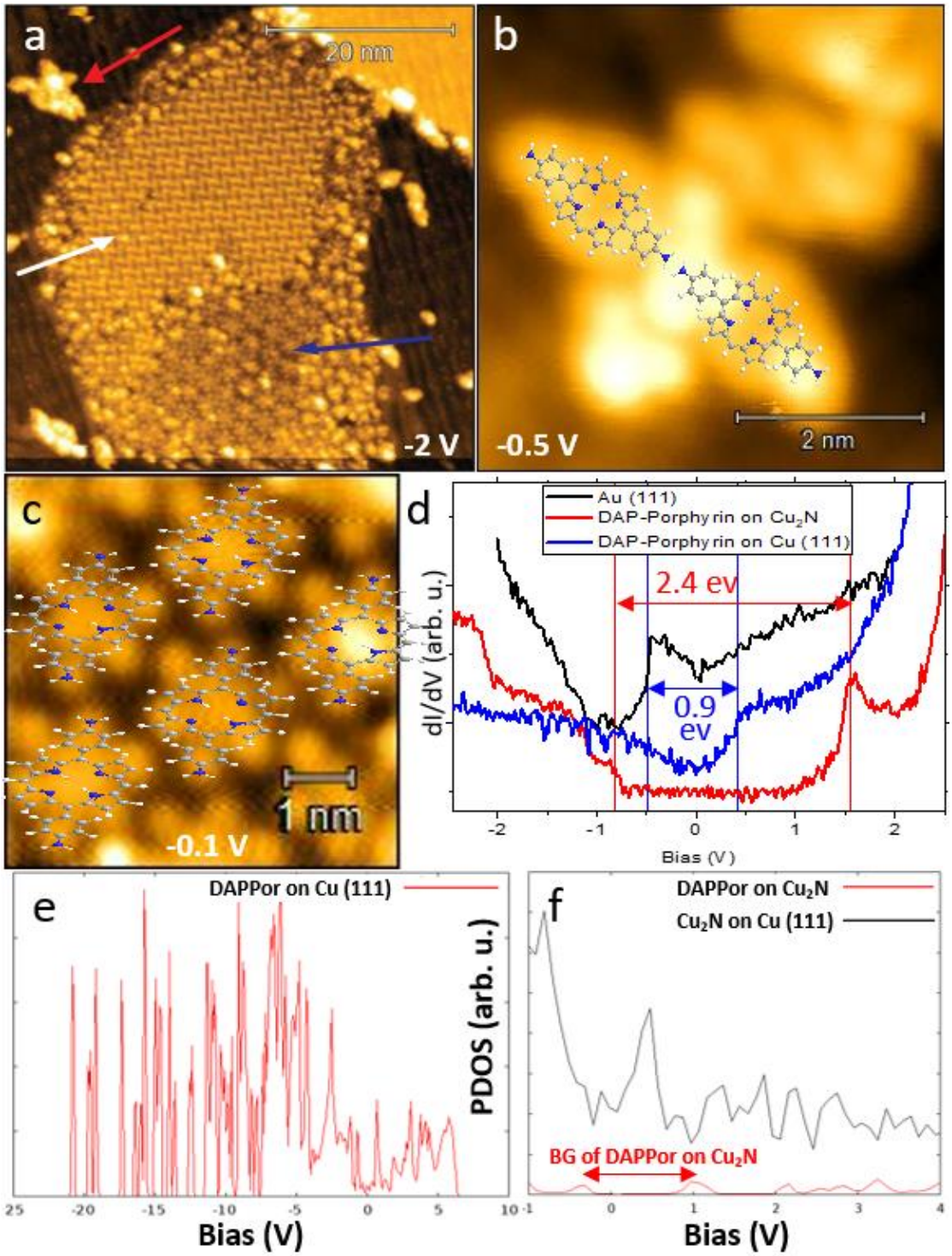

Fig. 4.6. (a) STM image of single and double layers of DAPPor assembly on Cu (111); Z-height = 0.38 nm, V_s = -2.0 V, I_t = 50 pA, rms-R = 0.07 nm. The red, white, and blue arrows indicate DAPPor on Cu_2N, a monolayer of DAPPor on Cu (111), and a double layer of DAPPor on Cu (111), respectively. (b) STM image of DAPPor molecules on a Cu_2N sub-monolayer on Cu (111) along with the corresponding proposed molecular model; Z-height = 0.36 nm, V_s = -0.5 V, I_t = 50 pA, rms-R = 0.09 nm. (c) STM image of single and double layers of DAPPor assembly on Cu (111) with the associated proposed molecular model; Z-height = 0.12 nm, V_s = -0.1 V, I_t = 50 pA, rms-R = 0.02 nm. (d) Tunneling spectra of clean Au (111), DAPPor on Cu_2N, and DAPPor on Cu (111). (e) DFT simulation of PDOS for DAPPor on Cu (111). (f) DFT simulation of PDOS for DAPPor on Cu_2N. STM acquisition temperature: 4.6 K.

4.5. Conclusion

As a conclusion, we developed a new replacement method for the production of Cu_2N submonolayers on Cu (111) by exchanging the O atoms of the copper oxide thin films with N atoms from NH_3 gas. The fabricated Cu_2N reveals a Cu (100) c(2×2)-N superstructure on Cu (111) with a square-like unit cell parameter of ≈ 0.54 nm, indicating a strain of the Cu_2N layer on Cu (111) compared to a relaxed free-standing one. This strain causes an increase in the band gap of Cu2N, as observed by STS and DFT simulations. STS of Cu_2N indicates a band gap of ≈ 3.8 eV at its Γ point in the BZ, based on DFT calculations. Cu_2N islands were grown in three dominant distorted elongation directions, crossing each other, forming Cu (111) islands with a QC effect, exhibiting standing waves of the electron density. Since our fabrication method comprises no destructive technique, we increased and tuned the Cu_2N coverage by repeating the oxidation and nitridation cycles. In addition, the molecular deposition on this surface reveal the high stability of the Cu2N surface reducing the molecular adsorption energy, leading to sparse molecular adsorption on Cu_2N, while double layers of DAPPor were observed on the Cu (111) surface. The limited interaction of Cu_2N with the DAPPor molecules is confirmed by the STM images, in which the DAPPor molecules on Cu_2N fit the relaxed and optimized model of free-standing DAPPor molecules. On the other hand, the single DAPPor model on Cu (111) is stretched, indicating the strong interaction between a DAPPor molecule and the Cu (111) surface. DAPPor molecules on Cu (111) islands assemble exclusively in a parallel orientation to one another, forming an angle of 20° relative to the $[\bar{1}\bar{1}2]$ direction. In contrast, on Cu_2N, these molecules exhibit both parallel and perpendicular orientations, aligning with the elongations of Cu_2N islands. Furthermore, STS of DAPPor on Cu (111) and Cu_2N proves the decoupling effect of the Cu_2N layer, preventing electronic transports between the molecules and the substrate.

Chapter 5

Ullmann Coupling and Poly(para-phenylene) Wires on Copper Nitride Monolayers on Copper (111)

This chapter explores Ullmann coupling and poly(para-phenylene) wires on copper nitride monolayers on copper (111). It includes content that is currently being prepared for submission, with permission from Rostami, M., Yang, B., Senge, M.O., Chi, L., and Barth, J.V., 2024.

5.1. Contributions

Mohammadreza Rostami: Experiments, data analysis, writing, review & editing, experiment discussion, model drawing. Biao Yang: Experiments, Experiment discussion, review & editing, supervision. Mathias O. Senge: Synthesis of molecules. Lifeng Chi: Review & editing, supervision. Johannes V. Barth: Review & editing, supervision.

5.2. Introduction

Ullmann coupling, discovered during synthesis of biphenyls from aryl halides in 1901 [250], as an on-surface reaction, can be used for on-surface synthesis of different low-dimensional (D) structures and covalent organic networks [1, 3]. This reaction is a form of aryl-aryl coupling following session of bonds between halogens and sp^2 or sp-hybridized carbons [2, 251-256], which is one of the most successful, efficient, simple, predictive and controllable reported on-surface coupling reactions [1, 251, 257]. For metallic surfaces, another intermediate step in Ullmann coupling involves the formation of metal-organic chains or networks [250]. This mechanism paves a bottom-up approach for the assembly of nano-architectures and structures [258]. The direct bonding of aromatic moieties is a useful method for π-conjugation formation, resulting in significant charge transfer [259]. In this case, it is advantageous to implement dehalogenation and Ullmann coupling reactions, because of the specific C-halogen bond dissociation energies of versatile halogens, allowing for adjustable activation temperatures for selective and directional nanoarchitectures [259]. In addition, fewer defects on the surface and

using planar precursors increase the temperature of dehalogenation [2]. for example, debromination of 1,4,5,8-tetrabromonaphthalene (TBN) [260] and 1,3-bis(p-bromophenyl)-5-(p-iodophenyl)benzene (BIB) occur at 100°C and 175°C, respectively [2]. Therefore, more control over the sequential activation of active sites and nano-architectures is acquired [252, 259]. This holds promise for designing desired complex structures, and molecular circuits and investigating the individual molecular entities electronics [259].

Different molecules have been reported for the on-surface synthesis of 2D materials like long-range order 2D sheets having extended regularity, organometallic networks and nAGNRs implementing Ullmann coupling, including iodine- [88, 97, 188, 257, 261], bromine- [1-3, 93, 259-264], chlorine- [252] and fluorine-containing molecules [265, 266]. nAGNRs are elongated graphene stripes with a width of less than 100 nm and contain n C atoms across their width [260]. They are classified based on n = 3p, 3p + 1, and 3p + 2, with each type indicates different electronic properties [260]. However, there are still many contradictory reports. The group of n = 3p + 2 exhibits a metallic nature according to tight-bonding approximation and a semiconducting nature according to DFT [260]. nAGNRs are promising structures for next-generation electronics because they possess a tunable band gap depending on their width and edge conformation [44].

Brominated porphyrins such as tetra(4-bromophenyl)porphyrin (Br_4TPP) [258] and 5,15-bis(4'-bromophenyl)-10,20-bis(4'-iodophenyl)porphyrin (trans-Br_2I_2TPP) [259] have been developed for Ullmann coupling reactions on metallic surfaces [240]. Porphyrins are macrocyclic molecules existing in living organisms and sediments containing organic materials such as oil and coal [240]. Porphyrins have various applications in biological and medical systems, metal-organic coordination, and covalent networks due to their interesting properties such as non-linear optical, field-responsive, catalytic, and photovoltaic properties [240, 267, 268]. Porphyrin is a building block for functional metalloporphyrin materials. Metalloporphyrins are a crucial part of many biomolecules, comprising heme as oxygen-binding group of red blood cells of mammals and chlorophyll as the basis of photosynthesis in plant leaves [240, 267, 268]. Porphyrins consist of peripheral substituents and a parent planar heteromacrocycle molecule called porphin, composed of four modified pyrrole subunits [240].

Due to their high conductivity and more convenient surface preparations, metals are the most compatible substrates with surface science techniques including STM [1-3, 5-7, 35, 269]. On the flip side, metallic substrates quench the electronic excitations of the overlying molecules and structures, thereby limiting their optical and electronic characterizations [1-3, 5-7, 35, 96, 97, 269]. Despite being metallic, copper nitride thin films exhibit a remarkable decoupling effect, minimizing interactions and electron transfer between the metallic substrates and the molecules and structures on top [18, 62, 68, 219, 224, 225, 230, 239, 241]. This strong decoupling effect, despite its metallic nature, makes this surface compatible with surface science techniques and a promising candidate for investigating on-surface reactions [62, 68, 238]. The high stability of Cu_2N monolayers, confirmed by phonon simulations and LEED experiments, reduces atomic and molecular adsorption on this surface and decouples electronic excitations of the adsorbents from the metallic substrate [68, 225]. Furthermore, studies on molecular depositions such as porphyrins on copper nitride thin films have been reported in the literature [225, 230].

Ullmann coupling on thin films on metallic substrates benefits from the ad-atoms on these surfaces, catalyzing this reaction [257, 270]. Reports on surface-assisted Ullmann coupling on semiconductor surfaces are limited due to alleviated catalytic efficiency and molecular desorption at the temperatures required for Ullmann coupling [257]. This work introduces the debromination of 4,4″-dibromo-p-terphenyl (DBTP) and 5,15-(di-4-bromophenyl)porphyrin ($(BrP)_2P$), Ullmann coupling reactions, and on-surface preparation of poly(para-phenylene) (PPP) wires (also called the narrowest nAGNRs (n=3) as a large band gap semiconductors [270]) on Cu_2N surface on Cu (111). The HOMO-LUMO gaps of the porphyrin molecules and PPP wires on the Cu_2N decoupling layer on Cu (111) were measured using STS and compared to results obtained on other substrates. The Cu_2N monolayer was produced by the replacement of O atoms in copper oxides [242, 246-248] by N atoms through ammonia annealing.

5.3. Experimental

Sample preparation: The single-crystal Cu (111) surface was prepared through iterative cycles of Ar^+ or Ne^+ sputtering (≈ 1 keV, 30 minutes, I_{ion} ≈ 7.5 μA, ≈ 0.014 C) followed by annealing at ≈ 700 K for 30 minutes. Cu_2N submonolayers were subsequently fabricated via repeated cycles of oxidation by dosing 60 L oxygen at the sample temperature of ≈ 600 K under a pressure of ≈ 10^{-6} mbar, and NH_3 annealing at ≈ 625 K by dosing 180 L NH_3 under a pressure of ≈ 10^{-7} mbar. The sample was heated from the backside using radiative heating and electron bombardment from a W filament, with concurrent O_2 or NH_3 gas dosing.
Characterization: Cu (111), Cu_2N, and adsorbed molecules were characterized by XPS with a Mg K_α photon line (≈ 1253.6 eV), LEED, STM, and STS after sample preparation in custom-built UHV chambers. In the XPS chamber, a K-type (Nickel-Chromium/Nickel-Alumel) thermocouple was affixed to the molybdenum plate supporting the Cu (111) sample, with the base pressure maintained below 2×10^{-10} mbar and the XPS acquisition conducted at liquid nitrogen temperature (77 K). For STM analysis, conducted in a commercial JT-STM (SPECS GmbH), the thermocouple was placed at the surface. The base pressures in the preparation and primary STM chambers were 1.1×10^{-10} mbar and 8.5×10^{-11} mbar, respectively. STM and STS measurements were performed at liquid nitrogen (77 K) and liquid He temperatures (4.6 K).
Molecular deposition: $(BrP)_2P$ and DBTP powders shown in Fig. 5.1, sourced from Mathias O. Senge's group and Shanghai Aladdin Bio-Chem Technology, respectively, were loaded into a quartz crucible housed within custom-built OMBEs. Molecular depositions occurred onto the as-grown Cu_2N/Cu (111) surface at ambient temperature. The resultant molecular films underwent rigorous characterization using STM and STS techniques. Subsequently, the molecular assemblies were scrutinized at ambient temperature via STM, while STS was employed to investigate the decoupling effect of Cu_2N films on molecules and polymers adhering Cu_2N and Cu (111).
Softwares: Structural models and their optimized freestanding configurations were generated using ChemDraw software [245]. Additionally, comprehensive analysis of STM images was carried out using Gwyddion software [183].

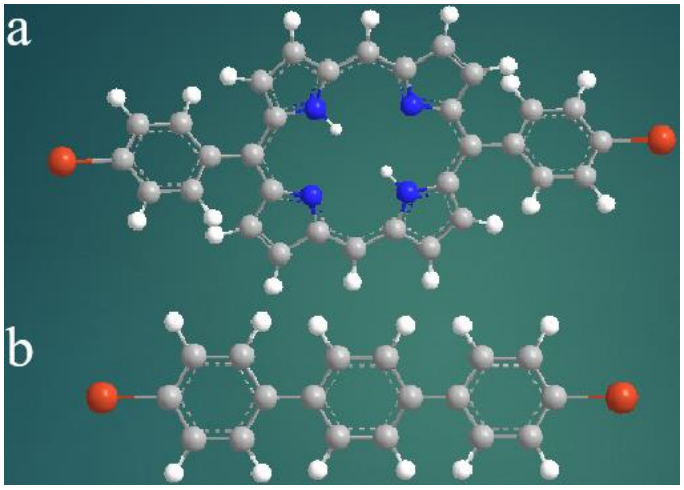

Fig. 5.1. Schematic views of a single (a) $(BrP)_2P$ and (b) DBTP molecules optimized by ChemDraw software. Gray, white, red and blue spheres represent C, H, Br and N atoms, respectively.

5.4. Results and Discussion

Fig. 5.2 shows the deposition of $(BrP)_2P$ molecules on Cu_2N islands on Cu (111) and Cu (111) islands surrounded by Cu_2N. The molecules preferentially decorate the copper surface rather than Cu_2N, since Cu_2N possesses a high chemical stability hindering the interaction and hybridization of the epilayer molecules and atoms with the substrate [68]. Fig. 5.2a reveals the linear assembly of $(BrP)_2P$ molecules on the Cu (111) surface at room temperature in three main directions with angles of about 10°, 50°, and -45° compared to [110] direction (see the AP, Fig. 10C.1). At 300 K, the $(BrP)_2P$ molecules at the Cu (111) surface arrange horizontally next to each other without any sign of polymerization (see Fig. 5.2b). Fig. 5.2c displays the bromine atoms and debrominated $(BrP)_2P$ molecules on the Cu (111) surface after annealing at 425 K. This figure shows that the all $(BrP)_2P$ molecules were already debrominated at this annealing temperature, surrounded by separated bromine atoms, and distributed randomly on this surface. However, after annealing at 425 K no polymer formation was observed. On the other hand, after annealing the sample at 475 K, Ullmann coupling and polymerization of molecules were observed as seen Fig. 5.2d. In Fig. 5.2e, unreacted $(BrP)_2P$ molecules deposited on Cu_2N at 300 K, exhibiting no occurrence of any reaction such as debromination or aryl-aryl coupling at this temperature. After annealing at 425 K, Fig. 5.2f indicates mostly single molecules or clusters of uncoupled $(BrP)_2P$ monomers, except a linear polymer at this temperature as a candidate for Ullmann coupling. This provides evidence that the Cu_2N surface catalyzed aryl-aryl coupling at lower temperatures than the Cu (111) surface since the Cu (111) islands were populated and saturated by molecules and bromine atoms, alleviating the coupling efficiency. By annealing at 475 K, the number of observed dimers and oligomers on Cu_2N increased. The observation of linear dimers and oligomers is more expected for Ullmann-type coupling. Fig. 5.2g shows a $(BrP)_2P$ dimer on Cu_2N on Cu (111) after annealing at 475 K. However, this bond as an Ullmann coupling candidate is surprisingly bent. Fig. 5.2h indicates a $(BrP)_2P$ oligomer on Cu_2N, in which four molecules have been assembled together from the phenyl groups side, which is a candidate for polymerization. Consequently, on Cu (111), cleavage and coupling occur more pronouncedly, and diffusion is significant [188], while on Cu_2N, adsorption is reduced, and limited C-Br bonds cleavage is observed, acting as a barrier to the formation of this covalent network. Versatile linear or zigzag structures of $(BrP)_2P$ molecules were found as candidates for on-surface coupling and reactions. Fig. 5.2i exhibits STS of $(BrP)_2P$ on Cu_2N and Cu (111) surfaces, calibrated by Cu_2N, clean Cu (111), and Au (111) surfaces. As expected, Cu (111) and Au (111) show the surface states starting at a bias voltage of about -0.5 V. The STS spectrum of Cu_2N indicates CB and VB at bias voltages of about 1.9 V and -2 V, respectively, exhibiting a band gap of about 3.9 eV at the Γ point of the BZ, which is comparable with the literature [219, 224, 230]. The STS spectra of $(BrP)_2P$ on Cu (111) reveal the quenching of the LUMO and HOMO states at different biases, exhibiting the Cu (111) surface states and shrinking the observed HOMO-LUMO gap of $(BrP)_2P$. In contrast to the Cu (111) surfaces, the Cu_2N surface prevented the transfer of excited electrons into the substrate, decoupling the $(BrP)_2P$ molecules from Cu (111) and exhibiting intense LUMO and significant HOMO states at bias voltages of about 1.6 V and -1.5 V, respectively.

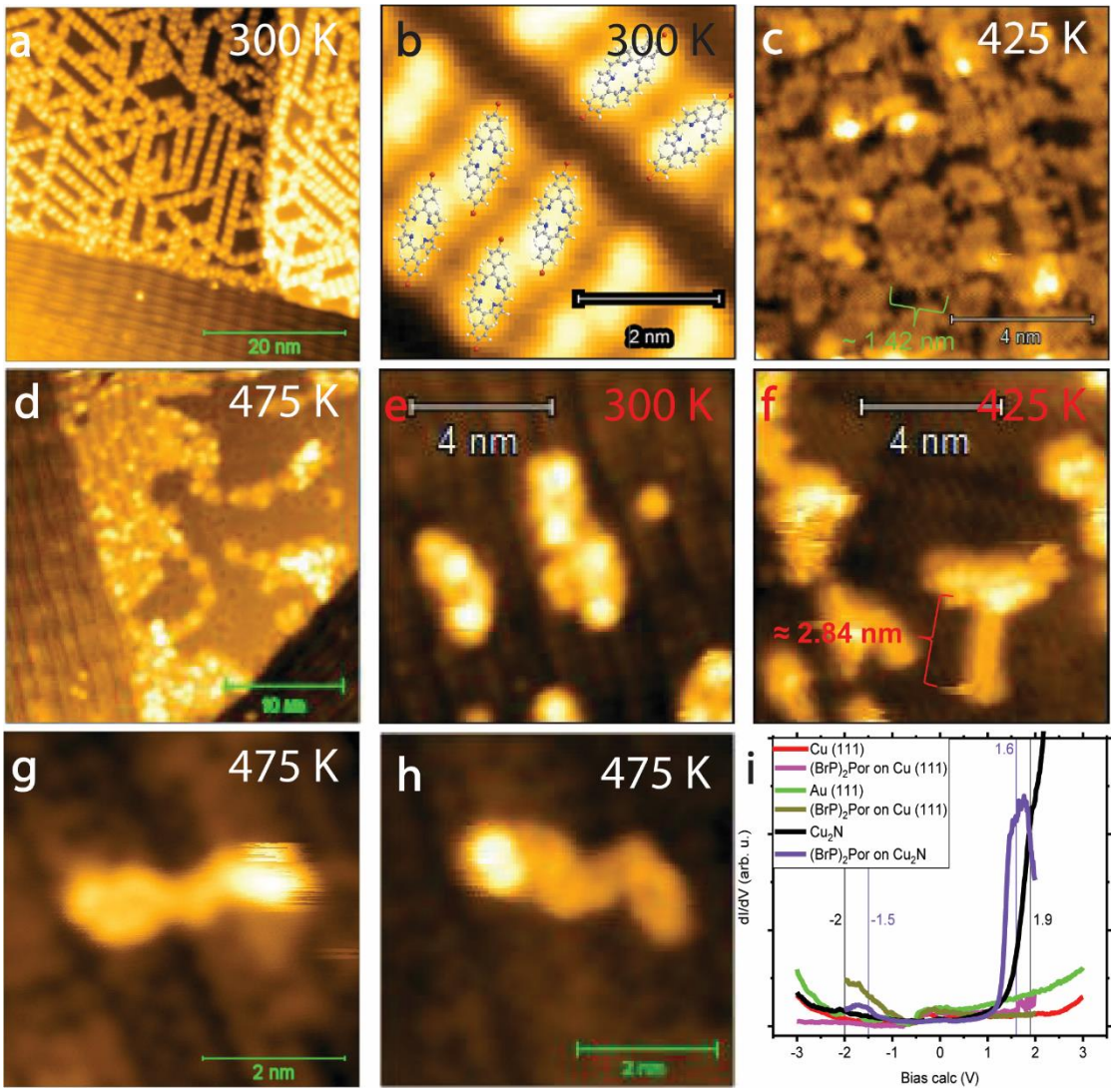

Fig. 5.2. (a) STM image of $(BrP)_2P$ on Cu (111) at room temperature; The distance between the brightest and darkest points (Z-height) = 0.54 nm, V_s = 1 V, I_t = 100 pA, rms-R = 0.09 nm. (b) Corresponding structural model created with ChemDraw software. (c) STM image of debrominated $(BrP)_2P$ molecules on Cu (111) after annealing at 425 K; Z-height = 0.16 nm, V_s = -1 V, I_t = 100 pA, rms-R = 0.02 nm. (d) STM image of $(BrP)_2P$ couplings and chains on Cu (111) after annealing at 475 K followed by Ullmann coupling and polymerization; Z-height = 0.44 nm, V_s = 1 V, I_t = 100 pA, rms-R = 0.08 nm. (e) STM image of unreacted $(BrP)_2P$ molecules on Cu_2N on Cu (111) at room temperature; Z-height = 0.32 nm, V_s = 0.1 V, I_t = 1 nA, rms-R = 0.07 nm. (f) STM image of $(BrP)_2P$ couplings and a linear dimer chain on Cu_2N on Cu (111) after annealing at 425 K; Z-height = 0.36 nm, V_s = -0.1 V, I_t = 50 pA, rms-R = 0.07 nm. (g) STM image of Ullmann coupling of two $(BrP)_2P$ molecules on Cu_2N on Cu (111); Z-height = 0.31 nm, V_s = 0.5 V, I_t = 1 nA, rms-R = 0.05 nm. (h) STM image of an oligomer on Cu_2N on Cu (111); Z-height = 0.45 nm, V_s = 0.1 V, I_t = 1 nA, rms-R = 0.07 nm. STM acquisition temperature: 4.6 K. (i) STS spectra of Cu (111), Au (111), Cu_2N, and $(BrP)_2P$ molecules on Cu (111) and Cu_2N.

To further investigate Ullmann coupling on Cu_2N and Cu (111) islands surrounded by Cu_2N elongations, we examined the on-surface thermal-induced reactions of DBTP molecules. However, STM imaging of a sub-monolayer of DBTP on the surface can be challenging, as the molecules tend to be mobile. Fig. 5.3 shows the deposition of DBTP molecules on this surface, indicating > 90% and ≈ 0% coverage of unreacted DBTP molecules on Cu (111) and Cu_2N surfaces at 300 K, respectively. Fig. 5.3a displays a large-scale STM image of Cu_2N and a Cu (111) island after deposition of DBTP at room temperature in UHV. Smaller adsorption

enthalpy of DBTP molecules on Cu (111) compared to Cu_2N islands, and the respective higher interaction between the molecules and the surfaces, are evidenced by the high coverage of DBTP molecules on Cu (111), despite the sparse distribution on Cu_2N. Fig. 5.3b and 5.3c show zoomed-in STM images of this region, revealing the atomic resolution of the Cu_2N elongations and the unreacted, unbonded molecules with an ellipse-like benzene chains connected to smaller, spheres-like bromine atoms on Cu (111) islands. These results highlight the absence of on-surface debromination and coupling of DBTP molecules at 300 K or lower temperatures.

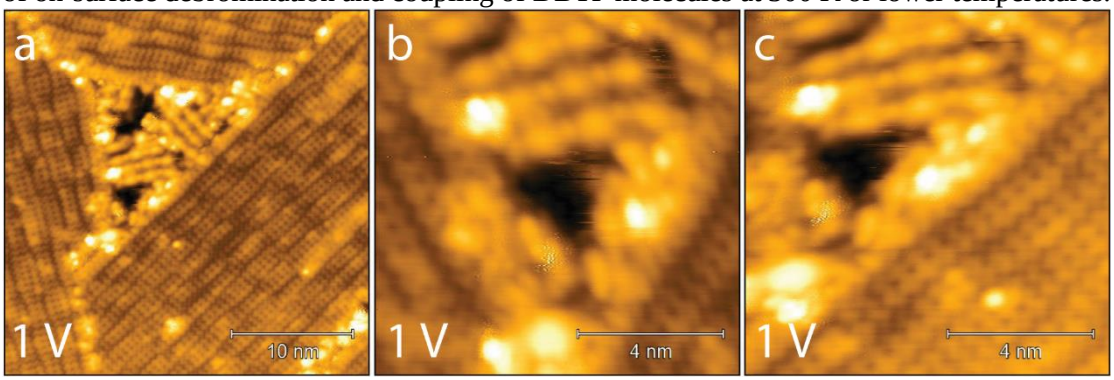

Fig. 5.3. STM images of > 90% and ≈ 0% coverages of unreacted DBTP molecules on Cu (111) and Cu_2N surfaces at room temperature, respectively. (a) Z-height = 0.32 nm, V_s = 1 V, I_t = 100 pA, rms-R = 0.04 nm. (b) Z-height = 0.34 nm, V_s = 1 V, I_t = 100 pA, rms-R = 0.05 nm. (c) Z-height = 0.31 nm, V_s = 1 V, I_t = 100 pA, rms-R = 0.04 nm. STM acquisition temperature: 77 K.

To deposit DBTP on Cu_2N, we increased the crucible temperature from 390 K (≈ 0.5 L) in Fig. 5.3 to 410 K (≈ 3.5 L) in Fig. 5.4, maintaining a deposition time of 10 minutes at a substrate temperature of 300 K. Subsequently, we annealed the sample at ≈ 475 K to promote on-surface debromination and Ullmann coupling. This process increased the coverage on Cu (111) islands to full monolayers and on Cu_2N islands to over 10%. An STM image at a bias voltage of -0.5 V (Fig. 5.4a) shows the formation of linear PPP wires on Cu (111) islands, aligned parallel to each other and forming an angle of about 45° with respect to the [110] direction of the Cu substrate. This finding implies that at 475 K, debromination and aryl-aryl coupling of DBTP molecules occurred, although dehydrogenation and lateral fusion of PPP wires to form larger GNRs did not occur. In Fig. 5.4b, changing the bias voltage to 0.5 V causes the PPP wires in the STM image to become much brighter, indicating a significantly higher density of LUMO states compared to HOMO states in these 1D structures. Near the edge of the Cu (111) islands, the PPP wires were bent, indicating the presence of crucial strains in these regions. Fig. 5.4c is a zoomed-in STM image of the same region, displaying the parallel PPP wires with separated bromine atoms regularly aligned between them [270]. This image shows the homogenous charge distribution along the PPP wires. Fig. 5.4d exhibits an STM image of a PPP wire on Cu_2N on Cu (111). This observation confirms the surface-assisted debromination and Ullmann coupling of DBTP molecules on Cu_2N islands. Annealing DBTP molecules on the Cu_2N surface at ≈ 475 K leads to the formation of a covalently bonded network of PPP wires, similar to Cu (111). However, there is a feature next to this PPP wires reminiscent of wider GNRs, which could be due to dehydrogenation and lateral fusion on this surface. By changing the bias voltage from -2 V in Fig. 5.4d to 0.5 V and -0.5 V in Fig. 5.4e and 5.4f, respectively, the brightness the PPP wire changed, indicating electronic modifications, as the HOMO of PPP wires located between -0.5 V and -2 V of the bias voltage (see the AP, Fig. 10C.2).

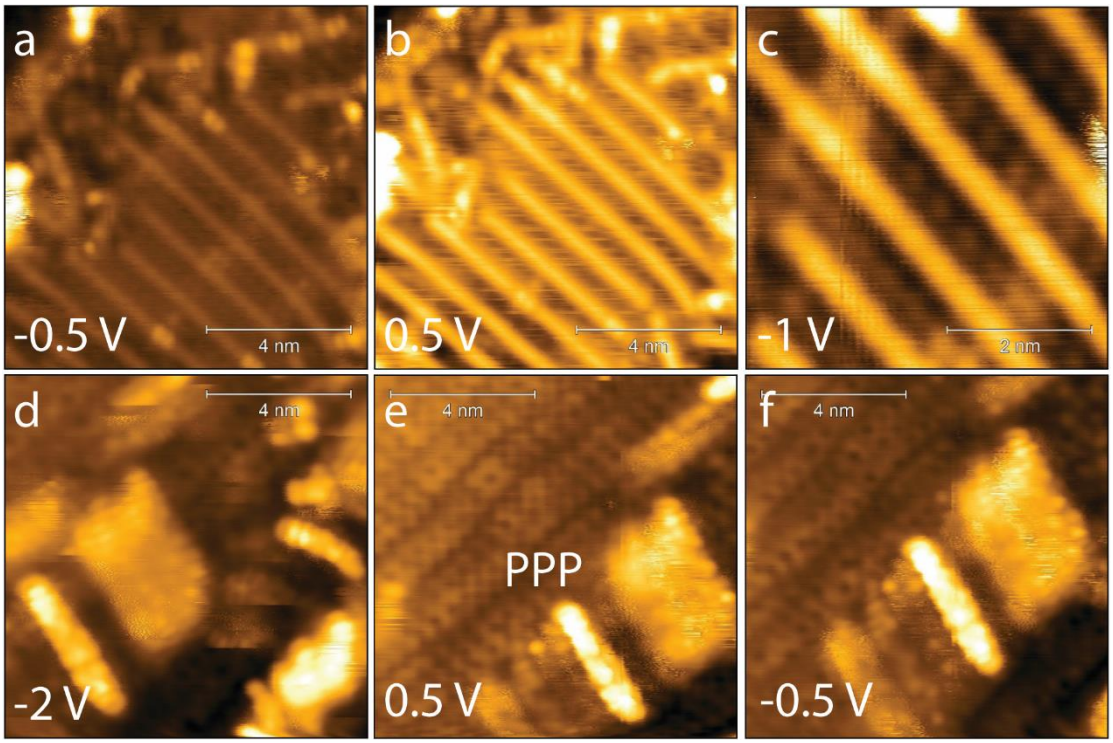

Fig. 5.4. Bias-dependent STM images of PPP wires (or PPP wires) on Cu (111) after annealing DBTP molecules at ≈ 475 K. (a) Z-height = 0.20 nm, V_s = -0.5 V, I_t = 100 pA, rms-R = 0.02 nm. (b) Z-height = 0.11 nm, V_s = 0.5 V, I_t = 100 pA, rms-R = 0.02 nm. (c) Z-height = 0.46 nm, V_s = -1 V, I_t = 100 pA, rms-R = 0.01 nm. Bias-dependent STM images of PPP wires on Cu_2N on Cu (111) after annealing DBTP molecules at ≈ 475 K. (d) Z-height = 0.32 nm, V_s = -2 V, I_t = 100 pA, rms-R = 0.06 nm. (e) Z-height = 0.24 nm, V_s = 0.5 V, I_t = 100 pA, rms-R = 0.04 nm. (f) Z-height = 0.24 nm, V_s = -0.5 V, I_t = 100 pA, rms-R = 0.04 nm. STM acquisition temperature: 77 K.

Fig. 5.5a presents an STM image of PPP wires on Cu (111) at a bias voltage of 2V, alongside the corresponding designed structural models. The structural models consist of 12 benzene rings formed by the polymerization of 4 debrominated DBTP molecules, taking the length of these wires (≈ 8 nm) into account, which extend from one edge of a Cu (111) island to the opposite edge. Fig. 5.5b depicts a non-uniform conformation and charge distribution along a PPP wire on Cu_2N. The structural model that fits the STM image shows a PPP wire in which every second benzene ring is tilted with alternating angles of ≈ 60° and ≈ -60°. Based on the length of this wire (≈ 4 nm), the structural model contains 6 benzene rings resulting from Ullmann coupling of 2 DBTP molecules. At the same time, Fig. 5.5c illustrates a longer PPP wire with a flat conformation and a homogenous charge distribution along its length and width, located on a different region of Cu_2N. Given the length of this wire (≈ 8 nm), the structural model, optimized by ChemDraw software, comprises 12 benzene rings formed through aryl-aryl coupling of 4 dehalogenated DBTP molecules. Fig. 5.5d shows the STS spectra of PPP wires on Cu (111) and Cu_2N islands, calibrated against clean Cu (111), Au (111), and Cu_2N surfaces (see the AP, Fig. 10C.2f). STS spectra of Cu (111) and Au (111) show only the corresponding surface states at the bias voltage of -0.5 V. STS spectra of Cu_2N reveal the CB and VB bands at bias voltages of about 1.8 V and -2 V, respectively, indicating a band gap of about 3.8 V. STS measurements of PPP wires on Cu (111) exhibit a LUMO state below 0.5 V and a HOMO state above -0.5 V, resulting in a HOMO-LUMO gap of about 0.6 eV. The STS spectrum of PPP wires is flat near the Fermi level. The presence of a LUMO (black line in Fig. 5.5d) and a HOMO state for these wires at bias voltages of about 1.23 V and -2.47 V, respectively, results in a HOMO-LUMO gap of approximately 3.7 eV. This enlargement of the observed HOMO-LUMO gap of PPP wires on Cu_2N, which is consistent with the literature [262-264], compared to PPP wires on Cu

(111), confirms the decoupling effect of the Cu_2N layer preventing the electronic transfer between the molecules or 3GNRs and the metallic substrate.

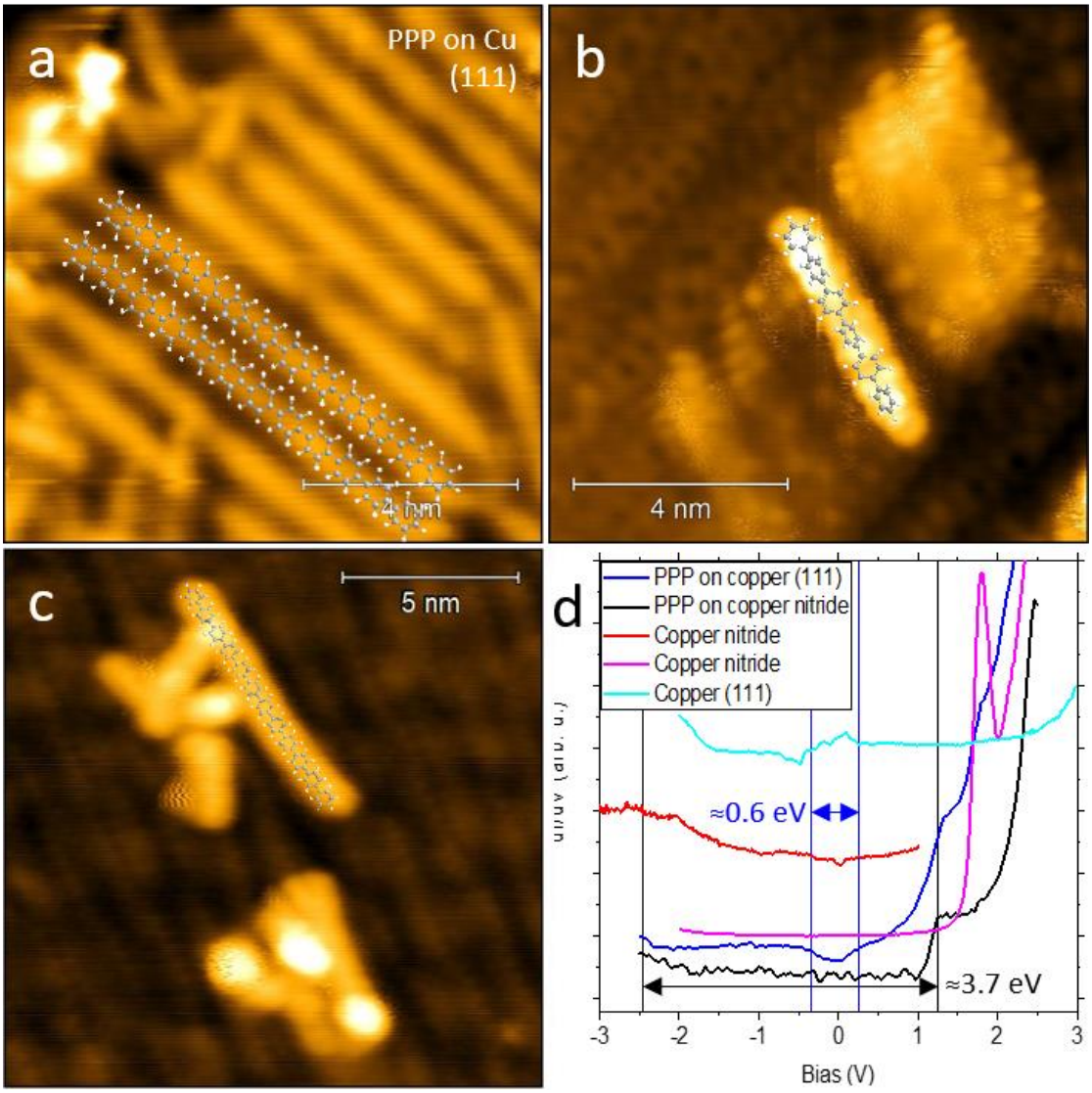

Fig. 5.5. A STM image of PPP wires on Cu (111) and its corresponding molecular model after annealing DBTP molecules at ≈ 475 K. (a) Z-height = 0.10 nm, V_s = 2 V, I_t = 100 pA, rms-R = 0.01 nm. STM images of PPP wires on Cu_2N on Cu (111) and its corresponding atomic models after annealing DBTP molecules at ≈ 475 K. (b) An asymmetric tilted PPP wire; Z-height = 0.26 nm, V_s = -1 V, I_t = 100 pA, rms-R = 0.04 nm. (c) A symmetric flat PPP wire; Z-height = 0.34 nm, V_s = 1 V, I_t = 100 pA, rms-R = 0.06 nm. STM acquisition temperature: 77 K. (d) STS spectra of copper, and PPP wires on copper and Cu_2N.

5.5. Conclusion

Due to the high stability of Cu_2N and its relatively weak interactions with on-surface molecules and structures, the majority of $(BrP)_2P$ and DBTP molecules adsorbs on Cu (111) patches. However, we managed to deposit over 10% of both molecules on the Cu_2N submonolayers as well. Although we observed the formation of porphyrinoid oligomers on Cu (111) islands and oligomers on Cu_2N as candidates of Ullmann coupling on this surface, given the complexity of the problem, we also investigated the DBTP molecules on these islands. By annealing these molecules at about 475 K, debromination and π-conjugation formation occurred as a result of the surface-assisted Ullmann coupling. This caused the formation of PPP wires with flat and

tilted conformations on Cu_2N, providing a silver lining for future investigations of the electronic and optical properties of versatile GNRs. Based on STS measurements, Cu_2N layers decouple the $(BrP)_2P$ molecules and PPP wires from the Cu (111) substrate, with HOMO-LUMO gaps of 3.1 eV and 3.7 eV, respectively. The capability of Ullmann coupling and formation of GNRs on Cu_2N as a stable metallic thin film compatible with surface science techniques and possessing the intriguing decoupling effect represents a unique combination of properties as a substrate. This finding highlights the promise of this surface, aiming to advance our fundamental understanding and provide transformative insights into surface phenomena and their future applications.

Chapter 6

Replacement Method Fabrication of Cu_2N on Cu(100): Analysis of Structure and Electronic Properties

This chapter explores the replacement method fabrication of Cu_2N on Cu(100): analysis of structure and electronic properties. It includes content that is currently being prepared for submission, with permission from Rostami, M., Kaderoğlu, C., Yang, B., Seyedmohammadzadeh, M., Kaya, P., Olgar, H., Senge, M.O., Aktürk, E., Chi, L., and Barth, J.V., 2024.

6.1. Contributions

Mohammadreza Rostami: Experiments, data analysis, writing, review & editing, experiment discussion, model drawing. Çağıl Kaderoğlu: DFT calculations. Biao Yang: Experiments, Experiment discussion, review & editing, supervision. Mahsa Seyedmohammadzadeh: DFT calculations. Pinar Kaya Fizmuh: DFT calculations. Handan Olgar: DFT calculations. Ethem Aktürk: DFT calculations. Peter Fuelner: Experiment discussion, review & editing. Mathias O. Senge: Synthesis of molecules. Lifeng Chi: Review & editing, supervision. Johannes V. Barth: Review & editing, supervision.

6.2. Introduction

A wide range of potential applications [18, 23, 24, 62, 64, 210, 212-214], including optical information storage devices [18-24], microelectronic semiconductor materials [18, 61, 209, 210], and new energy materials [65, 211], have made copper nitride thin films an interesting subject for surface studies [18, 209, 210]. Cu_3N and Cu_2N thin films exhibit promising physical properties [18, 21, 22, 63-67, 217]. Cu_2N [210, 212, 219-221, 224, 225, 227-229] and Cu_3N [18, 217, 230, 231] thin films have been produced by various methods [18, 23, 24, 61, 67, 69, 210, 215, 224-226, 232, 271], such as magnetron-sputtering single-crystal epitaxy [18, 216-218]. The corresponding lattice parameters (≈ 0.3385 - 0.382 nm) vary depending on the preparation

methods. Versatile lattice parameters can change the conductivity of copper nitride from an insulator to a conductor [18, 61, 215, 236]. The bandgap of these thin films increases in strained regions [236, 238]. On the other hand, Cu_4N has been reported as a metallic thin film [61]. However, there are contradictory reports regarding copper nitride (e.g., Cu_2N) thin films, which have been described as an insulator with a Scanning Tunneling spectroscopy (STS) band gap larger than 3 eV [18, 219, 220, 224, 230, 231] both with and without H atoms [23]; a semiconductor with ultra-fast pump-probe spectroscopies band gap value between 1.4-2 eV [23, 65, 236, 271]; a semimetal by some DFT calculations [238]; and a metallic thin film as claimed by theoretical calculations and ARPES measurements [62, 68, 239]. One reason for these contradictions could be that STS shows the valence (VB) and conduction bands (CB) at the Γ point of the Brillouin zone (BZ), while ARPES indicates that the band gap is zero at the M point of the BZ [62, 68, 239]. However, copper nitride thin films have weak interactions with the epilayer and provide a promising decoupling behavior of atoms and molecules from the local density of states of the copper substrates [1-7, 23, 35, 68, 219-221, 224, 225, 230], leading to more accurate molecular orbitals and vibronic states measurement and imaging due to the enhancement of the transient lifetime of molecular states [230, 240]. However, there are a limited number of reported molecular depositions on copper nitride thin films [225, 230, 241]. The challenge of achieving full coverage and a double layer of Cu_2N thin films under UHV conditions limits its characterization by XPS, STM, and STS, as well as its application as a decoupling layer in surface science [210, 212, 218-220, 224, 225, 227, 228]. consequently, the physical and chemical properties of Cu_2N are not well known [218]. However, the coverage of Cu_2N can be controlled by temperature; a Cu_2N monolayer desorbs from Cu above 700 K [217, 229].

Furthermore, copper nitride nano-islands can be utilized for plasmon-coupled nanostructures, plasmonic applications [19], electron confinement [19, 210], and the formation of standing waves (known as “quantum corrals") [210, 212-214]. The efficiency of photon emission via local electronic states in the tunneling gap can be adjusted by changing the elastic and inelastic tunneling rates at 4.9 K [19, 210]. Local electronic states were artificially created by synthesizing monoatomic thick copper nitride islands, defects, and clusters on Cu (100) using an STM tip [19]. Tip-induced plasmon mode reduction and enhancement on the surface, achieved by adjusting the bias voltage, allows for tuning the efficiency of photon emission [19]. The formation of Cu_3N powders by high-temperature annealing of a Cu surface at about 900-1000 ˚C in the presence of NH_3 [70, 233-235, 237] and through the replacement of oxygen or fluorine by annealing in the presence of dried NH_3 under non-UHV conditions has been reported [70-75, 272]. In this work, we produced copper oxides and developed the formation of Cu_2N submonolayers on a Cu (100) single crystal by replacing the O atoms of a CuO [242, 246-248] monolayer with N atoms from ammonia (NH_3) gas dissociating on the surface in UHV. We addressed the contradictory reports regarding the conductivity and band gap of Cu_2N and conducted further investigations to elucidate the metallic or insulating nature of this monolayer film. Besides that, the atomic structure, properties, charge confinement, thermal stability, capability of on-surface molecular adsorption, and the decoupling effect of Cu_2N were investigated using STM, STS, LEED, and DFT calculations. The deposition of pentacene, DAPPor, bicyclo[1.1.1]pentane-1,3-dicarboxylic acid (CBCP), and terephthalic acid (TPA) on Cu_2N/Cu (100), their effects on the Cu_2N charge confinement, and the impacts of O_2 and air exposure were investigated.

6.3. Experimental

Sample preparation: The Cu (100) single crystal substrate was subjected to a surface cleaning regimen comprising multiple cycles of argon (Ar^+) ion sputtering (≈ 1 keV, 30 minutes, I_{ion} ≈ 7.5 μA, ≈ 0.014 C) and subsequent annealing (≈ 700 K, 30 minutes). Cu_2N islands were synthesized through a sequence of 10 minutes of controlled oxidation at ≈ 675 K with an oxygen pressure of ≈ 10^{-6} mbar (≈ 800 L) and 20 minutes of annealing at ≈ 575-675 K in NH_3 atmosphere with the NH_3 pressure of ≈ 10^{-6} mbar (≈ 1600 L). Sample heating was handled via

a combination of radiative heating and electron bombardment from a W filament, with concurrent dosing of O_2 or NH_3 gas to ensure precise control over the surface reactions.

Characterization: We characterized the structural and electronic properties of the Cu (100) substrate, Cu_2N islands, and adsorbed molecular species using a suite of advanced surface science techniques, such as LEED, STM, and STS, after surface preparation in custom-built UHV chambers. The STM system, housed within a commercial JT-STM (SPECS GmbH) chamber, was equipped with a thermocouple directly affixed to the sample surface to ensure accurate temperature readings. The base pressures in the preparation and primary STM chambers were kept at UHV conditions of 8.5×10^{-11} mbar and 1.0×10^{-11} mbar, respectively. The STM and STS data were acquired at cryogenic temperatures using liquid nitrogen (77 K) and liquid He (4.6 K), enabling high-resolution imaging and spectroscopic analyses of the surface and molecular states.

Molecular deposition: Molecules including DAPPor and CBCP, synthesized by Mathias O. Senge's group, TPA and Pentacene molecules (Sigma Aldrich, 99% purity), were loaded into separate quartz crucibles of custom-built OMBEs, and deposited onto the pristine Cu_2N/Cu (100) surface. These depositions were carried out at the sample temperature of 300 K (room temperature) or 77 K (cryogenic liquid nitrogen temperature). The deposited molecular films were characterized utilizing STM and STS to study the thermally-induced molecular assemblies. The decoupling of on-surface molecules from the Cu (111) substrate by Cu_2N films was demonstrated by STS.

Analytical techniques: Detailed image analysis of the STM data was conducted using Gwyddion software [183], ensuring accurate measurement and interpretation of the observed height and electronic features. The structural models of the molecules and their freestanding optimizations were conducted using ChemDraw software [245].

Computational methods: DFT calculations were conducted to achieve a comprehensive theoretical framework to support the experimental analyses. These calculations and simulations provided deep insight into the atomic structure and electronic properties of the Cu_2N submonolayer, correlating with the experimental STS and STM data to elucidate the nature of Cu_2N thin films and corresponding electronic and confinement states (CSs).

6.4. Results and Discussion

This investigation not only details the nuanced interplay between Cu_2N synthesized using the O replacement method on Cu (100) and the consequent structural and physical properties of Cu_2N square-like islands, but also advanced our understanding of the nature of the Cu_2N film, the CSs formed in the Cu_2N islands, and the decoupling effect of the produced Cu_2N submonolayer. These findings hold critical promise for the applications of Cu_2N for the measurement of tailored electronic and optical properties of novel surface-assisted nanostructures, opening avenues for potential on-surface research in electronic excitations, plasmonics [273-277], quantum confinement, molecular electronics, and coupled quasi-particles [273-277].

6.4.1 Growth

Fig. 6.1 details the fabrication steps of our novel replacement method, substituting the O atoms in CuO with N atoms via on-surface dissociation of gaseous NH_3 using STM and LEED. Fig. 6.1a displays a STM image of the rectangular-like features of CuO on Cu (100), dosed with about 800 L O_2 at a surface temperature of 625 K. Smaller rectangular-like features of the Cu-O on Cu (100) are arranged in a larger repeating rectangular-like shape with an average side length of ≈ 5 nm [236]. As seen in Fig. 6.1b, the reduction of the copper oxide film by NH_3 annealing while dosing ≈ 160 L NH_3 at a substrate surface temperature ≈ 625 K resulted in the formation of twisted stripes resembling Cu(100)-c(2 × 2)-O reconstruction [278, 279], coexisting with the original CuO layer in some regions on the surface. At this intermediate stage, a combination of oxide and nitride likely exists on the copper surface, although the Cu_2N film

has not been formed yet. Since the nitrogen partial pressure (r) is a crucial parameter influencing the lattice constant, structures, and properties of the produced copper nitride [18, 61], the sample was annealed while dosing ≈ 1600 L NH_3 at a surface temperature of 675 K. Consequently, Fig. 6.1c shows the formation of randomly-distributed square-like features of the Cu(100)-c(2×2)N on Cu (100) arranged in a repeating square-like shape with an average length side of ≈ 5 nm [227] (see the AP, Fig. 10D.1). At a bias voltage of 1 V, the Cu_2N islands appear darker and the surrounding Cu (100) surface appears brighter, due to larger conductivity of Cu compared to the Cu_2N submonolayer. However, the border between Cu stripes and the Cu_2N islands possesses sharp edges, the sides and corners of the square-like features are not perfectly shaped and are random in form and size. The LEED pattern of Cu (100) substrate in Fig. 10D.1y (the AP) indicates the main diffraction spots of the surface (1×1) reconstruction with square-symmetry. The LEED pattern in Fig. 6.1d reveals the appearance of three spots between the (1×1) spots of the Cu (100) substrate on the diagonal of the unit cell, after the oxidation of Cu (100) shown in Fig. 6.1a, leading to the formation of the $\left(2\sqrt{2}\times\sqrt{2}\right)R45°$ CuO superstructure [243, 280]. In this superstructure, every 4th row of Cu atoms of the surface is missing and replaced by rows of O atoms at the edges, forming O-Cu-O chains [68, 244]. Fig. 6.1e shows a c(2×2) LEED pattern corresponding to Fig. 6.1b, where Cu (100) (1×1) spots have been indicated by bellow arrows, and c(2×2) spots by red arrows. This confirms the presence of a Cu(100)-c(2 × 2)-O reconstruction [278, 279] under these preparation parameters. Fig. 6.1f displays a $\left(\sqrt{2}\times\sqrt{2}\right)R45°$ or c(2×2) LEED pattern of Cu_2N on Cu (100) after dosing with 1600 L mbar at 675 K as in Fig. 6.1c with a square unit cell [68, 241]. In this LEED pattern, one extra LEED spot, indicated by a red arrow, appears between two main diffraction spots of the Cu (100) substrate on the diagonal of the unit cell.

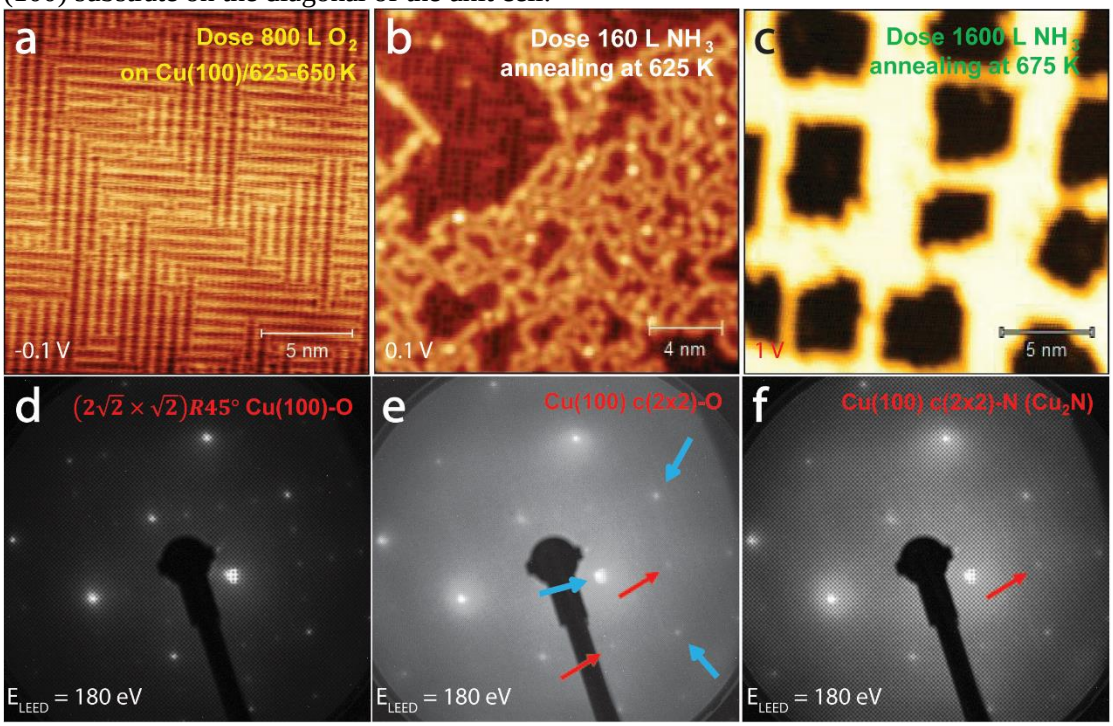

Fig. 6.1. (a) STM image of $\left(2\sqrt{2}\times\sqrt{2}\right)R45°$ Cu (100)-O after dosing ≈ 800 L O_2 on Cu (100) at 625-650 K; The distance between the brightest and darkest points (Z-height) = 0.07 nm, V_s = -0.1 V, I_t = 100 pA, rms-R = 0.01 nm. (b) STM image of the intermediate CuO_YN_X layer after dosing ≈ 160 L NH_3 on copper oxide on Cu (100) at 625 K, reminiscent of Cu(100)-c(2 × 2)-O superstructure; Z-height = 0.19 nm, V_s = 0.1 V, I_t = 1 nA, rms-R = 0.02 nm. (c) STM images of Cu_2N after dosing ≈ 1600 L NH_3 on copper oxide on Cu (100) at 675 K; Z-height = 0.18 nm, V_s = 1 V, I_t = 500 pA, rms-R = 0.06 nm. STM acquisition temperature: 4.6 K. (d) LEED pattern of $\left(2\sqrt{2}\times\sqrt{2}\right)R45°$ Cu (100)-O on Cu (100) after dosing ≈ 800 L O_2 on Cu (100) at 625-650 K. (e) LEED pattern of Cu (100) c(2×2)-O on Cu (100) after dosing ≈ 160 L NH_3 on CuO on Cu (100) at 675 K. (f) LEED pattern of Cu (100) c(2×2)-N (Cu_2N) on Cu (100) after dosing ≈

1600 L NH_3 on copper oxide on Cu (100) at 675 K. E_{LEED} = 180 eV. Blue and red arrows indicate the Cu (100) (1×1) and c(2×2) LEED spots, respectively.

6.4.2 Atomic Structure

Figs. 6.2a-e show high-resolution (HR)-STM images of Cu_2N after three cycles of oxidation followed by NH_3 annealing at a surface temperature of 575 K while dosing ≈ 1600 L NH_3. Fig. 6.2a indicates the formation of larger, randomly distributed square-like Cu_2N islands with an average side length of about 8 nm, surrounded by Cu stripes. The $c(2 \times 2)$ lattice of Cu_2N is 3% larger than Cu (100), which is incommensurate [241], causing strain in this 2D structure. Figs. 6.2b and 6.2c highlight the zoomed-in atomic resolution STM images of Cu_2N films. In Cu_2N islands, the sequence of darker and brighter features forms a regular atomic structure with a square symmetry. Additionally, brighter spots on Cu stripes correspond to excess Cu atoms displaced due to lattice mismatch between Cu_2N and underlying Cu substrate. The periodic features and brightness on Cu stripes around the Cu_2N islands indicate a non-uniform oscillating charge distribution in Cu (100) stripes between Cu_2N rectangles. Figs. 6.2d and 6.2e show the atomic model of the Cu_2N nanostructure on Cu (100), with Cu atoms represented by blue circles and N atoms by red circles, located at the brightest points of the iterative regular pattern of STM images of the Cu_2N submonolayer at the bias voltage of -1 V. Applying a positive bias voltage can invert the states, causing the N atoms to appear as the darkest features in STM images (see the AP, Fig. 10D.2 and 10D.3). Cu atoms in the Cu_2N epilayer are located between every two adjacent bright spots. Nitrogen atoms are situated between the copper atoms in the hollow sites, forming covalent bonds with the copper atoms [210, 219, 223-225, 227]. The unit cell, indicated by a black square in Fig. 6.2e, has a parameter of about 0.4 nm and an angle of 90°. Two types of defects are observed in this regular pattern of Cu_2N atomic resolution: dominant darker blackish spots, indicated by red arrows, and sparse brighter spots, matching the color of the Cu stripes around the Cu_2N, shown by blue arrows in Figs. 6.2b and 6.2c. The blackish and brighter defects in the Cu_2N islands in the STM images represent the missing N and Cu atoms, respectively, in the Cu_2N structures [241]. The Cu_2N structures remain in phase across the boundaries, with no antiphase boundary between two domains [227]. Fig. 6.2f is an STM image of Cu_2N on Cu (100) after three cycles of oxidation and NH_3 annealing at 575 K followed by one cycle oxidation and ammonia annealing at 675 K. The copper stripes between the Cu_2N islands shrank in width, and the Cu_2N coverage increased compared to Fig. 6.1c, which corresponds to one cycle of oxidation and ammonia annealing at 675 K. Besides that, Fig. 6.2f shows the temperature dependence of the shape of Cu_2N islands, which became more uniformly distributed, smaller, square-like islands with an average side length of about 5 nm, compared to Fig. 6.2a (see the AP, Fig. 10D.2 and 10D.3).

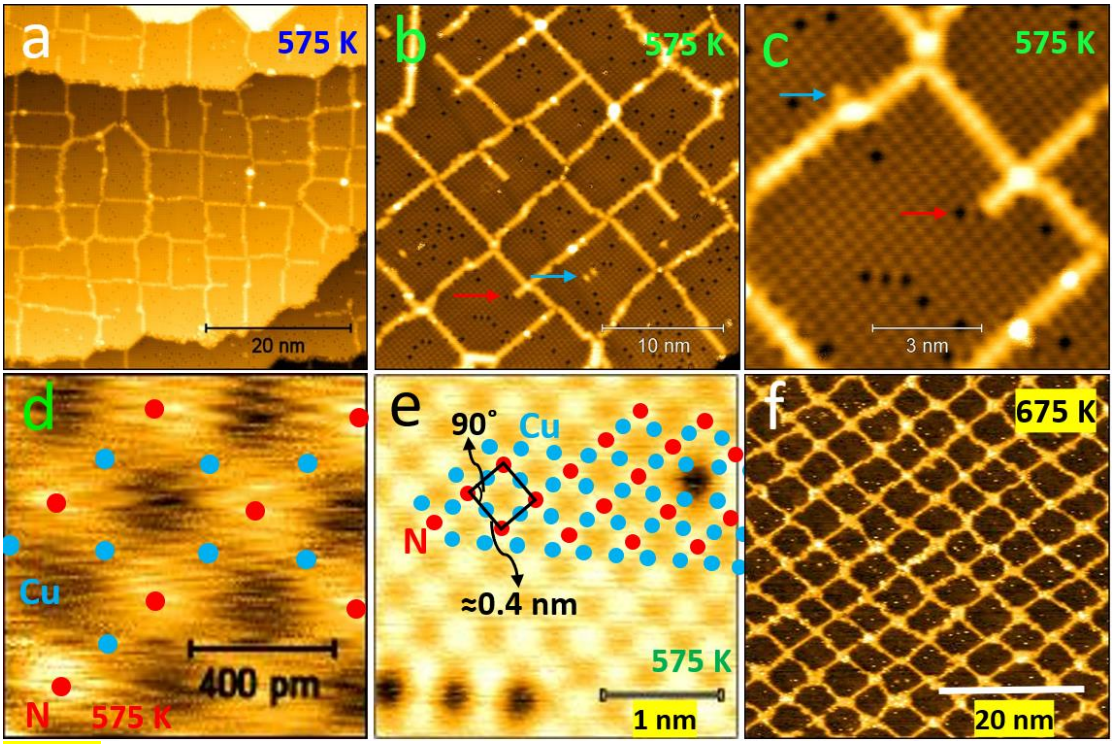

Fig. 6.2. (a) HR-STM and atomic models of Cu_2N on Cu (100) annealed at 575 K while dosing 1600 L NH_3. (a) Z-height = 0.48 nm, V_s = -1 V, I_t=100 pA, rms-R = 0.07 nm. (b) Z-height = 0.30 nm, V_s = -1 V, I_t = 100 pA, rms-R = 0.02 nm. (c) Z-height = 0.12 nm, V_s = -1 V, I_t = 100 pA, rms-R = 0.02 nm. (d) Z-height = 0.02 nm, V_s = -1 V, I_t = 100 pA, rms-R = 0.01 nm. (e) Z-height = 0.04 nm, V_s = -1 V, I_t = 100 pA, rms-R = 0.01 nm. The sample in (a) was annealed at 675 K while dosing 1600 L NH_3; (f) Z-height = 0.15 nm, V_s = -1 V, I_t = 100 pA, rms-R = 0.03 nm. STM acquisition temperature: 77 K.

Figs. 6.3a and 6.3b present the top-view and side-view of a computational modeling Cu_2N monolayer on Cu (100). The Cu atoms in the substrates depicted as blue spheres, while the Cu atoms in the on-surface Cu_2N monolayer are shown as orange spheres, and the N atoms as gray spheres. Corresponding STM images at various bias voltages were simulated using DFT, with Fig. 6.3c showing the simulation at a bias voltage of -1 V. The features in this simulation closely resemble those observed in experimental STM images in Fig. 6.2d. At negative bias voltages, both the simulated and experimental STM images show N atoms as the brightest spots, while at positive bias voltages, the states are inverted, and N atoms centered at the darkest spots of the iterative features (see the AP, Fig. 10D.4).

Fig. 6.3d shows the DFT simulation of the electron localization function on atoms on a Cu_2N ML slice confirming the Cu-N covalent bonds and the corresponding atomic model including twelve atoms (eight Cu and four N atoms). DFT simulations in Fig. 6.3e depict the projected band structure (PBAND) of the Cu_2N ML in Fig. 6.3d, using the Heyd-Scuseria-Ernzerhof hybrid functional (HSE) approach. The CB and VB overlap at the M point of the BZ, confirming the metallic nature of this 2D nanostructure. However, strain due to lattice mismatch between the epilayer and substrate, as well as spin-polarized simulations, introduces a band gap in Cu_2N, transforming it into a semiconductor (see the AP, Fig. 10D.5). Phonon simulations and LEED experiments further confirm the high stability of the Cu_2N layer, disfavoring molecular adsorption and enhances its decoupling effect [68]. Fig. 6.3f illustrates the PDOS simulation, confirming the VB and CB of the Cu_2N layer, consistent with its metallic nature.

Experimental STM images of Cu_2N islands on Cu (100) at bias voltages of -2 V and 4 V are shown in Figs. 6.3g and 6.3h, respectively. STM results reveal that the states of the islands, relative to the Cu (100) substrate, reverse between 3-3.5 V (see the AP, Fig. 10D.2-3). Below 3 V, the Cu_2N islands appear darker than the Cu (100) substrate, while above 3.5 V, the Cu_2N islands appear brighter. Two models for the Cu_2N islands on Cu (100) are proposed. Fig. 6.3i

shows the atomic model of an epilayer Cu_2N island on a Cu (100) substrate. DFT simulations of STM images of four adjacent islands, based on this model, are shown in Figs. 6.3j and k at bias voltages of -2 V and 4 V, respectively (see the AP, Fig. 10D.6). However, these simulation results are not consistent with the experimental data, as the states of the islands and substrate did not reverse between -2 V and 4 V. The second model proposes that the Cu_2N islands are embedded within the top atomic layer of the Cu (100) substrate, where only N atoms occupy hollow sites in the Cu (100) surface lattice, covalently bonded to four adjacent Cu atoms. Corresponding DFT simulations of STM images of four adjacent embedded Cu_2N islands on a Cu (100) surface at bias voltages of -2 V and 4 V are shown in Figs. 6.3m and 6.3n, respectively (see the AP, Fig. 10D.7). These simulations align with the experimental results, showing that the states of the Cu_2N islands and the Cu (100) substrate reverse at bias voltages between 3 to 3.5 V. This reversal is attributed to a significant CB-II feature of the Cu2N monolayer at the bias voltage of ≈3.3 V (see the AP, Fig. 10D.2f).

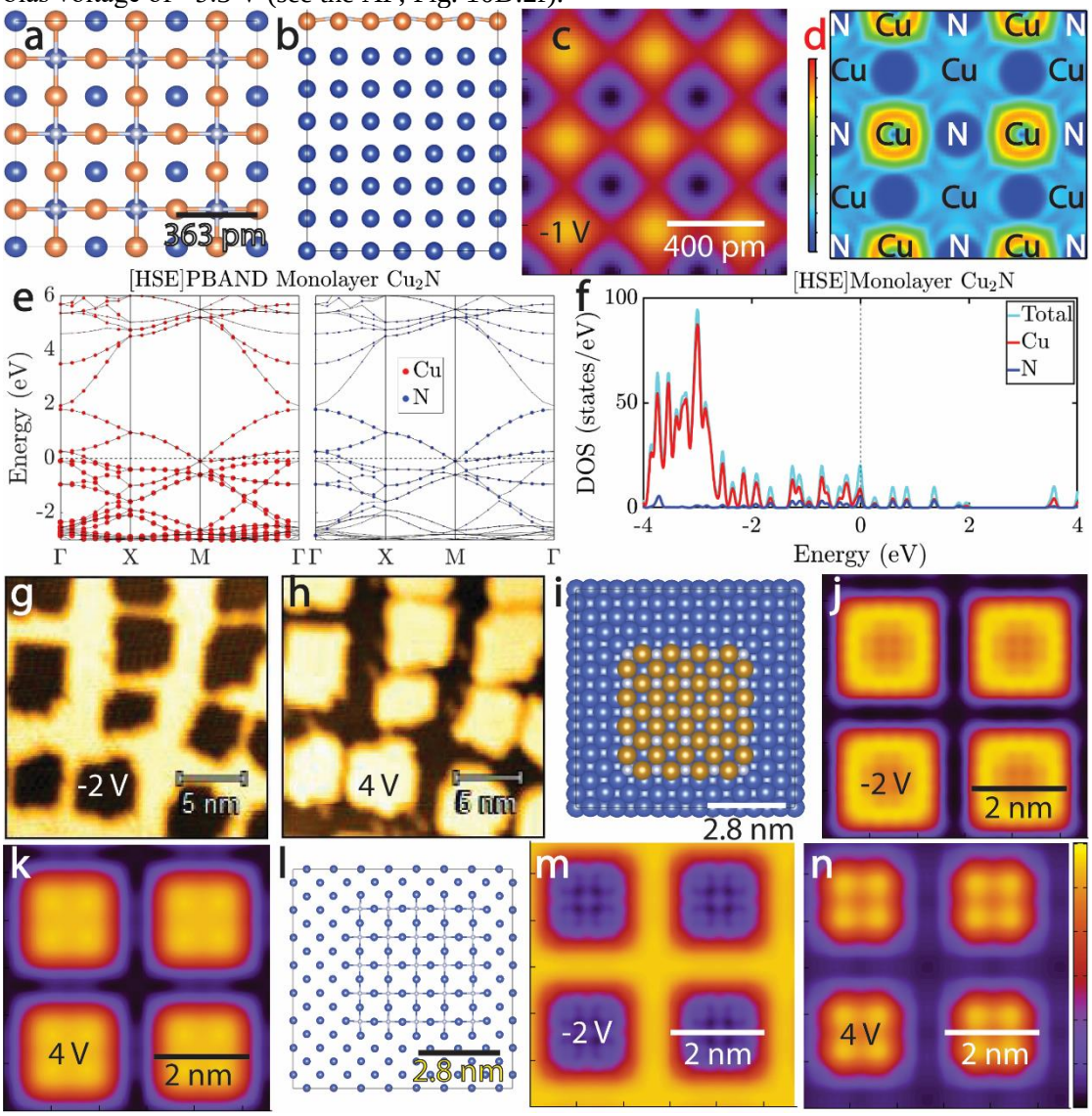

Fig. 6.3. (a) Top-view and (b) side-view DFT model of the atomic structure of Cu_2N on a Cu (100) substrate, and (c) the corresponding STM simulation at bias voltage of -1 V. Blue, orange, and white spheres represent the Cu atoms in the Cu (100) substrate, Cu atoms in the Cu_2N monolayer, and N atoms, respectively. (d) DFT simulation of the electron localization function on atoms on a Cu_2N ML slice confirming the Cu-N covalent bonds and the corresponding atomic model including twelve atoms (eight Cu and four N atoms). DFT simulations of (e) the PBAND and (f) the PDOS versus energy corresponding to applied bias voltages of the STS measurements of the Cu_2N monolayer, shown in Fig. 6.3d, performed using the HSE approach. Bias-dependent

STM measurements of Cu_2N islands on Cu (100); (g) STM image with Z-height = 0.13 nm, V_s = -2 V, I_t = 0.5 nA, rms-R = 0.04 nm. (h) STM image with Z-height = 0.24 nm, V_s = 4 V, I_t = 0.5 nA, rms-R = 0.07 nm. STM acquisition temperature: 4.6 K. (i) Structural atomic model of a Cu_2N island positioned on top of the Cu (100) surface. (j, k) DFT simulations of STM images for four Cu_2N islands on a Cu (100) substrate as shown in the model in Fig. 6.3i at bias voltages of -2 V and 4 V, respectively. (l) Structural atomic model of a Cu_2N island embedded within the top atomic layer of Cu (100) surface. (e, f) DFT simulations of STM images for four embedded islands within the Cu (100) surface as depicted in the structural model in Fig. 6.3l at bias voltages of -2 V and 4 V, respectively.

6.4.3 Molecular adsorption and robustness

We investigated the stability of the Cu_2N submonolayer by dosing with various molecules, O_2, and air as shown in Fig. 6.4 (see the AP, Fig. 10D.8). Fig. 6.4a displays the deposition of pentacene molecules on the surface. Pentacene molecules assembled mostly either perpendicular to the linear stripes between two square-like Cu_2N islands and parallel or perpendicular to each other at an angle of about 45° with respect to the [001] direction in the small islands between four square-like Cu_2N islands. Furthermore, sparse pentacene molecules were observed in the middle of the Cu_2N islands, moving orientation simply by applying larger bias voltages above 2V. Additionally, the pentacene molecules and Cu_2N islands remained intact after adsorption, exhibiting the high stability of Cu_2N films and negligible interaction between pentacene molecules and the Cu_2N surface. Fig. 6.4b shows a similar adsorption behavior for TPA molecules on this surface. TPA molecules accumulated on the Cu surface and mostly diffused closer to the edge of the Cu_2N stripes, although sparse TPA molecules in the middle of Cu_2N squares were also observed. Fig. 6.4c shows the sample after deposition of DAPPor molecules on Cu_2N on Cu (100). DAPPor molecules arranged either parallel to or at an angle of 45° with respect to the linear Cu stripes between two adjacent Cu_2N islands. Similar to pentacene molecules, DAPPor molecules did not react with the Cu_2N surface and were sparsely observed in the middle of Cu_2N squares, rotating by applying larger bias voltages above 2 V. In all three mentioned adsorption cases, the Cu_2N islands were recovered by ammonia annealing of the surface at 10^{-6} mbar of NH_3 at 675 K. However, the 3D CBCP adsorption behavior on Cu_2N is different from the other three molecules due to its O constituents as shown in Fig. 6.4d. After accumulating on Cu stripes and islands, CBCP molecules start reacting, oxidizing, and dissociating the Cu_2N islands, initiating from the edge and moving toward the center. A full monolayer of CBCP molecules on this surface completely decomposes the Cu_2N layer. Surprisingly, direct ammonia annealing of this surface does not recover the Cu_2N square patches but leaves the defected bare Cu (100) surface. Generally, the adsorption of these four molecules on Cu (100) is significantly more favorable compared to the Cu_2N layer; therefore, the majority of molecules were adsorbed on Cu stripes and islands [241]. The Cu_2N surface is very tolerant against adsorbents due to its significant stability indicated by LEED experiments, DFT, and phonon simulations [68, 225]. Cu_2N edges and defects are the most favorable spots for molecular adsorption in this monolayer [241]. Fig. 6.4e is an STM image of Cu_2N on Cu (100) after dosing with 800 L O_2 under UHV condition. As an intermediate phase on the Cu (100) surface, twisted stripes of copper oxynitride similar to Cu(100)-c(2 × 2)-O reconstruction [278, 279] formed, similar to those observed in Fig. 6.1b, with square-like features in between. At lower oxygen contents (< 10%), copper oxide does not form, and only copper nitride exists on the surface. The presence of Cu-O bonds reduces the copper nitride lattice and increases the compactness of copper nitride on the weakly bonded copper nitride islands. Copper oxynitride decomposes above 360˚ C [66]. The formation of Cu_2O and CuO phases on Cu_2N thin films was evidenced by resonance Raman spectroscopy [67]. However, previously reported LEED experiments indicate that Cu_2N thin films are stable in O_2 and ambient atmospheres [68]. Fig. 6.4f shows an STM image of Cu_2N on Cu (100) after 14 hours of exposure to atmospheric air. Recovering the previously observed Cu_2N square islands was not successful, neither by UHV nor NH_3 annealing. Although our STM results

highlight the instability of the pristine Cu_2N surface in the presence of O_2 and air, previous reports reveal that the Cu_2N monolayer LEED patterns were stable after exposure to air and solvents [68]. Therefore, there are two scenarios: the first scenario is the oxidation and dissociation of Cu_2N films by the molecules containing O atoms. The second scenario is that Cu_2O or CuO layers form above the Cu_2N layer, which is less likely [67].

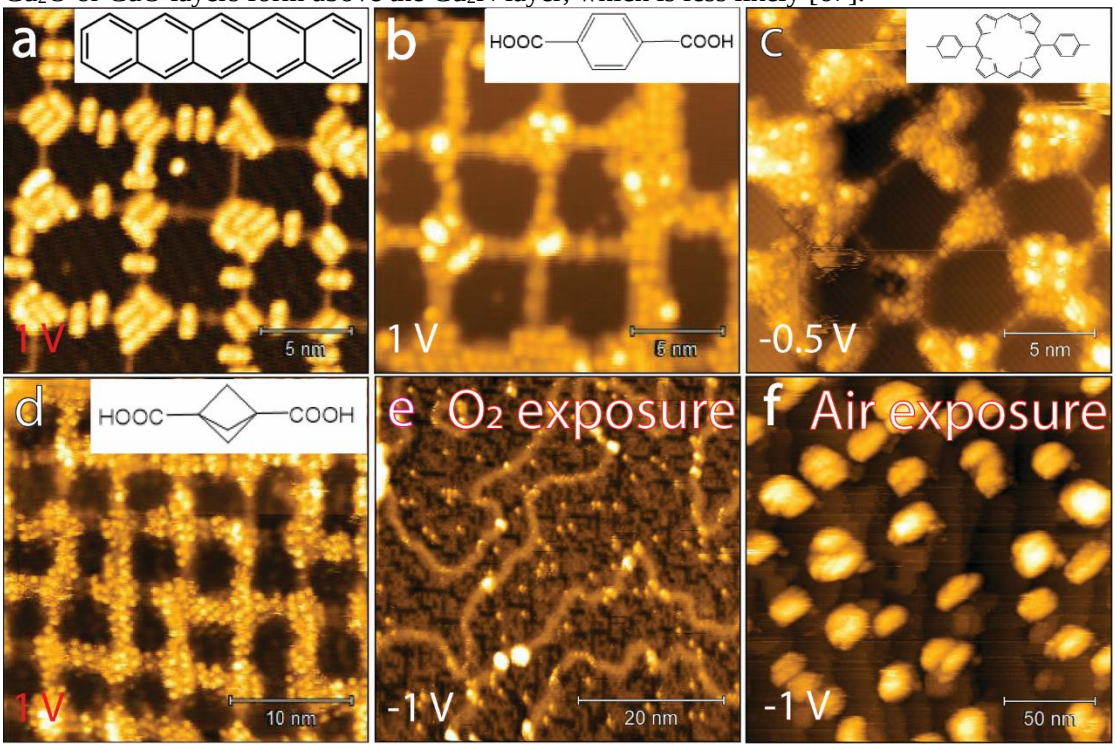

Fig. 6.4. (a) STM image of pentacene molecules on Cu_2N and Cu (100) after room temperature deposition; Z-height = 0.29 nm, V_s = 1 V, I_t = 200 pA, rms-R = 0.08 nm. (b) STM image of TPA molecules on Cu_2N and Cu (100) after room temperature deposition; Z-height = 0.60 nm, V_s = 1 V, I_t = 100 pA, rms-R = 0.10 nm. (c) STM image of DAPPor molecules on Cu_2N and Cu (100) after room temperature deposition; Z-height = 0.54 nm, V_s = -0.5 V, I_t = 100 pA, rms-R = 0.11 nm. (d) STM image of CBCP molecules on Cu_2N and Cu (100) after room temperature deposition; Z-height = 0.38 nm, V_s = 1 V, I_t = 200 pA, rms-R = 0.07 nm. STM acquisition temperature: 4.6 K. (e) STM image of Cu_2N on Cu (100) after dosing with about 800 L O_2 at room temperature; Z-height = 0.20 nm, V_s = -1 V, I_t = 100 pA, rms-R = 0.03 nm. (f) STM image of Cu_2N on Cu (100) after 14 hours of exposure to air at room temperature; Z-height = 2.17 nm, V_s = -1 V, I_t = 100 pA, rms-R = 0.43 nm. STM acquisition temperature: 77 K.

Fig. 6.5 shows the tunneling spectra of pentacene and DAPPor on Cu_2N and Cu (100) surfaces, calibrated by STS of bare Cu, Au, and Cu_2N surfaces. The spectra of Cu (100) (red curve, Fig. 6.5a), Au (111) (black curve), and Cu (111) (purple curve, Fig. 6.5b) exhibit no peak for positive and negative bias voltages, except for the presence of the step-like features due to surface states, starting at a bias voltage of approximately -0.5 V. In addition, STS results reveal a large band gap of over 3.5 eV for Cu_2N (green curve in Fig. 6.5a and blue curve in Fig. 6.5b), which is comparable with the Γ point of the BZ reported in the literature [219, 224, 230] and our DFT simulations (see Figs. 6.3 and the AP, 10D.5). The high chemical stability of the Cu_2N monolayer makes hybridization with molecules and atoms on this surface unlikely; therefore, this thin film is an ideal decoupling layer [68, 225]. Pentacene and DAPPor molecules were decoupled from the Cu (100) substrate by the Cu_2N layer due to the reduction of hybridization between the C atoms and Cu atoms, as concluded from the enlargement of their HOMO-LUMO gap on Cu_2N compared to on Cu (100) [224, 225, 230]. For pentacene molecules, the gap measured using STS enlarged from approximately 0.7 eV (black curve in Fig. 6.5a) to about 2.4 eV (blue curve in Fig. 6.5a). The HOMO-LUMO gap of DAPPor increased from below 1 eV (red curve in Fig. 6.5b) to about 2 eV (orange curve in Fig. 6.5b), as shown in Fig. 6.5b.

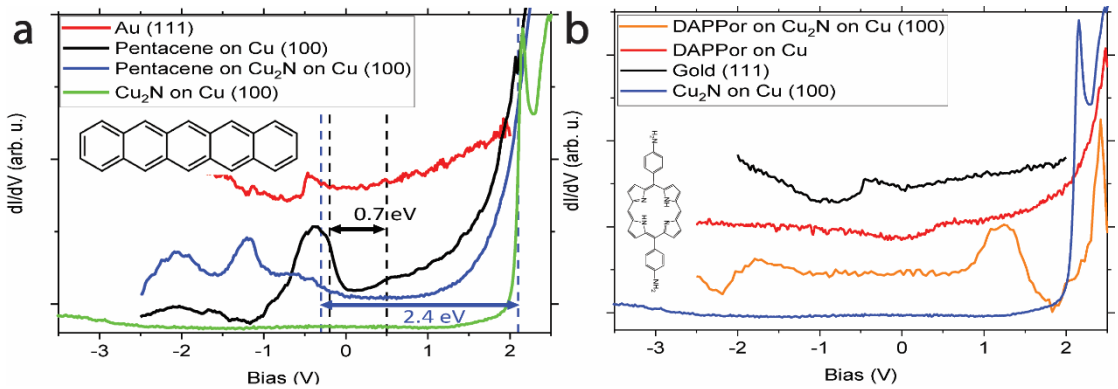

Fig. 6.5. STS spectra of (a) pentacene and (b) DAPPor on Cu_2N and copper surfaces, calibrated against bare Au, Cu, and pristine Cu_2N surfaces.

6.4.4 Confinement states

Fig. 6.6a shows a larger-scale STM image of Cu_2N islands at a bias voltage of 1 V. There are brighter point defects, due to missing N atoms, indicated by a blue arrow on darker Cu_2N islands, appearing as bright as the surrounding Cu stripes and island. Fig. 6.6b is the dI/dV map at a bias voltage of 2.2 V corresponding to the STM image in Fig. 6.6a, showing an intense state peak in the STS spectra, observed in the CB of the Cu_2N layer in Fig. 6.5. Cu_2N squares appear as extremely bright features compared to the surrounding Cu stripes, revealing the formation of CSs in these Cu_2N. Brighter point defects indicated by blue arrows in Fig. 6.6a appear darker in the middle of the CSs, indicating that the states are quenched at the defect points by the substrate. These defects are related to missing Cu atoms at a bias voltage of 1 V, as explained in Fig. 6.2. A better understanding of the nature of these CSs and the atomic-scale charge confinement in the defects in 2D Cu_2N atomic structure holds critical promise for quasiparticles formation, coupling, and investigations, useful for quantum emitters and quantum sensing [273-277]. At other bias voltages, including 2.4 V, no perfect CSs are observed. Figs. 6.6c-f display zoomed-in STM images of Cu_2N islands at a bias voltage of 2.2 V and corresponding dI/dV maps at this bias voltage. Brighter spots on the Cu stripes around the Cu_2N islands in the STM images correspond to excess Cu atoms due to the lattice mismatch between Cu (100) and Cu_2N submonolayer. Zoomed-in STM images of Cu_2N islands at a bias voltage of 2.2 V reveal that the brightness distributions of these islands are not uniform; the center of the islands and the edges near the borders appear darker than the regions in between. CSs have a dumbbell-like (or donut-like similar to a ring torus) charge distribution in the Cu_2N islands, which is darker at the edges near the Cu stripes and at the center of Cu_2N, and brighter between the edge and the center. The reason could be that the maximum strain due to lattice mismatch forms in the regions with larger charge density and brighter features. The larger the strain, the larger the band gap of Cu_2N appears [236, 238]. Further investigation of the molecular adsorption on these CSs are shown in Fig. 10D.8 (the AP).

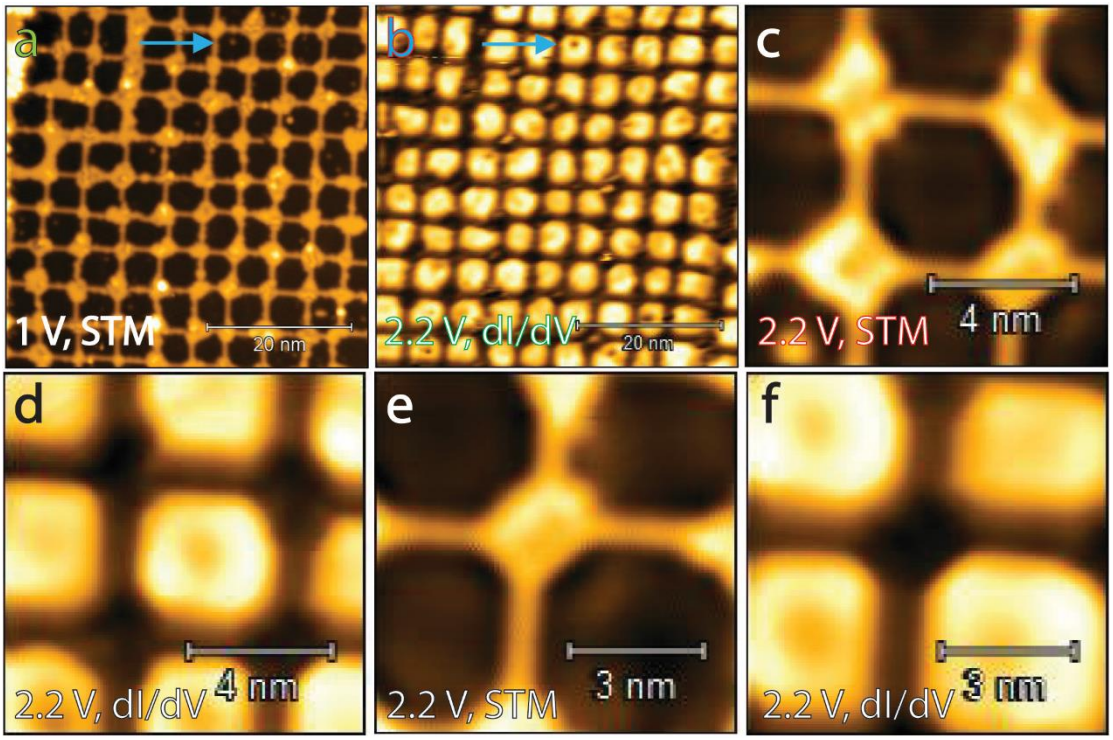

Fig. 6.6. (a) An STM image of Cu_2N square patches on Cu (100); Z-height = 0.37 nm, V_s = 1 V, I_t = 100 pA, rms-R = 0.07 nm. (b) A dI/dV map of Cu_2N CSs on Cu (100); V_s = 2.2 V, I_t = 500 pA, rms-R = 0.30 V. (c) An STM image of Cu_2N islands on Cu (100); Z-height = 0.10 nm, V_s = 2.2 V, I_t = 500 pA, rms-R = 0.02 nm. (d) A dI/dV map of Cu_2N CSs on Cu (100); V_s = 2.2 V, I_t = 500 pA, rms-R = 0.32 V. (e) An STM image of Cu_2N square patches on Cu (100); Z-height = 0.10 nm, V_s = 2.2 V, I_t = 500 pA, rms-R = 0.02 nm. (f) A dI/dV map of Cu_2N CSs on Cu (100); V_s = 2.2 V, I_t = 500 pA, rms-R = 0.32 V. STM acquisition temperature: 4.6 K.

6.5. Conclusion

The fabrication of $\left(2\sqrt{2} \times \sqrt{2}\right)R45°$ Cu_2N square patches on Cu (100) were developed by a novel replacement method under UHV conditions, replacing the O atoms in $\left(\sqrt{2} \times \sqrt{2}\right)R45°$ CuO with N atoms in NH_3 gas by NH_3 annealing at 675 K, as evidenced by LEED and STM. The coverage and size distribution of the Cu_2N islands were controlled meticulously using repeating oxidation followed by NH_3 annealing cycles and the substrate temperature. Atomic resolution STM images and atomic structural model of Cu_2N on Cu (100) were investigated using STM experiments and DFT simulations, indicating a square unit cell with a lattice parameter of approximately 0.4 nm. N atoms in 2D Cu_2N submonolayers are located in the hollow sites of the Cu (100) top atomic layer. The presence of N and Cu atom vacancies and defects were monitored by atomic resolution STM. These square patches of Cu_2N possess intense donut-like CSs at a bias voltage of 2.2 V, in which the states were quenched at the point defects, which are promising for future investigations of electronic and optical excitations and quasiparticles. The adsorption and assembly of pentacene, TPA, DAPPor, and CBCP molecules on Cu_2N is limited compared to Cu (100) stripes and islands. The Cu_2N layer possesses a decoupling effect, preventing hybridization of the epilayer molecules with the substrate, which is observed by the enlargement of the molecular HOMO-LUMO gap on Cu_2N compared to the metallic Cu surface. Exposure of this surface to O_2 and air either modifies and dissociates the Cu_2N islands or makes it non-recoverable for STM measurements, even using NH_3 annealing.

Chapter 7

Catalytic Effects of Iron Adatoms in Poly(para-phenylene) Synthesis on Rutile TiO_2(110)

This chapter delves into the catalytic effects of iron add-atoms and light on poly(para-phenylene) wires on TiO_2 surfaces, including content that has been submitted to Nanoscale and presented here with permission from Rostami, M., Yang, B., Ma, X., You, S., Zhou, J., Zhang, M., Cui, X., Zhang, H., Allegretti, F., Wang, B., Chi, L. and Barth, J.V., 2024.

7.1. Contributions

Mohammadreza Rostami: experiments, data analysis, writing, review and editing, scientific discussion, model drawing. Biao Yang: review and editing, scientific discussion. Xiaochuan Ma, Sifan You: assistance in experiments, scientific discussion. Jin Zhou, Meng Zhang, and Xuefeng Cui: assistance in experiments. Haiming Zhang: scientific discussion. Francesco Allegretti: review and editing, scientific discussion. Lifeng Chi: review and editing, scientific discussion, supervision. Johannes V. Barth: review and editing, scientific discussion, supervision.

7.2. Introduction

Ullmann coupling, a widely employed, controllable reaction for on-surface synthesis, is a versatile tool for fabricating surface-confined low-dimensional molecular nanostructures [1, 2]. Ullmann coupling is a simple, predictive, and efficient on-surface reaction [281], typically involving two main steps: the dehalogenation of molecules and the coupling of the resulting radicals to generate a desired product[1, 2]. Often the metal substrate initiates dehalogenation reactions [2], whereby the abstracted halogen atoms resulting from the dissociation of carbon-halogen (C-X) bonds remain chemisorbed at the substrate [250, 260]. This widespread mechanism enables the direct bonding of aromatics and the synthesis of π-conjugated structures. Selective and directional nanoarchitecture can be achieved by using different halogen substituents and molecular moieties, exploiting the associated specific C-X bond dissociation energies. This promising control of on-surface reaction paves the way for designing complex nanoarchitectures and molecular electronics [259]. Many custom-designed precursors have been reported [265] for the fabrication of 0D, 1D, and 2D covalent nanostructures, such as cyclic structures, linear or zigzag wires and ribbons, and 2D porous or dense networks [2] with extended regularity and long-range order through Ullmann coupling reactions. These include mostly brominated [1-3, 258, 259] and iodinated compounds [2, 188, 259].

Poly(*para*-phenylene) (PPP) wires, which represent the narrowest n-armchair graphene nanoribbons (nAGNRs) (*n*=3) are large band gap semiconductors [270]. The parameter "*n*" refers to the number of carbon atoms defining the width of an nAGNR [260]. PPP wires feature great potential for next-generation electronics due to their promising mechanical properties, high stability, low density, and tunable band gap controlled by doping [44, 270]. nAGNRs are typically formed via the polymerization of precursors containing bromine (Br) [44, 97, 260, 261], such as 4,4"-dibromo-p-terphenyl (DBTP) [262-264], or iodine [261]. The on-surface synthesis strategy offers a promising route to the successful preparation of nAGNRs, but unfortunately the typically applied metal surfaces limit the further study and application due to the quenching of electronic and optical excitations [270]. Thus, non-metal substrates, with well-defined surface structures and interactions, need to be explored for further studies of nAGNRs [260]. Utilizing such alternative substrates [15, 16, 96, 97] including semiconductors [1-3, 5-7, 44, 269, 282] or insulating oxides [242, 283-286], results in more reliable information about the electronic properties of nAGNRs [8, 46, 47, 282, 287-290].

Notably titanium dioxide (TiO_2) surfaces, as semiconducting oxide surfaces like rutile (011) [14, 88, 266], rutile (110) [14, 89-95], and anatase (101) [14, 81-87], are promising substrates for surface-assisted reactions, preventing electrons transfer between the on-surface structures and the substrate [14, 17]. The most energetically favorable and stable TiO_2 crystalline surface is rutile (110) [14, 76, 77, 79, 80, 94, 291]. Rutile is commonly synthesized in laboratories, reducing its price and promoting its applications [14, 82]. Although the absence of catalytically active metal substrates/adatoms and metal-organic intermediates reduces the efficiency of on-surface Ullmann coupling [88, 281], UV light can induce debromination of precursors, followed by Ullmann coupling and GNR formation, as confirmed by corresponding density functional theory (DFT) calculations and experiments [2, 76, 251, 253, 255, 256, 292, 293]. Additionally, the lower conductivity of semiconducting TiO_2 crystals compared to metals may hinder the implementation of surface science techniques, such as X-ray photoelectron spectroscopy (XPS), scanning tunneling microscopy (STM), and low-energy electron diffraction (LEED) [92]. Therefore, shrinking the rutile TiO_2 band gaps through reducing the crystal due to the creation of crystallographic shears, O vacancies, and anti-phase domains by repeated cycles of sputtering and annealing facilitates their application as substrates [14, 92, 94, 294, 295]. Annealing at temperatures lower than ≈ 973 K affords a clean surface with distinct LEED pattern [91]. Annealing at temperatures exceeding ≈ 973 K without O dosing results in the formation of (1×2) defects aligned along the $\langle 1\bar{1}0 \rangle$ direction [91]. Annealing at temperatures above 1200 K causes unwanted surface faceting and corrugating [91].

Debromination and Ullmann coupling of DBTP molecules [93] and 10,10"-dibromo-1',4'-difluoro-9,9':10',9"-teranthracene (DBDFTA) [266], leading to the formation of PPP wires [93], and 7AGNRs [266, 296] on rutile TiO_2(110) [297] and (011), respectively, have been reported. Moreover, recent findings report Ullmann coupling of DBTP and diiodo-terphenyl on TiO_2 boosted by the addition of cobalt (Co) adatoms, as demonstrated through XPS and angle-resolved photoelectron spectroscopy (ARPES) [281]. However, further and more detailed STM studies on the catalytic effects induced by different metallic adatoms and light irradiation on the on-surface synthesis of PPP wires are lacking. In this work, we investigated both iron (Fe) adatom and photo-catalytic effects[270] on the debromination of DBTP molecules, the subsequent Ullmann coupling on rutile TiO_2, and the desorption of the resulting Br atoms using STM and XPS. Moreover, the band gap of the prepared PPP wires could be determined using scanning tunneling spectroscopy (STS).

7.3. Experimental

Sample preparation: High-purity single crystals of rutile TiO_2(110) (10 mm × 5 mm) were purchased from Princeton Scientific Corporation, Pennsylvania, USA, and MaTecK, Jülich, Germany, respectively. O vacancies were engineered into these substrates through an extensive 8-hour process of argon ion (Ar^+) sputtering (≈ 2 keV, 10 minutes, I_{ion} ≈ 24 μA, ≈ 0.014 C) followed by annealing (≈ 900 K, 10 minutes). This treatment enhanced the substrate

conductivity, enabling the application of surface science techniques such as XPS, STM, and LEED. The treated TiO_2 crystals changed from transparent to a dark bluish color. Notably, the rutile TiO_2 surface emitted blue luminescence during sputtering and turned dark reddish upon annealing. Iterative sputtering and annealing cycles yielded atomically flat surfaces.

Characterization: Comprehensive characterization of the rutile TiO_2(110) and molecular samples was performed using XPS (Mg $K_\alpha \approx 1253.6$ eV), TP-XPS, LEED, STS, and STM, following meticulous cleaning in various UHV chambers. In the custom-built XPS chamber at the Technical University of Munich (TUM), a K-type (Nickel-Chromium/Nickel-Alumel) thermocouple was affixed between molybdenum stripes attached to the TiO_2 surfaces and secured by screws to a molybdenum plate supporting the TiO_2 samples. The chamber maintained a base pressure below 2×10^{-10} mbar, and XPS and LEED measurements were conducted at liquid nitrogen temperature (77 K). In the Omicron STM chamber at the University of Science and Technology of China (USTC), a constant current was applied via a tantalum (Ta) plate directly attached to the rutile TiO_2 underside of the sample. This setup allowed specific voltage applications, inducing resistance changes ($R = \frac{V}{I}$) and enabling precise sample temperature control according to a parabolic resistance-temperature relationship (see the AP, Fig. 10E.1). The preparation and principal STM chambers maintained base pressures below 4.0×10^{-10} mbar and 8.0×10^{-11} mbar, respectively. STM and STS measurements were performed at 77 K using a digital lock-in amplifier with a set point of 1.0 V, 10 pA, an oscillation frequency of 973 Hz, and an amplitude of 10-20 meV.

Molecular deposition: The DBTP molecules were obtained from Shanghai Aladdin Bio-Chem Technology and loaded into quartz crucibles of custom-built molecular organic beam evaporators (OMBEs) for deposition onto pristine TiO_2 (110) surfaces at controlled temperatures (300 K and 77 K). STM and STS characterization of the deposited films revealed insights into thermally- and photo-induced molecular assemblies. Sample heating was achieved through a combination of radiative heating and electron bombardment from a W filament in the XPS chamber, and by passing a constant current through a Ta plate in the STM chamber. In both the STM and XPS chambers, custom-built Fe evaporators facilitated the deposition of approximately 0.1-0.2 monolayer (ML) of Fe atoms at temperatures below 273 K to investigate the catalytic effects of adatoms on the formation of 3AGNRs on these surfaces. The CB and VB states of the rutile TiO_2(110) surface as well as the HOMO and LUMO of the synthesized PPP wires, and the resulting band gaps of both, were characterized via STS. Furthermore, surface irradiation in the STM chamber was ensured by a Xe lamp from Hamamatsu Photonics K. K. (C7535), with a round color filter (FGUV5) from Thorlabs filtering wavelengths below 240 nm and above 395 nm. A filtered Xe lamp beam with a size of about 20 mm × 25 mm and a power of 250 mW reached the sample surface in UHV in the STM chamber to study the influence of light on these surfaces.

Analytical techniques: Image processing of STM data was conducted using Gwyddion software [183], ensuring precise measurements and interpretations. Atomic structural models of molecular structures and 3AGNRs were generated and optimized using ChemDraw software [298].

7.4. Results and Discussion

The rutile TiO_2(110) surface was prepared by repeated cycles of sputtering and annealing at approximately 900 K. Fig. 7.1a shows a LEED pattern of rutile TiO_2(110) surface, indicating a (1×1) atomic lattice without interfering charging effects, i.e., there is an unperturbed clean surface, in agreement with the literature [14, 299]. Fig. 7.1b depicts corresponding large-scale STM data, displaying terraces of various sizes. The STM imaging is primarily influenced by the density of states rather than morphological features [14]. The Ti and O rows manifest as bright and dark lines, respectively [14], with an inter-row distance of approximately 6.5 Å, consistent with the reported unit cell lattice parameter [14]. The formation of some TiO_2 clusters and (1×2) defects (missing O rows, green arrow in Fig. 7.1b) was also observed. Heating the

rutile TiO_2(110) surface to approximately 973 K without O_2 treatment resulted in the formation of a (1×2) superstructure and likely TiO_2 strings oriented parallel to O and Ti rows ([001]) [91, 266, 300-305]. The zoomed-in STM image in Fig. 7.1c shows some TiO_2 clusters (marked by white arrows) centered on the Ti rows and on-surface hydroxyls (yellow arrow) at O rows. The most abundant surface donors, O vacancies, appear as bright bridges spanning the dark stripes of the O rows, connecting the bright O atom rows on the TiO_2 surface [295]. Fig. 7.1d shows an STM image of a DBTP submonolayer on rutile TiO_2(110) deposited at room temperature. Single, unreacted DBTP molecules (white arrow) are mostly adsorbed on the Ti rows, similar to isolated Br atoms (blue arrow) abstracted from DBTP. Hydroxyls (yellow arrow) located on O rows appear as smaller and darker spheres compared to the Br atoms in the STM image. In addition, the green arrow indicates an O vacancy in this region. Fig. 7.1e shows a zoomed-in STM image of a densely packed DBTP cluster, indicating the coexistence of a longer unreacted DBTP (≈ 1.9 nm, blue arrow, with the Br indicated by a green arrow) and an adjacent shorter debrominated DBTP species (≈ 1.6 nm, white arrow), reflecting some degree of on-surface debromination at 300 K. Fig. 7.1f presents structure models of the resulting rutile TiO_2(110) surface [306], including key features such as a bridging hydroxyl (yellow arrow) [307], a surface-bonded Br atom (red arrow), an O vacancy (green arrow), and both unreacted (blue arrow) and debrominated (white arrow) DBTP molecules (see the AP, Fig. 10E.1).

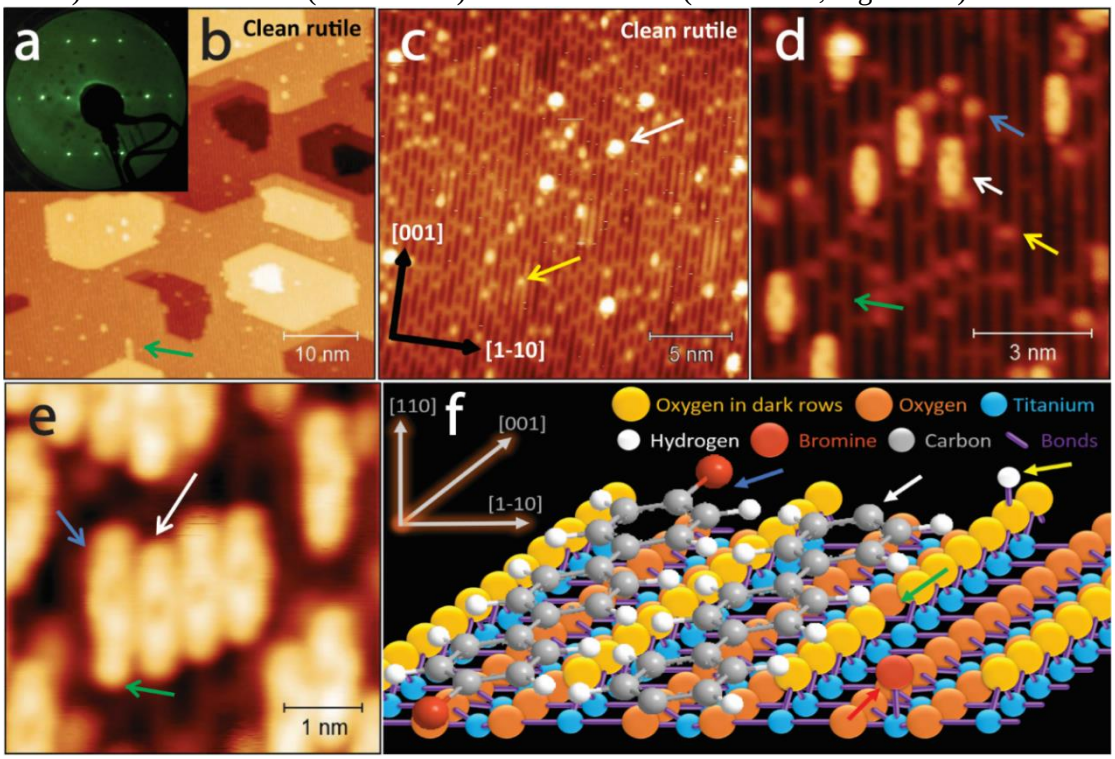

Fig. 7.1. (a) A (1×1) LEED pattern (primary energy: E_{LEED} = 109 eV) and (b, c) STM images of a clean rutile TiO_2(110) surface; the distance between the brightest and the darkest point in the STM image corresponds to z-height = 1.25 nm in (b) and z-height = 0.18 nm in (c). The white and yellow arrows highlight a TiO_2 cluster and a hydroxyl, respectively. (d, e) Zoom-in STM images of a DBTP sub-monolayer amount on the rutile TiO_2(110) surface with z-height = 0.27 nm (d) and z-height = 0.19 nm (e). In (d) blue, white, yellow, and green arrows denote a Br atom, a DBTP molecule, a hydroxyl, and an O vacancy, respectively. In (e) blue, white, and green arrows indicate a DBTP molecule, a debrominated DBTP molecule, and a Br atom in the DBTP molecule, respectively. (f) Schematic atomic models of the rutile TiO_2(110) surface, highlighting key features such as a bridging hydroxyl (yellow arrow), a surface-bonded Br atom (red arrow), an O vacancy (green arrow), an integral DBTP (blue arrow), and a debrominated DBTP (white arrow). The color scheme for the atomic species is as follows: bridging O atoms in dark rows in the STM images (yellow spheres), subsurface O atoms (orange spheres), titanium atoms (blue spheres), C atoms (gray spheres), hydrogen atoms (white

spheres), and Br atoms (red spheres). The surface covalent bonds are represented by purple cylinders. STM acquisition temperature: 77 K, tunneling parameters: V_s = -1 V, I_t = 10 pA.

Fig. 7.2a illustrates a DBTP submonolayer after annealing a 300 K-deposited DBTP monolayer at 400 K. Ullmann coupling and the formation of DBTP dimers on the Ti substrate rows are clearly observed, as indicated by blue arrows. The presence of Br adatoms and hydroxyl species is also inferred. Upon annealing at 500 K, PPP short wires formed and prevail on the surface, as seen in Fig. 7.2b, running parallel to the O and Ti rows, centered on the Ti rows (still coexisting with Br adatoms and hydroxyl compounds). Two types of PPP wires exist: one group appears thinner and darker with an asymmetrical shape and charge distribution, the other type, observed sparsely, appears wider and brighter with a symmetrical shape. As indicated in the STM image in Fig. 7.2c by yellow and blue arrows, we interpret the asymmetrical wires in terms of tilted PPP wires, as previously reported on rutile TiO_2 [93], and the symmetrical ones as flat PPP wires, similar to those reported on metallic surfaces, respectively [262-264]. Schematic atomic models of these two different wire conformations are shown in Fig. 7.2d, Additionally, upon annealing at 600 K, most Br atoms and hydroxyl compounds desorbed from the substrate (see Fig. 7.2c). Moreover, some ribbons shifted from their primary stable orientations to different orientations, such as a bent conformation extending at an angle of nearly 45° relative to the $\langle 1\bar{1}0 \rangle$ substrate direction. The appearance of shorter wires and more clusters indicates the onset of PPP wire dissociation. Upon annealing at 700 K, we ensured the complete desorption of Br atoms and hydroxyls (see STM image in Fig. 7.2e, whereby on the flip side, PPP wires were frequently dissociated, and the density of molecular clusters exceeds that of wires or ribbons (see the AP, Figs. 10E.2-4).
This process was further characterized chemically by XPS. The data in Fig. 7.2f, reveal, after deposition at liquid nitrogen (LN_2) temperature, a Br 3d signature with broad peak due to spin-orbit coupling [262-264]. By annealing at higher temperatures, as debromination increasingly occurs, the distinct shoulder at lower binding energies, related to separated Br atoms, is enhanced. In addition, with the formation of a covalent network, the C 1s XPS peak shifts to lower binding energies (see the AP, Fig. 10E.5). At approximately 500 K, the C-Br component vanished and Ti-Br counterpart dominates the Br 3d XP spectrum, in agreement with STM observations. Br desorption was also observed upon increasing the annealing temperature, which could be completed by further increasing the temperature and time.

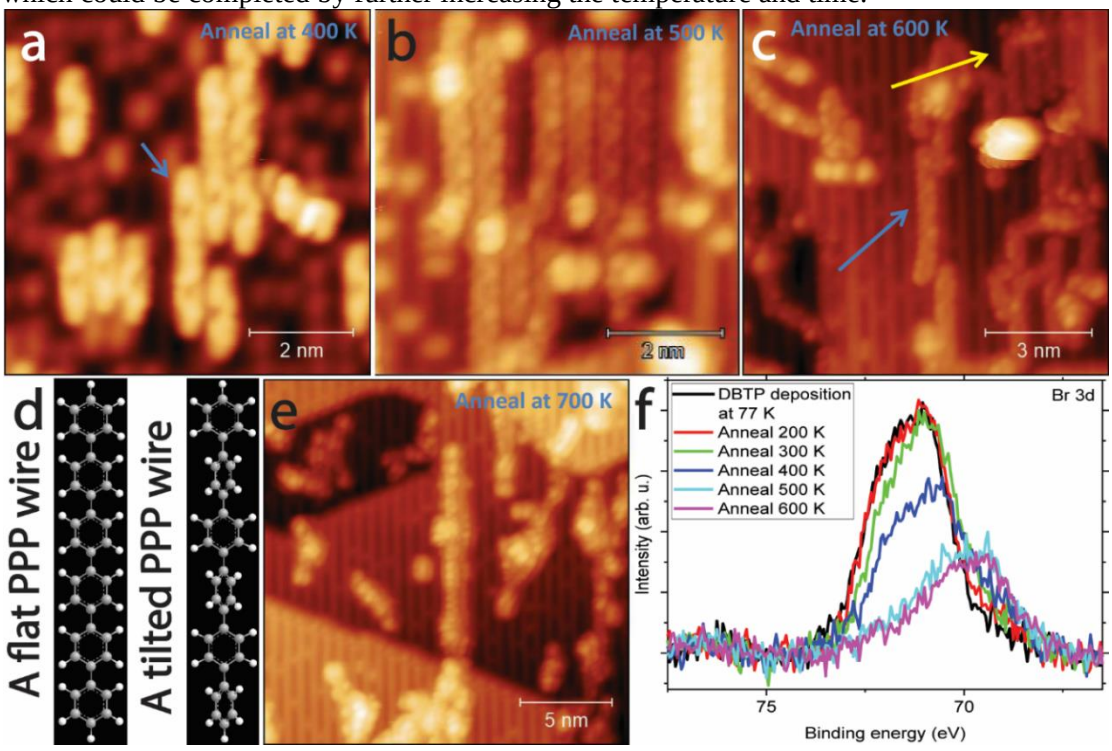

Fig. 7.2. (a) STM image of a DBTP sub-monolayer coverage on a rutile TiO_2(110) surface after annealing a DBTP monolayer at 400 K (z-height = 0.22 nm). The blue arrow denotes a DBTP dimer after Ullmann coupling. STM images of PPP wires on the rutile TiO_2(110) surface after annealing at (b) 500 K (z-height = 0.45 nm) and (c) 600 K (z-height = 0.68 nm). Yellow and blue arrows mark tilted and flat conformation of adsorbed PPP wires, respectively. Br atoms were desorbed at 600 K and the rutile TiO_2 surface appears cleaner. (d) Schematic atomic models of a flat (left) and a tilted (right) PPP wire made in ChemDraw software. Gray and white spheres represent C and H atoms, respectively. (e) STM image of the sample after annealing at 700 K, showing the dissociation of PPP (z-height = 0.78 nm). STM parameters: V_s = -1 V, I_t = 10 pA. (f) Br 3d narrow region scan XPS spectra of a rutile TiO_2(110) surface after deposition of a DBTP monolayer at 77 K and annealing it at different temperatures. All STM and XPS data were acquired at 77 K.

Leveraging light for on-surface reactions and polymerizations holds significant promise for promoting Ullmann coupling at reduced temperatures and on less reactive surfaces as compared to thermal activation [251]. Photo-induced coupling can improve the control of on-surface reactions through the precise adjustment of photon intensity and wavelength [251]. Photons with specific energies can selectively break various covalent bonds [251]. Therefore, we studied the effect of illuminating the surface with a Xe lamp filtered to deliver wavelengths in the UV range (240 - 395 nm). However, irradiation with Xe light did not change the onset temperature or the density of PPP evolution significantly; instead, the desorption of separated Br atoms from the surface was favoured by illumination. Figs. 7.3a and b depict PPP wires after annealing at 500 K without and with irradiating by the Xe lamp, respectively. Yellow, white, and blue arrows indicate a PPP wire with a flat conformation, a PPP wire with a tilted conformation, and a separated Br atom, respectively. At first glance, the surface exposed to irradiation appears cleaner, with fewer Br atoms compared to the surface without irradiation. Fig. 7.3c compares the Br surface density with and without irradiation. For each case, four different STM images were analyzed, the Br atoms were counted, normalized by area, and the average values were calculated and plotted in this histogram. As illustrated, an average of 0.34 and 0.06 Br atoms per nm^2 was measured on the surface without and with irradiation of a DBTP multilayer (≈ 3 × monolayer), respectively. Consequently, these measurements confirm photostimulated desorption of Br atoms after debromination of DBTP, and the formation of PPP wires upon annealing at 500 K.

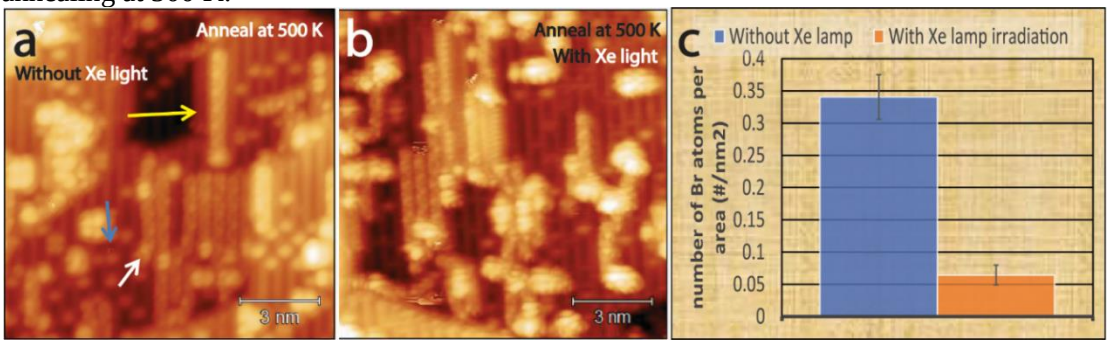

Fig. 7.3. (a) STM image of PPP wires on a rutile TiO_2(110) surface after annealing at 500 K without Xe lamp irradiation; z-height = 0.77 nm. Yellow, white, and blue arrows indicate PPP wires with flat conformation, PPP wires with tilted conformation, and a bromine atom, respectively. (b) STM image of PPP wires on the rutile TiO_2(110) surface after annealing at 500 K in the presence of a Xe lamp irradiation (wavelengths: 240-395 nm); z-height = 0.54 nm, V_s = -1 V, I_t = 10 pA. (c) Histogram of the average number of bromine atoms per nm^2 as detected on the surface with (orange) and without (blue) the Xe lamp irradiation. STM acquisition temperature: 77 K.

While light enhances the cleavage of Br bonds on the surface and possibly within the molecules, the length of the PPP wires remains limited to below 10 nm. Thus, the efficiency of PPP formation is limited, presumably due to the absence of the metal adatoms needed for the chain

formation of metal-organic intermediates. These reaction intermediates are frequently encountered as the second step of the Ullmann coupling on metallic surfaces before C-C coupling [262-264]. Therefore, we investigated the influence of codeposited Fe adatoms as catalysts. Fig. 7.4a shows the surface of rutile TiO_2(110) after deposition of a DBTP monolayer and annealing at 400 K, whereupon most of the molecules are single without any polymerization. Fig. 7.4b depicts an STM image after deposition of 0.1 ML coverage of Fe atoms at temperatures below 273 K and a DBTP monolayer using the same parameters as in Fig. 7.4a, followed by annealing at 400 K. The Fe atoms (white arrow) primarily assembled in lines perpendicular to the O and Ti rows. The formation of organometallic chains of debrominated DBTP and Fe atoms was both expected [281] and observed. Ullmann coupling was catalyzed by Fe adatoms, resulting in PPP wires (blue arrow) becoming dominant, mostly appearing around Fe adatoms, although Fe does not remain in the polymer chains. To confirm these results quantitatively, we analyzed four STM images of the surface and DBTP monolayer deposition after annealing at 400 K without Fe adatoms and four STM images with a precoverage of 0.1 ML Fe. In each case, the ratio of the DBTP monomers to polymers was counted, normalized by the area, and the average values were calculated and plotted in the histogram shown in Fig. 7.4c. As illustrated, for pure DBTP monolayer deposition and annealing, only ≈ 3% of adsorbed DBTP undergo a coupling reaction at 400 K. On the other hand, in the presence 0.1 ML Fe using the same procedure, about 77% of the DBTP compounds covalently connected at the same temperature, and merely ≈ 23% remaining in form of monomers. This finding thus supports the conclusion that Fe adatoms catalyze and enhance Ullmann coupling and the formation of PPP wires at reduced temperatures (see the AP, Figs. 10E.4).

Further XPS investigations were conducted to provide additional evidence and insight into this catalytic effect. After deposition a DBTP monolayer at LN_2 temperature on the rutile TiO_2(110) surface, 0.1 ML of Fe atoms were initially deposited, followed by an additional 0.1 ML (totaling 0.2 ML). Somewhat surprisingly, Fig. 7.4d shows an increase in the Br 3d shoulder for Br atoms detached from DBTP molecules and bonded to the surface and likely to the Fe adatoms at 77 K, in contrast to Fig. 7.2f. Therefore, the debromination reaction was initiated even at LN_2 temperature in the presence of Fe adatoms, demonstrating the remarkable catalytic effect of these metallic adatoms entailing PPP wire formation. Conversely, upon higher temperature annealing, more complexed Br atoms remain on the surface, pointing to strong bonds between Fe and Br that prevent Br desorption at lower temperatures. In addition, the C 1s core level XPS spectra in Fig. 7.4e also show different behavior in the presence of Fe adatoms. After Fe deposition on a DBTP monolayer, the C 1s core level peak initially shifts to higher binding energies and upon annealing at higher temperatures, to lower binding energies due to debromination and C-C coupling, whereby significant C desorption occurred, which is consistent with the STM results. Fig. 7.4f presents the XPS spectra of Fe 2p core level electrons on this surface. After deposition at 77 K, the Fe 2p peak is broadened, presumably due to the presence of various bonds involving Fe on the surface, such as Fe-O (≈ 710-711 eV [308, 309]), Fe-Br (≈ 710-711 eV [310, 311]), Fe-C (≈ 707-708 eV [312-314]), and Fe-Fe (≈ 707 eV [315]). Upon annealing, interestingly, we find a reduced full width at half maximum (FWHM), and a peak shift to higher binding energies, characteristic of Fe-halogen bonds, indicating that Fe-Br atoms clusters accumulate on the surface. Moreover, spectra by temperature-programmed XPS (TP-XPS) show that in the absence of Fe adatoms a significant debromination shift for both Br 3d (Fig. 7.4g) and C 1s (see the AP, Fig. 10E.5) core level regions occurs at ≈ 450 K (thus clearly above the 400 K used otherwise). In contrast, the dominant debromination shift for both the Br 3d (Fig. 7.4h) and C 1s (Fig. 7.4i) core levels in the presence of Fe ad-atoms starts already at 350 K. Consequently, Ullmann coupling and formation of 3AGNRs (PPP wires) are consistently catalyzed by Fe adatoms.

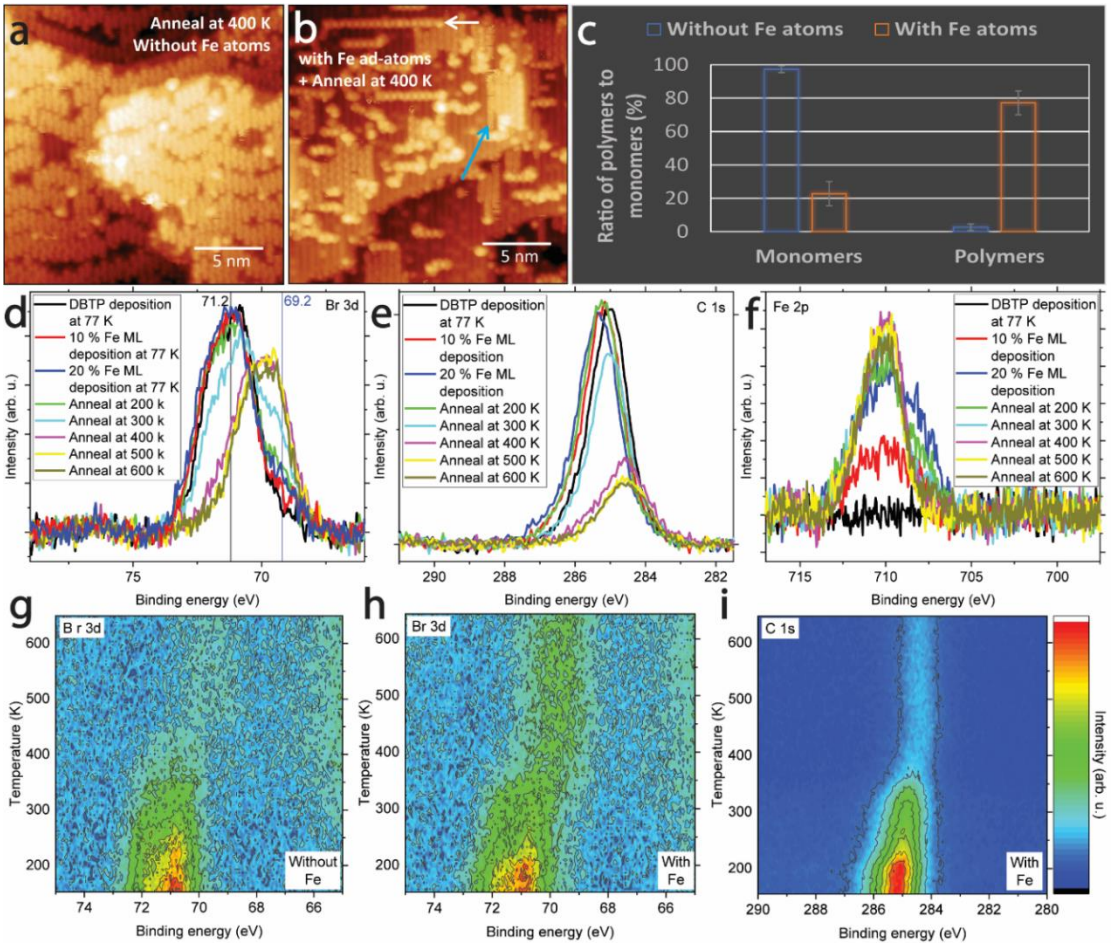

Fig. 7.4. (a) STM image of a DBTP monolayer on a rutile TiO_2(110) surface after annealing at 400 K; z-height = 0.62 nm. (b) STM image of PPP wires on rutile TiO_2(110) after DBTP molecule and Fe atom deposition on this surface and annealing at 400 K; z-height = 0.84 nm, V_s = -1 V, I_t = 10 pA. White and blue arrows indicate the Fe adatoms and PPP wires, respectively. (c) Histogram of the average number of the monomers and polymers observed on the surface with and without Fe atoms. (d) Br 3d, (e) C 1s, and (f) Fe 2p narrow region XP spectra of a rutile TiO_2(110) surface after deposition of a DBTP monolayer and subsequently an Fe sub-monolayer (coverages of 10% and 20%) at 77 K and annealing the sample at different temperatures. (g) TP-XPS of the zoomed-in Br 3d core level region after deposition of DBTP molecules on the surface. TP-XPS of the zoomed-in (h) Br 3d and (i) C 1s core level regions after deposition of DBTP molecules and Fe ad-atoms on the surface. XPS, STS, and STM acquisition temperature: 77 K.

Finally, Fig. 7.5a shows a flat adsorbed PPP wire along with the proposed, optimized atomic structural model. The PPP shape and extension suggests that it results from the Ullmann coupling of three DBTP units. Red, blue, and black crosses denote the PPP edge and center, and rutile surface, respectively, where STS studies were conducted and plotted in Fig. 7.5b. The corresponding black curve depicts spectra of a clean rutile TiO_2 surface, where the conduction band (CB) onset is located at a bias voltage of ≈ 0.3 V and the valence band (VB) appears at a bias voltage of approximately -3 V [316-320] (see the AP, Fig. 10E.1g). The overlap of the CB states with the PPP lowest unoccupied molecular orbital (LUMO) complicates their identification, yet the latter is visible as a shoulder at ≈ +0.8 V. Since the STS curves of rutile TiO_2 are flatter for negative bias, the highest occupied molecular orbital (HOMO) appears more pronounced in this region, peaking at -2.3 V and -2.4 V for the PPP center and edge, respectively. Thus, a band gap value of ≈ 3.1 and ≈ 3.2 eV can be assigned to the PPP center and edge, respectively, confirming wide-band gap semiconducting behavior. The band gap values of ≈ 3.3 eV [321], ≈ 3.2 eV [322], and ≈ 3.0 eV [323] for PPP on Au (111) and ≈ 1.1 eV

[324] on Cu (110) were reported in the literature. In addition, this demonstrates the decoupling effect of the surface, preventing the quenching of the electronic excitation of the fabricated GNRs, which is required for precise measurements of the electronic and optical properties of the on-surface nanoarchitectures.

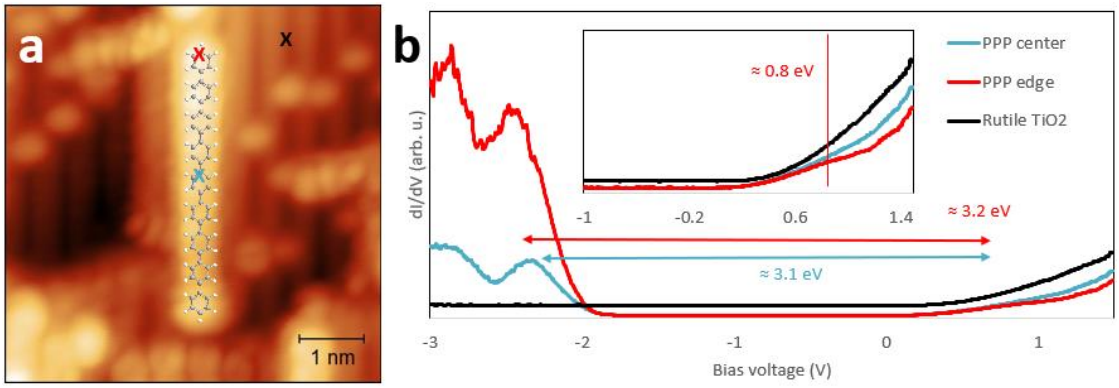

Fig. 7.5. (a) STM image with proposed atomic model of a flat PPP wire on rutile TiO_2 after annealing a DBTP monolayer at 500 K; z-height = 0.51 nm, V_s = -1 V, I_t = 10 pA. (b) Tunneling spectra of the spots shown in (a). STM / STS data acquisition at T=77 K.

7.5. Conclusion

In conclusion, we have investigated the behavior of DBTP submonolayers, monolayers, and multilayers on atomically well-defined rutile TiO_2(110). The debromination of DBTP molecules sets in at 200 K, and the desorption of the Br atoms abstracted from the molecules becomes appreciable for temperatures above 400 K. After annealing at 400 K, sparse DBTP dimers evolve through on-surface Ullmann coupling. Upon further annealing at 500 K, PPP wires prevail on the surface, undergoing dissociation reactions for T ≥ 700 K. Upon irradiating the surface with UV light (wavelength range 240-395 nm), Br-substrate and Br-C molecular bonds were cleaved at lower annealing temperatures, entailing desorption of most Br at a reduced temperature of ≈ 500 K, thus yielding a cleaner surface following PPP wire formation. Furthermore, the deliberate deposition of Fe adatoms exerts a remarkable catalytic effect on the Ullmann coupling reaction. Thus, with small doses of these metal adatoms partial debromination of DBTP occurs even at LN_2 temperature (77 K). This significant influence of Fe codeposited with DBTP entails a dominance of PPP wires upon annealing at 400 K, while under the same conditions but without Fe adatoms, molecular monomers prevail. Fe atoms and debrominated DBTP at low temperature (77 K) reduced the activation temperature required for aryl-aryl coupling to 300-400 K. On the other hand, upon higher temperature annealing, more Br atoms bind to Fe atoms on the surface, accumulating in unwanted clusters accounting for a rougher surface with the length of PPP wires limited to below 10 nm. This general feature is ascribed to weaker molecule-surface interactions as compared to metals, causing partial molecular desorption prior to coupling reactions. Furthermore, the reduced rutile substrate exhibits a semiconducting behavior, favoring the electronic and optical measurements of PPP wires. This property hinders the hybridization and charge transfer between the prepared wires and the substrate, making it suitable for more elaborate studies of the excitation of the on-surface nanostructures. STS results indicate PPP with a wide band gap, holding significant promise for next-generation electronics or other applications.

Chapter 8

Photocatalytic Fabrication of 5-Armchair Graphene Nanoribbons on TiO_2 Surfaces

This chapter explores the photocatalytic fabrication of 5-armchair graphene nanoribbons on TiO_2 surfaces. It includes content that is currently being prepared for submission, with permission from Rostami, M., Yang, B., Ma, X., You, S., Zhou, J., Zhang, M., Cui, X., Zhang, H., Allegretti, F., Wang, B., Chi, L., and Barth, J.V., 2024.

8.1. Contributions

Mohammadreza Rostami: experiments, data analysis, writing, review and editing, scientific discussion, model drawing. Biao Yang: review and editing, scientific discussion. Xiaochuan Ma, Sifan You: assistance in experiments, scientific discussion. Jin Zhou, Meng Zhang, and Xuefeng Cui: assistance in experiments. Haiming Zhang: scientific discussion. Francesco Allegretti: review and editing, scientific discussion. Lifeng Chi: review and editing, scientific discussion, supervision. Johannes V. Barth: review and editing, scientific discussion, supervision.

8.2. Introduction

n-Armchair graphene nanoribbons (n-AGNRs) with n carbon atoms and thus fixed widths[260] hold great promise for next-generation electronics because their band gap can be significantly tuned by varying their width and edge form [44, 260, 261, 325, 326]. n-AGNRs can be produced by various techniques, including nanotomy [327], epitaxy [328], and surface-assisted Ullmann coupling of halogenated molecules containing bromine [261-264] and iodine [261, 326] atoms. The later process leads to a well-controlled bottom-up on-surface synthesis of molecular nanoarchitecture using the corresponding building blocks [1, 250, 257, 259]. Single crystal metal surfaces are normally chosen as substrates for the fabrication of nAGNRs under thermal excitation conditions. Technological semiconductors and insulators are much less used

in on-surface synthesis due to the lack of metallic atoms, which play the catalytic roles and favor the formation of metal-organic intermediates. On the other hand, the direct syntheses using non-thermal techniques like photodissociation of halogens attracted increased attention[2, 3, 76, 142, 188, 258, 265]. The use of a UV light source alleviated the required temperature for the formation of n-AGNRs [2, 251-256].

Transition metal oxides have an important role in surface science and some surface-related applications [92, 242, 246, 284, 285, 329]. Titanium dioxide (TiO_2) is the most investigated metal oxide in the surface science field [14-17]. TiO_2 is used for various applications, including solar cells, corrosion protection, catalysis, bioimplants, memristors, and gas sensors [14, 76-80, 82]. Anatase [14, 81-87] and rutile [14, 88-95, 98] TiO_2 are introduced for the on-surface synthesis of 1D or 2D structures to avoid hybridization of the electron density of the epilayer molecules and structures from the substrate, unlike metallic substrates [1-7, 35, 88, 96, 326]. Reducing a TiO_2 crystal increases its conductivity and facilitates STM measurements of TiO_2 [92, 294]. Titania can exhibit varying levels of oxygen deficiency as n-type doping [14] due to a defect called crystallographic shear (CS) [92]. This occurs through several hours of repeating sputtering and annealing at an optimum temperature of about 900 K [92, 94]. Annealing at ≈ 973 K in the absence of oxygen treatment leads to the formation of a (1×2) superstructure and probable TiO_2 strings along $\langle 1\bar{1}0 \rangle$ direction [91]. Rutile TiO_2, as a semiconducting oxide, is a well-known substrate for on-surface reactions and Ullmann coupling, avoiding the quenching of electronic excitations as required for reliable optical and electronic measurements [88-93]. Surface-assisted Ullmann coupling of DBTP [93] and 10,10”-dibromo-1',4'-difluoro-9,9':10',9”teranthracene (DBDFTA) [266] molecules, then the formation of 3AGNRs (poly(para-phenylene) (PPP) wires), and 7AGNRs on clean reduced rutile TiO_2 (110) and (011), respectively, have been previously indicated.

5AGNRs have been produced on various metallic surfaces [44, 325, 326, 330, 331], including Au (111) [260] and Ag (111) [44]. 5AGNRs belong to 3p + 2 category group, which are predicted to possess a metallic nature by tight-binding approximations, while a semiconducting nature is suggested by DFT calculations [260]. There are contradictory reports on the band gap of 5AGNRs [44, 260, 325, 326, 330] and limited studies on the capability of TiO_2 surfaces for dehydrogenation to form n-AGNRs [266, 296, 297, 332]. In this work, we investigated the surface-assisted Ullmann coupling of TBN molecules on TiO_2 surfaces using x-ray photoelectron spectroscopy (XPS), LEED, temperature-programmed (TP)-XPS, and STM. We studied the possibility of debromination of TBN molecules on rutile (110) and anatase (101) surfaces, as well as the effect of photo-catalysis of the debromination and subsequent Ullmann coupling on TiO_2 surfaces. A schematic model of the rutile TiO_2 (110) surface and the Ullmann coupling of debrominated TBN molecules is described in Fig. 8.1. In this model, the yellow, orange, blue, gray, white, and red spheres correspond to oxygen (O) atoms in the dark rows of STM images, O atoms in the substrate plane, titanium (Ti), carbon (C), hydrogen (H), and bromine (Br) atoms, respectively. The blue, green, and red arrows represent a bridging hydroxyl, an O vacancy, and a surface-bonded Br atom. The band gap of the synthesized 5AGNRs was determined through STS and compared to the reported values obtained on other substrates. The STS measurements of 5AGNRs on rutile TiO_2 provided reliable information about the measured HOMO and LUMO states of these nanoribbons, which have been reported and discussed contradictorily in the literature.

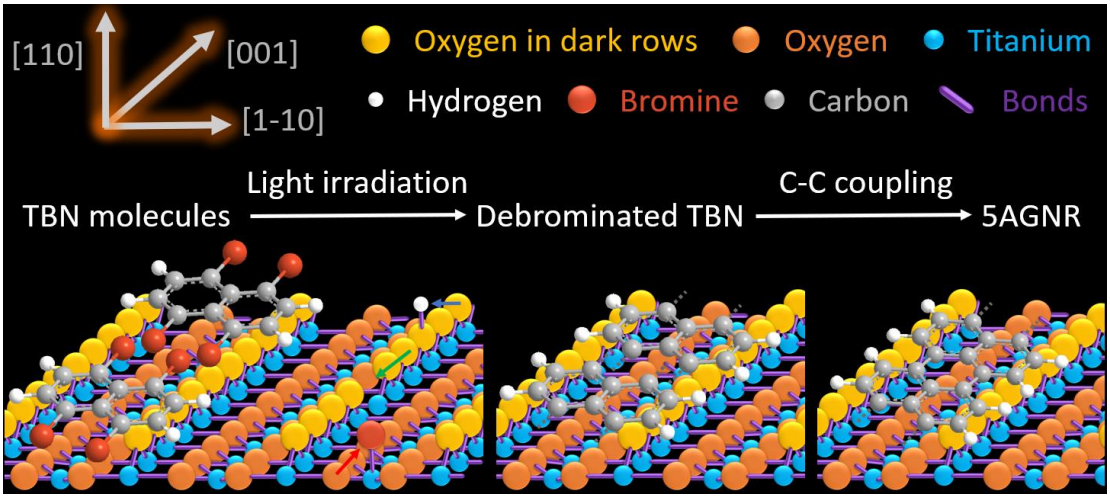

Fig. 8.1. Schematic view of our strategy for on-surface synthesis of 5AGNRs. Yellow, orange, blue, gray, white, and red spheres correspond to oxygen (O) atoms in the dark rows of STM images, O atoms in the substrate plane, titanium (Ti), carbon (C), hydrogen (H), and bromine (Br) atoms, respectively.

8.3. Experimental

Sample preparation: The 10 mm × 5 mm rutile TiO_2 (110) and the 5 mm × 5 mm anatase TiO_2 (101) single crystals were purchased from Princeton Scientific Corporation in Pennsylvania (USA) and Material-Technologie & Kristalle GMBH (MaTecK) in Jülich, Germany, respectively. Oxygen vacancies were produced in the rutile and anatase TiO_2 substrates by approximately 8 hours of multiple cycles of argon (Ar^+) ion sputtering (≈ 2 keV, 10 minutes, I_{ion} ≈ 24 μA, ≈ 0.014 C) and subsequent annealing (≈ 900 K, 10 minutes) to enhance conductivity, facilitating the implementation of surface science techniques including XPS, STM, and LEED on their surface. After these operations, the transparent TiO2 crystals turned dark bluish. During sputtering, the rutile TiO_2 surface emitted a blue luminescence, and upon annealing, the sample turned a dark reddish color (see the AP, Fig. 10F.1.). Atomically flat surfaces were achieved after sputtering and annealing cycles.

Characterization: We characterized the rutile (110) TiO_2, anatase (101) TiO_2, and molecules using XPS (photon line: Mg $K_\alpha \approx 1253.6$ eV), temperature-programmed (TP) XPS, LEED, STS, and STM, after cleaning the samples in various UHV chambers. In the home-built XPS chamber at the Technical University of Munich (TUM), a K-type (Nickel-Chromium/Nickel-Alumel) thermocouple was pressed between the molybdenum stripes attached to the TiO_2 surfaces, with screws securing the stripes to a molybdenum plate supporting the TiO_2 samples. The base pressure of the employed chamber was below 2×10^{-10} mbar. The XPS and LEED acquisition temperature was at liquid nitrogen (77 K). In a commercial Omicron STM chamber at the University of Science and Technology of China (USTC), a constant current was applied through a thin tantalum (Ta) plate directly attached to the bottom of the rutile TiO_2 sample by applying specific voltages leading to changes in resistance ($R = \frac{V}{I}$) and sample temperature following a parabolic relationship between the resistance and temperature (see the AP, Fig. 10F.1). The base pressures of the preparation and principal STM chambers were below 4.0×10^{-10} mbar and 8.0×10^{-11} mbar, respectively. The STM and STS acquisition temperatures were liquid nitrogen (77 K). STS measurements were conducted using a digital lock-in amplifier with a set point of 1.0 V, 10 pA, an oscillation frequency of 973 Hz, and an amplitude of 10-20 meV.

Molecular deposition: TBN molecules were synthesized by Long Chen's group, loaded into quartz crucibles of custom-built molecular organic beam evaporators (OMBEs), and deposited onto clean TiO_2 (100) surfaces. These depositions were carried out at different sample temperatures, including 300 K (room temperature) and 77 K (cryogenic liquid nitrogen

temperature). The deposited molecular films were characterized using STM and STS to study thermally- and photo- induced molecular assemblies. Sample heating was managed through a combination of radiative heating and electron bombardment from a W filament in the XPS chamber and by passing a constant current through a Ta plate in the STM chamber after dosing of TBN molecules through an OMBE or a dosing valve to control the surface reactions. Additionally, light-emitting diodes (LEDs) with wavelengths of 377 nm and 265 nm, used in the XPS chamber, were supplied by OSRAM LED ENGIN (LZ1-00UV00) in San Jose, California (USA) and Crystal IS, Inc., Asahi Kasei Company (Klaran® LA Series UVC LEDs) in New York (USA), with measured powers of 106 mW and 6.5 mW reaching the sample surface, respectively. LED beams were focused by a lens to about a 10 mm × 10 mm square placed at the center of the sample. A standard 400 W mercury lamp (Osram) was also used for surface irradiation in the home-built XPS chamber. Furthermore, a Xe lamp from Hamamatsu Photonics K. K. (C7535) in Japan, with a power of 250 mW reaching the surface and a beam size of about 20 mm × 25 mm, was used in the STM chamber. A round color filter (FGUV5) from Thorlabs company was used to filter wavelengths below 240 nm and above 395 nm. Custom-built Fe evaporators were used in the STM chamber for approximately 0.1 ML deposition of Fe atoms at temperatures below 273 K (filament current ≈ 2 A, flux ≈ 4 nA, emission current ≈ 10 mA, and voltage ≈ 800 V) as well as in the XPS chamber. HOMO and LUMO states and the consequent band gap of the rutile (110) TiO_2 surfaces and the produced 5AGNRs were demonstrated by STS. For further investigations, deposition and debromination of TBB molecules, supplied by Sigma Aldrich (97%), on rutile and anatase surfaces were studied.

Analytical techniques: Further image analysis of the STM data was achieved using Gwyddion software [183], confirming accurate measurement and interpretation of the obtained height and electronic features. The atomic structural models of the molecular structures and 5AGNRs and the corresponding freestanding optimizations were conducted using ChemDraw software [245].

8.4. Results and Discussion

After deposition of TBN molecules on rutile TiO_2 (110) at 77 K and annealing at various temperatures, XPS measurements were performed. Br 3d and C 1s core levels were studied to explore the activation of coupling by dehalogenation and the metastable intermediate transformation into the final covalent structure by heating, respectively. Fig. 8.2a and 8.2b show XPS spectra of zoomed-in Br 3d and C 1s core level regions, respectively. In Fig. 8.2a, the Br 3d component at a binding energy of 71.1 eV reduced, and the shifted component at 69.1 eV enlarged upon annealing the sample. Besides that, in Fig. 8.2b, the C 1s peak binding energy shifted from 285.1 eV to 284.7 eV. Since C-halogen bond strength is lower than C-C bonds, dehalogenation can occur without cleavage of C-C bonds [3]. After debromination of TBN on the surface, Br 3d and C 1s shifted to lower binding energies due to an increase in electron density around the Br atoms after bonding to titanium (Ti) atoms of the surface. C-Br and molecule bonds after lower temperatures annealing, and C-C coupling and surface-Br bonds after higher temperatures annealing dominate the XP spectra [3]. Most of the Br atoms desorb from the surface upon annealing at about 600 K. Complementary LEED patterns and XPS spectra (see the AP, Figs. 10F.2-5) reveal that the debromination of TBN molecules on rutile TiO_2 (110) and anatase (101) surfaces is limited compared to other molecules, such as 1,3,5-Tris(4-bromophenyl)benzene (TBB). This limitation is due to the weak interactions of TBN molecules with inert TiO_2 surfaces compared to metallic surfaces [260], the low evaporation temperature of the TBN molecules compared to TBB molecules, and the lack of free metallic atoms on TiO_2 [257].

Consequently, we investigated the catalytic effects of light on surface-assisted debromination of TBN molecules on rutile TiO_2 (110) surfaces. Photo-induced coupling increases the control over on-surface reactions by optimizing the light intensity and wavelength [251]. Different covalent bonds can be broken by a photon having a specific energy [251], and a wavelength of about 265-377 nm was sufficient for debromination in TBN molecules on TiO_2 surfaces. This

corresponds to the dissociation energy of a C-Br bond, which is about 276 kJ/mol [333]. Considering the equation of $E = \frac{hc}{\lambda}$, where E, h, c and λ are a photon energy, the Planck's constant, the speed of light, and photon wavelength, respectively [139], a photon with a wavelength below 400 nm has sufficient energy to dissociate a C-Br bond [252]. Therefore, using light for catalyzing on-surface reactions and polymerizations holds a great promise for developing debromination required for Ullmann coupling at lower temperatures and on more inert surfaces compared to thermally induced chemistry [251]. C-Br bond fission through $\pi \rightarrow \pi^*$ excitation by light at a wavelength of 248 nm was evidenced in previous reports [256]. Figs. 8.2c-f exhibit XPS spectra of the Br 3d core level region after TBN deposition on rutile (110) TiO_2 surfaces at 300 K and then kept at room temperature for 20 minutes or 40 minutes without irradiation, with irradiation by a mercury lamp, with irradiation by the 377 nm LED (106 mW), and with irradiation by the 265 nm LED (6.5 mW), respectively. At each step XPS measurements in the absence of any irradiations took about 1.5 hours. In all cases, due to desorption at room temperature, the main Br 3d peak related to Br atoms in the unreacted molecules on the surface decreased over time. While for the test experiment in Fig. 8.2c, the debromination shoulder at 69.1 eV did not increase, a clear increase in the debromination shoulder of the Br 3d core level was observed under irradiation from both the mercury lamp and the LEDs. Generally, the mercury lamp increased the ratio of separated to unreacted Br atoms comparable to the surface irradiated by the LED at a wavelength of 377 nm, due to the high intensity of the LED lamp for this specific wavelength (see the AP, Fig. 10F.6u). By dividing the mentioned ratio by the power of LEDs reaching the surface, the efficiency of debromination by the LED at a wavelength of 265 nm (6.5 mW) compared to 377 nm (106 mW) was found to be drastically higher, resulting in 8 times more debromination at the same power (see the AP, Fig. 10F.6v and Table. 10F.1). These results are also consistent with previous reports. For example, since C-Cl bonds are stronger than C-Br or C-I bonds, higher energy violet light with wavelength of 405 nm and 254 nm is sufficient for the corresponding bond cleavage [252]. For both wavelengths, dechlorination starts at about 365 K [252]. Using light with shorter wavelength leads to the formation of longer polymer chains [252]. However, in general, due to lower substrate temperature and limited molecular diffusion, shorter chains form compared to thermally-induced coupling [252]. As a result, not only UV light but also violet light is energetically sufficient to cause dehalogenation [252]. Higher energy, longer illumination time, and greater light intensity increase the efficiency of on-surface photo-induced reactions [252]. The transition state comprises the C-Br cleavage, leaving positively charged molecules with an empty p-orbital [255, 256]. Despite the fact that (π, π^*) is a bonding state of the C-Br coordinate, during a rotational displacement due to the high translational distribution of Br ($^2P_{3/2}$ and $^2P_{1/2}$), the destruction of C-Br bonds begins [255]. See Fig. S6 for more detailed XPS and TPXPS results.

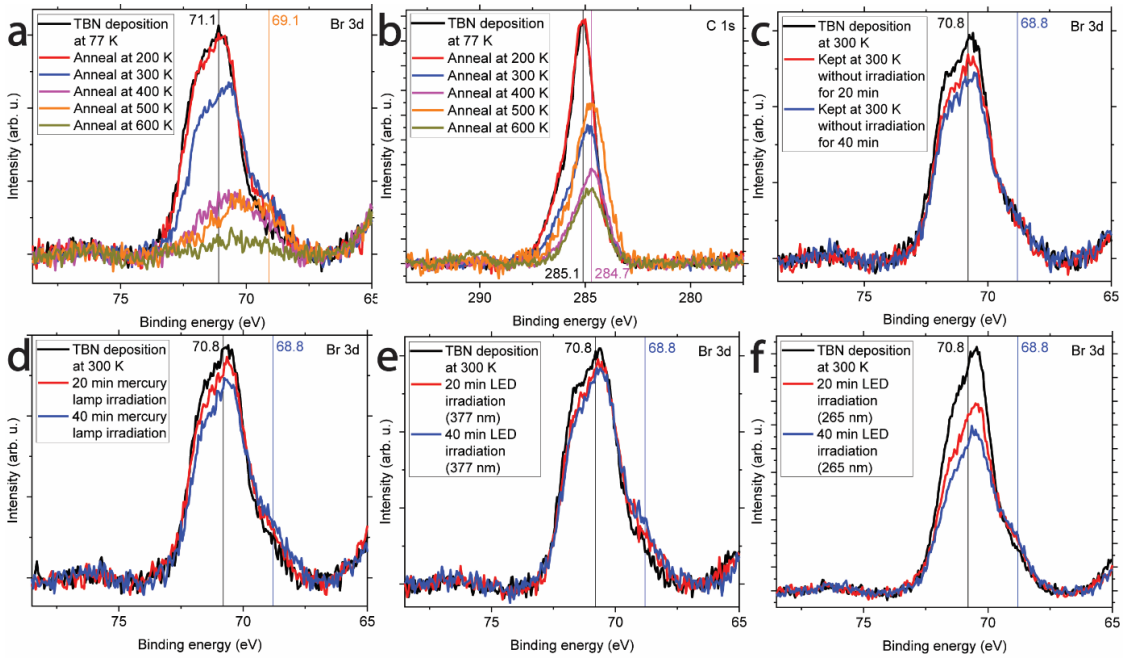

Fig. 8.2. (a) Br 3d and (b) C 1s narrow region scan XPS spectra of a rutile TiO_2 (110) surface after deposition of a TBN monolayer at 77 K, followed by annealing at different temperatures. XPS acquisition temperature: 77 K. Br 3d narrow region scan XPS spectra of a rutile TiO_2 (110) surface after deposition of a TBN monolayer at 300 K: (c) without any irradiation, (d) with irradiation by a mercury lamp, (e) with irradiation by a 377 nm LED (106 mW), and (f) a TBN ≈ 1.5 monolayer at 300 K with irradiation (f) a 265 nm LED (6.5 mW). XPS acquisition temperature: 300 K.

Same as XPS, for STM measurements, clean rutile TiO2 (110) surfaces were prepared through iterative cycles of sputtering and annealing. The annealing temperature was optimized at about 900 K to avoid the formation of defects and remove the contaminations. Annealing at ≈ 973K in the absence of oxygen treatment leads to the formation of (1×2) superstructure and probable TiO_2 strings along $\langle 1\bar{1}0 \rangle$ directions [91]. Fig. 8.3a shows an STM image of a clean rutile TiO_2 (110) surface revealing the (1×1) surface reconstruction with brighter and darker stripes. The contrast of the (1×1) rutile TiO_2 (110) surface STM images is often dominated by electronic properties rather than morphology. This means the brighter lines indicate the Ti rows, and the darker lines display the O rows [14]. The row distance is about 6.5 Å, consistent with the expected unit cell [14]. The hydroxyls were highlighted as brighter spheres placed on darker O rows. O vacancies, as the most abundant TiO_2 surface donors, appear as bright bridges on the dark stripes belonging to O atom rows, bridging two adjacent Ti rows [295]. In addition, a few intact TBN molecules with a width of approximately 0.7 nm remained on the surface, preferentially on Ti rows, where the benzene chains are perpendicular to, and C-Br bonds are parallel to, the Ti rows. Fig. 8.3b shows the surface after annealing the on-surface TBN multilayer at 400 K. TBN molecules desorbed from the rutile TiO_2 (110) surface. However, the surface is not as clean as after cleaning, due to the presence of more hydroxyls deposited at the same times as the TBN molecules, which have a high evaporation pressure even at room temperature, and remnant bromine atoms separated from TBN molecules before desorption. To this end, despite XPS indicating the thermally-induced debromination reaction upon annealing, STM shows sparsely C-C coupling (see the AP, Fig. 10F.7j), leading to the formation of 5AGNRs. We distinguished the 5AGNRs and (1×2) defects on the rutile TiO_2 (110) surface [334] (see the AP, Fig. 10F.8). The (1×1) LEED pattern in Fig. 8.3c indicates the clean, defect-free surface of the prepared rutile TiO_2 (110), as observed in the literature [14, 335], which is consistent with the STM image in Fig. 8.2a. Fig. 8.3d displays a LEED pattern of the surface after deposition of TBN molecules and annealing at 400 K, indicating the attenuated LEED spots of the substrate with extremely weak linear shadows, which could be due to the extremely

sparse distribution of the formed 5AGNRs on the surface upon annealing, consistent with the STM image in Fig. 8.3b and Fig. 10F.7 (the AP). However, LEED measurements after deposition might have a destructive effect on the top molecular layer [1]. Therefore, thermally-induced dehalogenation and Ullmann coupling, especially on inert surfaces, are limited by the low desorption temperature [253]. This is why photocatalysis by a photon source is a useful and promising method to diminish the energy barrier of this surface-assisted reaction [253].

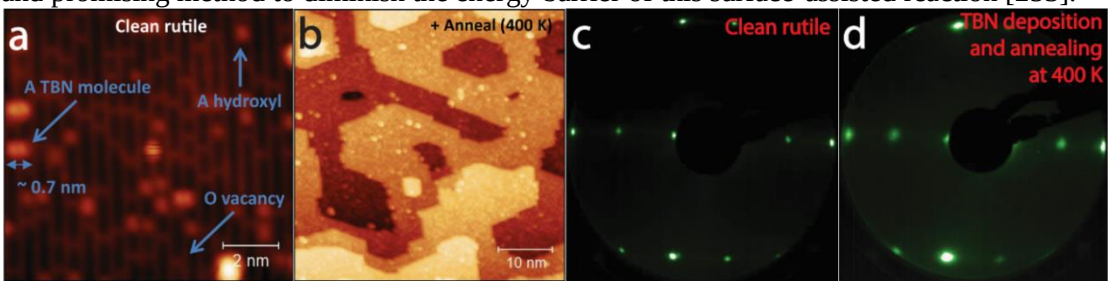

Fig. 8.3. (a) An STM image of a > 95% cleaned rutile TiO_2 (110) surface, with a few TBN molecules on this region of the surface; the distance between the darkest and brightest spots of the STM image (Z-height) = 339 pm. (b) An STM image of a TBN multilayer on a clean rutile TiO_2 (110) surface after annealing at 400 K and the desorption of the molecules; Z-height = 917 pm, V_s = 1 V, I_t = 10 pA. (c) A LEED pattern of a clean rutile TiO_2 (110) surface (E_{LEED} = 60 eV). (d) A LEED pattern of a TBN multilayer on a clean rutile TiO_2 (110) surface after annealing at 400 K (E_{LEED} = 60 eV). STM and LEED acquisition temperature: 77 K.

Consequently, we irradiated the TBN multilayer on the surface at room temperature with light of wavelength 240-395 nm using a filtered Xe lamp. Fig. 8.4a reveals a significantly increased number of 5AGNRs formed on the rutile TiO_2 (110) surface after irradiation with the Xe lamp. A more zoomed-in STM image of the surface in Fig. 8.4b indicates that the width of the formed ribbon is about 0.7 nm, comparable to the width of a single TBN molecule observed in Fig. 8.3a. Considering the width of the ribbons, we could distinguish them from other polymers, such as alkanes (see the AP, Fig. 10F.7j). In addition, there are a significant number of hydroxyls on O rows and Br atoms on Ti rows. Fig. 3c shows a zoomed-in STM image of an 5AGNR with a width of 0.7 nm and a uniform charge distribution along its length. More 5AGNRs nucleated from the defects and step edges of the rutile TiO_2 (110) surface. Defects on the surface act as catalysts, increasing the rate and decreasing the temperature of dehalogenation and polymerization [2]. Upon annealing at about 325 K, Fig. 8.4d shows fewer 5AGNRs on the surface, revealing that desorption had already started at this temperature. Fig. 8.4e indicates that after annealing this sample at about 400 K, more significant desorption of 5AGNRs occurred. However, the desorption of more hydroxyls and bromine atoms results in a cleaner rutile TiO_2 (110) surface, facilitating the STM and STS measurements. In Fig. 8.4f, a structural model of a 5AGNR, formed using Xe light, is exhibited. Considering its dimensions, this 5AGNR is formed through aryl-aryl couplings of three debrominated TBN molecules. Conversely, introducing Fe ad-atoms did not increase the number of 5AGNRs on the rutile TiO_2 (110) surface (see the AP, Fig. 10F.7).

Two mechanisms for photopolymerization are suggested: one is the excitation of single molecules followed by relaxation to the ground state through dehalogenation and the production of radicals. After debromination of TBN molecules, these extremely reactive radicals bond to each other and polymerize to form 5AGNRs due to the octet rule. The other is the excitation of molecules and direct coupling to adjacent molecule to relax into a covalently bonded polymer [253]. In the second mechanism, the pre-assembly of molecules is required, increasing the polymerization probability for molecules with a smaller evaporation barrier [253]. This is why neither annealing a TBN monolayer or submonolayer, nor their irradiation by light, has led to a significant number of 5AGNRs observed on the surface, despite the multilayer. Therefore, C-C coupling is significantly catalyzed upon surface irradiation by violet and UV light. On the flip side, we have not seen any sign of dehydrogenation and lateral fusion of the 5AGNRs to form wider GNRs upon annealing, irradiation by the Xe lamp, or catalysis by Fe atoms. However, applying a large bias voltage to a few adjacent 5AGNRs led to an STM image of a

wider feature, suspicious of a wider ribbon due to dehydrogenation and subsequent lateral fusion (see the AP, Fig. 10F.8).

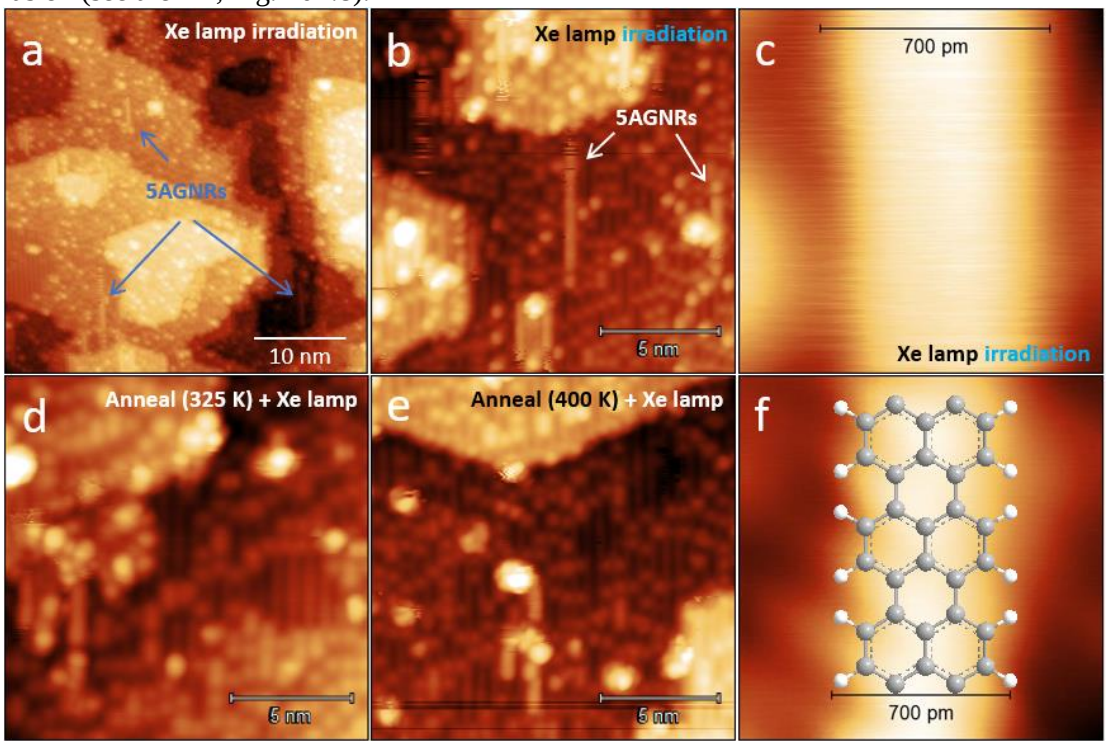

Fig. 8.4. STM images of 5AGNRs (width ≈ 0.7 nm) on a rutile TiO_2 (110) surface after irradiating a TBN multilayer with a Xe lamp; (a) Z-height = 1.31 nm. (b) Z-height = 598 pm. (c) Z-height = 111 pm. (d) An STM image of 5AGNRs on a rutile TiO_2 (110) surface after irradiation a TBN multilayer with a Xe lamp and concurrently annealing at 325 K; Z-height = 642 pm. (e) An STM image of 5AGNRs on a rutile TiO_2 (110) surface after irradiating a TBN multilayer with a Xe lamp and concurrently annealing at 400 K; Z-height = 841 pm. (f) An STM image of a 5AGNR on a rutile TiO_2 (110) surface after irradiation a TBN multilayer with a Xe lamp and the corresponding speculated atomic structural model of the 5AGNRs; Z-height = 190 pm. V_s = 1 V, I_t = 10 pA. STM acquisition temperature: 77 K.

Fig. 8.5a shows a zoomed-in STM image of two adjacent 5AGNRs nucleated from a step edge, characterized by STS. The measured spots are depicted by colored crosses on the image. At the bottom of the image, a clean region of the rutile TiO_2 (110) surface is used for calibration of the STS measurements. The thinner bright spheres on the O rows are hydroxyls, and the wider brighter spheres on the Ti rows are Br atoms. 5AGNRs are formed mostly parallel to the O and Ti rows, with a greater tendency to be centered on the Ti rows. The limited interactions between 5AGNRs and the surface were concluded from bias-dependent STM measurements, which showed changes in the orientation of the 5AGNRs when a larger bias voltage, either larger than 2 V or lower than -0.5 V, was applied. Due to the weak interactions of the TBN molecules and 5AGNRs with the rutile TiO_2 (110) surface, their high mobility results in noise on the 5AGNR features in the STM image. Fig. 8.5b displays STS spectra of a clean TiO2 surface, showing a VB at about -3 eV and a CB at about 0.3 eV. This is why STM measurements at a bias voltage of 1 V are more stable, while STM at a bias voltage of -1 V, which is within the band gap of rutile TiO_2 (110), is less stable. To elucidate the contradictory reports about the band gap and nature of the 5AGNRs, we conducted STS of 5AGNRs on rutile TiO_2 (110) surfaces to avoid coupling and hybridization with the substrate, thereby improving the precision of the electronic excitation measurements. With the VB and CB of 5AGNRs at bias voltages of about -1.35 V and 0.75 V, respectively, a band gap of about 2.1 eV is obtained. This finding reinforces that these ribbons are semiconductors, though in some previous reports have discussed the presence of some in-gap excitonic states and a smaller band gap for 5AGNRs on Au (111) and NaCl islands [96].

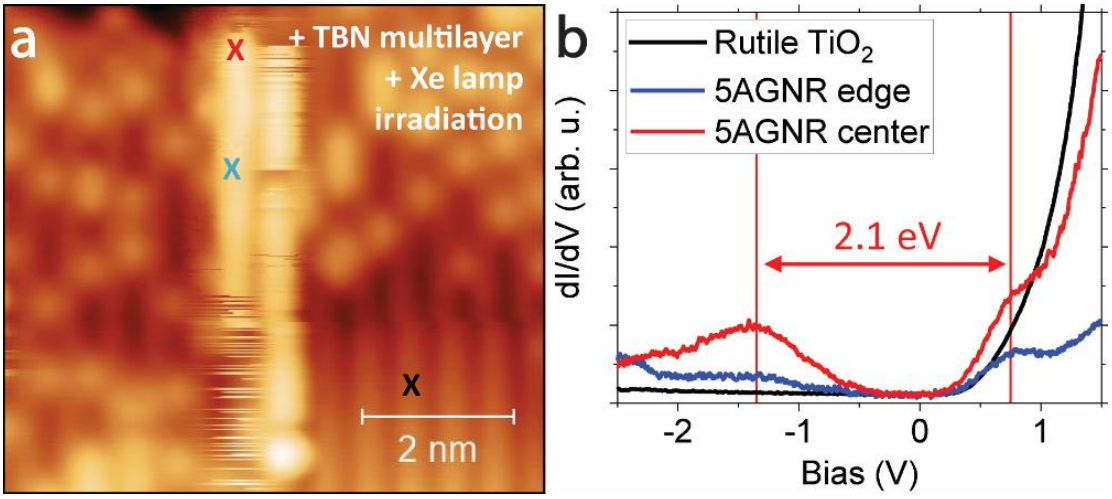

Fig. 8.5. An STM image of 5AGNRs on a rutile TiO_2 (110) surface after irradiation of a TBN multilayer with a Xe lamp; (a) ≈ 8.7 nm × ≈ 8.7 nm, V_s = 1 V, I_t = 10 pA, Z-height = 341 pm. (b) STS spectra of the 5AGNRs and rutile TiO_2 shown in (a). STM and STS acquisition temperature: 77 K.

8.5. Conclusion

Although the debromination of TBN molecules on rutile TiO_2 (110) and anatase TiO_2 (101) surfaces upon annealing are indicated by XPS, STM observations revealed limited C-C coupling and 5AGNR formation. However, exposure to violet and UV light significantly increased the number of products. The produced 5AGNRs were identified by comparing their width in STM images to those of intact single TBN molecules on these surfaces. The photo-induced reaction occurs due to the relaxation of excited molecules by dehalogenation and consequent aryl-aryl coupling with adjacent molecules. XPS analysis reveals that the most efficient wavelength for boosting the debromination reactions on these surfaces corresponds to UV light at 265 nm. However, light with a wavelength of 377 nm, near the violet range, also enhances the surface-assisted debromination required for Ullmann coupling. In addition, the higher the intensity of light, the more on-surface debromination occurs. Using a semiconducting substrate like rutile TiO_2 for the on-surface preparation of 5AGNRs can avoid the charge transfer between the nanostructures and the substrate, allowing for more accurate electronic and optical excitation measurements. Our STS study of 5AGNRs on this surface indicated a band gap of ≈ 2.1 eV, suggesting the semiconducting nature of this nanoarchitecture.

Chapter 9

Conclusion and Outlook

The key conclusions from each chapter have been summarized in their respective sections, and here, we compare and assess the potential of various wide band gap semiconducting single crystals and decoupling layers as alternatives of metallic substrates for surface science. This approach aims to avoid quenching the electronic and optical excitations of on-surface nanostructures, enabling more precise electronic and optical measurements. However, insulating substrates can cause charging effects during surface science techniques such as XPS and LEED, limiting elaborate measurements. If the substrate is not sufficiently conductive, tunneling does not occur between the tip and the substrate, preventing STM and STS measurements on these surfaces. To this end, we evaluated HVPE and AMMONO free-standing wurtzite GaN (0001) and $(000\bar{1})$, rutile TiO_2 (110), and the more expensive anatase TiO_2 (101) single crystals, and Cu_2N thin films on Cu (111) and Cu (100) for surface studies and on-surface reactions/assemblies, such as surface-assisted dehalogenation and Ullmann coupling. In this section, we compare the critical parameters, characteristics, and limitations of these substrates for surface science studies, and for each substrate, we present the outlook and suggested future directions.

The first critical characteristic that limits the implementation of surface science techniques on a substrate is conductivity. A proper substrate must be sufficiently conductive to allow the tunneling current to pass from the tip to the surface when a bias voltage is applied. For instance, electrons did not tunnel from the tip to the undoped diamond (001) surface with a band gap of about 5.5 eV, preventing our STM measurements [45-48]. In addition, the conductivity of the substrate leads to charging effects in XPS and LEED measurements. For example, if rutile TiO_2 is not reduced by creating O vacancies to increase its conductivity, unwanted binding energy shifts are observed in XPS spectra, and sharp LEED patterns are not obtained. We observed that Si- and Ge-doped HVPE GaN (0001) and $(000\bar{1})$, O-doped AMMONO GaN (0001), reduced rutile TiO_2 (110), and reduced anatase TiO_2 (101) single crystals, despite their wide band gaps, are conductive enough to allow tunneling between a tip and their surface and to avoid charging effects in XPS and LEED. A sample with a conductivity below 10^{-10} $\Omega^{-1}m^{-1}$ shows a significant charging effect [336], such as a non-reduced rutile TiO_2 [337]. Furthermore, Cu_2N monolayers exhibit metallic natures, making them highly compatible substrates for surface studies, facilitating tunneling and preventing any charging effect in XPS and LEED measurements. Besides that, low conductivity limits the achieved STM resolution.

In addition to conductivity, the stability of the substrates plays a key role in surface studies, such as surface-assisted synthesis and reactions, and the application of on-surface nanoarchitectures in ambient conditions. Based on our observations, reduced TiO_2 surfaces are very stable in ambient conditions, except for the adsorption of contaminations such as C compounds. Both experiments and simulations indicate that Cu_2N thin films are also very stable against molecular adsorption, although we observed the modification of Cu_2N on Cu (100)

under O_2 conditions in UHV and upon exposure to air. Generally, exposing crystals and surfaces to air or gases such as O_2 and CO in UHV chambers results in surface contamination, impurities, and modifications. Therefore, cleaning is a crucial step to access pristine surfaces for precise surface studies and on-surface reactions. For example, it is reported that sputtering the diamond surface using gas ions in UHV leads to the formation of a graphene monolayer, preventing direct access to the diamond surfaces [45-48]. Additionally, upon exposure to air or O_2 gas, about 1 nm of an oxide layer forms on the reactive GaN surface. Thereby, surface studies of ex-situ grown GaN single crystals are limited. Complete removal of the gallium oxide layer on GaN and C and other contaminants on GaN, TiO_2, and Cu surfaces was reproducibly attained after sputtering and annealing these surfaces. Although sputtering and annealing result in the surface cleaning, they have some disadvantages. Sputtering causes permanent damage to the surface of GaN, which is not compensated by high-temperature annealing with or without NH_3 gas and electron bombardment. Another consequence of sputtering surfaces with gas ions is the preferential removal of lighter atoms in the diatomic lattices. An elaborate control over this selective removal of lighter atoms is advantageous for TiO_2 surfaces, forming CS planes, O vacancies, and reduced crystals, making them conductive. On the flip side, sputtering TiO_2 surfaces using heavier gases like Ne for extended periods, in the absence of O_2 in the chamber, results in surface reconstruction and faceting, similar to what we observed for FeSi crystals [213, 214, 338-344]. This preferential removal of N atoms was also observed for GaN crystals upon sputtering, leading to the formation of randomly shaped and sized unwanted hillocks on the surface, limiting further STM studies. Although, we compensated for the preferential removal of N atoms by adding N atoms to the surface during annealing under NH_3 and etching excess Ga atoms and Ga-rich hillocks using Br atoms from TBB molecules, we were unable to achieve an atomically flat GaN surface. Moreover, sputtering the surfaces causes the removal of the Cu_2N thin film on Cu surfaces. Therefore, although we cleaned the Cu surfaces using sputtering and annealing, we avoided sputtering in our developed technique for fabricating Cu_2N films to achieve better control over the coverage of these submonolayers. Cu_2N submonolayers are obtained by replacing O atoms in copper oxides with N atoms cleaved by annealing them on the surface at 625-675 K. Without sputtering, repeating the oxidation and nitridation cycles can increase the coverage. However, annealing at an optimized temperature and conditions compensates for the preferential removal of lighter atoms to some degrees, as we observed for FeSi crystals [213, 214, 338-344]. Nevertheless, annealing at very high temperatures can also cause negative preferential removal of lighter atoms, faceting on the surfaces and in the bulks, and dissociation of the crystals or films. Annealing temperature is a crucial parameter for achieving atomically flat TiO_2 surfaces. Annealing rutile TiO_2 (110) at 825-925 K results in the formation of an atomically flat (1×1) surface reconstruction, suitable for STM measurements. However, preparing an atomically flat anatase TiO_2 (101) surface proper for STM is more challenging. This surface is more sensitive to annealing temperature and at around 900 K, it slowly begins a phase transformation to rutile, as reported previously [345, 346]. For metallic substrates like our Cu (111) and Cu (100) surfaces, optimized cycles of sputtering and annealing are sufficient to gain an atomically flat and clean surface for the fabrication of flat Cu_2N submonolayers and molecular depositions.

Achievement of atomically flat surfaces provides more information about the superstructures and atomic defects on the surfaces. These surface defects exhibit both advantages and disadvantages. Extreme damage and defect on the surface, such as those on GaN surfaces after UHV treatments, prevent STM studies. Annealing rutile TiO_2 (110) at higher temperatures leads to the formation of (1×2) defects, which makes identifying 1D structures, such as ribbons and wires, on these surfaces more difficult. In addition, O vacancies are easily recognized on rutile TiO_2 (110) surfaces as bridges between two Ti rows, which are necessary to increase conductivity, facilitating the STM of these crystals. Furthermore, atomic resolution STM images of Cu_2N films on Cu surfaces reveal different defects on these surfaces as well. The lattice mismatch of the Cu_2N layer with both Cu (111) and Cu (100) surfaces prohibits the formation of an extended full monolayer, resulting in the formation of Cu_2N islands forms on both surfaces. On Cu (111), Cu_2N appears as adjacent elongations in three directions. These adjacent elongations are nearly parallel, but corrugate without order and have varying distances

from each other along their length. These Cu_2N islands, elongated in different directions, cross each other and form Cu islands, indicating standing wave features characteristic of the formed QCs. On Cu (100), Cu_2N islands possess two dominant defects: N atom vacancies and Cu atom vacancies. These atomic vacancies quench the confinement states formed on Cu_2N islands at the defected point, indicating the possibility of electronic modifications on these surfaces at the atomic scale. This could be promising for the investigations of versatile quasi-particles and their couplings.

Our STS measurements indicated band gaps of approximately 3.4 eV, 3.3 eV, and 3.8 eV for GaN, rutile TiO_2, and Cu_2N, respectively, all of which fall within the range of wide band gap semiconductors. This is promising for avoiding hybridization and charge transfer between the on-surface molecules, atoms, and structures, and the surface. However, DFT simulations and reported ARPES measurements have introduced Cu_2N thin films as metals [68]. This inconsistency arises because STS results are dominated by information about the Γ point of the BZ, while Cu_2N CB and VB overlap at the M point in the band structure. Nonetheless, phonon simulations, LEED [68], and STS reveal the high stability of these thin films and the weak interaction between the Cu_2N surfaces and on-surface atoms, molecules, and nanostructures, known as the decoupling effect. The significant stability of the Cu_2N surface and its high adsorption enthalpy compared to Cu islands make the adsorption of molecules on Cu_2N less probable, although it is still possible depending on the substrate and the molecule. Greater molecular adsorption was observed on Cu_2N on Cu (111) compared to Cu (100). In both cases, STS confirms the decoupling effect of these films, preventing the hybridization of the C compounds in the adsorbed molecules and the surface.

While molecular adsorption was more convenient on single crystals, achieving proper adsorption on Cu_2N islands was more difficult, as molecules tended to adsorbed on Cu islands or stripes instead. However, we developed methods for adsorbing different molecules on these surfaces to investigate surface behaviors and on-surface self-assembly and reactions. Here, we concisely mention the different molecules investigated in this thesis on various surfaces. DAPPor molecules assembled with highly extended order on Cu (111) islands and were less ordered on Cu_2N on Cu (111). Ullmann coupling of $(BrP)_2P$ and DBTP molecules on Cu (111) and Cu_2N islands were demonstrated. Aryl-aryl coupling of debrominated DBTP molecules on Cu (111) and Cu_2N islands led to the formation of PPP wires on both surfaces. On Cu (100), Pentacene, TPA, DAPPor, and CBCP molecules adsorbed on Cu stripes and islands around Cu_2N square-like islands, although fewer molecules on Cu_2N were also observed. For all the measured molecules and nanostructures, Cu_2N submonolayers exhibited a decoupling property, preventing hybridization and charge transfer with the metallic substrate. STM of molecules on GaN single crystals was not successful due to their rough surface, while XPS revealed the debromination of TBB molecules on these surfaces. TPD revealed the preferential etching of Ga-rich hillocks through the preferential removal of Ga atoms by desorbing Br atoms. Moreover, XPS monitored the compensation of the N to Ga ratio upon NH_3 annealing. These treatments favor the reversal of the near-stochiometric ratio of N to Ga atoms and the smoothening of the surface. On rutile TiO_2 (110) and anatase TiO_2 (101), the debromination of DBTP, TBN, and TBB molecules was monitored using XPS. Using STM, C-C coupling and the formation of 3AGNRs and 5AGNRs on rutile TiO_2 (110) were monitored, although no strong evidence for dehydrogenation and lateral fusion to form wider GNRs was collected. STS measurements were fulfilled on these surfaces, demonstrating the excellent capability of these substrates for electronic and optical measurements of on-surface molecules and structures. Additionally, the catalytic effects of light and Fe ad-atoms on Ullmann coupling and the formation of GNRs on rutile TiO_2 (110) surfaces were studied and confirmed, lowering the debromination and C-C coupling temperatures. Our further investigation of on-surface reactions and Ullmann coupling on FeSi substrates (beyond the scope of this thesis) shows a strong interaction between the molecules and the surface, preventing diffusion and coupling. However, debromination occurred based on XPS measurements.

Looking ahead, we propose several future directions for these substrates. For GaN surface preparation, we propose using pure Br atoms and Br_2 molecules to etch the Ga-rich hillocks, favoring surface smoothening and flattening. Besides, the AMMONO GaN surface we prepared

is flat enough to deposit supra-large molecules for STM investigations. Furthermore, further molecular studies on atomically flat Cu_2N and TiO_2 surfaces are proposed, given their promising capability for molecular assemblies, reactions, and measurements of electronic and optical properties of on-surface nanostructures. Additionally, utilizing atomic defects in Cu_2N on Cu (100), considering the CSs on these islands, holds promise for future investigations of versatile quasiparticles. Further investigations and growth of Cu_2N on different surfaces to achieve a full monolayer or multilayer growth are of great importance. Besides that, as the future step, we propose depositing a Cu monolayer on Cu_2N on Cu (111), oxidizing it, and annealing it in NH_3 to facilitate the growth of multilayer Cu_2N on these surfaces.

List of Publications

1- Rostami, M., Yang, B., Haag, F., Allegretti, F., Chi, L., Stutzmann, M. and Barth, J.V., 2024. Influencing the surface quality of free-standing wurtzite gallium nitride in ultra-high vacuum: Stoichiometry control by ammonia and bromine adsorption. Applied Surface Science, p.160880.

2- Rostami, M., Yang, B., Ma, X., You, S., Zhou, J., Zhang, M., Cui, X., Zhang, H., Allegretti, F., Wang, B., Chi, L. and Barth, J.V., 2024. Catalytic effects of iron add-atoms and light on poly(para-phenylene) wires on TiO_2 surfaces. Submitted.

3- Rostami, M., Yang, B., Seyedmohammadzadeh, M., Kaya, P., Kaderoğlu, C., Olgar, H., Aktürk, E., Chi, L., and Barth, J.V., 2024. Post-synthesis of Cu_2N monolayers on Cu (111) from copper oxide films and their decoupling effects. In preparation.

4- Rostami, M., Yang, Chi, L., and Barth, J.V., 2024. Ullmann coupling and poly(para-phenylene) wires on copper nitride monolayers on copper (111). In preparation.

5- Rostami, M., Yang, B., Seyedmohammadzadeh, M., Kaya, P., Kaderoğlu, C., Olgar, H., Aktürk, E., Chi, L., and Barth, J.V., 2024. Fabrication of Cu_2N confinement states on Cu (100). In preparation.

6- Rostami, M., Yang, B., Ma, X., You, S., Zhou, J., Zhang, M., Cui, X., Zhang, H., Allegretti, F., Wang, B., Chi, L., and Barth, J.V., 2024. Photocatalytic fabrication of 5-armchair graphene nanoribbons on TiO_2 surfaces. In preparation.

7- Rostami, M., Haag, F., Allegretti, Yang, B., F., Chi, L., and Barth, J.V., 2024. Formation of peptide bonds on TiO_2 surfaces as a potential pathway for the origin of life. In progress.

List of Conferences

1- Rostami, M., Yang, B., Haag, F., Vezzoni, P., Allegretti, F., Chi, L., Stutzmann, M. and Barth, J.V., 2022. Evaluation and processing of Si/Ge-doped free-standing Ga and N-terminated c-plane wurtzite GaN surface quality. ECOSS 35, 35th European Conference on Surface Science, Luxembourg. Poster.

2- Rostami, M., Yang, B., Haag, F., Allegretti, F., Chi, L., Stutzmann, M. and Barth, J.V., 2022. Assessing and processing the surface quality of free-standing wurtzite GaN in ultra-high vacuum. e-conversion Conference in Venice, Italy. Poster.

3- Rostami, M., Yang, B., Haag, F., Vezzoni, P., Allegretti, F., Chi, L., Stutzmann, M. and Barth, J.V., 2022. Evaluation and processing of Si/Ge-doped free-standing Ga and N-terminated c-plane wurtzite GaN surface quality. The International Workshop on Nitride Semiconductors, Berlin. Poster.

4- Rostami, M., Yang, B., Haag, F., Allegretti, F., Chi, L., Stutzmann, M. and Barth, J.V., 2023. Assessing and processing the surface quality of free-standing wurtzite GaN in ultra-high vacuum. Deutsche Physikalische Gesellschaft e. V. DPG Spring, Dresden. Poster.

5- Rostami, M., Yang, B., Allegretti, F., Chi, L., and Barth, J.V., 2023. Post-synthesis of copper nitride monolayers from copper oxide films. Deutsche Physikalische Gesellschaft e. V. DPG Spring, Dresden. Talk.

Chapter 10

Appendix

Appendix A: Influencing the Surface Quality of Free-Standing Wurtzite Gallium Nitride in Ultra-High Vacuum: Stoichiometry Control by Ammonia and Bromine Adsorption

Experimental setup and detailed parameters

Fig. 10A.1 shows the experimental setup used for ammonia annealing in the XPS (a) and STM (b) chambers. Using these instruments, we performed various experiments as shown in Table 10A.1. For the gallium nitride (GaN) substrates, two different photon energies (1253.6 eV and 1486.6 eV) were used to disentangle the intense Auger and core-level C 1s, N 1s, and O 1s peaks. The HVPE (Table 10A.2) and AMMONO (Table 10A.3) samples were mounted on molybdenum plates.

Overview and narrow scans XPS in normal (0˚) and grazing (70˚) emission geometries were used. XPS peak fitting analyses were performed with Casa XPS [347], IGOR, and OriginPro software. All XP spectra are calibrated by the Ga $2p_{3/2}$ and N 1s core levels at 1117.8 eV and 397.1 eV binding energies, respectively [348, 349].

Respectively, TBB (Fig. 10A.1d) and DBTP evaporators were baked at 363 K and 373 K for 18 hours. Upon introduction into the UHV chamber, the powders were outgassed by slowly ramping the temperature to the sublimation temperature of 413 K in steps of 10 K and keeping the powder at the sublimation temperature for several minutes.

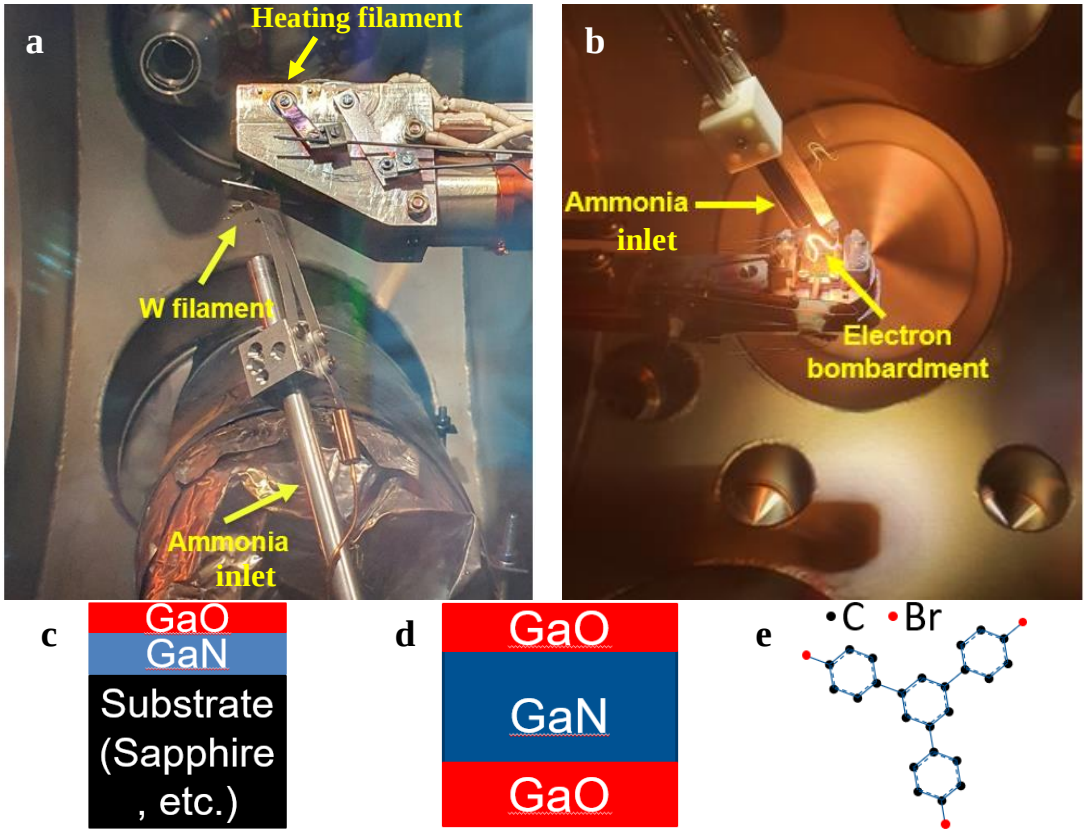

Fig. 10A.1. Experimental setup for the ammonia annealing experiment in an (a) XPS and TPD chamber having a Phoibos 100 Specs analyzer and a (b) JT-STM UHV chamber. (c) Schematic structure of GaN supported on a solid substrate. (d) Schematic structure of free-standing GaN in air. (e) Schematic structure of a TBB molecule.

Table 10A.1. Different experiments including ammonia annealing for HVPE Gallium Nitride (GaN) (0001) surface preparation done in the PSD chamber.	
Label	Experiment
1	7 × (Sputtering (300K) + UHV annealing (950K))
2	… + 2 × (Sputtering (300K) + UHV annealing (950K))
3	… + NH3 annealing together with electron bombardment (220V, 950K)
4	… + 2 × (Sputtering (300K) + NH3 annealing together with electron bombardment (220V, 950K))
5	… + 2 × (Sputtering (300K) + NH3 annealing together with electron bombardment (220V, 950K)) + UHV annealing (950K)
6	… + 2 × (Sputtering (300K) + NH3 annealing together with electron bombardment (220V, 950K)) + UHV annealing (950K)
7	… + 3 × (Sputtering (300K) + NH3 annealing together with electron bombardment (220V, 950K)) + UHV annealing (950K)
8	… + Electron bombardment (220V, ≥245K)
9	… + 2 × (Sputtering (300K) + NH3 annealing together with electron bombardment (220V, 950K)) + UHV annealing (950K) + UHV annealing (950K) and electron bombardment (220V) + Electron bombardment (220V, ≥245K)
10	… + 2 × (Sputtering (300K) + NH3 annealing together with electron bombardment (220V, 950K)) + UHV annealing (950K) and electron bombardment (220V) + Electron bombardment (220V, ≥245K)
11	… + 2 × (Sputtering (300K) + NH3 annealing together with electron bombardment (220V, 950K)) + UHV annealing (950K) and electron bombardment (220V) + Electron bombardment (220V, ≥245K)
12	… 5 × (Sputtering (300K) + UHV annealing (950K))

13	… + Electron bombardment (220V, ≥245K)
14	Without preparation
15	… + 3 × (Sputtering (300K) + NH3 annealing without electron bombardment (950K))
16	… + Electron bombardment (220V, ≥245K)
17	… + 2 × (Sputtering (300K) + High energy electron bombardment in the presence of NH_3 (1000V, 300K) + NH3 annealing without electron bombardment (950K) + UHV annealing (950K))
18	… + Sputtering (300K)
19	… + UHV annealing (950K)

Table 10A.2. Properties of Si and Ge-doped free-standing wz GaN (0001)/(000$\bar{1}$) from MSE supplies[1].

Thickness	Resistivity (300K)	Carrier Concentration	rms-roughness	Mobility	dislocation density
350 ± 25 um	<0.05 Ohm.cm	$10^{18}cm^{-3}$	<0.2 nm	220 $cm^2V^{-1}s^{-1}$	$5x10^5$ - $3x10^6$ cm^{-2}

Table 10A.3. Properties of O-doped free-standing wz GaN (0001) from IHPP PAS[2].

Thickness	Resistivity (300K)	Carrier Concentration	rms-roughness	Mobility	dislocation density
350 ± 100 um	~0.01 Ohm.cm	2 x 10^{17} - 2 x $10^{18}cm^{-3}$	<0.5 nm	250 $cm^2V^{-1}s^{-1}$	$5x10^4$ cm^{-2}

Results and Discussion

HVPE GaN (0001) Surface Cleaning

As shown in Fig. 10A.2, 10mm × 10.5mm HVPE free-standing Silicon (Si) (Fig. 10A.2a) and Germanium (Ge) (Fig. 10A.2b and c)-doped c-plane wz HVPE GaN samples are transparent, having mostly the same properties (Table S2 and S3). Fig. 10A.2b displays a Ge-doped N polar GaN sample on the STM holder before loading into the UHV chamber undergoing any cleaning cycles. Fig. 10A.2c shows the same sample after heating from the bottom (Ga polar surface [350-354]) by electron bombardment (high voltage). We speculate that the bottom was heated locally to a temperature higher than 1050K, where it was close to the filaments, while the temperature of the surface was lower. A whitish color appeared at the region of contact between filaments and the bottom of the sample which is due to faceting caused by the high temperature close to the decomposition temperature of GaN (>1050 K [52]).

a 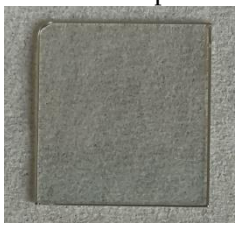 **b**  **c** 

Fig. 10A.2. HVPE free-standing Ga polar Si-doped GaN (0001) and N polar Ge-doped GaN (000$\bar{1}$). (a) A sample before mounting on a holder. (b) A sample after mounting on the JT-STM holder and before any cleaning cycle. (c) A sample on the holder of JT-STM after the

[1]https://www.msesupplies.com/collections/free-standing-gan-crystal

[2]https://www.unipress.waw.pl/growth/images/Articles/Ammono_GaN_wafers_sales/Ammono_GaN_High_electron_concentration_v_20220830.pdf

last annealing step, and observation of faceting (whitish color). Faceting occurred at the bottom of the sample attached to the heating filament.

Different GaN crystal surface cleaning and preparation methods have been reported in the literature [355-357]. Fig. 10A.3 shows an overview and zoomed-in XPS spectra of a cleaned HVPE GaN sample after 7 cycles of sputtering (E_{ion} = 0.5 keV for 5-10 minutes (min) and I_{ion} = 10-15 µA corresponding to 0.003-0.010 C) and annealing (600-950K for 5-20min), recorded with Mg K_α and Al K_α radiation, respectively. The most important spectroscopic features are assigned in Fig. 10A.3a and b. Fig. 10A.3e shows the (1×1) LEED pattern of the HVPE Ge-doped free-standing GaN $(000\bar{1})$ sample after the removal of the oxide layer.

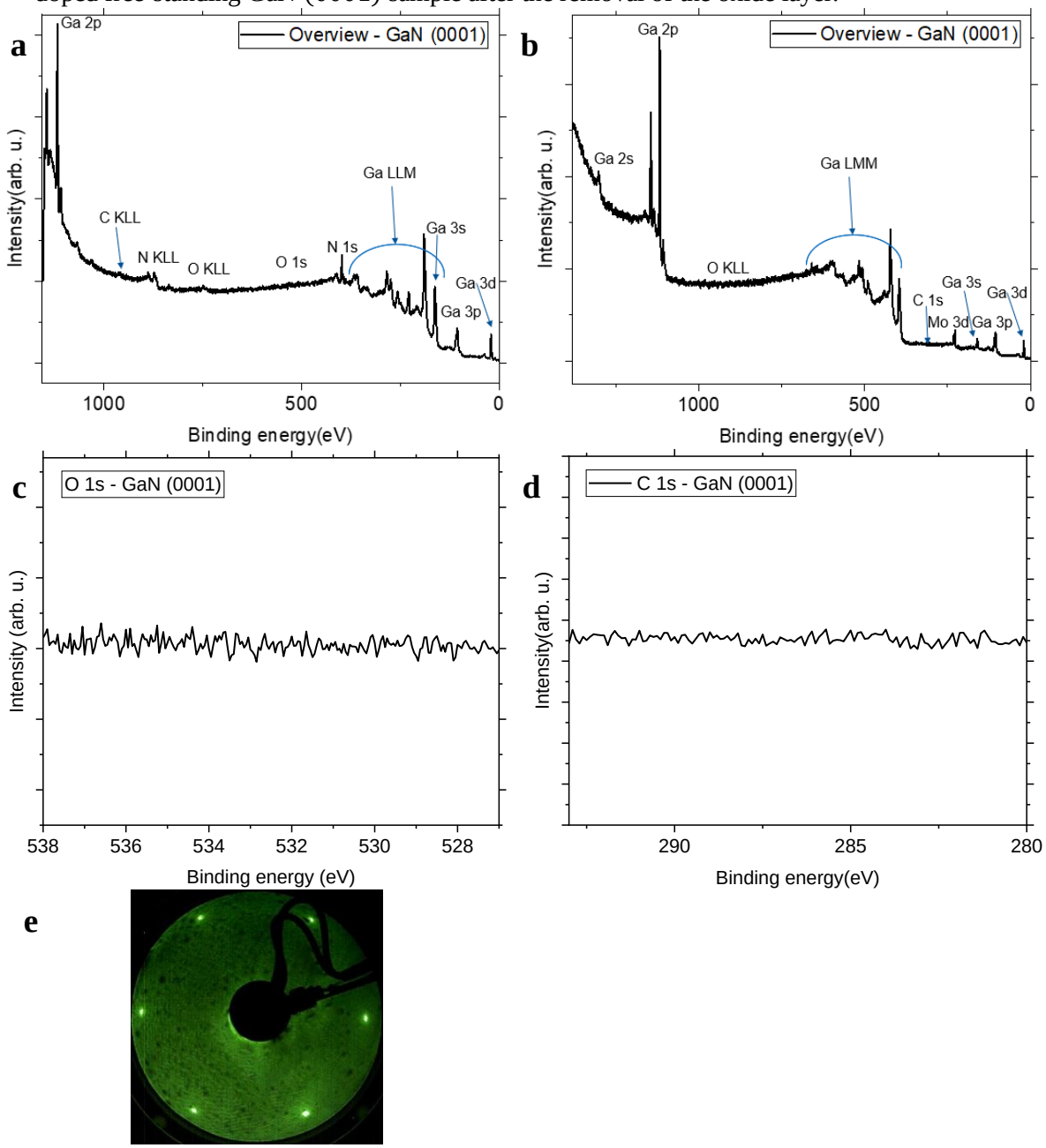

Fig. 10A.3. XP spectra of the cleaned surface of Si-doped free-standing Ga polar c-plane wz HVPE GaN. Overview scan by (a) Mg and (b) Al anode-based X-ray sources (photon energy: 1253.6 eV and 1486.6 eV, respectively). Zoomed-in scans into the (a) O 1s and (b) C 1s core level regions for the Mg and Al sources (photon energy: 1253.6 eV and 1486.6 eV), respectively. (e) (1×1) LEED pattern (electron energy = 63eV) of cleaned HVPE Ge-doped free-standing GaN $(000\bar{1})$.

Fig. 10A4a shows the component analyses of an XPS Ga 2p narrow region scan of the HVPE GaN $(000\bar{1})$ surface after 7 cycles of sputtering and annealing (950 K). A pass energy of 5 eV is used to achieve a better resolution for comparison of GaN and atomic Ga components. The presence of an atomic Ga component in the spectrum proves the existence of Ga-rich clusters on the surface of GaN. Furthermore, Fig. 10A4b shows the component analysis of an XPS N 1s narrow region scan of the HVPE GaN $(000\bar{1})$ surface after ammonia exposure.

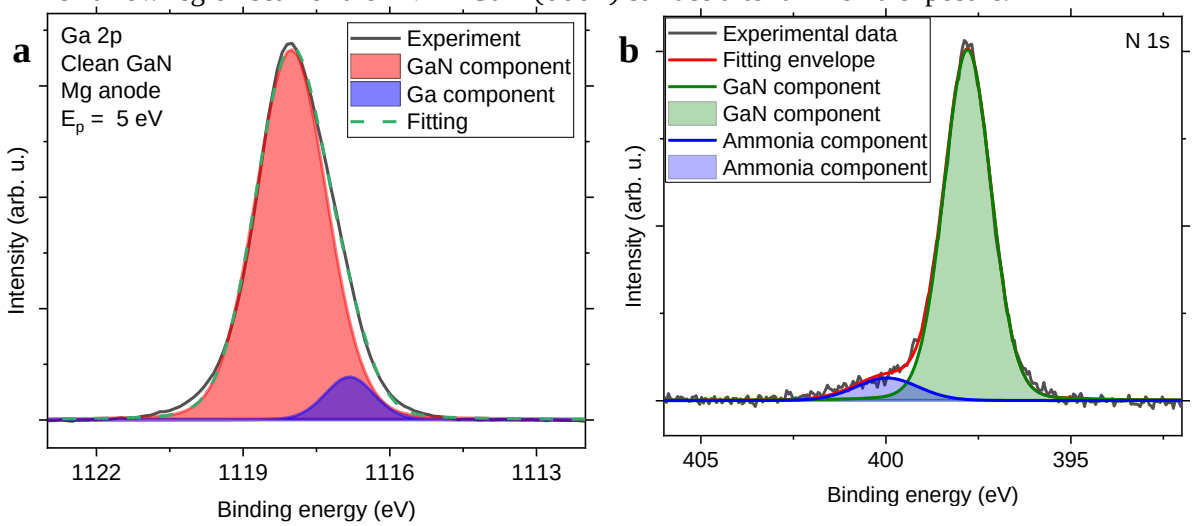

Fig. 10A.4. (a) XPS Ga 2p narrow region scan of a clean HVPE GaN $(000\bar{1})$ surface with a pass energy (E_P) is 5 eV. (b) An example of the N 1s peak area fitting (E_P = 15 eV) used for calculation of the N 1s to Ga 2p ratio in Fig. 10A.11 and AA.12, after several cycles of sputtering and UHV annealing.

Fig. 10A.5a and b show STM results of Si-doped HVPE GaN (0001) after specific cleaning cycles involving sputtering (10 min at ≈ 400 K, $I_{emission}$ ≈ 11.0 µA, ≈ 0.007-0.013 C, $E_{sputtering}$ = 1 kV) and subsequent annealing at 773 K and 873 K, respectively. After annealing at 773 K, we still observed the oxide layer surface by XPS, but was removed by annealing at higher temperatures.

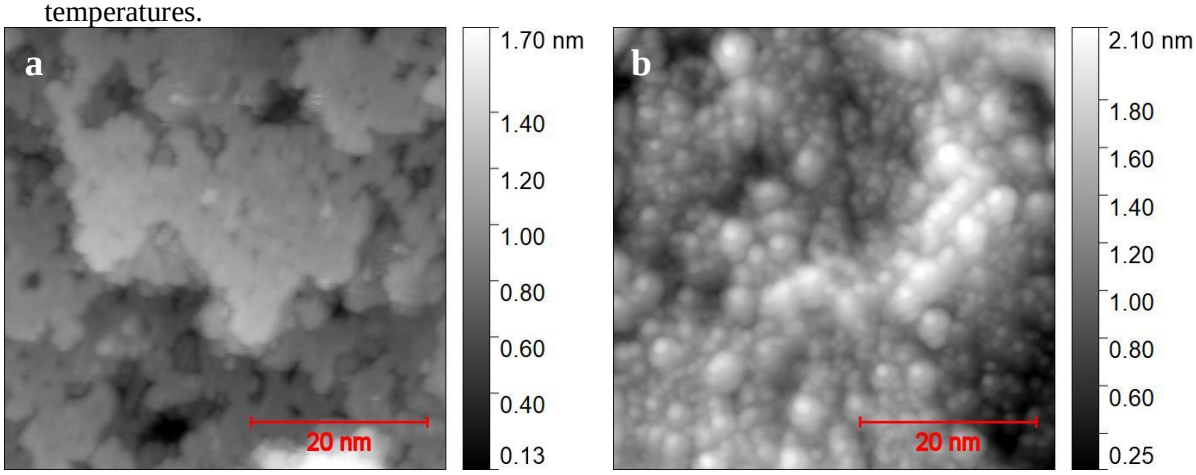

Fig. 10A.5. (a) STM images of Si-doped free-standing HVPE GaN (0001) after cleaning with four cycles of sputtering and annealing up to 773 K; 50 nm × 50 nm, V_s = -4.00 V, I_t = 100 pA, rms-roughness (rms-R) = 0.20 nm. (b) STM images of Si-doped HVPE GaN (0001) after an additional cycle of sputtering and annealing up to 873 K; 50 nm × 50 nm, V_s = -3.00 V, I_t = 100 pA, rms-R = 0.34 nm. STM was performed at 4.6 K.

Fig. 10A.6a and b depict the surface of Ge-doped HVPE GaN $(000\bar{1})$ after four cycles of sputtering (10-20min at ≈ 400K, $I_{emission}$ ≈ 11.0µA, ≈ 0.007-0.013 C, $E_{sputtering}$ = 1 keV) and annealing (at 643-823 K for 10-30 min). The surfaces appear rough, lacking atomically flat areas, thereby precluding atomic resolution. The rms roughness is around 0.21 nm for Fig.

10A.6a, similar to the surface roughness before cleaning. Therefore, based on these findings and previous XPS results, the surface is not completely cleaned by four cycles of sputtering and annealing up to 823 K. Subsequently, the sample undergoes further cleaning with three cycles of sputtering (30 min, ~0.020 C) and annealing (853-873 K for 60 min). As depicted in Fig. 10A.6c and d, these seven cleaning cycles result in an increased surface rms roughness exceeding 0.5 nm, accompanied by surface faceting and the formation of larger clusters and crystallites.

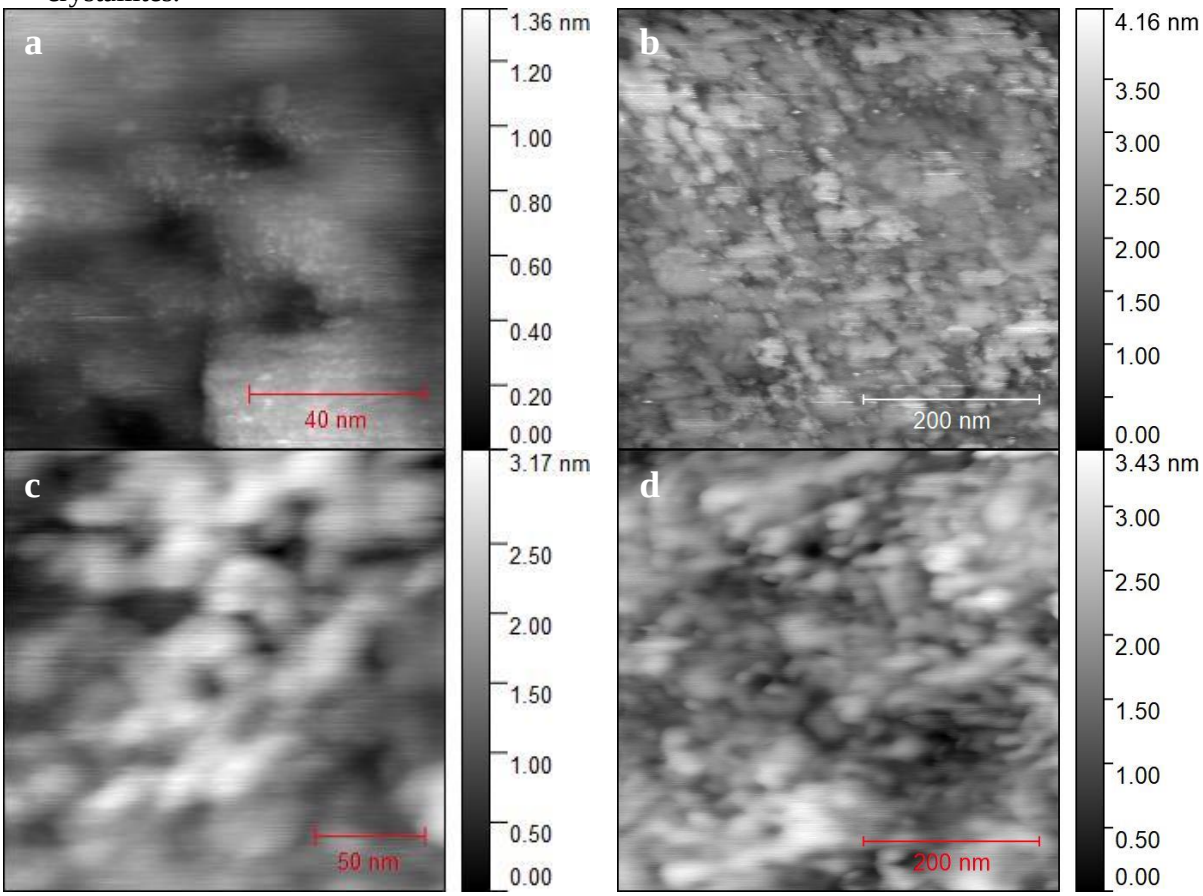

Fig. 10A.6. STM images of Ge-doped free-standing HVPE GaN $(000\bar{1})$ after cleaning by four cycles of sputtering and annealing up to 823 K; (a) 100 nm × 100 nm, V_s = -3.00 V, I_t = 100 pA, rms-R = 0.21 nm and (b) 500 nm × 500 nm, V_s = -5.00 V, I_t = 2 nA, rms-R = 0.49 nm. STM images of Ge-doped HVPE GaN $(000\bar{1})$ after three additional cycles of sputtering and annealing up to 873 K; (c) 200 nm × 200 nm, V_s = -3.00 V, I_t = 20 pA, rms-R = 0.59 nm. (d) 500 nm × 500 nm, V_s = -3.00 V, I_t = 20 pA, rms-R = 0.56 nm. STM was performed at liquid nitrogen (77 K) temperature.

Ammonia Annealing of the Surface of GaN Samples

For various sequences of experiments in Table. S1, overview XPS scans of a Ge-doped HVPE GaN $(000\bar{1})$ are shown in Fig. 10A.7a, b and c for normal emission and grazing emission XPS by Mg Kα radiation (1253.6 eV) and normal emission XPS by Al Kα radiation (1486.6), respectively. It is important to avoid water and oxygen in the UHV chamber to prohibit the formation of N-O bonds, reducing the efficiency of the GaN formation on the surface. Using a cold trap and titanium sublimation pump (TSP) with liquid nitrogen cooling significantly helps to remove the reactive oxygen species in the chamber.

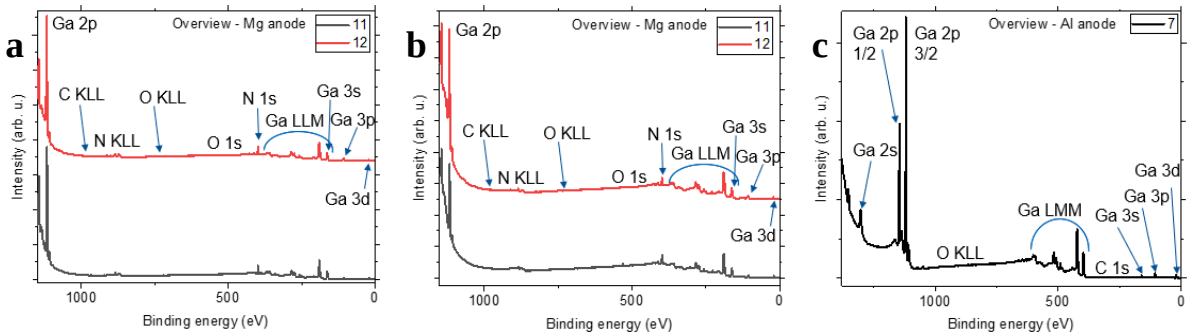

Fig. 10A.7. (a) Normal emission and (b) grazing emission XPS overviews of the Ge-doped HVPE GaN $(000\bar{1})$ surface using Mg Kα radiation, and (c) normal emission XPS overview using Al Kα radiation for different experiments detailed in Table 10A.1.

Fig. 10A.8 shows the ratio of XPS peaks between N 1s (GaN component) to Ga 2p for normal and grazing (70°) emission XPS using Mg Kα radiation (1253.6 eV) for different experiments shown in Table S1. In this figure, simply the ratio of the peaks area without any cross-section, mean free path and analyzer transfer function corrections is displayed.

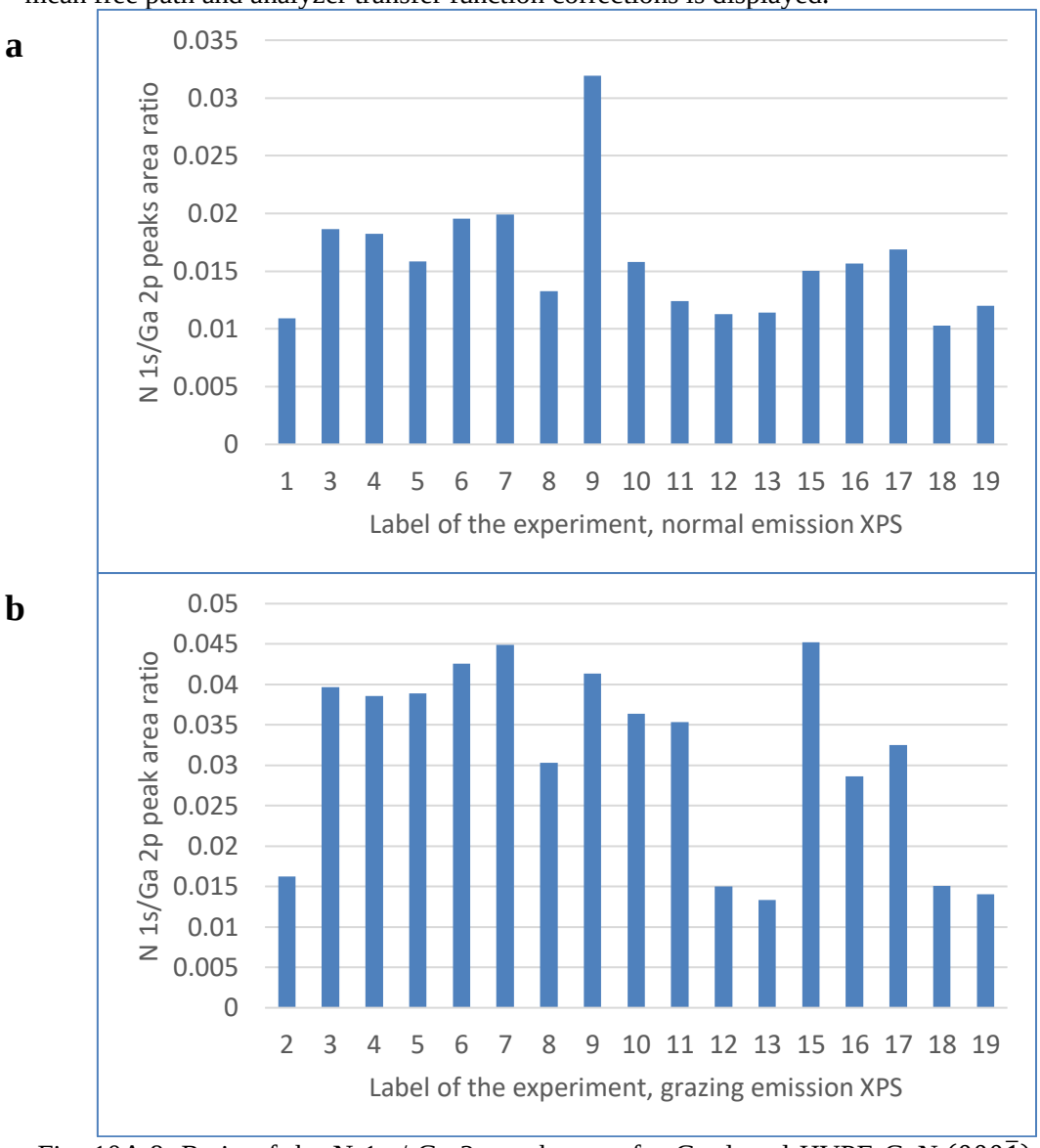

Fig. 10A.8. Ratio of the N 1s / Ga 2p peak areas for Ge-doped HVPE GaN $(000\bar{1})$ using (a) normal emission and (b) grazing angle emission XPS by Mg Kα radiation, before or after

annealing at 950K for 20 minutes in the presence of ammonia with and without electron bombardment for different experiments shown in Table 10A.1.

Fig. 10A.9a, b display normal emission and grazing emission narrow region scan XP spectra, respectively, for Ge-doped HVPE GaN $(000\bar{1})$ N 1s using Mg kα radiation, corresponding to different experiments categorized in Table S1.

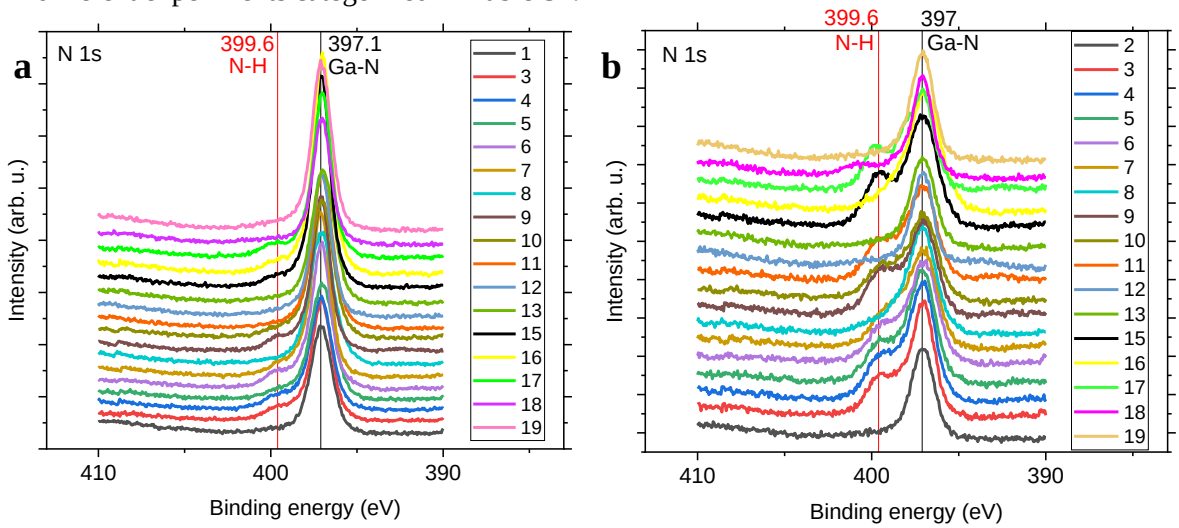

Fig. 10A.9. (a) Normal emission and (b) grazing angle emission narrow region XPS spectra of Ge-doped HVPE GaN $(000\bar{1})$ N 1s using Mg Kα radiation, corresponding to different experiments shown in Table. 10A.1.

Notably, Fig. S10a and b prove the absence of C atoms on the surface and in the bulk of HVPE GaN (0001), confirming the cleanness of the surface.

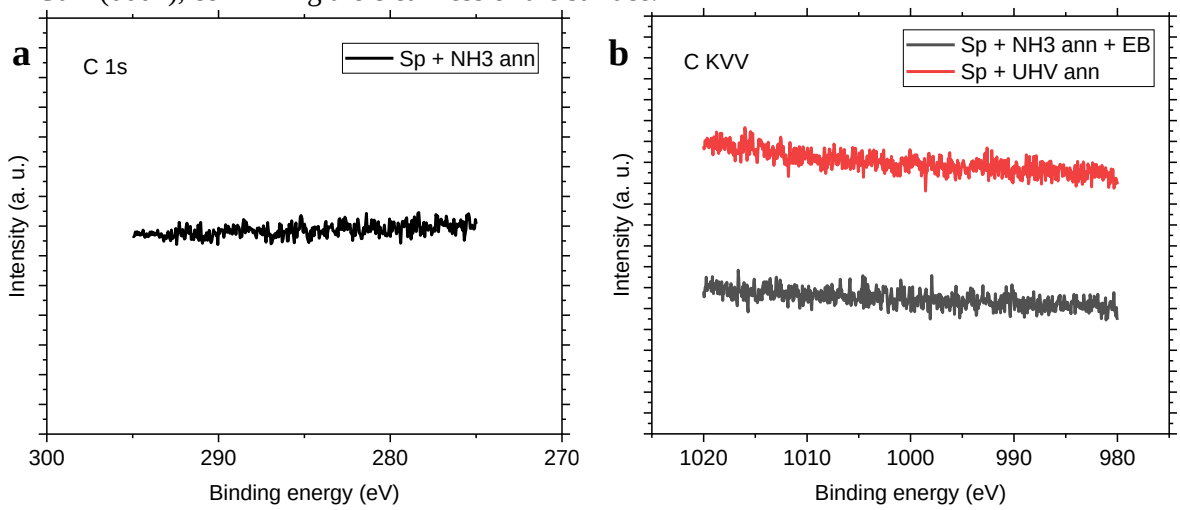

Fig. 10A.10. Normal emission and grazing angle emission narrow region XPS spectra of (a) Ge-doped HVPE GaN $(000\bar{1})$ for C 1s with Al Kα radiation and (b) C KVV Auger region with Mg Kα radiation, respectively. The abbreviations Sp, UHV, ann, NH3, and EB refer to sputtering, ultra-high vacuum, annealing, ammonia and electron bombardment, respectively.

Fig. 10A.11 and Fig. 10A.12 show the Ge-doped HVPE GaN $(000\bar{1})$ surface after ammonia annealing together with and without electron bombardment. In Section 3.5.1 (Fig. 10A.2), we have shown that the GaN surface decomposition starts at temperatures higher than 1000 K, leading to a significant faceting and changing of the color of the substrate. On the other hand, in this experiment (Fig. 10A.11e and f) we observed that annealing the sample to temperatures higher than 1000 K in the presence of ammonia gas in the chamber does not lead to significant GaN decomposition, faceting and changes in crystal color.

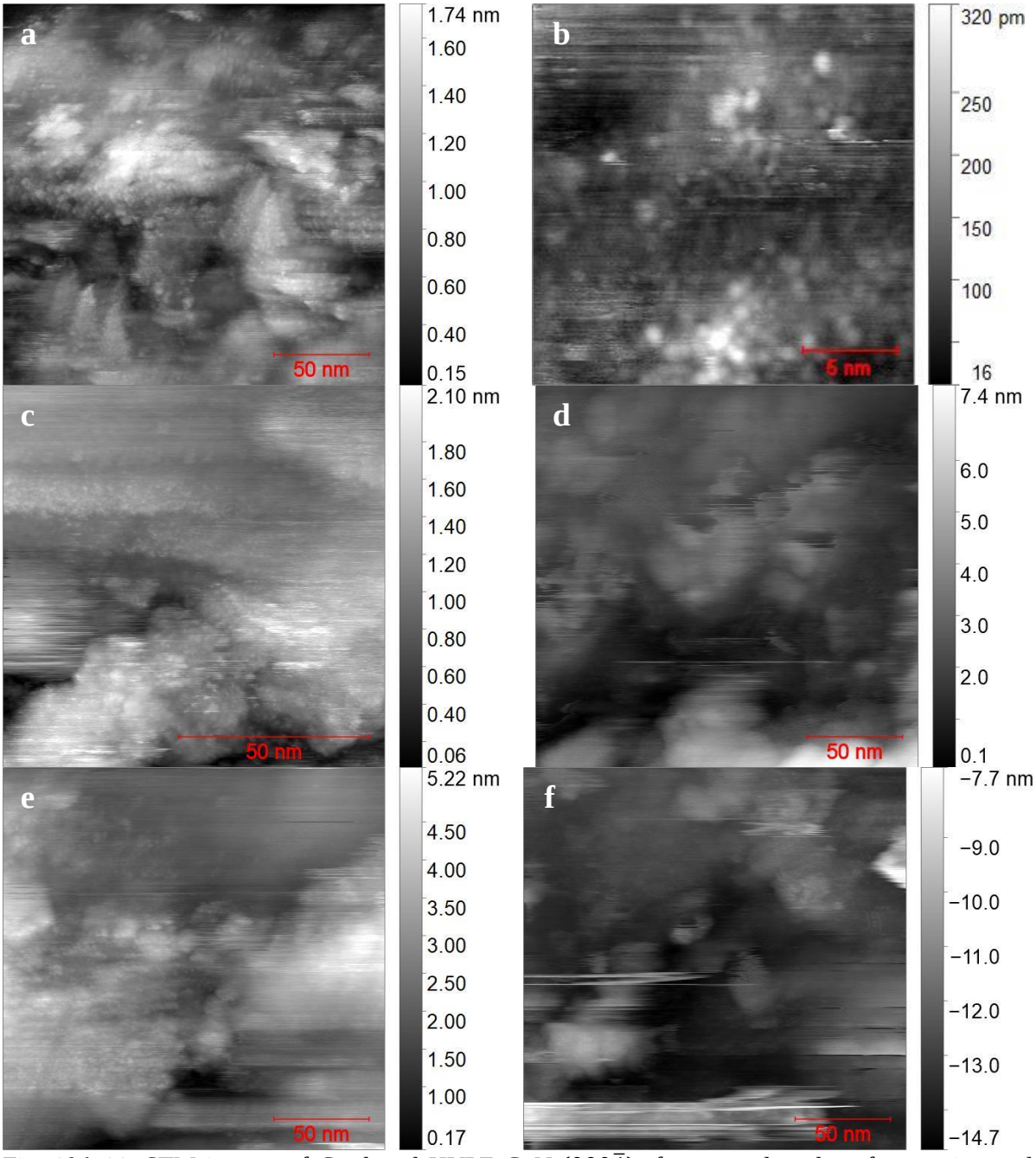

Fig. 10A.11. STM images of Ge-doped HVPE GaN $(000\bar{1})$ after several cycles of sputtering and ammonia annealing up to 923 K without electron bombardment; (a) 200 nm × 200 nm, V_s = -3.00 V, I_t = 100 pA, rms-R = 0.28 nm and (b) another region of the same sample; 200 nm × 200 nm, V_s = -3.00 V, I_t = 100 pA, rms-R = 0.28 nm. STM images of Ge-doped HVPE GaN $(000\bar{1})$ after one additional cleaning cycle of sputtering and ammonia annealing up to 973 K together with electron bombardment ($I_{emission}$ = 1.5 mA); (c) 100 nm × 100 nm, V_s = -3.00 V, I_t = 100 pA, rms-R = 0.33 nm and (d) another region of the same sample; 200 nm × 200 nm, V_s = -3.00 V, I_t = 100 pA, rms-R = 1.05 nm. STM images of Ge-doped HVPE GaN $(000\bar{1})$ after one more cleaning cycle of sputtering and ammonia annealing up to 1010 K together with electron bombardment ($I_{emission}$ = 1.5 mA); (e) 200 nm × 200 nm, V_s = -3.00 V, I_t = 100 pA, rms-R = 0.79 nm and (f) another region of the same sample; 200 nm × 200 nm, V_s = -3.00 V, I_t = 100 pA, rms-R = 1.10 nm. STM was done at 4.6 K.

In addition, we deposited TBB molecules on the surface of Ge-doped HVPE GaN $(000\bar{1})$ to investigate if we can image these molecules on the slightly flatter areas of the surface. As seen in Fig. 10A.12a and b, since the GaN nitride surface is not flat enough, we cannot image the

TBB molecules on the surface to learn more about these molecules. Our XPS intensity and resolution are also limited; however, the potential Ullmann coupling reaction can be understood more by monochromatic XPS by Synchrotron radiation. Nonetheless, the appearance of this rough surface can limit the Ullmann coupling and its potential applications. For investigation of the effect of the orientation of the GaN sample on the surface quality after ammonia annealing, we also imaged the Ge-doped free-standing HVPE GaN (0001) surface. As displayed in Fig. 10A.12c, d, e, and f, after ammonia annealing at different temperatures, the surface was still rough and no significant changes compared to the previous results were observed. Since the surface at the beginning was not atomically flat with rough areas and facets, an atomically flat surface is still not achieved. The epitaxial formation of GaN layers on the rough surface maintains the rough morphology.

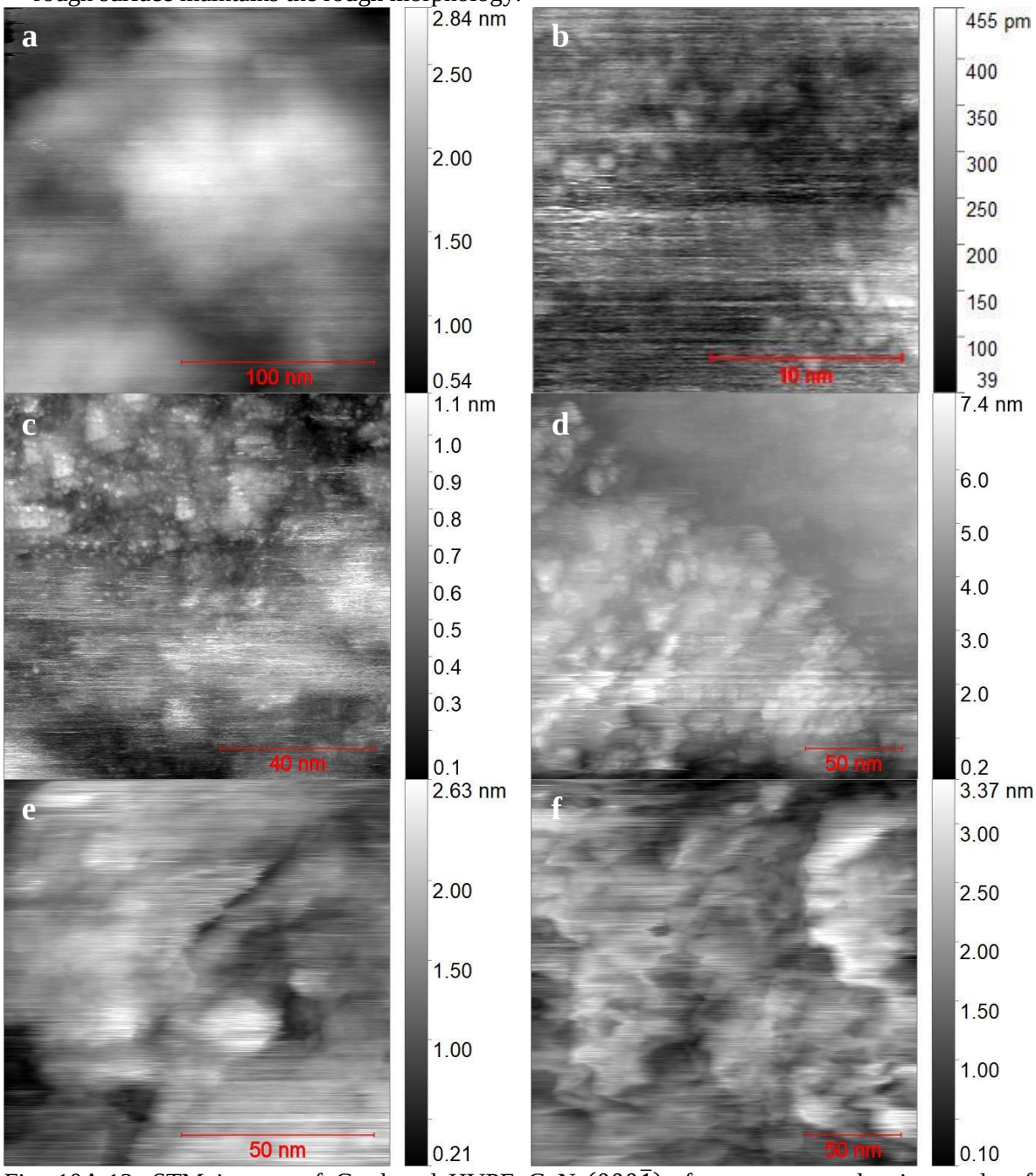

Fig. 10A.12. STM images of Ge-doped HVPE GaN $(000\bar{1})$ after one more cleaning cycle of sputtering and ammonia annealing up to 963 K together with electron bombardment ($I_{emission}$ = 1.5 mA) followed by deposition of TBB molecules on the surface at room temperature; (a) 200 nm × 200 nm, V_s = -3.00 V, I_t = 100 pA, rms-R = 0.45 nm and (b) another region of the same sample; 20 nm ×

20 nm, V_s = -3.00 V, I_t = 100 pA, rms-R = 0.07 nm. STM images of Ge-doped free-standing GaN (0001) after cleaning by seven cycles of sputtering (0.010 C) and annealing up to 900 K; (c) 200 nm × 200 nm, V_s = -3.00 V, I_t = 100 pA, rms-R = 0.18 nm and (d) another region of the same sample; 200 nm × 200 nm, V_s = -3.00 V, I_t = 100 pA, rms-R = 1.08 nm. (e) STM images of Ge-doped free-standing GaN (0001) after cleaning by one more cycle of sputtering (0.010 C) and annealing up to 933 K; 100 nm × 100 nm, V_s = -3.00 V, I_t = 100 pA, rms-R = 0.44 nm and (f) another region of the same sample; 200 nm × 200 nm, V_s = -3.00 V, I_t = 100 pA, rms-R = 0.55 nm. STM was done at 4.6 K.

In addition to HVPE GaN, different properties and aspects of MBE and AMMONO GaN also have also been investigated and compared in the literature. MBE GaN crystal surface preparation by UHV annealing at 800 ˚C was reported by Lamnet et al. [358]. Fig. 10A.13 shows STM images and STS of O-doped AMMONO GaN (0001) after four cycles of ammonia annealing (1.3 x 10^{-06} mbar) up to 950 K, without sputtering and electron bombardment, followed by the deposition of DBTP. The DBTP molecules are not distinguishable; however, the surface is much smoother than that of the HVPE GaN samples. STS data show a band gap of about 3.4 eV that is comparable with the literature [359-366]. STS measurements were conducted using a digital lock-in amplifier belonging to the JT-STM instrument, in which the bias voltage was modulated by an AC voltage with a frequency and amplitude of 1 kHz and 10 mV, respectively.

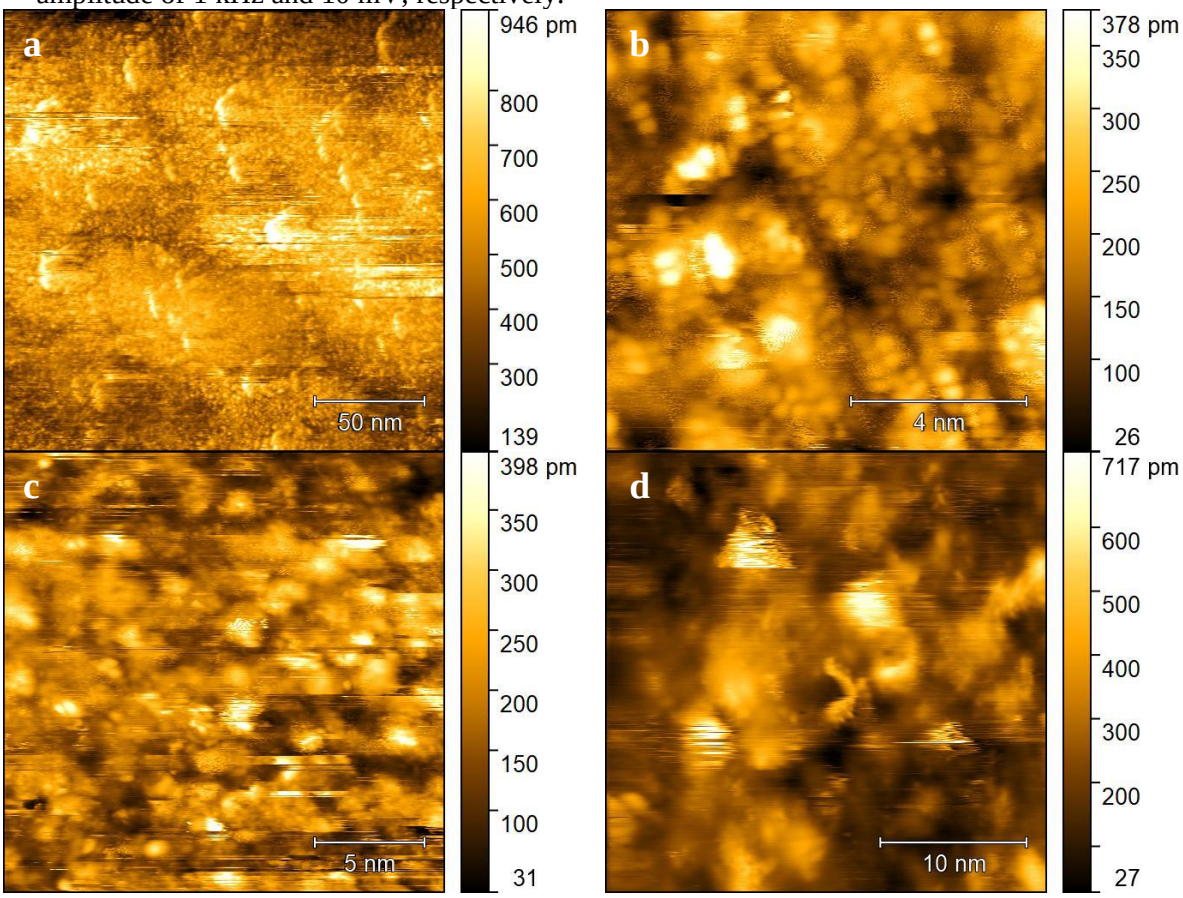

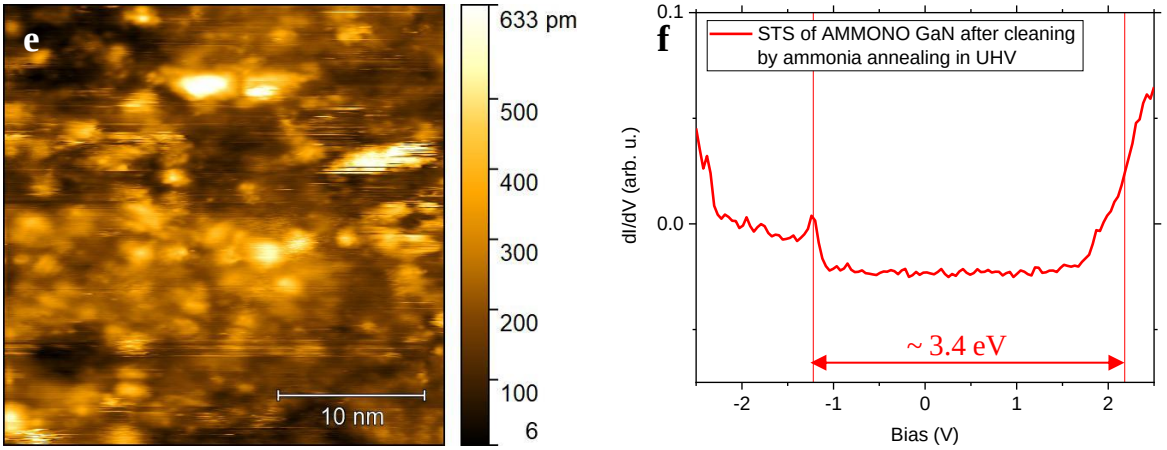

Fig. 10A.13. STM images of O-doped AMMONO GaN (0001) after four cycles of ammonia annealing up to 950 K without sputtering and electron bombardment. (a) 200 nm × 200 nm, V_s = -1.00 V, I_t = 100 pA, rms-R = 0.12 nm and (b) another region for the same sample; 10 nm × 10 nm, V_s = -1.00 V, I_t = 100 pA, rms-R = 0.06 nm. STM images of O-doped free-standing AMMONO GaN (0001) after deposition of DBTP molecules on the surface at room temperature and 10 min annealing at 200 ˚C. (c) 20 nm × 20 nm, V_s = -1.00 V, I_t = 100 pA, rms-R = 0.06 nm and (d) another region for the same sample; 30 nm × 30 nm, V_s = 1.50 V, I_t = 100 pA, rms-R = 0.10 nm. (e) 30 nm × 30 nm, V_s = 1.50 V, I_t = 100 pA, rms-R = 0.10 nm and (f) STS of O-doped AMMONO GaN (0001) . STM and STS were done at liquid N_2 temperature (77 K).

Deposition of TBB on HVPE GaN

In Fig. 10A.14, we observed two components of the C 1s peak after annealing the TBB monolayer on Si-doped HVPE GaN (0001) at 400 K. The main peak of the organic backbone before annealing was at ≈285.7 eV. After annealing at 400 K, two main components of the C 1s spectrum were observed at binding energies of 285.3 eV and 284.5 eV. The appearance of an asymmetric C 1s peak and an increase in two different components corresponding to C atoms of the organic backbones were observed in the literature when the polymerization and Ullmann coupling occurred on different surfaces [1-3]. Therefore, these results are promising for the observation of Ullmann coupling on the GaN surfaces. Fig. 10A.14a and b show the dehalogenation shift of the Br 3d core level and C KVV Auger peaks of a TBB sub-monolayer on Ge-doped HVPE GaN ($000\bar{1}$). Similar as for the Si-doped HVPE GaN (0001), both peaks shift to smaller binding energies due to the achievement of more negative charge during the debromination procedure. Fig. 10A.14c and d show Ga 2p and N 1s peaks for the same surface. By adsorption of TBB on the surface, three components appear for the Ga 2p core level peak. The peak at the lower binding energies is related to Ga atoms adsorbing molecules, the middle component is the GaN peak, and at larger binding energies the Ga 2p component related to brominated Ga atoms is observed. This third peak shifts to higher binding energies as the debromination is enhanced by increasing the annealing temperature. Fig. 10A.14e and f show Br 3d and C 1s narrow region XP spectra, respectively, corresponding to the deposition of ≈ 5 layers of TBB and heating to 400 K, 600 K, and 800 K, then cooling immediately. The results are compatible with the observed TPD measurements. In addition, Fig. 10A.14g-l show the component analyses of Br 3d after TBB deposition and annealing at different temperatures for 10 minutes.

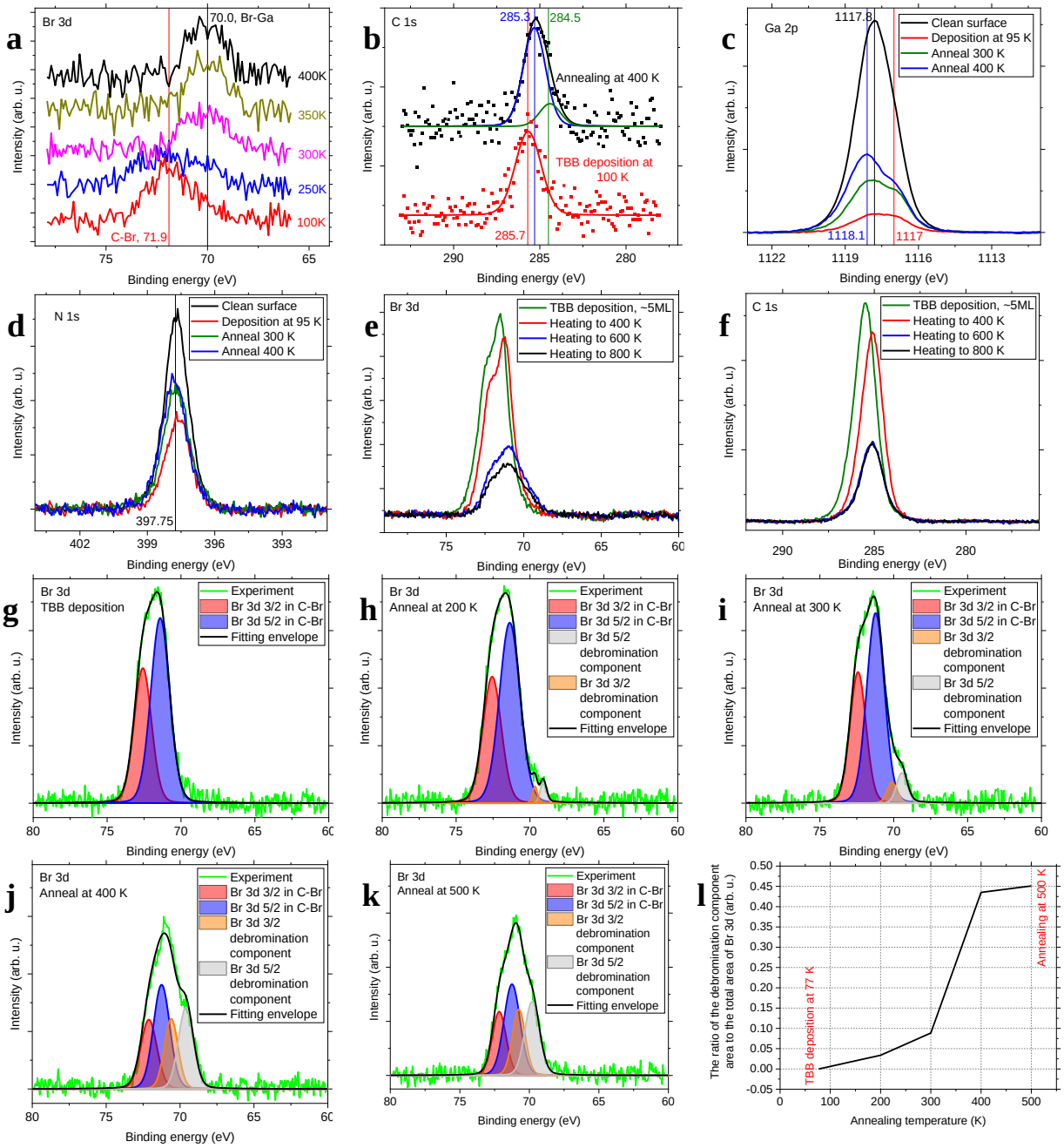

Fig. 10A.14. Zoomed-in XPS spectra of (a) Br 3d and (b) C 1s core-level regions after the deposition of TBB on Si-doped HVPE GaN (0001) and their evolution upon annealing. Zoomed-in XPS spectra of the (c) Ga 2p (coverage ≈ 1.7) and (d) N 1s (coverage ≈ 1.7) regions after the deposition of TBB on Ge-doped HVPE GaN ($000\bar{1}$) and their evolution upon annealing. (e) Br 3d and (f) C 1s narrow region XP spectra after the deposition of ≈5 layers TBB and heating to 400 K, 600 K, and 800 K, then cooling immediately, measured by irradiation energies of 1253.6 and 1486.6 eV, respectively. Component analyses of zoomed-in XPS spectra of Br 3d core-level regions after (g) deposition of a TBB monolayer, then annealing at (h) 200 K, (i) 300 K, (j) 400 K, and (k) 500 K for 10 minutes, measured with an X-ray energy of 1253.6 eV. (l) The ratio of the debromination component area to the total area of Br 3d shown in g-k versus the annealing temperature.

After the deposition of TBB molecules for 5 min (Fig. 10A.15b) and 10 min (Fig. 10A.15c) on Si-doped HVPE GaN (0001), LEED patterns did not change, and an attenuated pattern with (1×1) periodicity was observed. This observation reinforces the conclusion that the surface is rough, and only the LEED pattern related to the sub-surface crystalline layers is detected. After 15 min of deposition, the LEED pattern completely disappeared, showing that the thickness of

the deposited organic layer is greater than the electron inelastic mean free path in the multilayer regime. Therefore, considering the inelastic mean free path of electrons and our XPS studies, we investigated a 10 min deposition of TBB on HVPE GaN (0001) to achieve a near monolayer deposition.

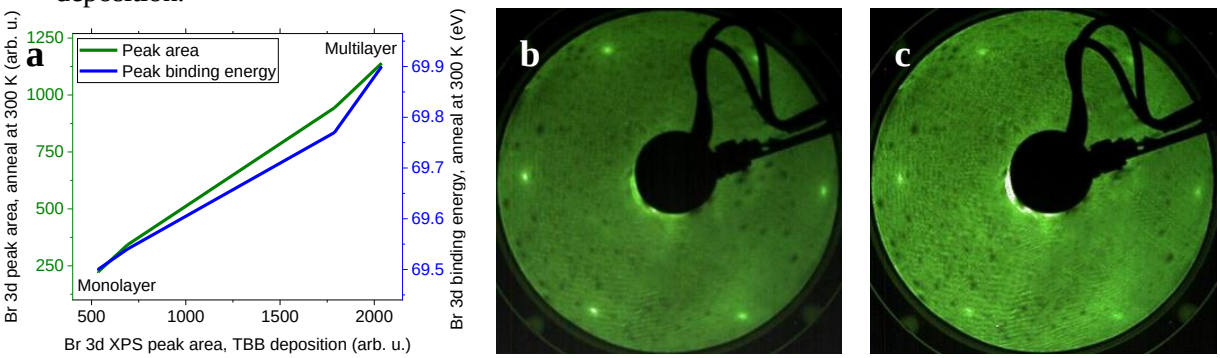

Fig. 10A.15. (a) The ratio of the Br 3d XPS peak area right after deposition of different TBB coverages on the Si-doped HVPE GaN (0001) surface with respect to the shifted Br 3d peak area due to debromination by 15 minutes annealing at 300K and bonding the bromine atoms to the Ga atoms at the surface. In addition, the peak binding energy of the Br 3d XPS narrow region scan versus increase in deposited TBB coverage is shown. (1×1) LEED patterns of Si-doped free-standing HVPE GaN (0001) after (b) 5 min and (c) 10 min deposition of TBB on the as-cleaned surface.

Depositions of different elements on GaN have been reported in the literature [367]. While the reaction of bromine (Br) with the GaN surface in solutions has been reported [368, 369], bromine deposition on GaN in UHV has not been investigated. Fig. 10A.16a displays the mass spectrometry of TBB molecules evaporated from a crucible of an OMBE at approximately 200 °C. The largest peak is related to the parent molecules' mass at 543 amu. The other peaks correspond to Br isotopes at 79 and 81 amu and benzene rings at around 75 amu. In addition, two other large peaks at 151 and 302 amu are observed that are related to debrominated molecules containing a benzene ring bonded to one and three phenyl rings, respectively. These results prove that the molecule batch has negligible impurities.

Fig. 10A.16c indicates the TPD of about 0.8 layers of TBB deposited on Ge-doped HVPE GaN $(000\bar{1})$ right after annealing at 950 K (black) or sputtering by Ne ions (red). Sputtering makes the surface rougher, leading to the formation of deeper holes and rougher hillocks, resulting in a reduction of the coverage by deposition at the same OMBE crucible, sample temperatures, and deposition time. However, as the coverage decreased due to roughening from sputtering, the ratio of separated bromine to the total amount of bromine increased. In addition, the surface roughening and the presence of more edges lead to a decrease in the activation energy of molecules to diffuse to edges and a reduction in desorption temperature.

Fig. 10A.16d and e show the TPD of parent mass (543 amu) and bromine atoms (79-81 amu) of TBB molecules for different coverages, respectively. By increasing the coverage, the desorption peak temperature increases, indicating the zero-order desorption [370-372] of TBB on Ge-doped HVPE GaN $(000\bar{1})$. There is a significant decrease in desorption peak temperature when moving from the multilayer desorption to near monolayer desorption, indicating that the interactions between molecules are stronger than those between molecules and the rough Ga-rich Ge-doped GaN $(000\bar{1})$ surface. Since the molecules at the surface polymerize due to Ullmann coupling, the excess molecules in the monolayer became more unstable, reducing the desorption energy and peak temperature compared to the multilayer regime. The larger the coverage (near monolayer regime), the more molecules are present on the surface to form larger TBB polymers, desorbing at higher temperatures due to difficult diffusion on the rough surface. For multilayer spectra, a smaller peak is observed at the lower temperatures, having the same edges as the monolayer desorption peak reducing by increasing coverage. This phenomenon could be due to the presence of more TBB on the surface and a longer time to diffuse and react for higher coverage multilayers to form larger polymers. Therefore, by increasing the multilayer thickness, less unstable and smaller polymers and

clusters stay on the surface, still desorbing from the surface at lower temperatures compared to the multilayer regime due to the rough and nonuniform surface. A second reason for the reduction of the smaller peak by increasing the coverage is that the larger the coverage of the multilayer, the molecular epilayer becomes more uniform on the surface, and fewer small polymers and clusters can desorb before the multilayer regime. The other interesting observation is that by reducing the coverage from about 1.7 to 0.6 layer, the reduction in the parent mass area is more significant than the bromine mass area. This observation displays that for sub-monolayers, there are more debrominated molecules staying on the surface which, could be another indication for Ullmann coupling and polymerization of the debrominated molecules at the surface.

Surprisingly, in Fig. 10A.16e, we observed that the high-temperature tail area of the Br (79-81 amu) TPD peak and the Br-to-Ga ratio (X) increase with the multilayer thickness, while the tail is expected to be saturated for thicker multilayers. One reason could be that, in addition to bromine atoms in $GaBr_X$ products desorbed at higher temperatures, thicker multilayers provide more bromine-contained molecules on the surface and, allowing for a longer time for diffusion and reaction of the molecules on the surface to form larger polymers that desorb at higher temperatures. Another reason could be that a thicker multilayer provides more bromine atoms on the surface and, allowing for more on-surface debromination during multilayer desorption and increasing the stochiometric ratio of Br-to-Ga in desorbed $GaBr_X$ products (see Fig. 3.6.).

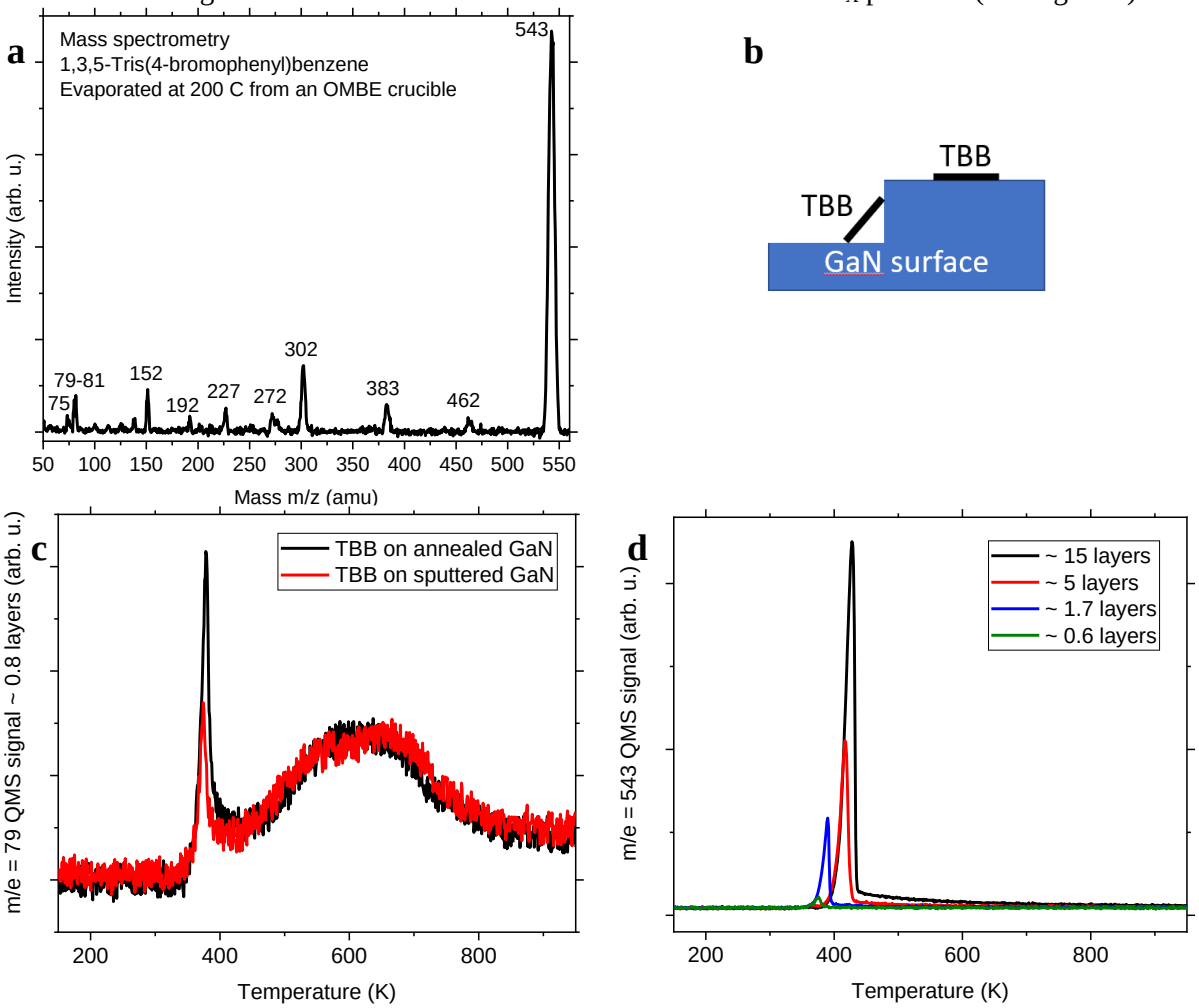

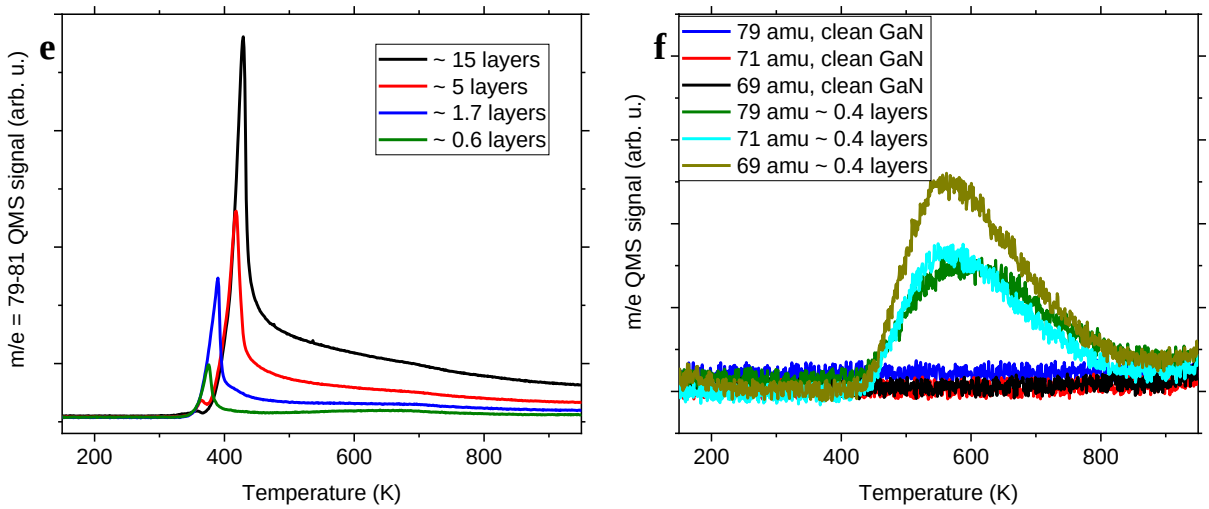

Fig. 10A.16. (a) mass spectrometry of TBB molecules evaporated from a crucible of an OMBE at 200 °C. (b) Side-view schematic of TBB molecules adsorbed on the HVPE GaN $(000\bar{1})$ surface. TPD of (c) ~0.8 layers TBB molecules on Ge-doped HVPE GaN $(000\bar{1})$ and multilayers of TBB molecules on HVPE GaN related to masses of (d) 543 and (e) 79-81 amu. (f) TPD spectra of Ga (69 and 71 amu) and Br (79 amu) for clean GaN and a TBB submonolayer on Ge-doped HVPE GaN $(000\bar{1})$.

Appendix B: Post-Synthesis of Cu_2N Monolayers on Cu (111) from Copper Oxide Films and Their Decoupling Effects

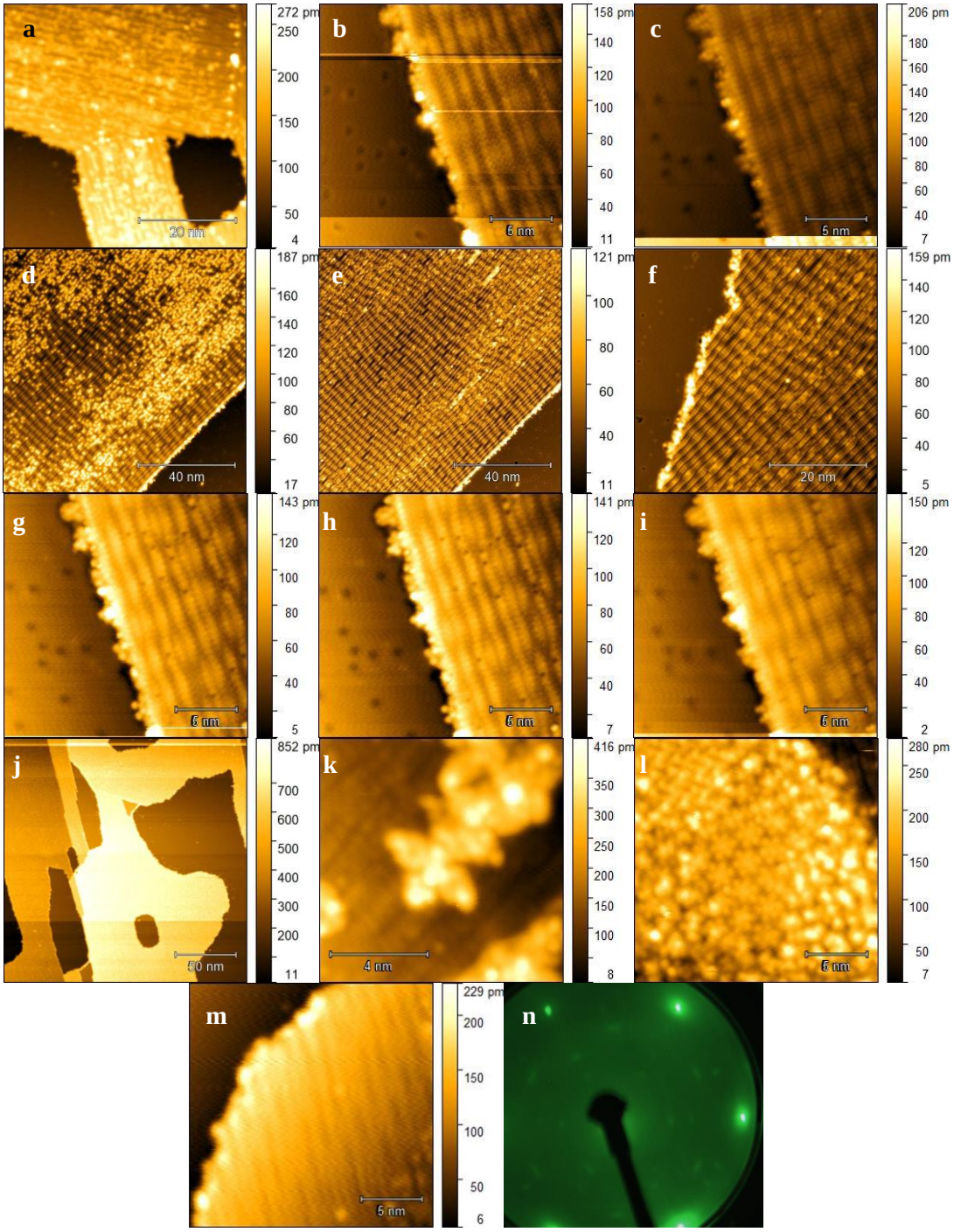

Fig. 10B.1. Bias-dependent STM measurements at LHe temperature (≈ 4.6 K) of Cu_2N sub-monolayers on Cu (111) after dosing with 10^{-7} mbar NH_3 in UHV; (a) 50 nm × 50 nm, V_s = 2 V, I_t = 1 nA, rms-R = 0.06 nm. (b) 20 nm × 20 nm, V_s = 1 V, I_t = 300 pA, rms-R = 0.02 nm. (c) 20 nm × 20 nm, V_s = -0.5 V, I_t = 300 pA, rms-R = 0.03 nm. (d) 100 nm × 100 nm, V_s = 1.5 V, I_t = 100 pA, rms-R = 0.03 nm. (e) 100 nm × 100 nm, V_s = 1 V, I_t = 100 pA, rms-R = 0.02 nm. (f) 50 nm × 50 nm, V_s = 1 V, I_t = 100 pA, rms-R = 0.02 nm. (g) 20 nm × 20 nm, V_s = -1 V, I_t = 300 pA, rms-R = 0.02 nm. (h) 20 nm × 20 nm, V_s = -2 V, I_t = 300 pA, rms-R = 0.02 nm. (i) 20 nm × 20 nm, V_s = -2.5 V, I_t = 300 pA, rms-R = 0.02 nm. (j) 200 nm × 200 nm, Vs = 4 V, It = 1 nA, rms-R = 0.20 nm. (k) STM of DAPPor molecules on a Cu_2N sub-monolayer on Cu (111); 10 nm × 10 nm, V_s = -0.5 V, I_t = 50 pA, rms-R = 0.08 nm. (l) STM of single and double layers of DAPPor assembly on Cu (111); 20 nm × 20 nm, V_s = 0.5 V, I_t = 50 pA, rms-R = 0.04 nm. (m) A Cu_2N island on Cu (111); V_s = 2 V, I_t = 1 nA, rms-R = 0.05 nm. (n) LEED pattern (electron energy: 60 eV) of an intermediate oxynitride submonolayer on Cu (111), resembling a coexistence of $\left(\sqrt{3} \times \sqrt{3}\right)R30°$ and additional superstructures [248].

Cu 2P peak binding energy shifts to a higher binding energy upon the formation of copper nitride [24]. Du and coworkers studied the influence of oxygen inclusion on the microstructure and thermal stability of copper nitride thin films. They produced copper oxynitride by reactive magnetron sputtering in the presence of nitrogen and oxygen gases. At lower oxygen contents (< 10%), XRD does not show copper oxide, but only copper nitride. The presence of Cu-O bonds reduces the copper nitride lattice and increases the compactness of copper nitride on weakly bonded copper nitride crystallites. Copper oxynitride decomposes at temperatures above 650 K [66]. Mavridou and coworkers studied the formation of copper oxide (Cu_2O, CuO) phases on copper nitride thin films by resonance Raman spectroscopy [67].

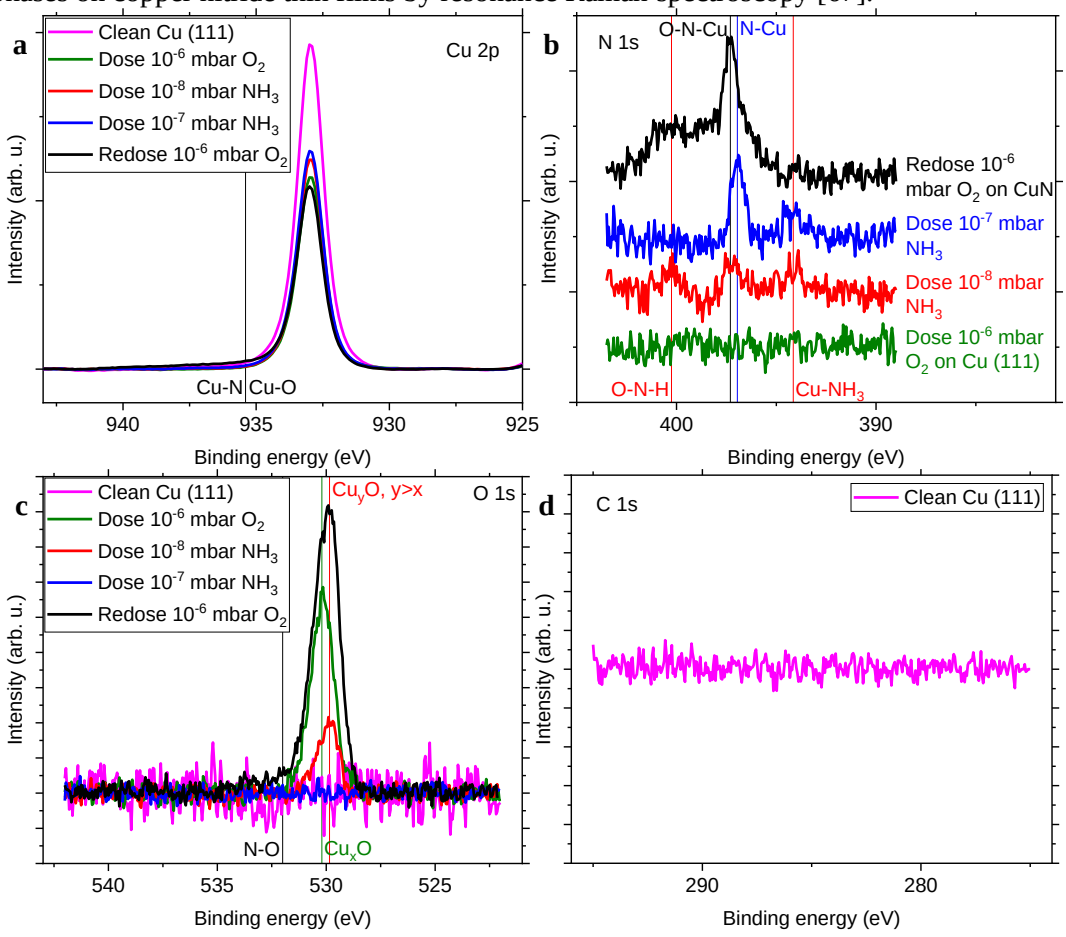

Fig. 10B.2. Zoomed-in XPS spectra of (a) Cu 2p, (b) N 1s, and (c) O 1s after copper surface cleaning and fabrication of copper oxide and nitride films (coverage ≈ 0.5 monolayer (ML)), and (d) C 1s after Cu (111) surface cleaning.

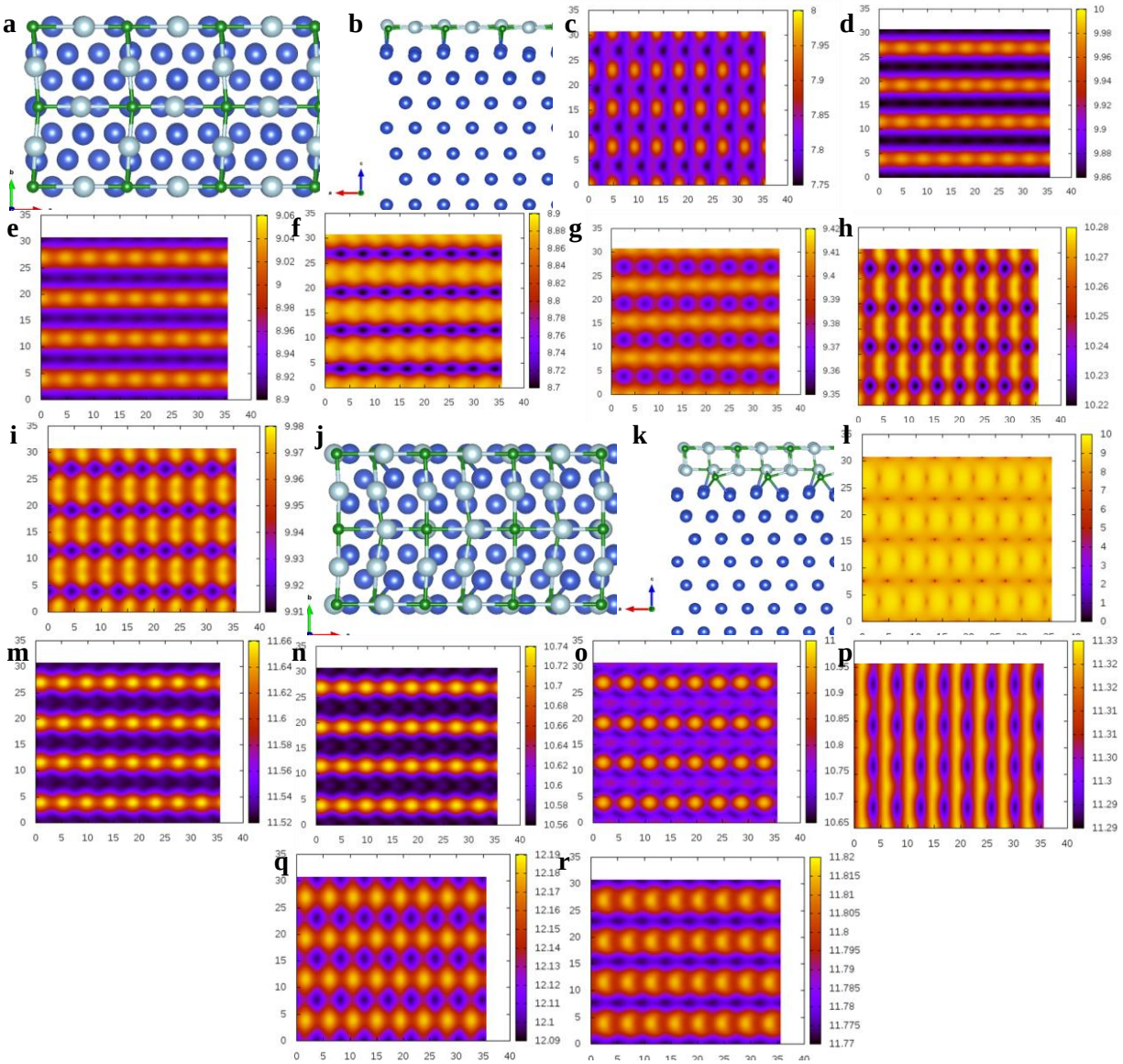

Fig. 10B.3. DFT simulation, bias-dependent STM images of Cu_2N on Cu (111), represented in (a) and (b). The blue, white, and green spheres represent Cu atoms in Cu (111), Cu atoms in reconstructed top layer, and N atoms, respectively. STM images simulated at various bias voltages and currents: (c) V = -0.10 V, I = 1 nA. (d) V = 1.00 V, I = 100 pA. (e) V = 1.00 V, I = 1 nA. (f) V = -0.50 V, I = 300 pA. (g) V = 2.00 V, I = 1 nA. (h) V = 4.00 V, I = 1 nA. (i) V = -2.5 V, I = 300 pA. DFT simulation of bias-dependent STM images of Cu_2N on Cu (111) shown in (j) and (k). Bias voltages and tunneling currents are as follows: (l) V = -0.10 V, I = 1 nA. (m) V = 1.00 V, I = 100 pA. (n) V = 1.00 V, I = 1 nA. (o) V = -0.50 V, I = 300 pA. (p) V = 2.00 V, I = 1 nA. (q) V = 4.00 V, I = 1 nA. (r) V = -2.5 V, I = 300 pA.

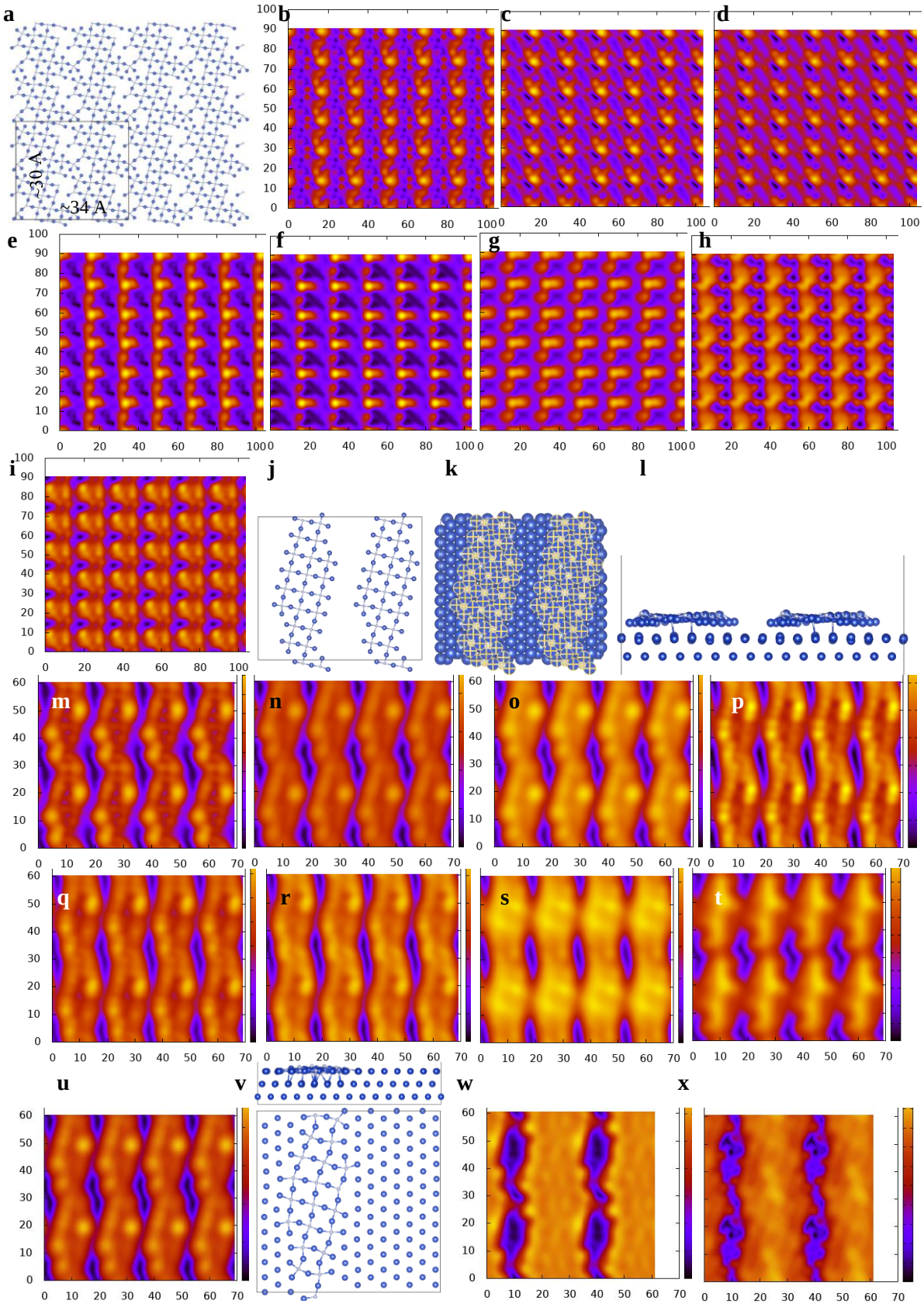
a
~30 A
~34 A
b
c
d
e
f
g
h
i
j
k
l
m
n
o
p
q
r
s
t
u
v
w
x

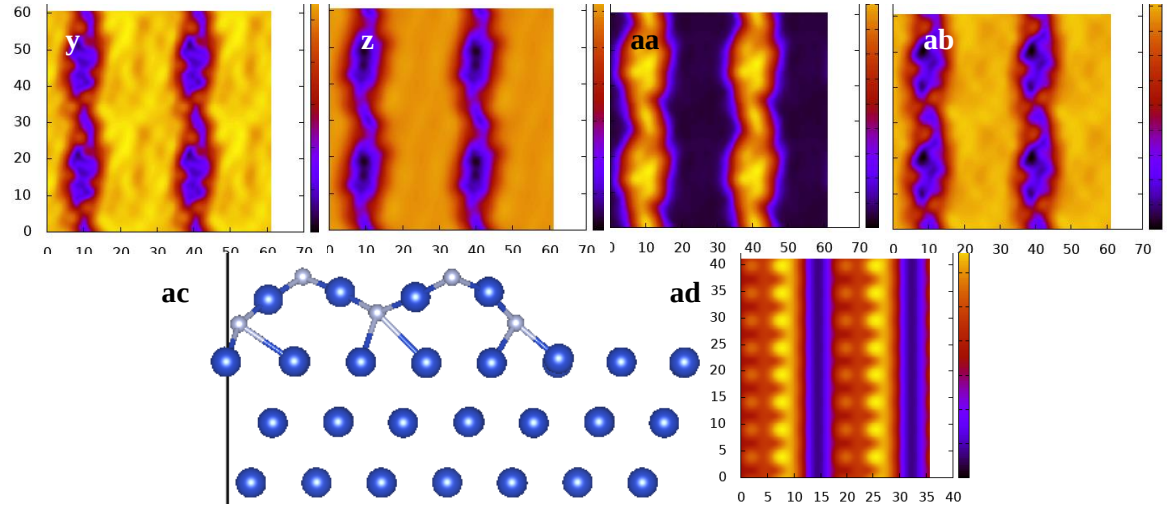

Fig. 10B.4. DFT simulations of (a) Cu_2N elongations on Cu (111) after reconstruction and relaxation of the top atomic layer to Cu (100) superstructure. DFT model showing cracked Cu_2N elongations on Cu (111), with Cu atoms represented in blue and N atoms in gray. The work function for these DFT simulations is calculated to be 4.85 eV. DFT-simulated, bias-dependent STM images of the model shown in (a) at various bias voltages: (b) -1.0 V, (c) -2.0 V, (d) -2.5 V, (e) 1.0 V, (f) 2.0 V, (g) 2.5 V, (h) 3.0 V, and (i) 4.0 V. All at I_t = 1 nA. The scale unit is given in Å. DFT simulations of Cu_2N elongations: (j) Top view of free-standing Cu_2N elongations, (k) Cu_2N elongations on Cu (111), and (l) side view of the model shown in (k). Bias-dependent DFT-simulated STM images of four adjacent Cu_2N elongations on Cu (111), as modeled in (j-l), at the following bias voltages: (m) -0.5 V, (n) -2.0 V, (o) -4.0 V, (p) 0.5 V, (q) 1.0 V, (r) 2.0 V, (s) 3.0 V, (t) 4.0 V, and (u) -2.5 V. I_t = 0.1 nA. The scale unit is Å. (v) DFT models of top and side views of Cu_2N elongations embedded in the top atomic layer of Cu (111). Bias-dependent DFT-simulated STM images of three adjacent Cu_2N elongations on Cu (111), similar to the model shown in (v), at the following bias voltages: (w) 2.0 V, (x) -0.1 V, (y) -0.5 V, (z) 1.0 V, (aa) 4.0 V, and (ab) -2.5 V. I_t = 1 nA. (ac) DFT models of a side view of Cu_2N elongations buckled on the Cu (111) surface. Bias-dependent DFT-simulated STM images of two adjacent buckled Cu_2N elongations on Cu (111), similar to the model shown in (ac), at the following bias voltages: (ad) 1.0 V, I_t = 1 nA. The scale unit is Å.

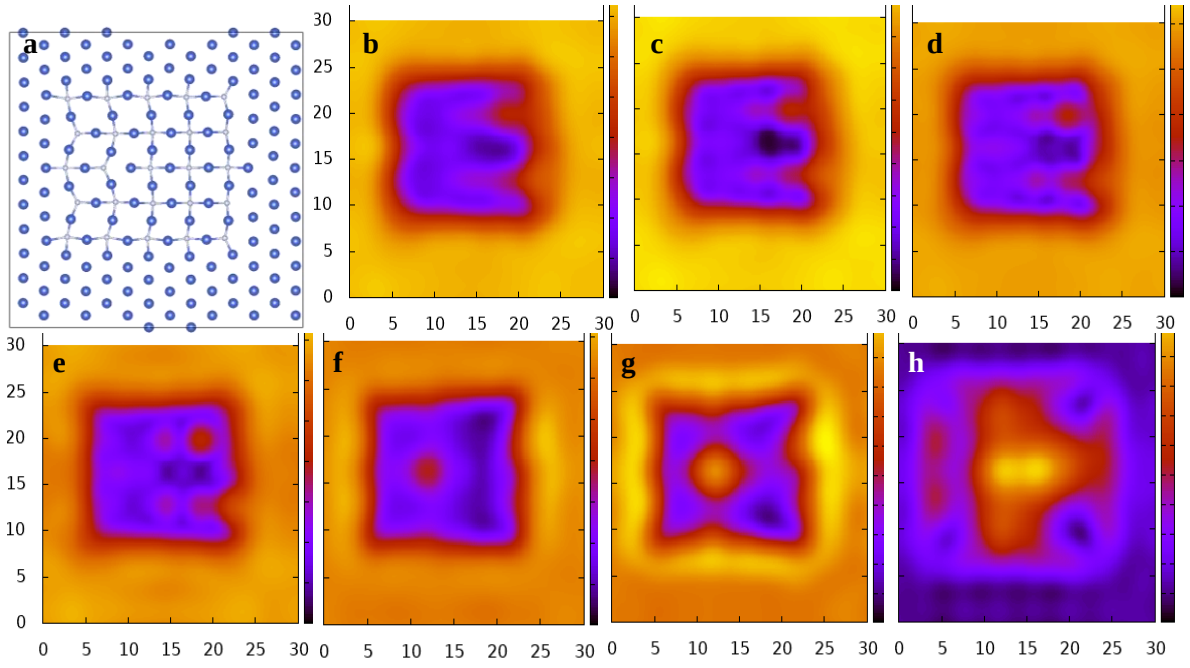

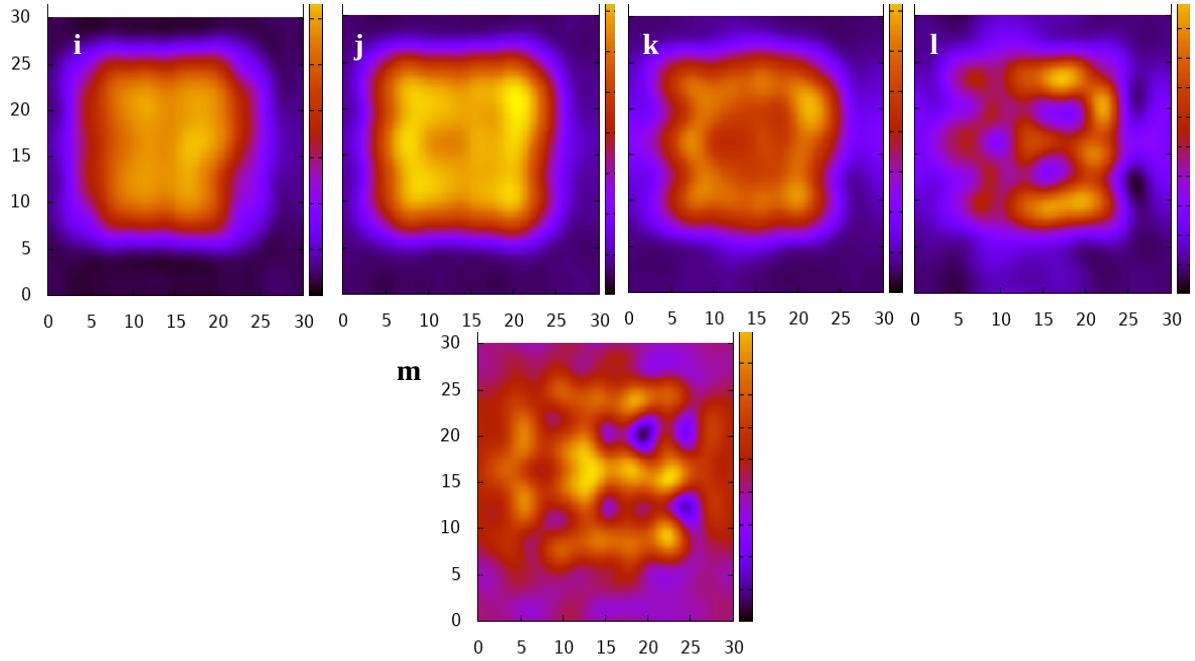

Fig. 10B.5. DFT simulations of (a) a Cu_2N island embedded within the top atomic layer of Cu (111), where Cu atoms in the top layer have been reconstructed to Cu (100), and some bonds were cleaved after relaxation. Cu and N atoms are represented by blue and gray spheres, respectively. DFT-simulated, bias-dependent STM images of the model in (a) at various bias voltages: (b) -2.0 V, (c) -1.5 V, (d) -1.0 V, (e) -0.5 V, (f) 2.0 V, (g) 2.5 V, (h) 3.0 V, (i) 3.5 V, (j) 4.0 V, (k) 4.5 V, (l) 5.0 V, and (m) 5.5 V. I_t = 0.5 nA. The scale unit is Å.

DFT simulation reveal that the Cu_2N islands rotated by 45˚, as shown in Fig. S6b, are more stable than those aligned parallel to the edges, depicted in Fig. S6a.

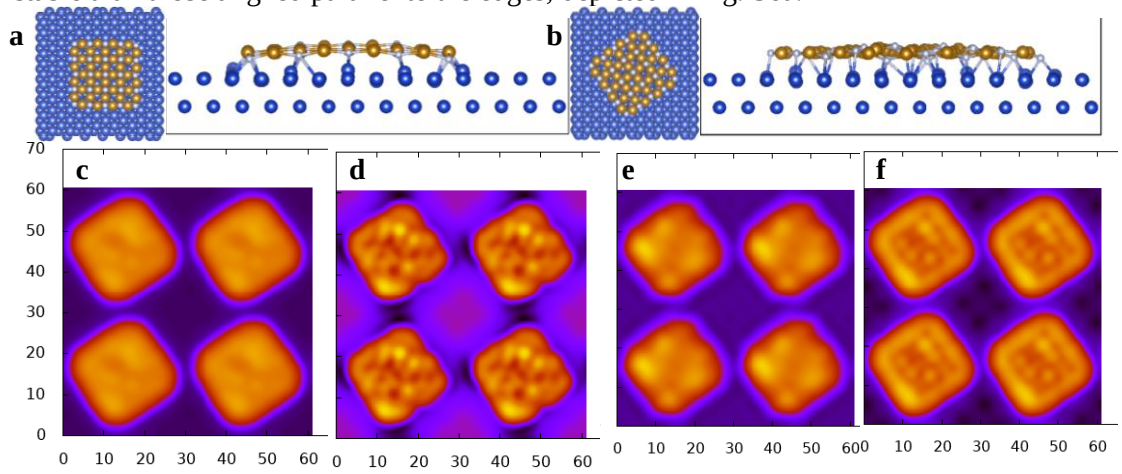

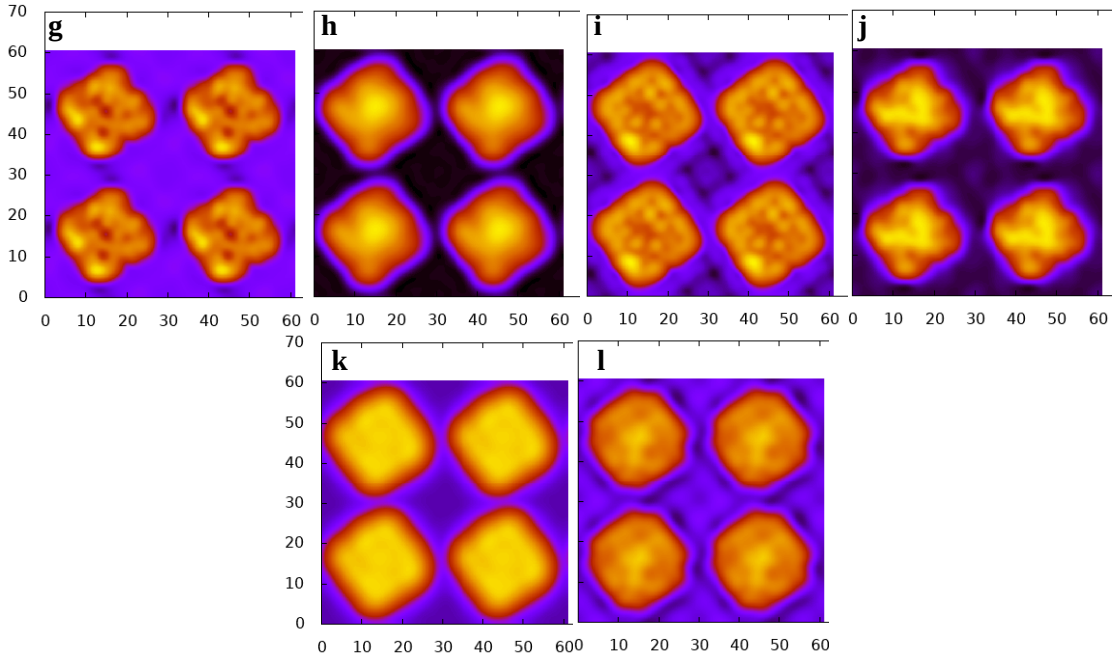

Fig. 10B.6. DFT simulations of (a) Cu_2N islands aligned parallel to the Cu (111) high density direction and (b) more stable Cu_2N islands rotated by 45˚. The substrates exhibit (7 × 12) periodicity across two atomic layers, containing a total 336 Cu atoms (blue spheres). The islands are composed of 40 Cu (orange spheres) and 25 N (gray spheres) atoms. DFT simulations of bias-dependent STM images of the structural model shown in (b) are presented for bias voltages of (c) -2.35 V, (d) 0.5 V, (e) 2.5 V, (f) -1 V, (g) 1 V, (h) 3 V, (i) -0.5 V, (j) 1.5 V, (k) 4V, and (l) 5 V. The scale unit is Å.

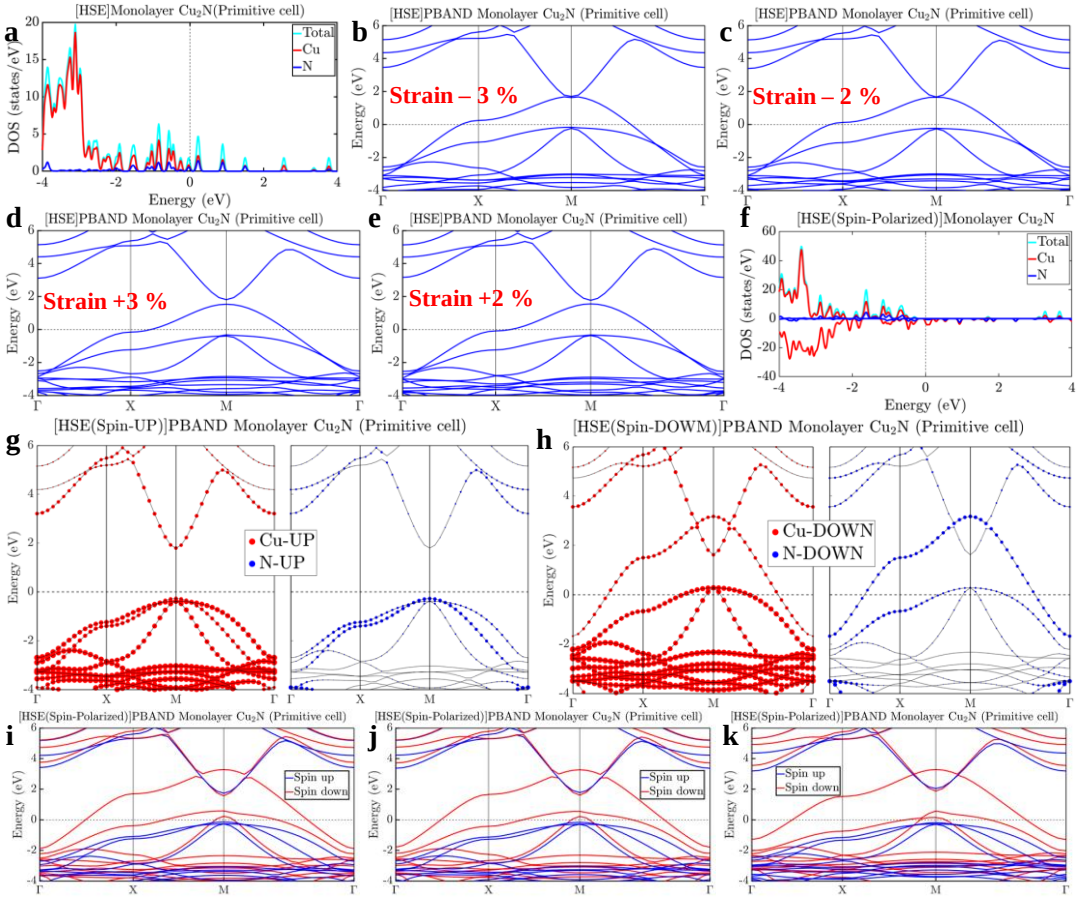

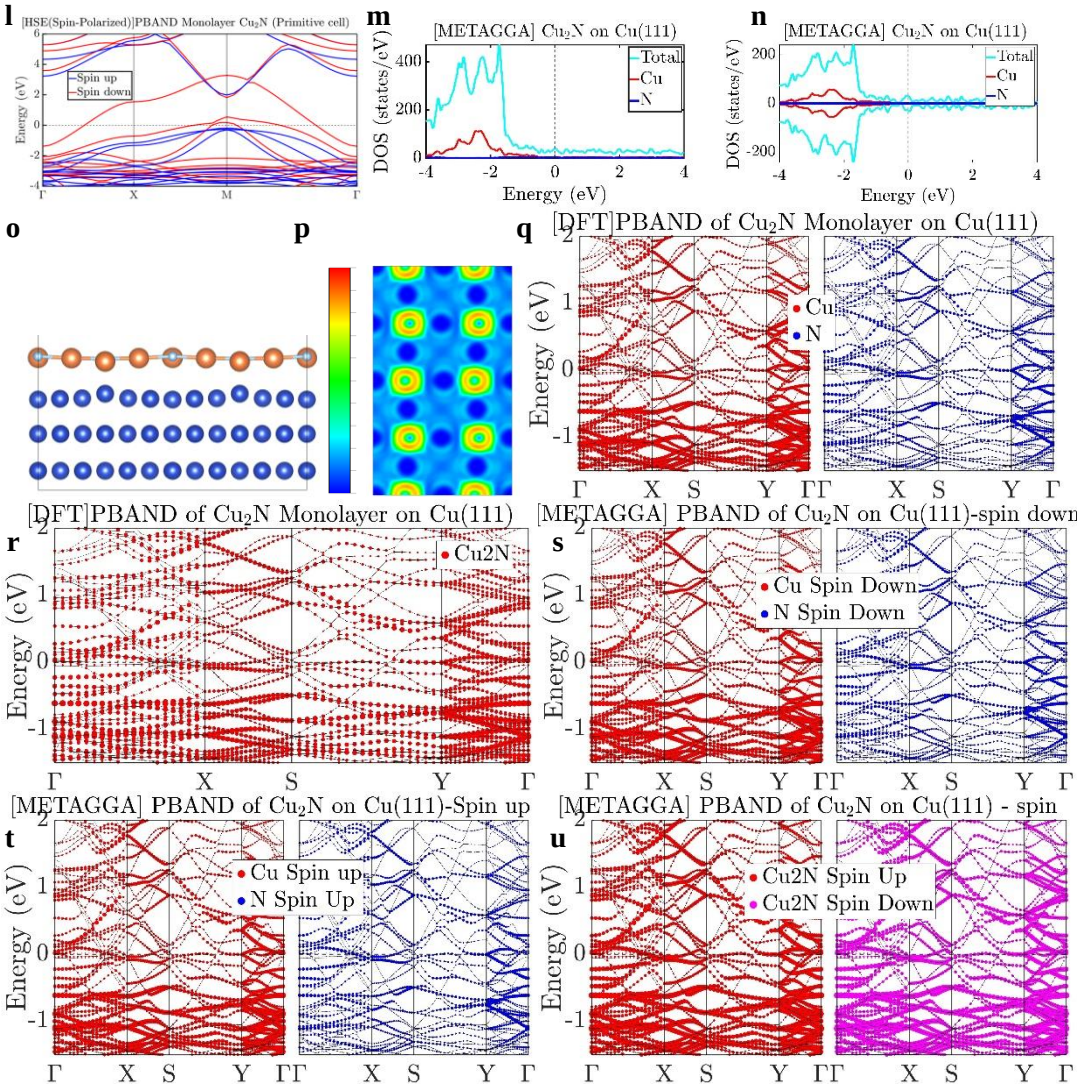

Fig. 10B.7. DFT simulations of (a) the projected density of states (PDOS) for a free-standing Cu_2N monolayer without strain. The band structure (BS) under (b) 3% and (c) 2% compression strains, and (d) 3% and (e) 2% expansion strains, were calculated using the Heyd-Scuseria-Ernzerhof hybrid functional (HSE) method without spin polarization. Spin-polarized DFT simulations of (f) PDOS and the corresponding BS are shown (g,h) without strain, together with BS under (i) 3% (Spin-UP: band gap ≈ 1.88 eV, Spin-DOWN: band gap = 0 eV), and (j) 2% (Spin-UP: band gap ≈ 1.94 eV, Spin-DOWN: band gap = 0 eV) compression strains. Expansion strains are analyzed in (k) 3% (Spin-UP: band gap ≈ 2.18 eV, Spin-DOWN: band gap ≈ 0.01 eV) and (l) 2% (Spin-UP: band gap ≈ 2.23 eV, Spin-DOWN: band gap ≈ 0.05 eV). DFT simulations of PDOS of Cu_2N on Cu (111) are provided (m) without and (n) with spin polarization. (o) Side-view schematic atomic model of the Cu_2N monolayer on Cu (111) (d_{Ads}= 2.00 Å) and (p) the electron localization function on atoms on the corresponding Cu_2N ML slice confirming the Cu-N covalent bonds. The BS of Cu_2N on Cu (111) is shown (q,r) without and (s,t,u) with spin polarization (Spin-UP: band gap ≈ 0.01 eV, Spin-DOWN: band gap = 0.02 eV, Total: band gap = 0.01 eV).

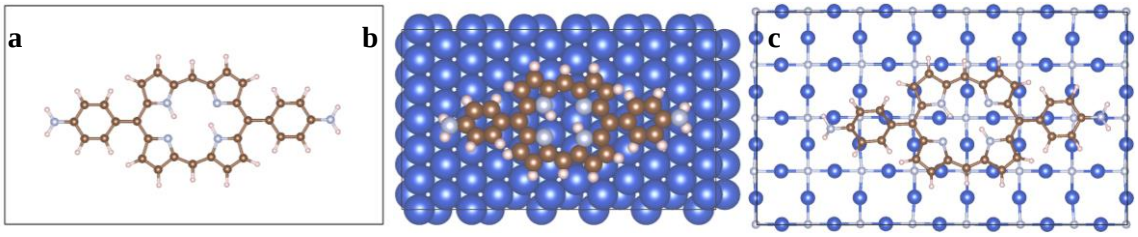

Fig. 10B.8. Schematic atomic models of (a) a free-standing DAPPor molecule, a DAPPor molecule on Cu (111), and (c) a DAPPor molecules on Cu_2N. These models were used for DFT simulations of PDOS to investigate the decoupling effect of the Cu_2N layer. The blue, gray, brown, and pink spheres represent Cu, N, C, and H atoms, respectively.

Fig. 10B.9 illustrates the coexistence of both single and double layers of DAPPor on Cu (111), and along with DAPPor molecules assembled on Cu_2N at different bias voltages.

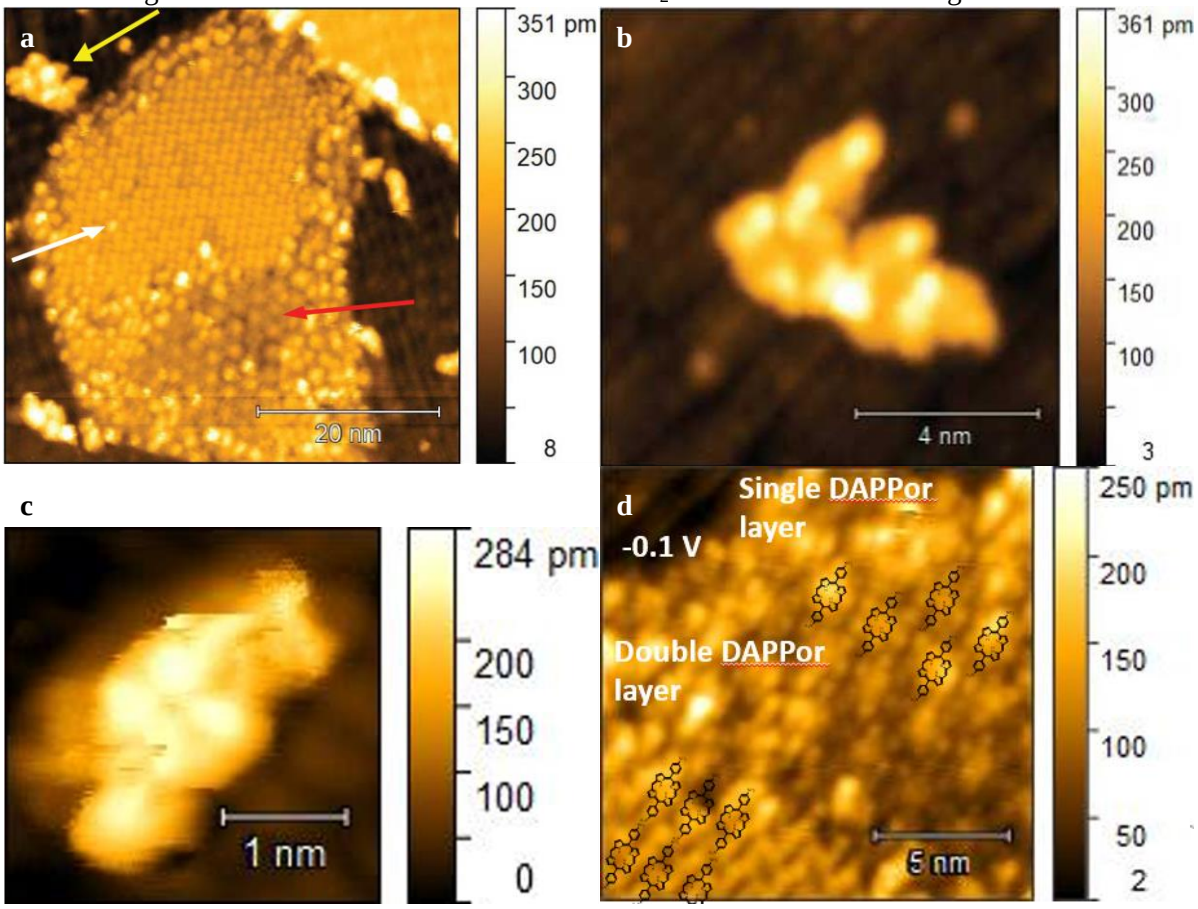

Fig. 10B.9. (a) STM image of single and double layers of DAPPor assembly on Cu (111); Z-height = 0.35 nm, V_s = -0.5 V, I_t = 50 pA, rms-R = 0.07 nm. Yellow, white, and red arrows indicate DAPPor on Cu_2N, a monolayer of DAPPor on Cu (111), and a double layer of DAPPor on Cu (111), respectively. (b) STM images of DAPPor molecules on a Cu_2N sub-monolayer on Cu (111); Z-height = 0.36 nm, V_s = -0.5 V, I_t = 100 pA, rms-R = 0.07 nm. (c) Z-height = 0.28 nm, V_s = -0.5 V, I_t = 50 pA, rms-R = 0.08 nm. (d) STM image of single and double layers of DAPPor assembly on Cu (111), along with the proposed molecular model; Z-height = 0.25 nm, V_s = -0.1 V, I_t = 100 pA, rms-R = 0.04 nm. STM acquisition temperature: 4.6 K.

Appendix C: Ullmann Coupling and Poly(para-phenylene) Wires on Copper Nitride Monolayers on Copper (111)

Fig. 10C.1d displays the presence of two triangle-like and bent $(BrP)_2P$ dimers next to each other. These are candidates of Ullmann coupling.

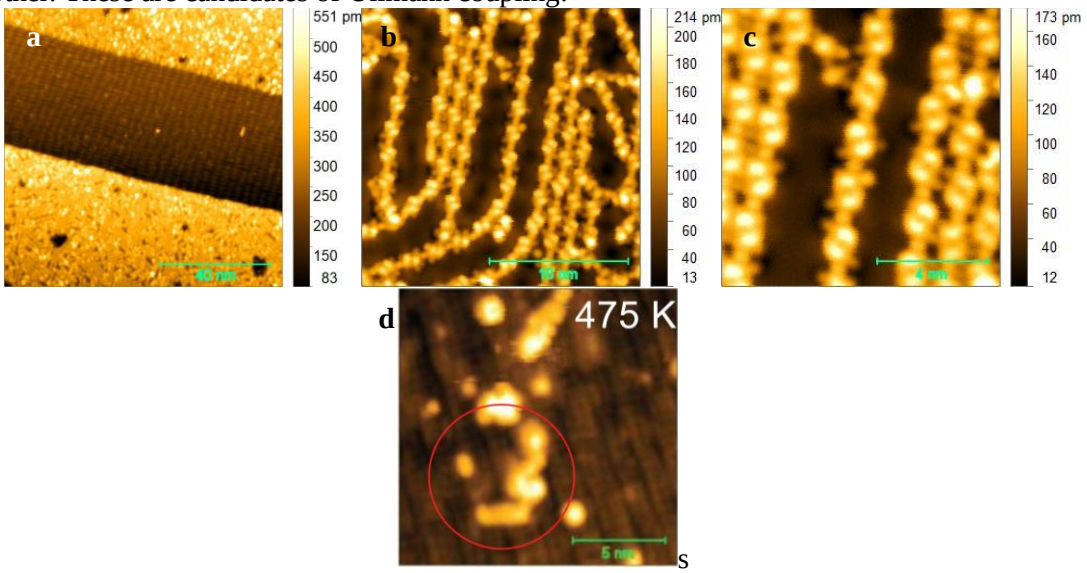

Fig. 10C.1. (a-c) Ullmann coupling of $(BrP)_2P$ molecules on Cu (111) islands surrounded by Cu_2N after annealing 400 K. (d) STM image of $(BrP)_2P$ molecules assemblies, showing two dimers in the red circle on Cu2N on Cu (111) after annealing at 475 K. Z-height = 0.35 nm, Vs = 0.5 V, It = 1 nA, rms-R = 0.06 nm. STM acquisition temperature: 4.6 K.

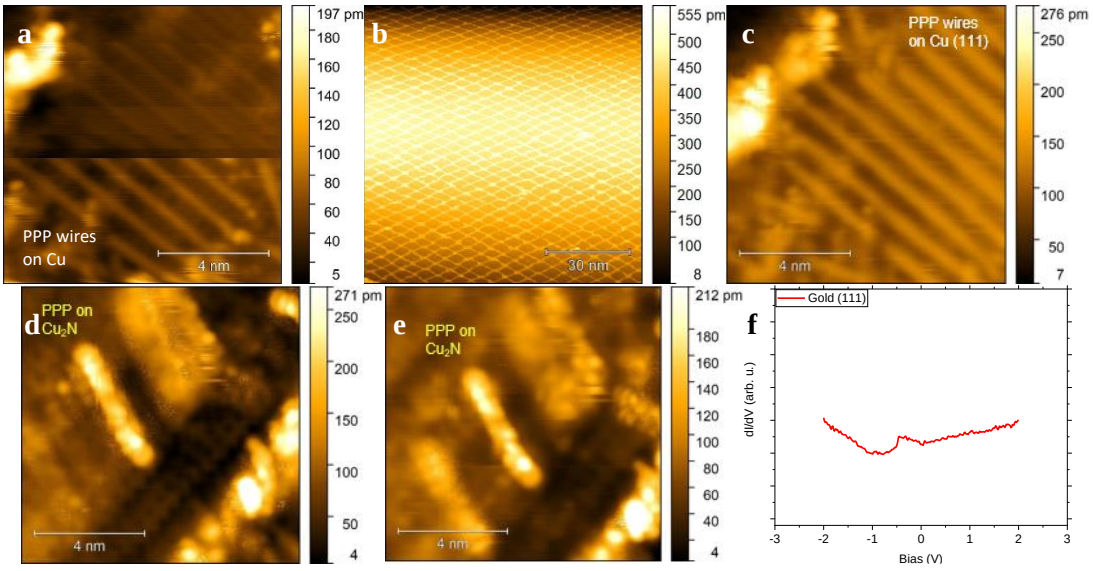

Fig. 10C.2. (a) DBTP on a Cu (111) island surrounded by Cu_2N, (10 nm × 10 nm) Vs = -2.00 V; I_t = 100 pA, rms-R ≈ 0.03 nm. (b) Cu_2N on Cu (100), (100 nm × 100 nm) V_S = -1.00V; I_t = 100 pA, rms-R ≈ 0.11 nm. Bias-dependent STM images of PPP wires on Cu (111) after annealing DBTP molecules at ≈ 475 K. (c) 10 nm × 10 nm, V_s = 1 V, I_t = 100 pA, rms-R = 0.03 nm. Bias-dependent STM images of 3AGNRs on Cu_2N on Cu (111) after annealing DBTP molecules at ≈ 475 K. (d) 10 nm × 10 nm, V_s = 1 V, I_t = 100 pA, rms-R = 0.05 nm. (e) 10 nm

× 10 nm, V_s = 2 V, I_t = 100 pA, rms-R = 0.04 nm. (f) Tunneling spectrum of Au (111). STM acquisition temperature: 77 K.

Appendix D: Replacement Method Fabrication of Cu_2N on Cu(100): Analysis of Structure and Electronic Properties

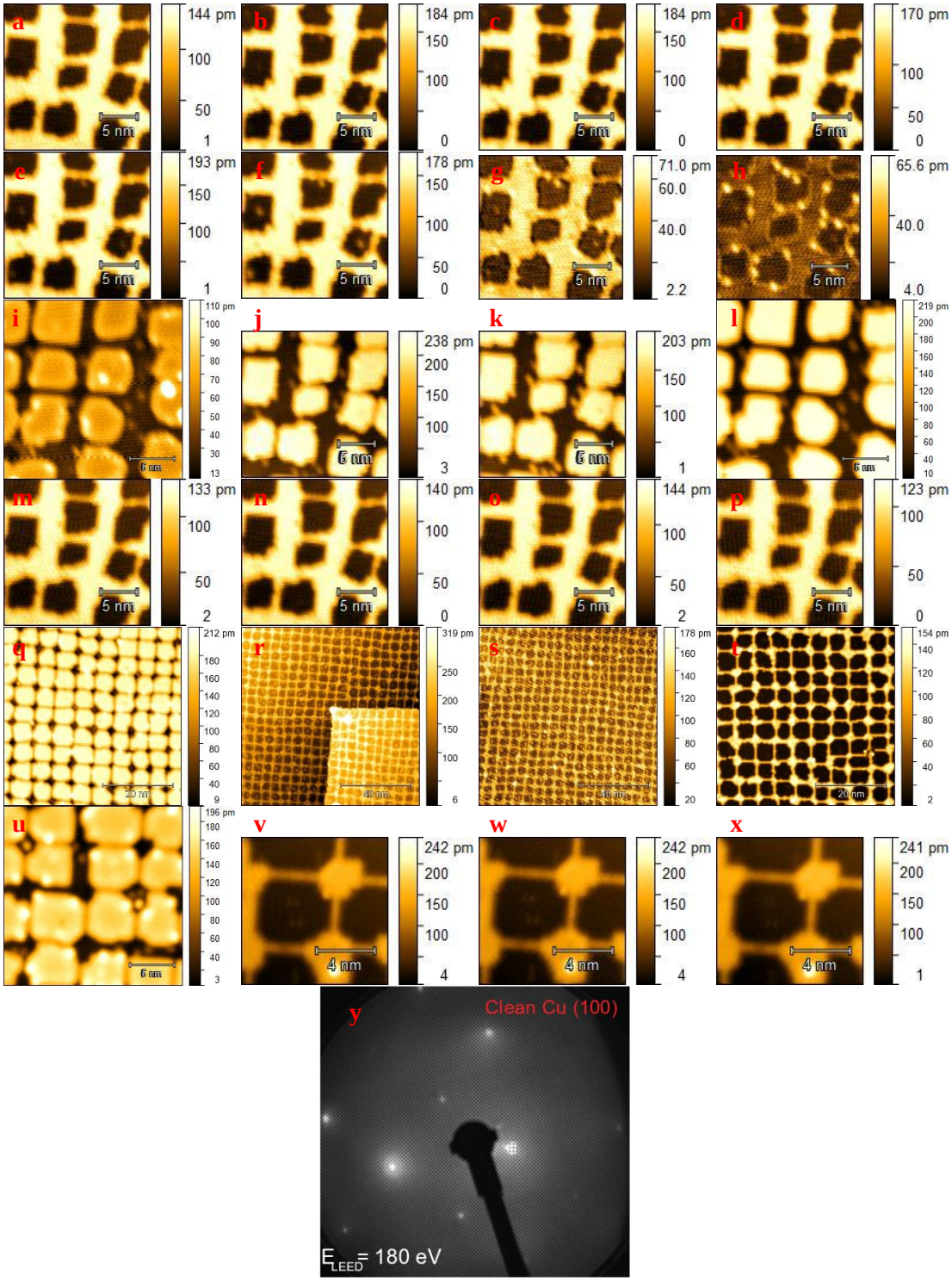

Fig. 10D.1. Bias dependent STM images of Cu_2N on Cu (100). (a) 20 nm × 20 nm, V_s=-1 V, I_t=500 pA, rms-R=0.05 nm. (b) 20 nm × 20 nm, V_s=1 V, I_t=500 pA, rms-R=0.06 nm. (c) 20 nm × 20 nm, V_s=0.1 V, I_t=500 pA, rms-R=0.05 nm. (d) 20 nm × 20 nm, V_s=0.5 V, I_t=500 pA, rms-R=0.06 nm. (e) 20 nm × 20 nm, V_s=1.5 V, I_t=500 pA, rms-R=0.06 nm. (f) 20 nm × 20 nm, V_s=2 V, I_t=500 pA, rms-R=0.06 nm. (g) 20 nm × 20 nm, V_s=2.5 V, I_t=500 pA, rms-R=0.02 nm. (h) 20 nm × 20 nm, V_s=3 V, I_t=500 pA, rms-R=0.01 nm. (i) 20 nm × 20 nm, V_s=3.5 V, I_t=1 nA, rms-R=0.02 nm. (j) 20 nm × 20 nm, V_s=4 V, I_t=500 pA, rms-R=0.07 nm. (k) 20 nm × 20 nm, V_s=4.5 V, I_t=500 pA, rms-R=0.06 nm. (l) 20 nm × 20 nm, V_s=5 V, I_t=1 nA, rms-R=0.07 nm. (m) 20 nm × 20 nm, V_s=-2 V, I_t=500 pA, rms-R=0.04 nm. (n) 20 nm × 20 nm, V_s=-3 V, I_t=500 pA, rms-R=0.05 nm. (o) 20 nm × 20 nm, V_s=-4 V, I_t=500 pA, rms-R=0.05 nm. (p) 20 nm × 20 nm, V_s=-5 V, I_t=500 pA, rms-R=0.04 nm. (q) 50 nm × 50 nm, V_s=3.8 V, I_t=100 pA, rms-R=0.04 nm. (r) 100 nm × 100 nm, V_s=2.15 V, I_t=500 pA, rms-R=0.07 nm. (s) 100 nm × 100 nm, V_s=2.2 V, I_t=100 pA, rms-R=0.03 nm. (t) 50 nm × 50 nm, V_s=0.2 V, I_t=500 pA, rms-R=0.05 nm. (u) 20 nm × 20 nm, V_s=3.7 V, I_t=100 pA, rms-R=0.04 nm. (v) 10 nm × 10 nm, V_s=-0.01 V, I_t=100 pA, rms-R=0.05 nm. (w) 10 nm × 10 nm, V_s=0.01 V, I_t=100 pA, rms-R=0.05 nm. (x) 10 nm × 10 nm, V_s=-0.1 V, I_t=100 pA, rms-R=0.05 nm. STM acquisition temperature: 4.6 K. (y) (1×1) LEED pattern of clean Cu (100).

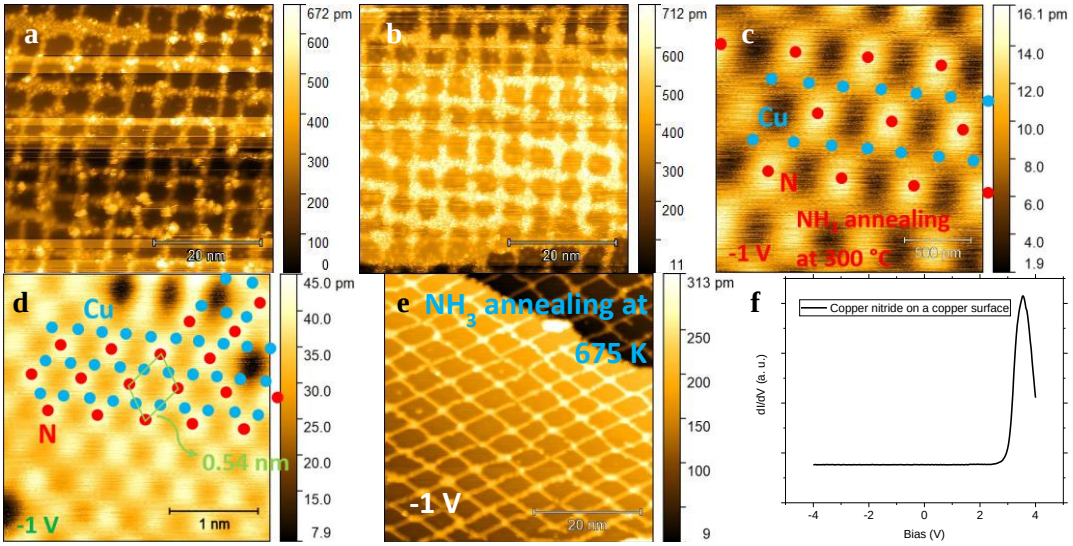

Fig. 10D.2. (a) TPA on Cu_2N on Cu (100), (50nm×50nm) V_s=2.20V; I_t~500 pA, rms-R~0.11 nm. (b) CBCP on Cu2N on Cu (100), (50nm×50nm) Vs=2.20V; It~500 pA, rms-R~0.12 nm. STM acquisition temperature: 4.6 K. (a) HR-STM and atomic models of Cu_2N on Cu (100) annealed at 575 K in the presence of NH_3. (c) 2 nm × 2 nm, V_s=-1 V, I_t=100 pA, rms-R=0.01 nm. (d) 3 nm × 3 nm, V_s=-1 V, I_t=100 pA, rms-R=0.01 nm. Cu_2N on Cu (100) annealed at 675 K in the presence of NH_3 (e) 50 nm × 50 nm, V_s = -1 V, I_t = 100 pA, rms-R = 0.06 nm. (f) STS of Cu_2N layer on a Cu surface. STM acquisition temperature: 77 K.

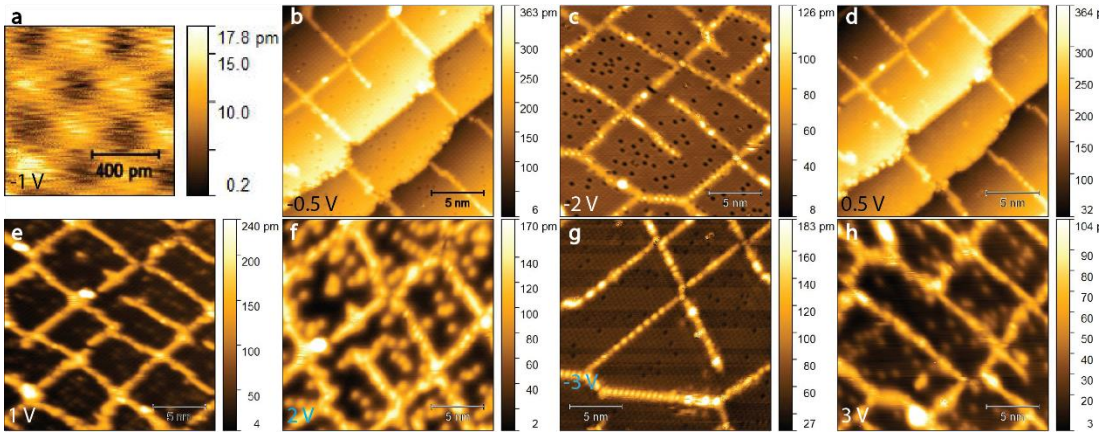

Fig. 10D.3. Bias dependent HR-STM images of Cu_2N on Cu (100) after oxidation and NH_3 annealing at about 575 K. (a) 1 nm × 1 nm, V_s = -1 V, I_t = 100 pA, rms-R = 0.03 nm. (b) 20 nm × 20 nm, V_s = -0.5 V, I_t = 100 pA, rms-R = 0.07 nm. (c) 20 nm × 20 nm, V_s = -2 V, I_t = 100 pA, rms-R = 0.07 nm. (d) 20 nm × 20 nm, V_s = 0.5 V, I_t = 100 pA, rms-R = 0.07 nm. (e) 20 nm × 20 nm, V_s = 1 V, I_t = 100 pA, rms-R = 0.05 nm. (f) 20 nm × 20 nm, V_s = 2 V, I_t = 100 pA, rms-R = 0.04 nm. (g) 20 nm × 20 nm, V_s = -3 V, I_t = 100 pA, rms-R = 0.03 nm. (h) 20 nm × 20 nm, V_s = 3 V, I_t = 100 pA, rms-R = 0.02 nm. STM acquisition temperature: 77 K.

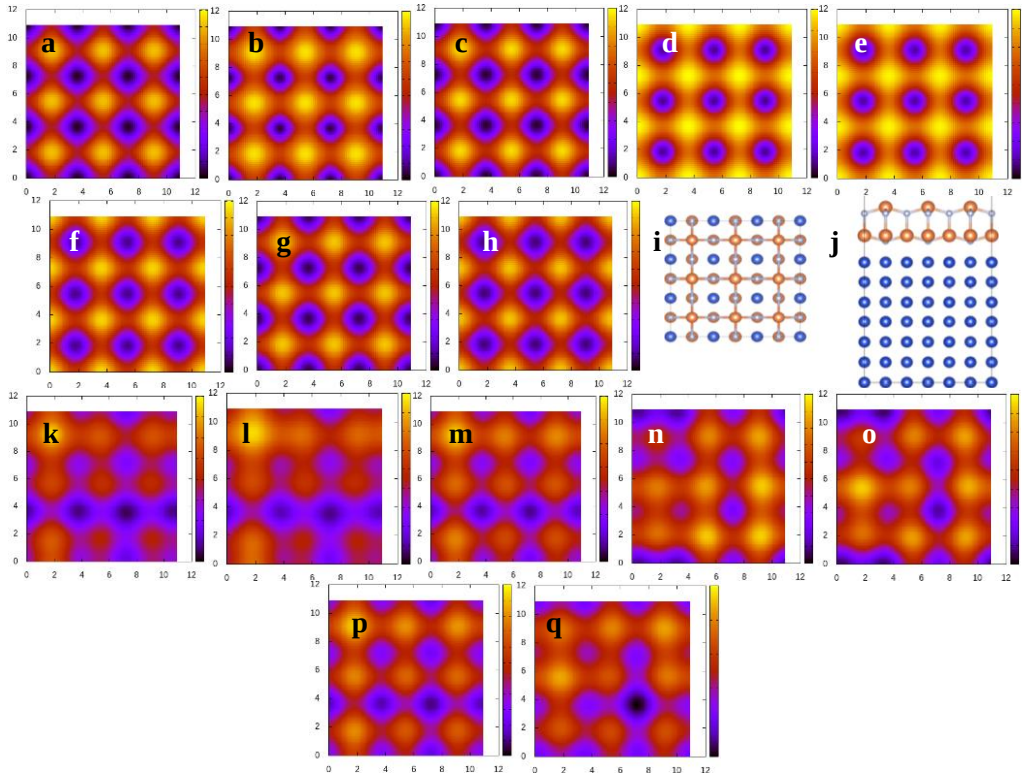

Fig. 10D.4. DFT simulation, bias-dependent STM images of Cu_2N on Cu (111), represented in Fig. 6.3a and 6.3b. STM images simulated at various bias voltages and currents: (a) V = -1.0 V, I = 0.1 nA. (b) V = -0.5 V, I = 0.1 nA. (c) V = -2.0 V, I = 0.1 nA. (d) V = 0.50 V, I = 0.1 nA. (e) V = 1.0 V, I = 0.1 nA. (f) V = 2.00 V, I = 0.1 nA. (g) V = -3.0 V, I = 0.1 nA. (h) V = 3.0 V, I = 0.1 nA. DFT simulation of bias-dependent STM images of bilayer Cu_2N on Cu (111) shown in (i) and (j). The blue, orange, and gray spheres represent Cu atoms in Cu (100), Cu atoms in the bilayer Cu_2N, and N atoms, respectively. Bias voltages and tunneling currents are as follows: (k) V = -1.0 V, I = 0.1 nA. (l) V = -0.5 V, I = 0.1 nA. (m) V = -2.0 V, I = 0.1 nA. (n) V = 1.0 V, I = 0.1 nA. (o) V = 2.0 V, I = 0.1 nA. (p) V = -3.0 V, I = 0.1 nA. (q) V = 3.0 V, I = 0.1 nA. (r) V = -2.5 V, I = 300 pA.

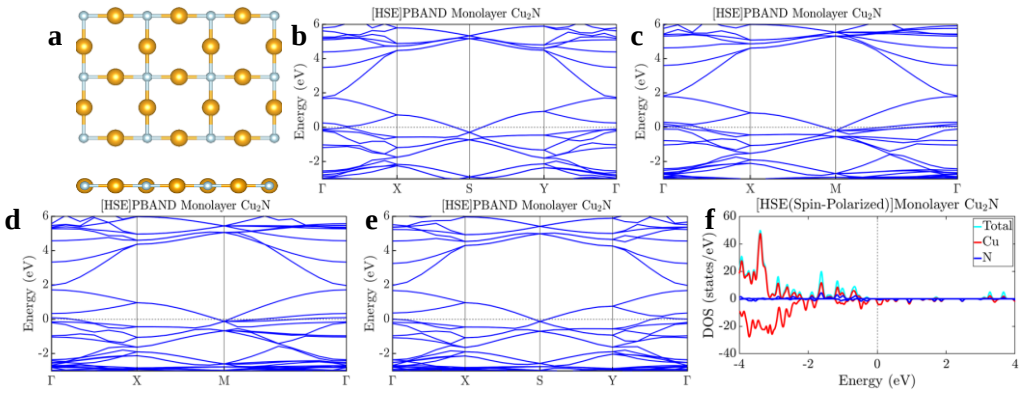

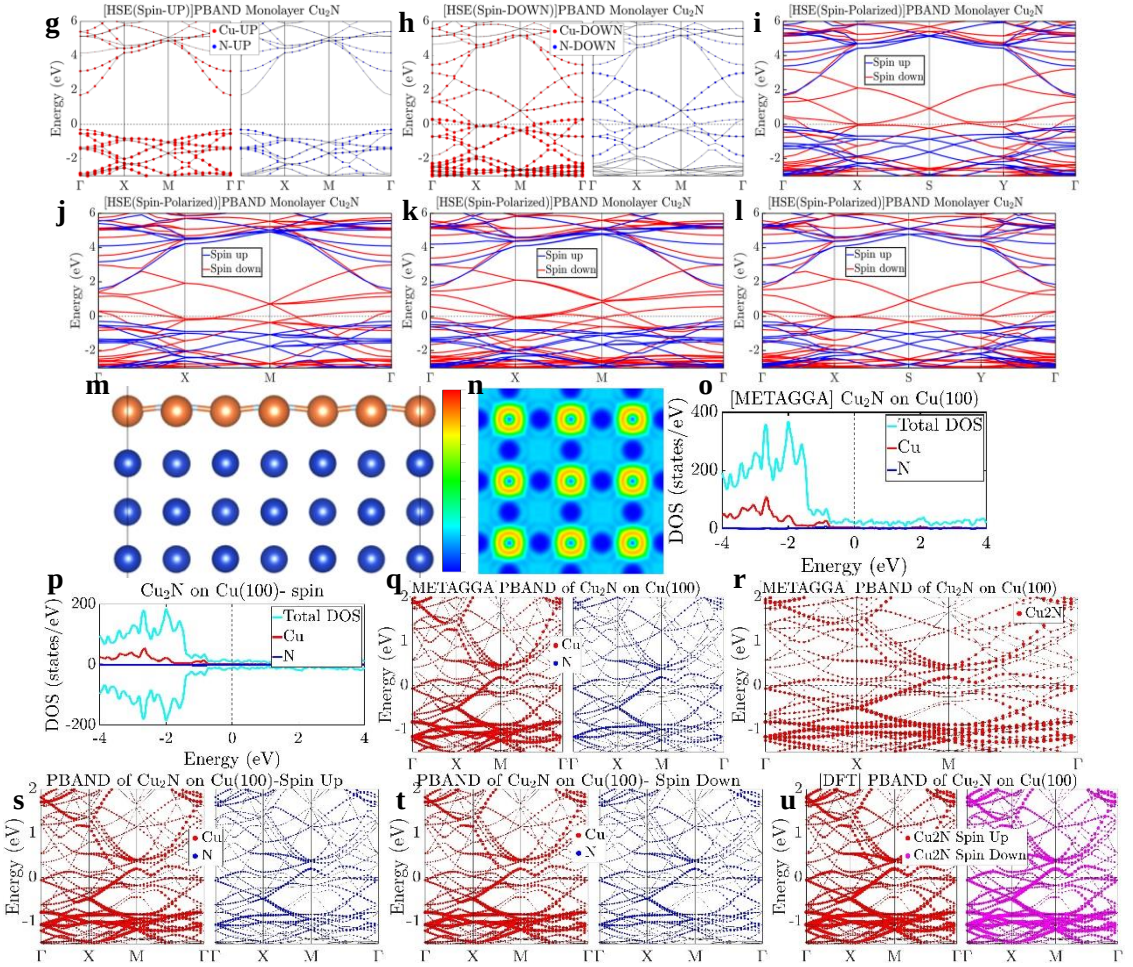

Fig. 10D.5. (a) Structural atomic model of a free-standing Cu_2N unit cell including twelve atoms (8 Cu (yellow spheres) and 4 N (gray spheres) atoms). DFT simulations of the band structure (BS) under (b) 3% and (c) 2% compression strains, and (d) 2% and (e) 3% expansion strains, were calculated using the Heyd-Scuseria-Ernzerhof hybrid functional (HSE) method without spin polarization. Spin-polarized DFT simulations of (f) PDOS and the corresponding BS are shown (g,h) without strain (Spin-UP: band gap ≈ 2.01 eV, Spin-DOWN: band gap = 0.05 eV), together with BS under (i) 3% (Spin-UP: band gap ≈ 1.86 eV, Spin-DOWN: band gap = 0.02 eV), and (j) 2% (Spin-UP: band gap ≈ 1.89 eV, Spin-DOWN: band gap = 0.05 eV) compression strains. Expansion strains are analyzed in (k) 2% (Spin-UP: band gap ≈ 2.11 eV, Spin-DOWN: band gap ≈ 0.04 eV) and (l) 3% (Spin-UP: band gap ≈ 2.18 eV, Spin-DOWN: band gap ≈ 0.05 eV). (m) Side-view structural atomic model of a Cu_2N monolayer on a Cu (100) substrate (d_{Ads}= 2.14 Å) and (n) the electron localization function on atoms on the corresponding Cu_2N ML slice confirming the Cu-N covalent bonds. Blue spheres represent the Cu atoms in the substrate. DFT simulations of PDOS of Cu_2N on Cu (111) are provided (o) without and (p) with spin polarization. The BS of Cu_2N on Cu (111) is shown (q,r) without and (s,t,u) with spin polarization (Spin-UP: band gap ≈ 0.01 eV, Spin-DOWN: band gap = 0.01 eV, Total: band gap = 0.01 eV).

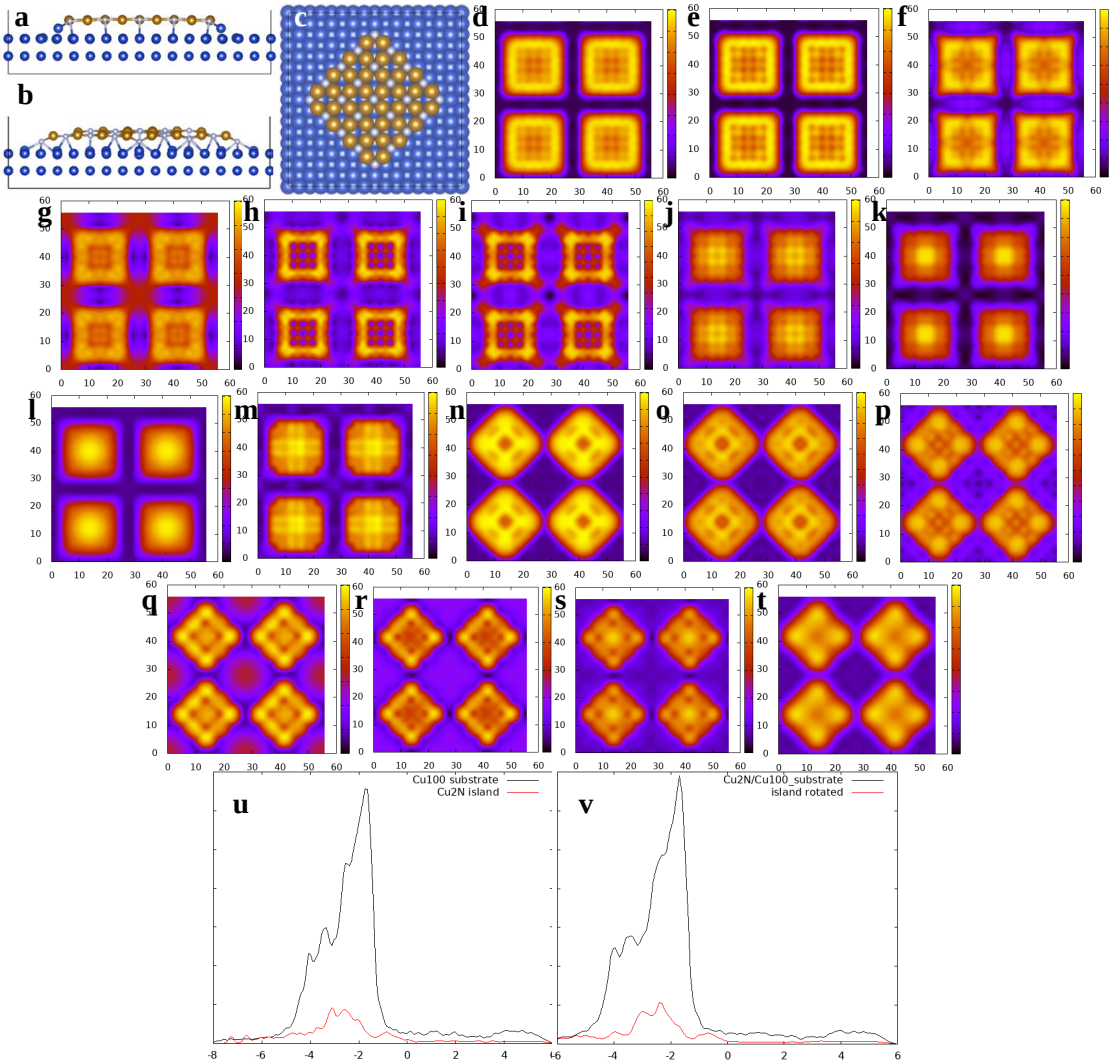

Fig. 10D.6. Side-view structural atomic model for DFT simulations of (a) Cu_2N islands rotated by 45˚ compared to and (b) aligned parallel to the Cu (100) high-density direction. (c) Top-view structural atomic model for (a). DFT simulations of bias-dependent STM images of the structural model shown in Fig. 10D.6a and Fig. 6.3i are presented for bias voltages of (d) -1.5 V, (e) -1.0 V, (f) 0.4 V, (g) 1.0 V, (h) 1.5 V, (i) 1.7 V, (j) 2.0 V, (k) 2.1 V, (l) 3.5 V, and (m) 6 V. DFT simulations of bias-dependent STM images of the structural model shown in Fig. 10D.6b and Fig. 10D.6c are presented for bias voltages of (n) -1.3 V, (o) -1.0 V, (p) 0.5 V, (q) 1.0 V, (r) 1.5 V, (s) 2.0 V, and (t) 3.0 V. The scale unit is Å. (u) and (v) represent the DFT simulation of PDOS versus applied bias voltage for islands shown in (a) and (b), respectively.

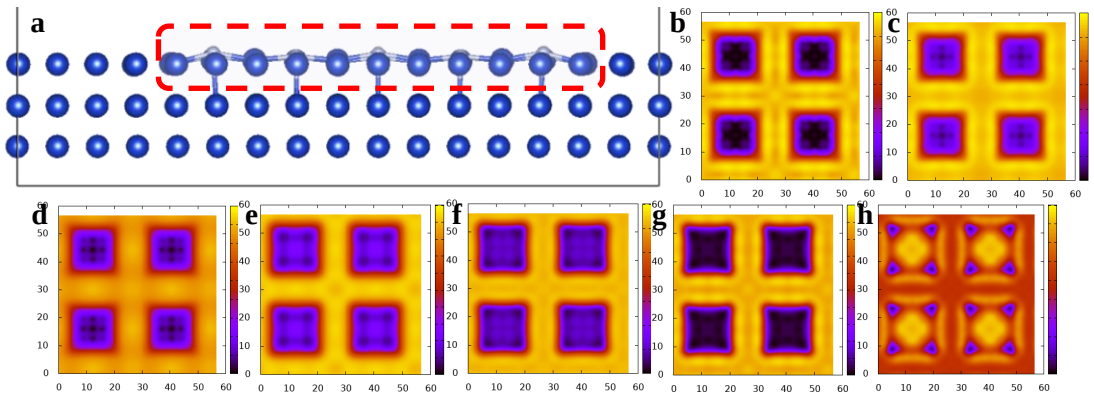

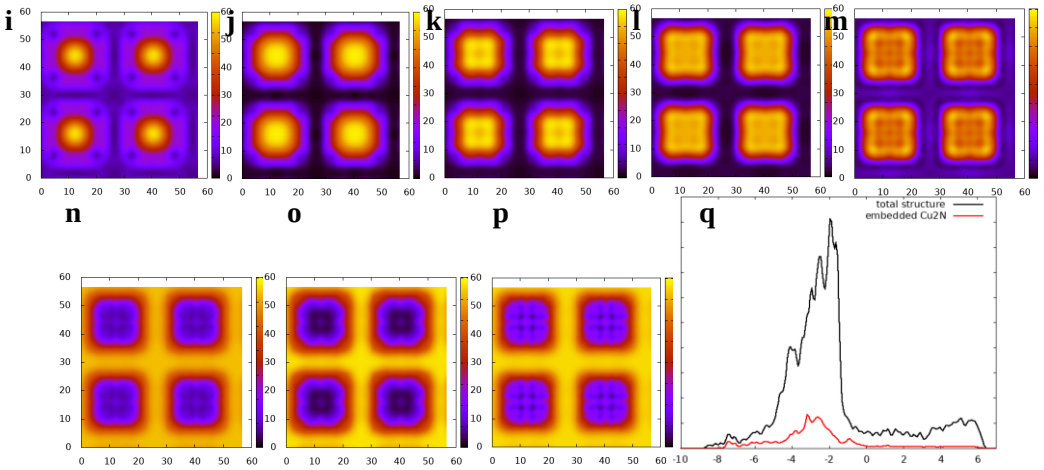

Fig. 10D.7. DFT simulations of (a) a Cu_2N island embedded within the top atomic layer of Cu (100) as shown in Fig. 6.3l. Cu and N atoms are represented by blue and gray spheres, respectively. DFT-simulated, bias-dependent STM images of the model in (a) at various bias voltages and tunneling currents: (b) 0.5 V, I_t = 0.5 nA. (c) 1.0 V, I_t = 0.5 nA. (d) 1.5 V, I_t = 0.5 nA. (e) 2.0 V, I_t = 0.5 nA. (f) 2.5 V, I_t = 0.5 nA. (g) 3.0 V, I_t = 0.5 nA. (h) 3.4 V, I_t = 0.5 nA. (i) 3.5 V, I_t = 1.0 nA. (j) 3.7 V, I_t = 0.1 nA. (k) 3.8 V, I_t = 0.1 nA. (l) 4.5 V, I_t = 0.5 nA. (m) 5.0 V, I_t = 1.0 nA. (n) -3.0 V, I_t = 0.5 nA. (o) -4.0 V, I_t = 0.5 nA. (p) -1.0 V, I_t = 0.1 nA. The scale unit is Å. (q) DFT simulation of PDOS versus applied bias voltage for islands shown in (a).

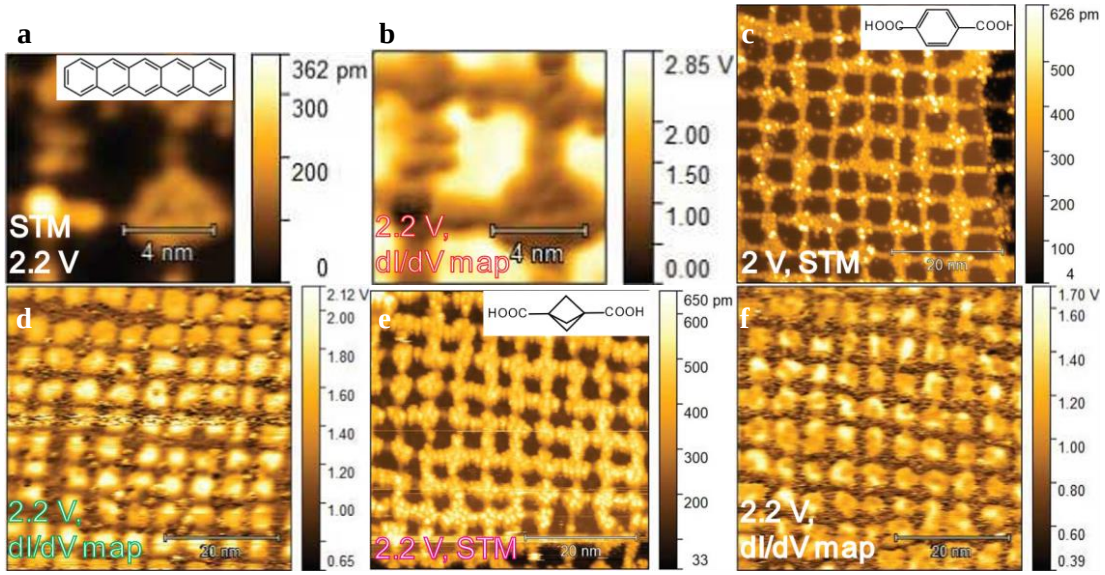

Fig. 10D.8. (a) An STM image of Pentacene on Cu_2N and Cu (100); 10 nm × 10 nm, V_s = 2.2 V, I_t = 500 pA, rms-R = 0.06 nm. (b) A dI/dV map of Pentacene on Cu_2N and Cu (100); 10 nm × 10 nm, V_s = 2.2 V, I_t = 500 pA, rms-R = 0.63 V. (c) An STM image of TPA on Cu_2N and Cu (100); 50 nm × 50 nm, V_s = 2 V, I_t = 100 pA, rms-R = 0.11 nm. (d) A dI/dV map of TPA on Cu_2N and Cu (100); 50 nm × 50 nm, V_s = 2.2 V, I_t = 500 pA, rms-R = 0.27 V. (e) An STM image of CBCP on Cu_2N and Cu (100); 50 nm × 50 nm, V_s = 2.2 V, I_t = 500 pA, rms-R = 0.23 nm. (f) A dI/dV map of CBCP on Cu_2N and Cu (100); 50 nm × 50 nm, V_s = 2.2 V, I_t = 500 pA, rms-R = 1.44 V. STM acquisition temperature: 4.6 K.

Appendix E: Catalytic Effects of Iron Adatoms in Poly(para-phenylene) Synthesis on Rutile TiO2(110)

Supplement measurements and results

In Fig. 10E.1g, STS exhibits a band gap of about 3.3 eV for rutile TiO_2 (110) surface [373-377].

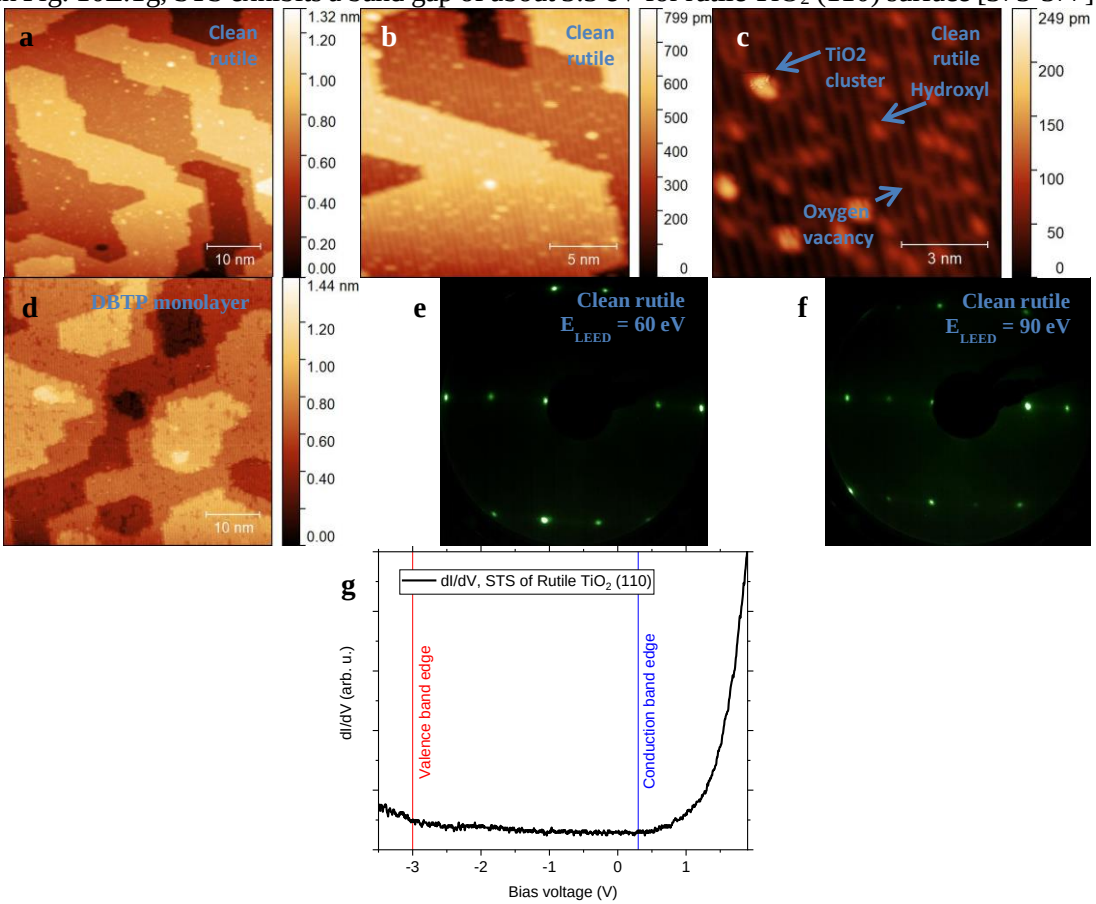

Fig. 10E.1. STM images of a clean rutile TiO_2 (110) surface; (a) 50 nm × 50 nm, V_s = -1 V, I_t = 10 pA. (b) 20 nm × 20 nm, V_s = -1 V, I_t = 10 pA. (c) ≈ 8.8 nm × ≈ 8.8 nm, V_s = -1 V, I_t = 10 pA. (d) An STM image of a DBTP monolayer after deposition at room temperature on a rutile TiO_2 surface; 50 nm × 50 nm, V_s = -1 V, I_t = 10 pA. STM acquisition temperature: 77 K. (1×1) LEED patterns of a clean rutile TiO_2 (110) surface with (e) E_{LEED} = 60 eV and (f) E_{LEED} = 90 eV. (g) Tunneling spectra of rutile TiO_2 (110). STM / STS data acquisition at T=77 K.

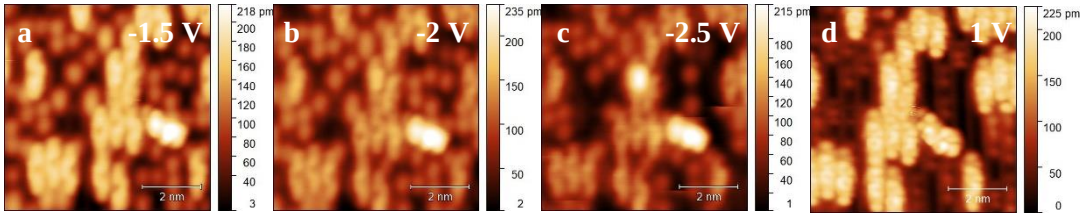

Fig. 10E.2. Bias-dependent STM images of DBTP dimers after annealing at 400 K on a rutile TiO_2(110) surface and subsequent coupling. (a) ≈ 7 nm × ≈ 7 nm, V_s = -1.5 V, I_t = 10 pA. (b) ≈ 7 nm × ≈ 7 nm, V_s = -2 V, I_t = 10 pA. (c) ≈ 7 nm × ≈ 7 nm, V_s = -2.5 V, I_t = 10 pA. (d) ≈ 7 nm × ≈ 7 nm, V_s = 1 V, I_t = 10 pA. STM acquisition temperature: 77 K.

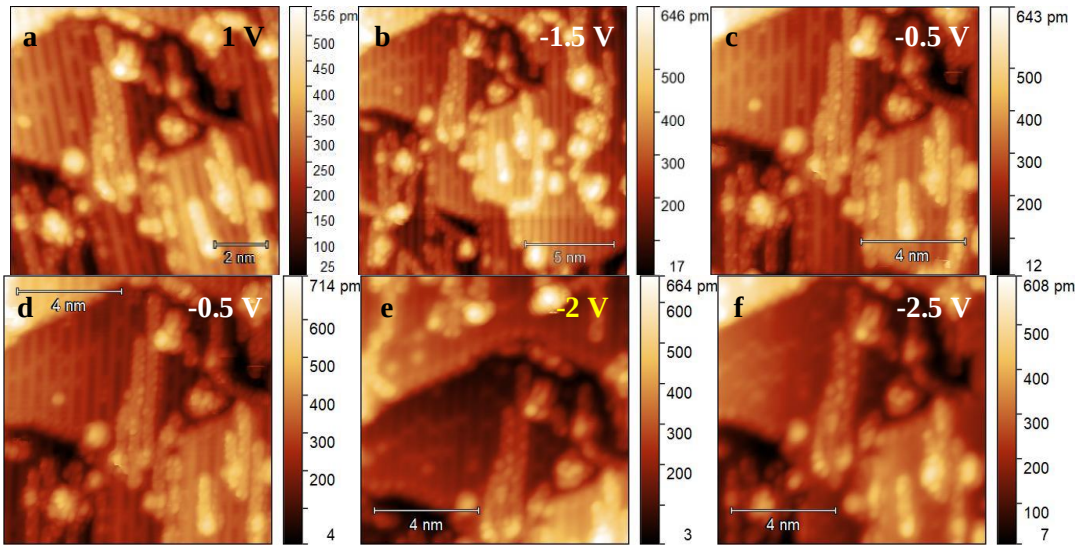

Fig. 10E.3. Bias-dependent STM images of 3AGNRs after annealing at 600 K on a rutile TiO_2 (110) surface. (a) 10 nm × 10 nm, V_s = -1 V, I_t = 10 pA. (b) ≈ 15 nm × ≈ 15 nm, V_s = -1.5 V, I_t = 10 pA. (c) ≈ 10 nm × ≈ 10 nm, V_s = -0.5 V, I_t = 10 pA. (d) ≈ 10 nm × ≈ 10 nm, V_s = -0.5 V, I_t = 10 pA. (e) ≈ 10 nm × ≈ 10 nm, V_s = -2 V, I_t = 10 pA. (f) ≈ 10 nm × ≈ 10 nm, V_s = -2.5 V, I_t = 10 pA. STM acquisition temperature: 77 K.

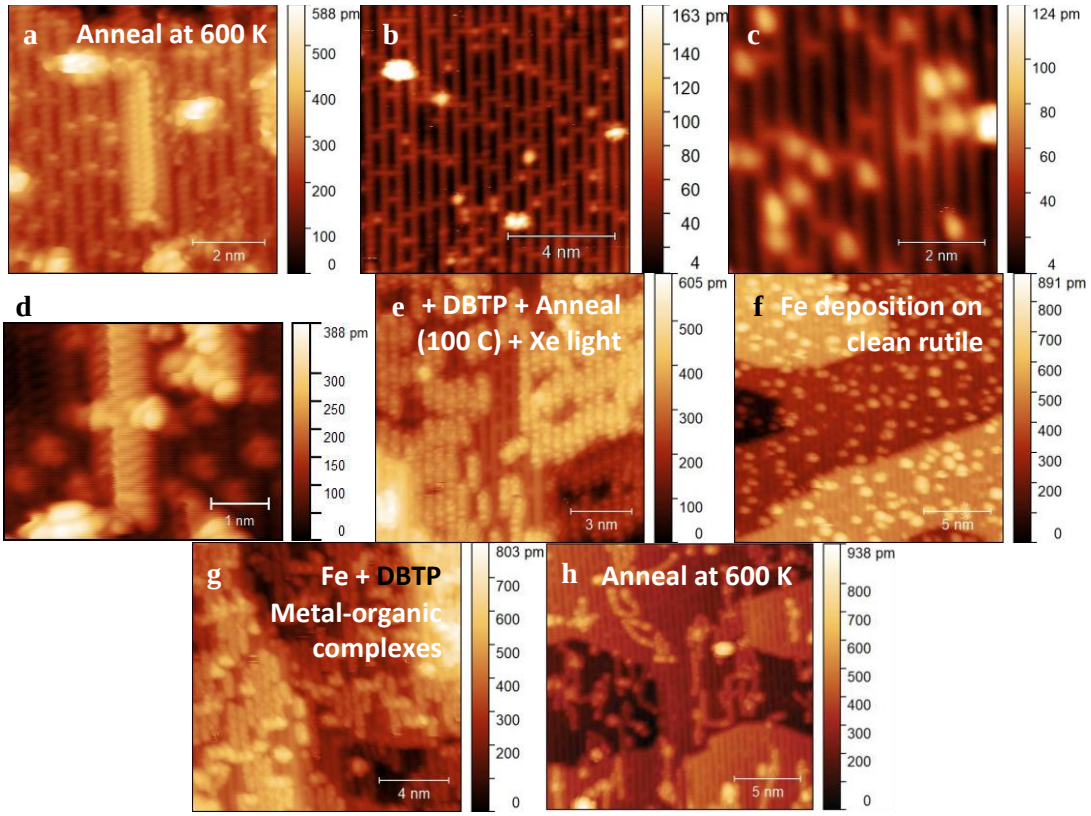

Fig. 10E.4. An STM image of a 2×1 defect on rutile TiO_2 after annealing at 600 K. (a) ≈ 7.4 nm × ≈ 7.4 nm, V_s = -1 V, I_t = 10 pA. STM images of a clean rutile TiO_2 (110) surface; (b) ≈ 10 nm × ≈ 10 nm, V_s = -1 V, I_t = 10 pA. (b) ≈ 6.2 nm × ≈ 6.2 nm, V_s = -1 V, I_t = 10 pA. An STM image of a 3AGNR on a clean rutile TiO_2 (110) surface after annealing at 600 K; (c) ≈

3.7 nm × ≈ 4.8 nm, V_s = -0.5 V, I_t = 10 pA. (e) An STM image of DBTP molecules on a clean rutile TiO_2 (110) surface after annealing at 100 ˚C; ≈ 13.2 nm × ≈ 13.2 nm, V_s = -1 V, I_t = 10 pA. (f) An STM image of rutile TiO_2 (110) after Fe atoms deposition on this surface; 20 nm × 20 nm, V_s = -1 V, I_t = 10 pA. (g) An STM image of 3AGNRs on rutile TiO_2 (110) after Fe atoms and DBTP molecules deposition on this surface (sample temperature ≤ 0 ˚C) and irradiation by a Xe lamp (filter: 240-395 nm); ≈ 15.4 nm × ≈ 15.4 nm, V_s = -1 V, I_t = 10 pA. (h) An STM image of PPP wires on a clean rutile TiO_2 (110) surface after annealing a DBTP multilayer at 600 K, in the absence of Fe ad-atoms; V_s = -1 V, I_t = 10 pA. STM acquisition temperature: 77 K.

In Fig. 10E.5, annealing DBTP molecules on TiO_2 surfaces leads to the breaking of C-halogen bonds, which are replaced by C-C coupling with lower binding energies. Furthermore, the presence of oxygen vacancies leads to turning Ti^{+4} cations into Ti^{+3} cations, which can be detected by the related shoulder in XPS spectra [77].

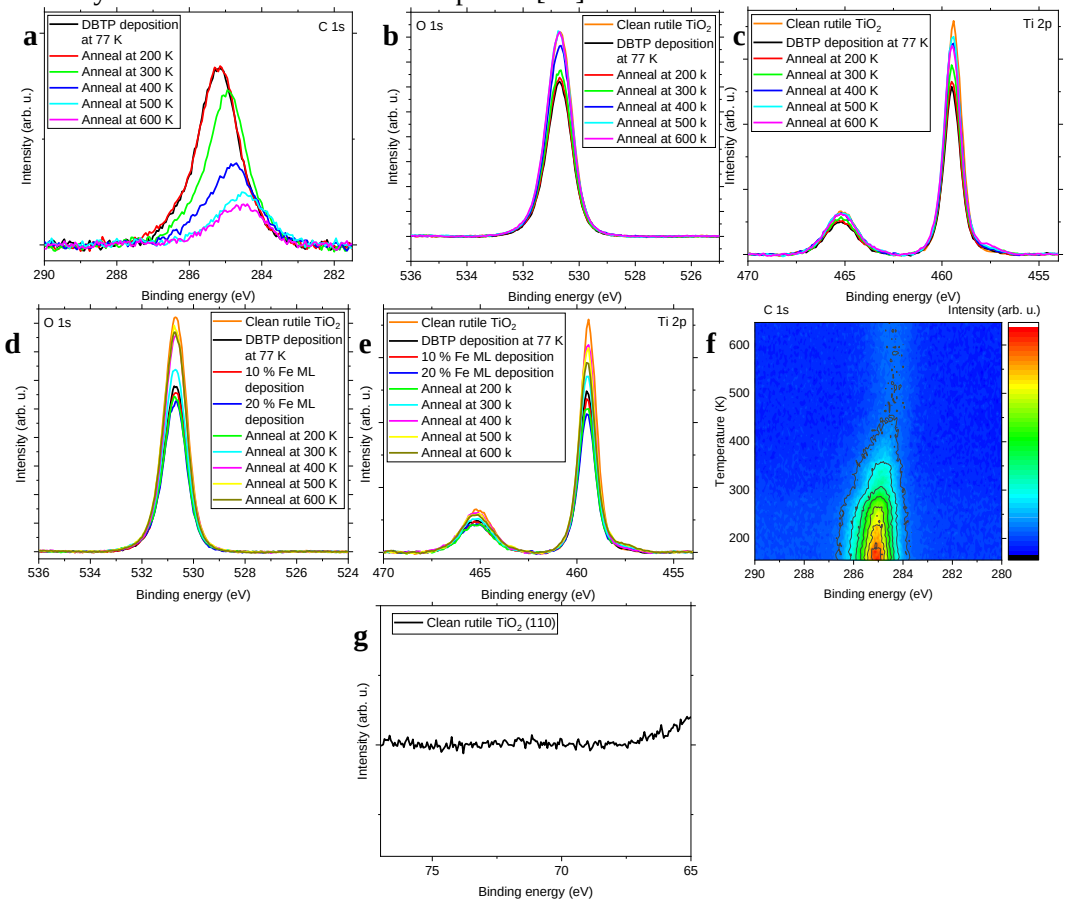

Fig. 10E.5. (a) Br 3d, (b) O 1s, and (c) Ti 2p narrow region XP spectra of a rutile TiO_2 (110) surface after deposition of a DBTP monolayer and annealing the monolayer at different temperatures. (d) O 1s and (d) Ti 2p narrow region XP-spectra of a rutile TiO_2 (110) surface after deposition of a DBTP monolayer and sub-monolayer coverage of Fe atoms (coverages of 10% and 20% ML) and annealing at different temperatures. (f) Temperature-programmed TP-XPS contour of the zoomed-in C 1s core level region after deposition of DBTP molecules on the surface without Fe atoms. (g) Br 3d narrow region XP spectra of a rutile TiO_2 (110) surface after cleaning. XPS acquisition temperature: 77 K.

Appendix F: Photocatalytic Fabrication of 5-Armchair Graphene Nanoribbons on TiO_2 Surfaces

Experimental section

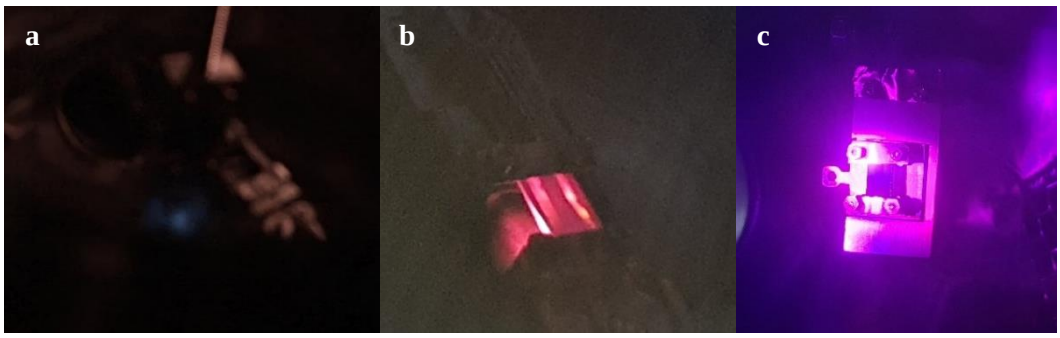

Fig. 10F.1. Photos of a rutile TiO_2 (110) sample during (a) sputtering, (b) annealing at approximately 900 K, and (c) Xe light irradiation.

Results and discussion

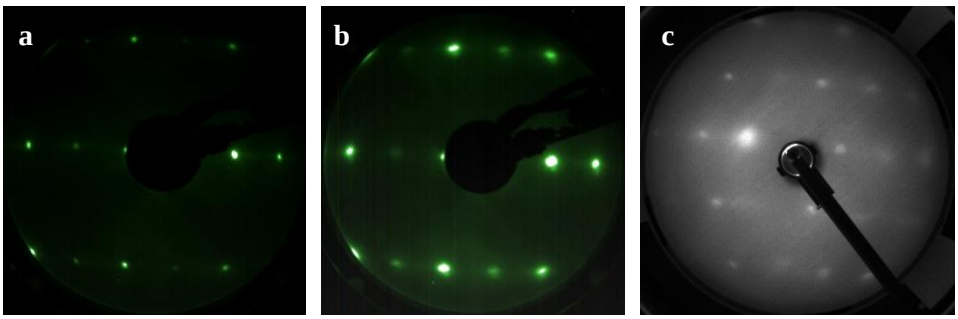

Fig. 10F.2. (a) A (1×1) LEED pattern of a cleaned rutile TiO_2 (110) surface (E_{LEED} = 90 eV). (b) An attenuated (1×1) LEED pattern of a TBN multilayer on a clean rutile TiO_2 (110) surface after annealing at 400 K (E_{LEED} = 90 eV). (c) A LEED pattern of a TBN monolayer on a clean anatase TiO_2 (101) surface after annealing at 350 K (E_{LEED} = 120 eV). LEED acquisition temperature: 77 K.

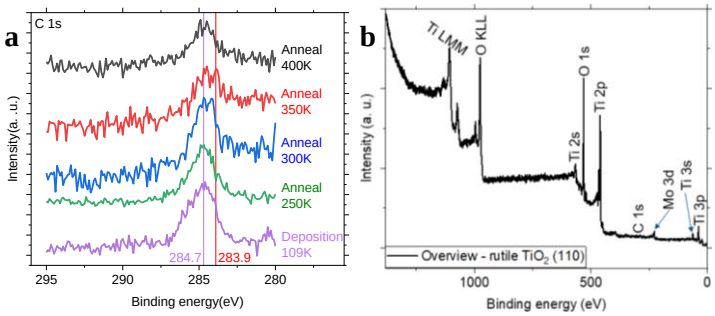

Fig. 10F.3. (a) C 1s narrow region scan XPS spectra of a rutile TiO_2 (110) surface after deposition of a TBN monolayer and annealing the monolayer at different temperatures. XPS

acquisition by a Mg anode at 77 K. (c) An overview scan XPS spectrum of a clean (C- and N-free) rutile TiO_2 (110) surface. XPS acquisition by an Al anode at 77 K.

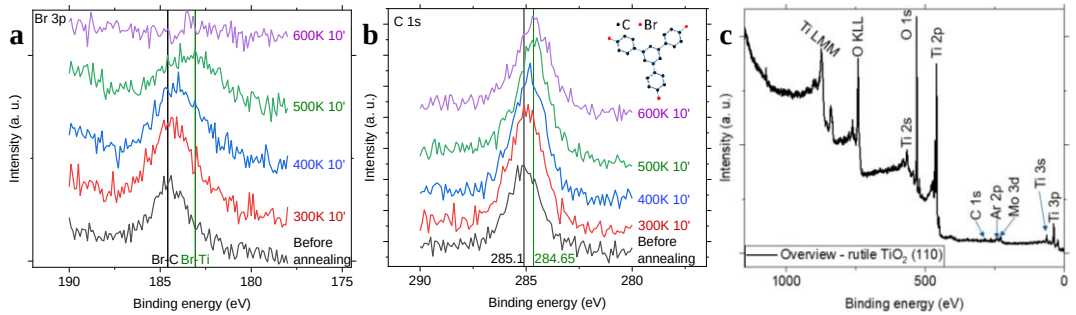

Fig. 10F.4. (a) Br 3p, (b) C 1s narrow region and (c) an overview XPS spectra of a rutile TiO_2 (110) surface after deposition of a TBB monolayer at 77 K and annealing the monolayer at different temperatures. XPS acquisition using a Mg anode at 77 K.

The presence of oxygen vacancies leads to the reduction of Ti^{+4} cations to Ti^{+3} cations, which can be detected by the corresponding shoulder in XPS spectra [77]. When Ti is fully oxidized to Ti^{+4}, the XPS Ti $2p_{3/2}$ symmetrical peak appears at binding energies of 458.4 eV (for the (101) surface) to 458.8 eV (for the (001) surface), while the shoulder corresponding to the Ti^{+3} component is observed at ≈ 1.7 eV lower binding energy. This shift in binding energy is likely due to different band bending of these two distinct anatase surfaces [82].

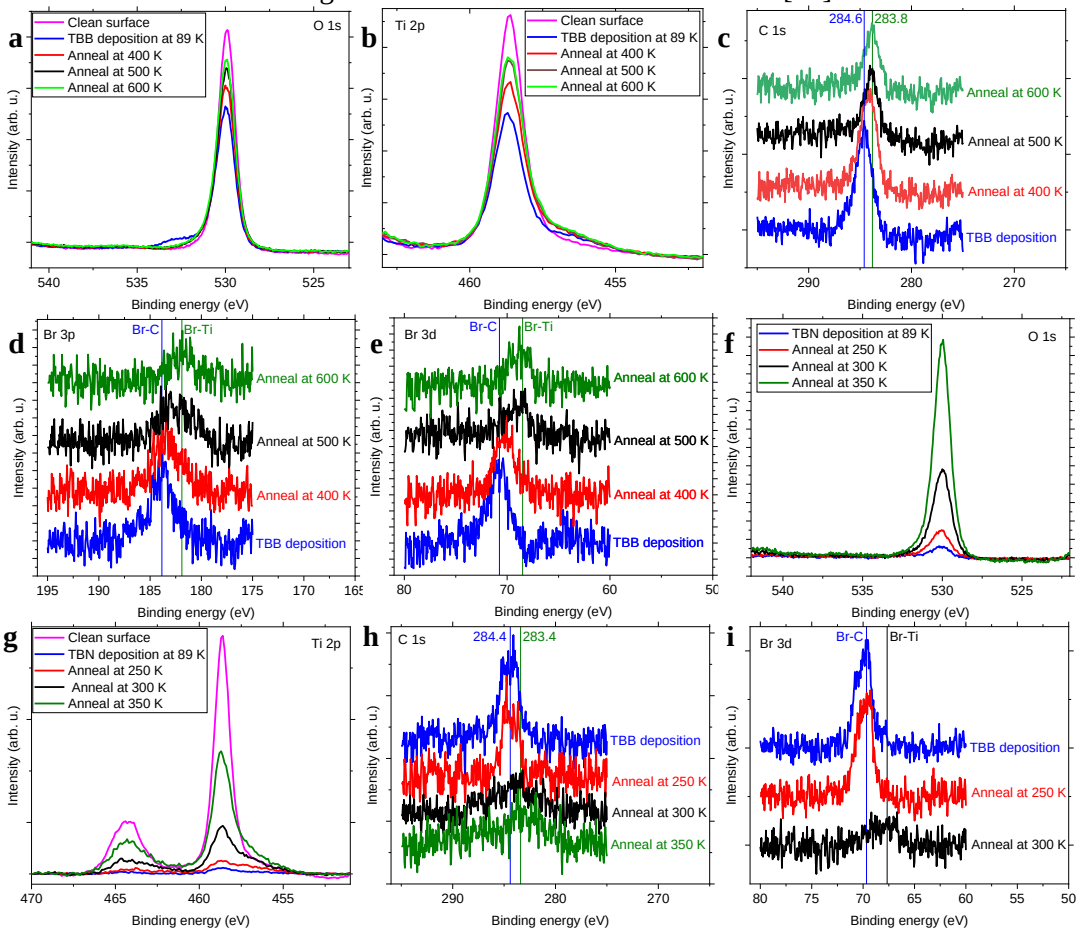

Fig. 10F.5. (a) O 1s, (b) Ti 2p, (c) C 1s, (d) Br 3p, and (e) Br 3d narrow region scan XPS spectra of an anatase TiO_2 (101) surface after deposition of a TBB monolayer and annealing at different temperatures. (f) O 1s, (g) Ti 2p, (h) C 1s and (i) Br 3d narrow region scan XPS spectra of an anatase TiO_2 (101) surface after deposition of a TBN monolayer and annealing at different temperatures. XPS acquisition by a Mg anode at 77 K.

Both Br ($^2P_{3/2}$) and Br* ($^2P_{1/2}$) distributions feature high translational energy components with vigorous angular anisotropy [255]. The excitation by UV light can cause the $\pi \rightarrow \pi^*$ band transition, resulting in the (π, π^*) state photoexcitation [255]. Despite the fact that (π, π^*) is a bonding state of the C-Br coordinate, during a rotational displacement due to the high translational distribution of Br ($^2P_{3/2}$ and $^2P_{1/2}$), the destruction of C-Br bonds begins [255]. Optically-excited (π, π^*) and repulsive $(n(Br)\ or\ \pi(Br), \sigma^*(C-Br))$ states of the halogen interfere destructively, leading to C-Br bond cleavage [255]. Another dissociation channel is the internal conversion of the Br atom in the C-Br bond, with low translational energy, to the ground state [255].

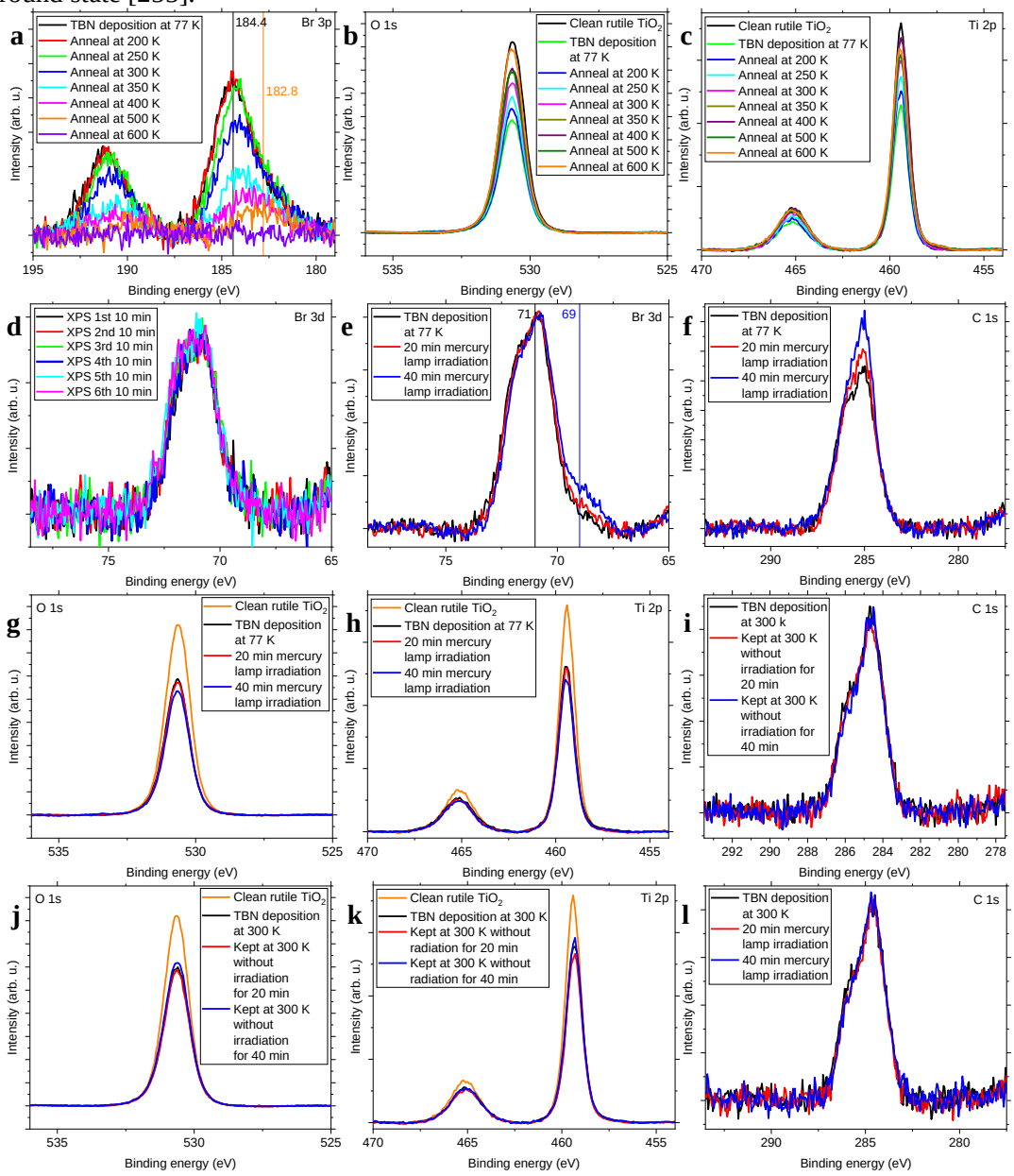

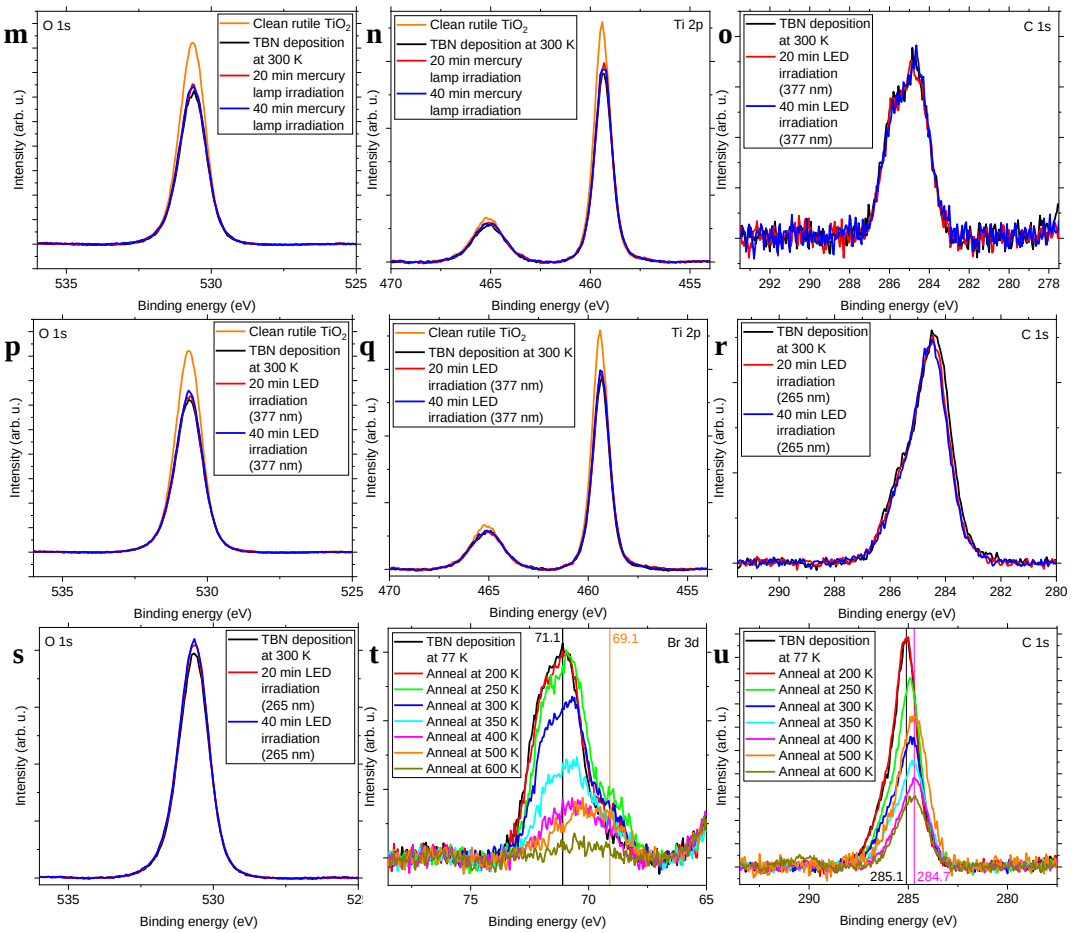

Fig. 10F.6. (a) Br 3p, (b) O 1s and (c) Ti 2p narrow region scan XPS spectra of a rutile TiO_2 (110) surface after deposition of a TBN monolayer and annealing at different temperatures. (d) Br 3d narrow region XPS spectra of a rutile TiO_2 (110) surface after deposition of a TBN monolayer followed by specific measurement times to assess the impact of X-ray radiation on the TBN monolayer. (e) Br 3d, (f) C 1s, (g) O 1s, and (h) Ti 2p narrow region scan XPS spectra of a rutile TiO_2 (110) surface after deposition of a TBN monolayer and irradiation for 20 and 40 minutes using a mercury lamp. XPS acquisition temperature: 77 K. (i) C 1s, (j) O 1s and (k) Ti 2p narrow region scan XPS spectra of a rutile TiO_2 (110) surface after deposition of a TBN monolayer and holding at 300 K for a specific duration without irradiation. (l) C 1s, (m) O 1s, and (n) Ti 2p narrow region scan XPS spectra of a rutile TiO_2 (110) surface after deposition of a TBN monolayer and irradiation with a mercury lamp at 300 K for a specific duration. (o) C 1s, (p) O 1s, and (q) Ti 2p narrow region scan XPS spectra of a rutile TiO_2 (110) surface after deposition of a TBN monolayer and irradiation with a 377 nm LED at 300 K for a specific duration. (r) C 1s and (s) O 1s narrow region scan XPS spectra of a rutile TiO_2 (110) surface after deposition of a TBN monolayer and irradiation with a 265 nm LED at 300 K for a specific duration. (t) Br 3d and (u) C 1s narrow region scan XPS spectra of a rutile TiO_2 (110) surface after deposition of a TBN monolayer at 77 K, followed by annealing at different temperatures. XPS acquisition temperature: 77 K.

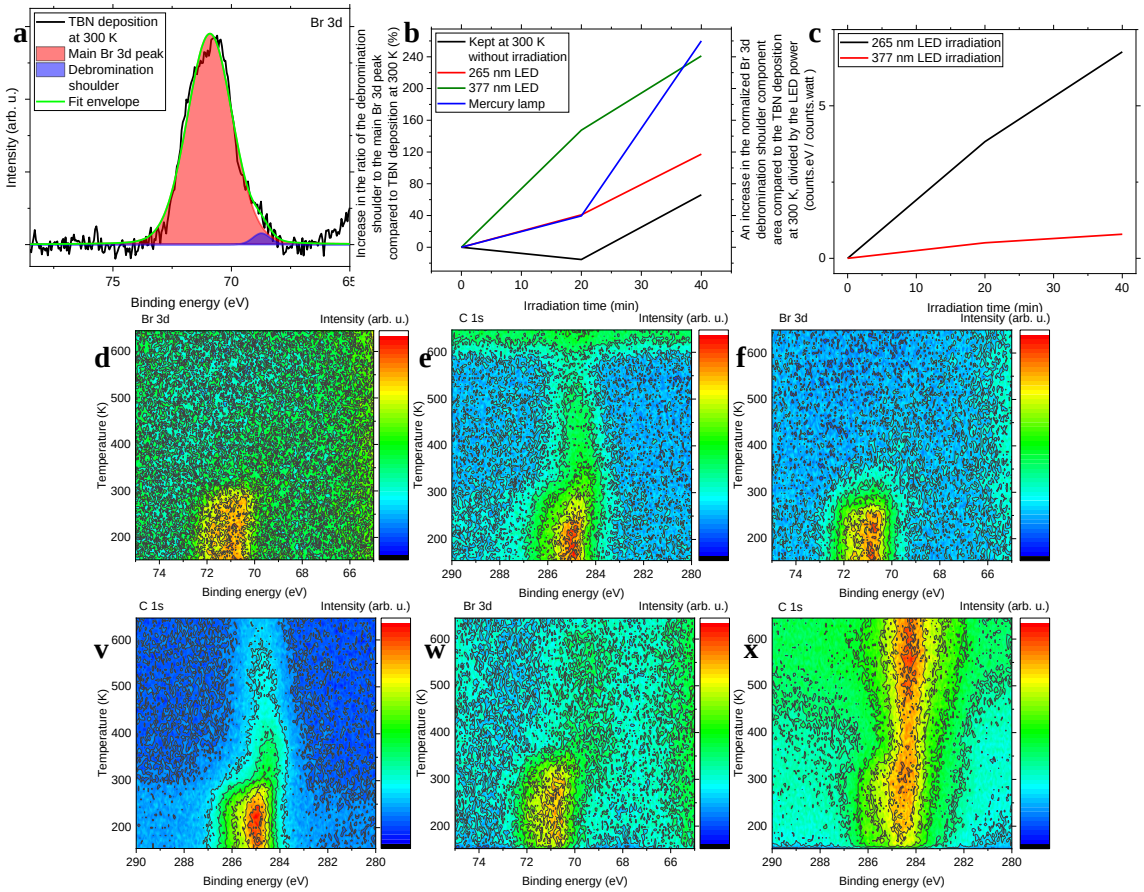

Fig. 10F.7. (a) A Br 3d narrow region XPS spectrum of a rutile TiO_2 (110) surface after deposition of a TBN monolayer with fitting of the main Br 3d peak and the debromination shoulder. (b) An increase in the ratio of the debromination shoulder area to the main Br 3d peak after holding at 300 K with and without irradiation compared to TBN deposition at 300 K. (c) An increase in the normalized area of the Br 3d debromination shoulder relative to TBN deposition at 300 K, divided by LED power, plotted versus irradiation time for 265 nm and 377 nm LEDs. LED powers reaching to the surface are 6.5 and 106 mW, respectively. XPS acquisition temperature: 300 K. Temperature-programmed (TP) XPS of zoom-in (d) Br 3d and (e) C 1s core level regions after TBN deposition on the surface. TPXPS of zoom-in (f) Br 3d and (g) C 1s core level regions after TBN deposition on the surface with 377 nm LED irradiation. TPXPS of zoom-in (h) Br 3d and (i) C 1s core level regions after TBN deposition on the surface with 265 nm LED irradiation. XPS acquisition temperature: 77 K.

Table. 10F.1. The ratio of the debromination shoulder area to the main Br 3d peak area of TBN molecules on rutile TiO_2 and the corresponding increase in the ratio compared to TBN deposition at 300 K.

TBN deposition at 300 K	Kept at 300 K without irradiation for 20 min	Increase in the ratio after 20 min compared to deposition	Kept at 300 K without irradiation for 40 min	Increase in the ratio after 40 min compared to deposition
0.0319	0.02697	-15.43 %	0.052976415	66.11 %
TBN deposition at 300 K	20 min mercury lamp irradiation	Increase in the ratio after 20 min compared to deposition	40 min mercury lamp irradiation	Increase in the ratio after 40 min compared to deposition
0.0207	0.02888	39.60 %	0.07447	259.98 %

TBN deposition at 300 K	20 min LED irradiation (377 nm)	Increase in the ratio after 20 min compared to deposition	40 min LED irradiation (377 nm)	Increase in the ratio after 40 min compared to deposition
0.0204	0.0505	147.54 %	0.0696	241.08 %
TBN deposition at 300 K	20 min LED irradiation (265 nm)	Increase in the ratio after 20 min compared to deposition	40 min LED irradiation (265 nm)	Increase in the ratio after 40 min compared to deposition
0.0286	0.0402	40.86 %	0.0621	117.34 %

Fig. 10F.8l exhibits the multilayer deposition of TBN molecules on a clean rutile (110) TiO_2 surface at a cryogenic temperature close to LN_2 temperature. Since the image has a larger scale compared to Fig. 8.2a, the flat steps on the surface are visible, although the mobility of the deposited TBN molecules at 77 K makes it difficult to achieve higher resolution at this stage.

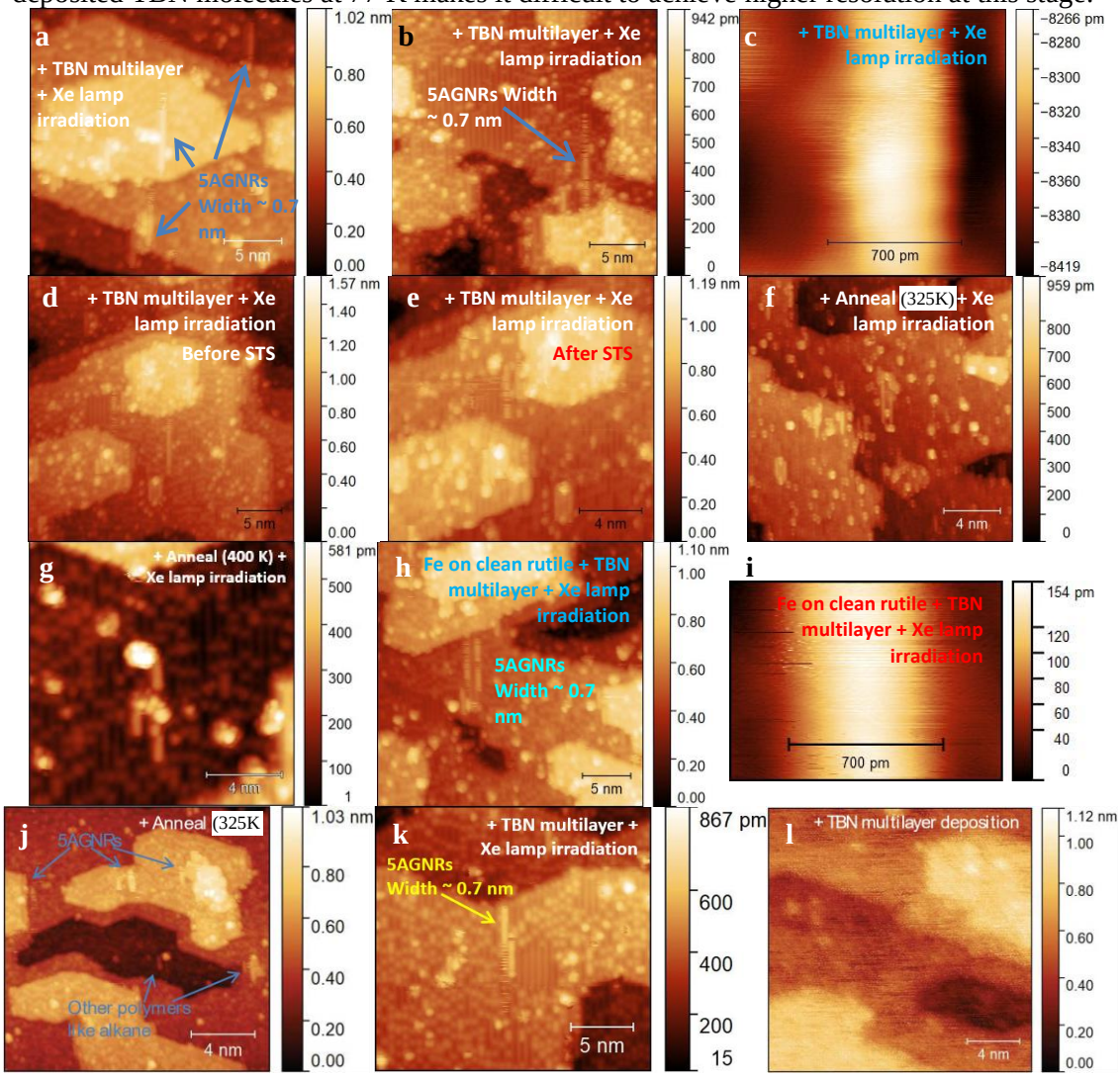

Fig. 10F.8. STM images of 5AGNRs on a rutile TiO_2 (110) surface after irradiating a TBN multilayer with a Xe lamp; (a) ≈ 25.7 nm × ≈ 25.7 nm, V_s = 1 V, I_t = 10 pA. (b) ≈ 22.6 nm × ≈ 22.6 nm, V_s = 1 V, I_t = 10 pA. (c) ≈ 1.4 nm × ≈ 1.4 nm, V_s = 1 V, I_t = 10 pA. (d) An STM image of 5AGNRs on a rutile TiO_2 (110) surface after irradiating a TBN multilayer with a Xe lamp before STS measurements; 30 nm × 30 nm, V_s = 1 V, I_t = 10 pA. (e) An STM image of 5AGNRs on a rutile TiO_2 (110) surface after irradiating a TBN multilayer with a Xe lamp and performing STS measurements; ≈ 16.9 nm × ≈ 16.9 nm, V_s = 1 V, I_t = 10 pA. (f) An STM image of 5AGNRs on a rutile TiO_2 (110) surface after irradiating a TBN multilayer with a Xe lamp and annealing at

325 K; 40 nm × 40 nm, V_s = 1 V, I_t = 10 pA. (g) An STM image of 5AGNRs on a rutile TiO_2 (110) surface after irradiating a TBN multilayer with a Xe lamp and annealing at 400 K; 14 nm × 14 nm, V_s = 1 V, I_t = 10 pA. STM images of 5AGNRs on a rutile TiO_2 (110) surface after deposition of Fe atoms and irradiation of a TBN multilayer with a Xe lamp; (h) ≈ 27.3 nm × ≈ 27.3 nm, V_s = 1 V, I_t = 10 pA. (i) ≈ 1.2 nm × ≈ 0.9 nm, V_s = 1 V, I_t = 10 pA. (j) An STM image of a TBN multilayer on a clean rutile TiO_2 (110) surface annealed at 325 K without irradiation and limited formation of 5AGNRs; 50 nm × 50 nm, V_s = 1 V, I_t = 10 pA. (k) An STM image of 5AGNRs on a rutile TiO_2 (110) surface after irradiating a TBN multilayer with a Xe lamp; ≈ 21.7 nm × ≈ 21.7 nm, V_s = 1 V, I_t = 10 pA. (b) An STM image of a TBN multilayer on a clean rutile TiO_2 (110) surface; 100 nm × 100 nm, Vs = 1 V, It = 10 pA. STM acquisition temperature: 77 K.

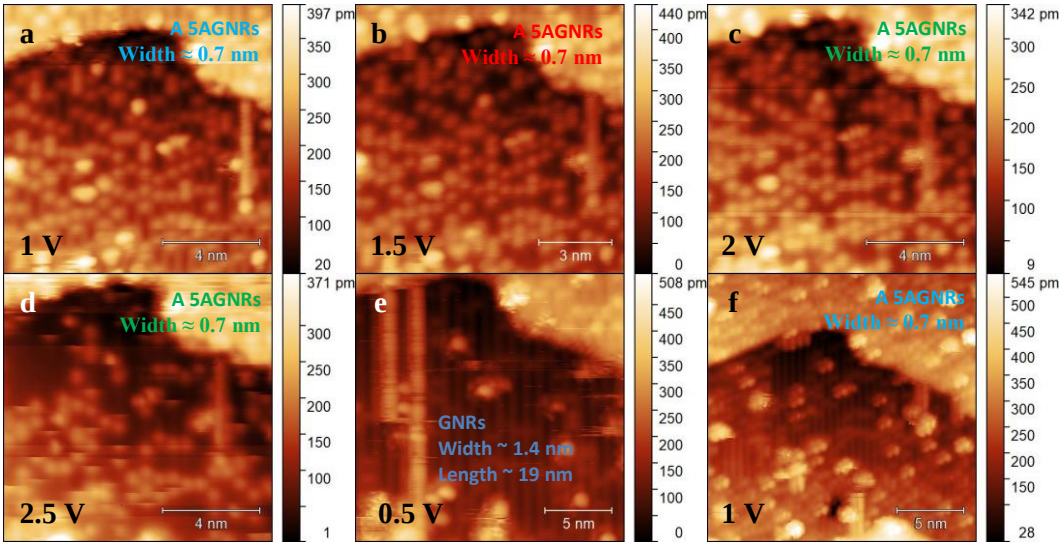

Fig. 10F.9. Bias-dependent STM images of GNRs on a rutile TiO_2 (110) surface after irradiating a TBN multilayer with a Xe lamp; (a) 11 nm × 11 nm, V_s = 1 V, I_t = 10 pA. (b) 11 nm × 11 nm, V_s = 1.5 V, I_t = 10 pA. (c) 11 nm × 11 nm, V_s = 2 V, I_t = 10 pA. (d) 11 nm × 11 nm, V_s = 2.5 V, I_t = 10 pA. (e) 11 nm × 11 nm, V_s = 0.5 V, I_t = 10 pA. (f) 20 nm × 20 nm, V_s = 1 V, I_t = 10 pA. STM acquisition temperature: 77 K.

Chapter 11

Bibliography and References

1. Fritton, M., et al., *The role of kinetics versus thermodynamics in surface-assisted Ullmann coupling on gold and silver surfaces.* Journal of the American Chemical Society, 2019. **141**(12): p. 4824-4832.
2. Lackinger, M., *Surface-assisted Ullmann coupling.* Chemical Communications, 2017. **53**(56): p. 7872-7885.
3. Doyle, C.M., et al., *Surface Mediated Synthesis of 2D Covalent Organic Networks: 1, 3, 5‐Tris (4‐bromophenyl) benzene on Au (111).* physica status solidi (b), 2019. **256**(2): p. 1800349.
4. Bhanu, U., et al., *Photoluminescence quenching in gold-MoS 2 hybrid nanoflakes.* Scientific Reports, 2014. **4**(1): p. 1-5.
5. Lin, N., et al., *Surface-confined supramolecular coordination chemistry.* Templates in Chemistry III, 2009: p. 1-44.
6. Clair, S. and D.G. de Oteyza, *Controlling a chemical coupling reaction on a surface: tools and strategies for on-surface synthesis.* Chemical reviews, 2019. **119**(7): p. 4717-4776.
7. Grill, L. and S. Hecht, *Covalent on-surface polymerization.* Nature Chemistry, 2020. **12**(2): p. 115-130.
8. Walenta, C.A., et al., *Anhydrous ethanol dehydrogenation on metal–organic chemical vapor deposition grown GaN (0001).* The Journal of Physical Chemistry C, 2017. **121**(30): p. 16393-16398.
9. Bermudez, V., *The fundamental surface science of wurtzite gallium nitride.* Surface Science Reports, 2017. **72**(4): p. 147-315.
10. Han, W., et al., *Synthesis of gallium nitride nanorods through a carbon nanotube-confined reaction.* Science, 1997. **277**(5330): p. 1287-1289.
11. Patra, S.K. and S. Schulz, *Exploring the potential of c-plane indium gallium nitride quantum dots for twin-photon emission.* Nano Letters, 2019. **20**(1): p. 234-241.
12. Saleem, U., et al., *Electronic and Optical Modulation of Pine Tree-like Nanostructures of Gallium Nitride.* The Journal of Physical Chemistry C, 2021. **125**(25): p. 13917-13924.
13. Anders, A., et al., *Hollow‐anode plasma source for molecular beam epitaxy of gallium nitride.* Review of scientific instruments, 1996. **67**(3): p. 905-907.
14. Diebold, U., *The surface science of titanium dioxide.* Surface science reports, 2003. **48**(5-8): p. 53-229.
15. Ma, X., et al., *Hydrogen-bond network promotes water splitting on the TiO_2 surface.* Journal of the American Chemical Society, 2022. **144**(30): p. 13565-13573.

16. Guo, D., et al., *Two-dimensional Dirac-line semimetals resistant to strong spin–orbit coupling.* Science Bulletin, 2022. **67**: p. 1954.
17. Ma, X., et al., *Formation of plasmonic polarons in highly electron-doped anatase TiO_2.* Nano Letters, 2020. **21**(1): p. 430-436.
18. Jiang, A., M. Qi, and J. Xiao, *Preparation, structure, properties, and application of copper nitride (Cu3N) thin films: A review.* Journal of materials science & technology, 2018. **34**(9): p. 1467-1473.
19. Chen, P., et al., *Manipulating photon emission efficiency with local electronic states in a tunneling gap.* Optics Express, 2014. **22**(7): p. 8234-8242.
20. Cremer, R., et al., *Deposition and Characterization of Metastable Cu 3 N Layers for Applications in Optical Data Storage.* Microchimica Acta, 2000. **133**: p. 299-302.
21. Asano, M., K. Umeda, and A. Tasaki, *Cu3N thin film for a new light recording media.* Japanese Journal of Applied Physics, 1990. **29**(10R): p. 1985.
22. Maruyama, T. and T. Morishita, *Copper nitride and tin nitride thin films for write‐once optical recording media.* Applied Physics Letters, 1996. **69**(7): p. 890-891.
23. Borsa, D., S. Grachev, and D. Boerma, *Development of epitaxial nitride-based bilayers for magnetic tunnel junctions.* IEEE transactions on magnetics, 2002. **38**(5): p. 2709-2711.
24. Soto, G., J. Dıaz, and W. De la Cruz, *Copper nitride films produced by reactive pulsed laser deposition.* Materials Letters, 2003. **57**(26-27): p. 4130-4133.
25. Nakamura, S., T. Mukai, and M. Senoh, *Candela‐class high‐brightness InGaN/AlGaN double‐heterostructure blue‐light‐emitting diodes.* Applied Physics Letters, 1994. **64**(13): p. 1687-1689.
26. Humphreys, C.J., *Solid-state lighting.* MRS Bulletin, 2008. **33**(4): p. 459-470.
27. Morkoc, H. and S.N. Mohammad, *High-luminosity blue and blue-green gallium nitride light-emitting diodes.* Science, 1995. **267**(5194): p. 51-55.
28. Shur, M., *GaN based transistors for high power applications.* Solid-State Electronics, 1998. **42**(12): p. 2131-2138.
29. Zheng, Z., et al., *Gallium nitride-based complementary logic integrated circuits.* Nature Electronics, 2021. **4**(8): p. 595-603.
30. Kang, J.S., et al., *Integration of boron arsenide cooling substrates into gallium nitride devices.* Nature Electronics, 2021. **4**(6): p. 416-423.
31. Ravi, L., et al., *Growth of gallium nitride nanowires on sapphire and silicon by chemical vapor deposition for water splitting applications.* Applied Surface Science, 2018. **449**: p. 213-220.
32. Zeng, G., et al., *Development of a photoelectrochemically self-improving Si/GaN photocathode for efficient and durable H2 production.* Nature Materials, 2021. **20**(8): p. 1130-1135.
33. Zhangyang, X., et al., *Structural, electrical and optical properties of InxGa1-xN nanowires photocathode.* Applied Surface Science, 2022. **593**: p. 153394.
34. Oliver, R.A., *Critical Assessment 23: Gallium nitride-based visible light-emitting diodes.* Materials Science and Technology, 2016. **32**(8): p. 737-745.
35. Barth, J.V., *Molecular Architectonic on Metal Surfaces.* Annual Review of Physical Chemistry, 2007. **58**: p. 375-407.
36. Elemans, J.A., S. Lei, and S. De Feyter, *Molecular and Supramolecular Networks on Surfaces: From Two‐Dimensional Crystal Engineering to Reactivity.* Angewandte Chemie International Edition, 2009. **48**(40): p. 7298-7332.
37. Bartels, L., *Tailoring molecular layers at metal surfaces.* Nature chemistry, 2010. **2**(2): p. 87-95.
38. Mali, K.S., et al., *Exploring the complexity of supramolecular interactions for patterning at the liquid–solid interface.* Accounts of Chemical Research, 2012. **45**(8): p. 1309-1320.
39. Gourdon, A., *On‐surface covalent coupling in ultrahigh vacuum.* Angewandte Chemie International Edition, 2008. **47**(37): p. 6950-6953.

40. Perepichka, D.F. and F. Rosei, *Extending polymer conjugation into the second dimension.* Science, 2009. **323**(5911): p. 216-217.
41. Palma, C.-A. and P. Samorì, *Blueprinting macromolecular electronics.* Nature chemistry, 2011. **3**(6): p. 431-436.
42. Klappenberger, F., et al., *On-surface synthesis of carbon-based scaffolds and nanomaterials using terminal alkynes.* Accounts of chemical research, 2015. **48**(7): p. 2140-2150.
43. Sun, K., et al., *Surface-assisted alkane polymerization: investigation on structure–reactivity relationship.* Journal of the American Chemical Society, 2018. **140**(14): p. 4820-4825.
44. Sun, K., et al., *Substrate-controlled synthesis of 5-armchair graphene nanoribbons.* The Journal of Physical Chemistry C, 2020. **124**(21): p. 11422-11427.
45. Wieghold, S., et al., *Photoresponse of supramolecular self-assembled networks on graphene–diamond interfaces.* Nature Communications, 2016. **7**(1): p. 1-8.
46. Li, J., et al., *Three-dimensional bicomponent supramolecular nanoporous self-assembly on a hybrid all-carbon atomically flat and transparent platform.* Nano letters, 2014. **14**(8): p. 4486-4492.
47. Mayne, A.J. and G. Dujardin, *STM characterization of hydrogenated diamond surfaces.* New Diamond and Frontier Carbon Technology, 2005. **15**(5).
48. RE Stallcup, I. and J.M. Pérez, *Scanning tunneling microscopy studies of temperature-dependent etching of diamond (100) by atomic hydrogen.* Physical Review Letters, 2001. **86**(15): p. 3368.
49. Chen, Y., et al., *Growth of 2D GaN single crystals on liquid metals.* Journal of the American Chemical Society, 2018. **140**(48): p. 16392-16395.
50. Xiao, Y., et al., *Crystallographic Effects of GaN Nanostructures in Photoelectrochemical Reaction.* Nano Letters, 2022. **22**(6): p. 2236-2243.
51. Grodzicki, M., *Properties of Bare and Thin-Film-Covered GaN (0001) Surfaces.* Coatings, 2021. **11**(2): p. 145.
52. Manske, W.T., et al., *Morphology of GaN (0001) and GaN (0001) surfaces: Persistence of surface clusters.* Journal of Vacuum Science & Technology A: Vacuum, Surfaces, and Films, 2003. **21**(2): p. 506-514.
53. Hellman, E., *The polarity of GaN: a critical review.* Materials Research Society Internet Journal of Nitride Semiconductor Research, 1998. **3**.
54. Henning, A., et al., *Aluminum Oxide at the Monolayer Limit via Oxidant-free Plasma-Assisted Atomic Layer Deposition on GaN.* Advanced Functional Materials, 2021. **31**(33): p. 2101441.
55. Chaudhuri, R., et al., *A polarization-induced 2D hole gas in undoped gallium nitride quantum wells.* Science, 2019. **365**(6460): p. 1454-1457.
56. Oliver, R., et al., *Gallium nitride surface preparation optimised using in situ scanning tunnelling microscopy.* Applied Surface Science, 2003. **214**(1-4): p. 1-10.
57. Kollmannsberger, S.L., et al., *Doping-dependent adsorption and photon-stimulated desorption of CO on Gan (0001).* The Journal of Physical Chemistry C, 2017. **121**(15): p. 8473-8479.
58. Ni, C.-J. and F. Chau-Nan Hong, *Low-temperature growth of gallium nitride films by inductively coupled-plasma-enhanced reactive magnetron sputtering.* Journal of Vacuum Science & Technology A: Vacuum, Surfaces, and Films, 2014. **32**(3): p. 031514.
59. Feenstra, R.M., et al., *Recent developments in surface studies of GaN and AlN.* Journal of Vacuum Science & Technology B: Microelectronics and Nanometer Structures Processing, Measurement, and Phenomena, 2005. **23**(3): p. 1174-1180.
60. Smith, A., et al., *Reconstructions of the GaN (000 1) surface.* Physical Review Letters, 1997. **79**(20): p. 3934.

61. Lu, Q., et al., *Reproducible resistive‐switching behavior in copper‐nitride thin film prepared by plasma‐immersion ion implantation.* physica status solidi (a), 2011. **208**(4): p. 874-877.
62. Sufyan, A., M. Sajjad, and J.A. Larsson, *Evaluating the potential of planar checkerboard lattice Cu2N monolayer as anode material for lithium and sodium-ion batteries using first-principles methods.* Applied Surface Science, 2024: p. 159474.
63. Moreno-Armenta, M.G., A. Martínez-Ruiz, and N. Takeuchi, *Ab initio total energy calculations of copper nitride: the effect of lattice parameters and Cu content in the electronic properties.* Solid State Sciences, 2004. **6**(1): p. 9-14.
64. Mondal, S. and C.R. Raj, *Copper nitride nanostructure for the electrocatalytic reduction of oxygen: kinetics and reaction pathway.* The Journal of Physical Chemistry C, 2018. **122**(32): p. 18468-18475.
65. Yamada, N., et al., *P-to n-type conversion and nonmetal–metal transition of lithium-inserted Cu3N Films.* Chemistry of Materials, 2015. **27**(23): p. 8076-8083.
66. Du, Y., et al., *Effect of oxygen inclusion on microstructure and thermal stability of copper nitride thin films.* Journal of Materials Research, 2007. **22**: p. 3052-3057.
67. Mavridou, K., *Oxidation of Cu_3N studied by resonance Raman Spectroscopy*, in *Post Graduate Course Program Materials Physics & Technology*. 2021, Aristotle University of Thessaloniki.
68. Hu, X., et al., *Realization of a Two-Dimensional Checkerboard Lattice in Monolayer Cu2N.* Nano Letters, 2023.
69. Ali, H.T., et al., *A new approach for the growth of copper nitrides thin films by thermal evaporation using nitrogen as source gas.* Optik, 2021. **245**: p. 167666.
70. Hansen, M. and K. Anderko, *Constitution of Binary Alloys*. Metallurgy and Metallurgical Engineering, ed. R.F. Mehl and B.M. B. 1958, New York, Toronto, London: McGRAW-HILL book company. 1305.
71. Schrötter, A., Liebigs Annalen, 1841. **37**: p. 131.
72. Douglas, J., *Journal of the Society for Arts, Vol. 43, no. 2230.* The Journal of the Society of Arts, 1895. **43**(2230): p. 821-832.
73. Guntz, A. and H.B. Junior, Bulletin de la Société Chimique, 1906. **35**: p. 201-207.
74. Juza, R. and H. Hahn, *Kupfernitrid metallamide und metallnitride. vii.* Zeitschrift für anorganische und allgemeine Chemie, 1939. **241**(2‐3): p. 172-178.
75. Juza, R. and H. Hahn, *Über die kristallstrukturen von Cu_3N, GaN und InN metallamide und metallnitride.* Zeitschrift für anorganische und allgemeine Chemie, 1938. **239**(3): p. 282-287.
76. Linsebigler, A.L., G. Lu, and J.T. Yates Jr, *Photocatalysis on TiO2 surfaces: principles, mechanisms, and selected results.* Chemical reviews, 1995. **95**(3): p. 735-758.
77. Scheiber, P., et al., *(Sub) Surface mobility of oxygen vacancies at the TiO 2 anatase (101) surface.* Physical review letters, 2012. **109**(13): p. 136103.
78. Waser, R. and M. Aono, *Nanoionics-based resistive switching memories.* Nanoscience And Technology: A Collection of Reviews from Nature Journals, 2010: p. 158-165.
79. Suntivich, J., et al., *Design principles for oxygen-reduction activity on perovskite oxide catalysts for fuel cells and metal–air batteries.* Nature chemistry, 2011. **3**(7): p. 546-550.
80. He, Y., et al., *Evidence for the predominance of subsurface defects on reduced anatase TiO 2 (101).* Physical Review Letters, 2009. **102**(10): p. 106105.
81. Dankovic, D.A. and E.D. Kuempel, *Occupational exposure to titanium dioxide.* 2011.
82. Herman, G. and Y. Gao, *Growth of epitaxial anatase (001) and (101) films.* Thin Solid Films, 2001. **397**(1-2): p. 157-161.
83. Liang, Y., et al., *Surface structure of anatase TiO 2 (001): reconstruction, atomic steps, and domains.* Physical Review B, 2001. **63**(23): p. 235402.
84. Tanner, R., Y. Liang, and E. Altman, *Structure and chemical reactivity of adsorbed carboxylic acids on anatase TiO2 (001).* Surface science, 2002. **506**(3): p. 251-271.

85. Setvín, M., et al., *Reaction of O2 with subsurface oxygen vacancies on TiO2 anatase (101).* Science, 2013. **341**(6149): p. 988-991.
86. Setvin, M., et al., *Electron transfer between anatase TiO2 and an O2 molecule directly observed by atomic force microscopy.* Proceedings of the National Academy of Sciences, 2017. **114**(13): p. E2556-E2562.
87. Mao, Y., et al., *Interfacial polarons in van der Waals heterojunction of monolayer $SnSe_2$ on $SrTiO_3$ (001).* Nano Letters, 2020. **20**(11): p. 8067-8073.
88. Kolmer, M., et al., *On-surface polymerization on a semiconducting oxide: aryl halide coupling controlled by surface hydroxyl groups on rutile TiO 2 (011).* Chemical Communications, 2015. **51**(56): p. 11276-11279.
89. Papageorgiou, A.C., *Surface studies of titania related nanostructures*. 2007, University of London.
90. Papageorgiou, A.C., et al., *Low-dimensional, reduced phases of ultrathin TiO2.* ACS nano, 2007. **1**(5): p. 409-414.
91. Bennett, R., et al., *STM and LEED observations of the surface structure of TiO 2 (110) following crystallographic shear plane formation.* Physical Review B, 1999. **59**(15): p. 10341.
92. Rohrer, G.S., V.E. Henrich, and D.A. Bonnell, *Structure of the reduced TiO2 (110) surface determined by scanning tunneling microscopy.* Science, 1990. **250**(4985): p. 1239-1241.
93. Vasseur, G., et al., *Π band dispersion along conjugated organic nanowires synthesized on a metal oxide semiconductor.* Journal of the American Chemical Society, 2016. **138**(17): p. 5685-5692.
94. Tan, S., et al., *Interfacial hydrogen-bonding dynamics in surface-facilitated dehydrogenation of water on TiO_2 (110).* Journal of the American Chemical Society, 2019. **142**(2): p. 826-834.
95. Chu, W., et al., *Ultrafast charge transfer coupled to quantum proton motion at molecule/metal oxide interface.* Science Advances, 2022. **8**(24): p. eabo2675.
96. Jiang, S., et al., *Topologically localized excitons in single graphene nanoribbons.* Science, 2023. **379**(6636): p. 1049-1054.
97. Ruffieux, P., et al., *On-surface synthesis of graphene nanoribbons with zigzag edge topology.* Nature, 2016. **531**(7595): p. 489-492.
98. Zhao, Y., et al., *What are the adsorption sites for CO on the reduced TiO2 (110)-1× 1 surface?* Journal of the American Chemical Society, 2009. **131**(23): p. 7958-7959.
99. Weston, G.F., *Ultrahigh vacuum practice*. 2013: Elsevier.
100. Oura, K., et al., *Surface science: an introduction*. 2003: Springer Science & Business Media.
101. Gokhale, S., et al., *Silicon bonding for ultrahigh vaccuum surface science studies.* Journal of Vacuum Science & Technology A: Vacuum, Surfaces, and Films, 2001. **19**(2): p. 706-708.
102. Stevie, F.A. and C.L. Donley, *Introduction to x-ray photoelectron spectroscopy.* Journal of Vacuum Science & Technology A: Vacuum, Surfaces, and Films, 2020. **38**(6): p. 063204.
103. Kakavandi, R., *Highly controlled deposition of organic magnets on metal-oxide surfaces*. 2015, Eberhard Karls Universität Tübingen.
104. Alford, T.L., L.C. Feldman, and J.W. Mayer, *Fundamentals of nanoscale film analysis*. 2007: Springer Science & Business Media.
105. Carlson, T., *Basic assumptions and recent developments in quantitative XPS.* Surface and Interface analysis, 1982. **4**(4): p. 125-134.
106. Allegretti, F. *ELECTRON SPECTROSCOPY OF SURFACES: Elemental and Chemical Analysis with X-ray Photoelectron Spectroscopy*. 2020; Versuch Nr. 35, F-Praktikum in den Bachelor- und Masterstudieng¨angen]. Available from: https://www.ph.tum.de/academics/org/labs/fopra/docs/userguide-35.en.pdf.

107. Biesinger, M.C., et al., *Resolving surface chemical states in XPS analysis of first row transition metals, oxides and hydroxides: Sc, Ti, V, Cu and Zn.* Applied surface science, 2010. **257**(3): p. 887-898.
108. Fuggle, J., et al., *X-ray excited Auger and photoelectron spectra of magnesium, some alloys of magnesium and its oxide.* Journal of Physics F: Metal Physics, 1975. **5**(2): p. 375.
109. Nix, R., *Surface Science*. 2020: Queen Mary, University of London.
110. Engelhard, M.H., et al., *Introductory guide to backgrounds in XPS spectra and their impact on determining peak intensities.* Journal of Vacuum Science & Technology A: Vacuum, Surfaces, and Films, 2020. **38**(6): p. 063203.
111. Bravo Sanchez, M., et al., *Composition assessment of ferric oxide by accurate peak fitting of the Fe 2p photoemission spectrum.* Surface and Interface Analysis, 2017. **49**(4): p. 253-260.
112. Willmott, P., *An introduction to synchrotron radiation: techniques and applications*. 2019: John Wiley & Sons.
113. Lüth, H., *Solid surfaces, interfaces and thin films*. Vol. 4. 2001: Springer.
114. Romberg, R., et al., *Photon stimulated desorption of neutral hydrogen atoms from condensed water and ammonia by resonant O1s and N1s excitation: search for the signature of ultrafast bond breaking.* Surface science, 2000. **451**(1-3): p. 116-123.
115. Douglas, D.J., *Linear quadrupoles in mass spectrometry.* Mass spectrometry reviews, 2009. **28**(6): p. 937-960.
116. Zhang, Y.Q., Lin, T., Allegretti, F. *Basic techniques of surface physics: surface analysis with temperature programmed desorption and low-energy electron diffraction.* 2020; Available from: https://www.ph.nat.tum.de/fileadmin/w00bya/e20/_my_direct_uploads/abstract-89.en.pdf.
117. Kolasinski, K.W., *Surface science: foundations of catalysis and nanoscience*. 4 ed. 2012: John Wiley & Sons.
118. King, D.A., *Thermal desorption from metal surfaces: A review.* Surface Science, 1975. **47**(1): p. 384-402.
119. De Jong, A. and J. Niemantsverdriet, *Thermal desorption analysis: Comparative test of ten commonly applied procedures.* Surface Science, 1990. **233**(3): p. 355-365.
120. Woodruff, D.P., *Modern techniques of surface science*. 2016: Cambridge university press. 490.
121. Silva, J.L.D., C. Stampfl, and M. Scheffler, *Adsorption of Xe atoms on metal surfaces: New insights from first-principles calculations.* Physical review letters, 2003. **90**(6): p. 066104.
122. Smedh, M., et al., *Vibrationally resolved C 1s photoemission from CO absorbed on Rh (1 1 1): the investigation of a new chemically shifted C 1s component.* Surface science, 2001. **491**(1-2): p. 99-114.
123. Smith, R.S., R.A. May, and B.D. Kay, *Desorption kinetics of Ar, Kr, Xe, N2, O2, CO, methane, ethane, and propane from graphene and amorphous solid water surfaces.* The Journal of Physical Chemistry B, 2016. **120**(8): p. 1979-1987.
124. Gragnaniello, L., et al., *Surface structure of nickel oxide layers on a Rh (111) surface.* Surface science, 2013. **611**: p. 86-93.
125. Binnig, G. and H. Rohrer, *Scanning tunneling microscopy—from birth to adolescence.* Reviews of Modern Physics, 1987. **59**(3): p. 615.
126. Voigtländer, B., *Scanning probe microscopy: Atomic force microscopy and scanning tunneling microscopy*. 2015: Springer.
127. Chen, C.J., *Origin of atomic resolution on metal surfaces in scanning tunneling microscopy.* Physical review letters, 1990. **65**(4): p. 448.
128. Lang, N.D., *Theory of single-atom imaging in the scanning tunneling microscope.* Physical Review Letters, 1986. **56**(11): p. 1164.
129. Bardeen, J., *Tunnelling from a many-particle point of view.* Physical review letters, 1961. **6**(2): p. 57.

130. Tersoff, J. and D.R. Hamann, *Theory of the scanning tunneling microscope.* Physical Review B, 1985. **31**(2): p. 805.
131. Lang, N.D., *Vacuum tunneling current from an adsorbed atom.* Physical Review Letters, 1985. **55**(2): p. 230.
132. Barth, J.V., et al., *Scanning tunneling microscopy observations on the reconstructed Au (111) surface: Atomic structure, long-range superstructure, rotational domains, and surface defects.* Physical Review B, 1990. **42**(15): p. 9307.
133. Barth, J.V., G. Costantini, and K. Kern, *Engineering atomic and molecular nanostructures at surfaces.* Nature, 2005. **437**(7059): p. 671-679.
134. Love, J.C., et al., *Self-assembled monolayers of thiolates on metals as a form of nanotechnology.* Chemical reviews, 2005. **105**(4): p. 1103-1170.
135. Lehn, J.M., *Supramolecular chemistry—scope and perspectives molecules, supermolecules, and molecular devices (Nobel Lecture).* Angewandte Chemie International Edition in English, 1988. **27**(1): p. 89-112.
136. Rostami, M., et al., *Multi‐and Gray‐Scale Thermal Lithography of Silk Fibroin as Water‐Developable Resist for Micro and Nanofabrication.* Advanced Science, 2024. **11**(12): p. 2303518.
137. Henß, A.-K., et al., *Density fluctuations as door-opener for diffusion on crowded surfaces.* Science, 2019. **363**(6428): p. 715-718.
138. Joshi, S., et al., *Boron nitride on Cu (111): an electronically corrugated monolayer.* Nano letters, 2012. **12**(11): p. 5821-5828.
139. Halliday, D., R. Resnick, and J. Walker, *Fundamentals of physics*. 10 ed. 2013: John Wiley & Sons.
140. Hellwig, R., *Alkyne‐Based Nanostructures on Silver Substrates*. 2018: Springer.
141. Kaya, P., et al., *A DFT investigation for the Dopamine adsorption on the pristine and defected blue arsenic-phosphorus monolayers.* Surfaces and Interfaces, 2024. **46**: p. 104087.
142. Rostami, M., et al., *Influencing the surface quality of free-standing wurtzite gallium nitride in ultra-high vacuum: Stoichiometry control by ammonia and bromine adsorption.* Applied Surface Science, 2024: p. 160880.
143. Takanabe, K. and K. Domen, *Toward visible light response: overall water splitting using heterogeneous photocatalysts.* Green, 2011. **1**(5-6): p. 313-322.
144. Winnerl, A., R.N. Pereira, and M. Stutzmann, *Kinetics of optically excited charge carriers at the GaN surface: Influence of catalytic Pt nanostructures.* Journal of Applied Physics, 2015. **118**(15): p. 155704.
145. Zhou, B., et al., *Gallium nitride nanowire as a linker of molybdenum sulfides and silicon for photoelectrocatalytic water splitting.* Nature Communications, 2018. **9**(1): p. 1-8.
146. Liu, C., et al., *Gallium nitride catalyzed the direct hydrogenation of carbon dioxide to dimethyl ether as primary product.* Nature Communications, 2021. **12**(1): p. 1-10.
147. Frentrup, M., et al., *X-ray diffraction analysis of cubic zincblende III-nitrides.* Journal of Physics D: Applied Physics, 2017. **50**(43): p. 433002.
148. Gundimeda, A., et al., *Influence of AlxGa1-xN nucleation layers on MOVPE-grown zincblende GaN epilayers on 3C-SiC/Si (001).* Journal of Physics D: Applied Physics, 2022.
149. Wang, D., et al., *Efficient Heterojunctions via the in Situ Self-Assembly of $BiVO_4$ Quantum Dots on SiC Facets for Enhanced Photocatalysis.* ACS Applied Nano Materials, 2018. **1**(9): p. 4594-4601.
150. Graham, S. and S. Choi, *Integrating boron arsenide into power devices.* Nature Electronics, 2021. **4**(6): p. 380-381.
151. Signore, M., et al., *Effect of silicon-based substrates and deposition type on sputtered AlN thin films: physical & chemical properties and suitability for piezoelectric device integration.* Applied Surface Science, 2022: p. 154017.

152. Smith, A., et al., *Reconstructions of GaN (0001) and (0001) surfaces: Ga-rich metallic structures.* Journal of Vacuum Science & Technology B: Microelectronics and Nanometer Structures Processing, Measurement, and Phenomena, 1998. **16**(4): p. 2242-2249.
153. Smith, A., et al., *Scanning tunneling microscopy of the GaN (000-1) surface.* Applied Physics A, 1998. **66**(1): p. S947-S951.
154. Xue, Q., et al., *Imaging wurtzite GaN surfaces by molecular beam epitaxy-scanning tunneling microscopy.* Thin Solid Films, 2000. **367**(1-2): p. 149-158.
155. Shen, C., et al., *Development of in situ characterization techniques in molecular beam epitaxy.* Journal of Semiconductors, 2024. **45**(3): p. 031301-24.
156. Banfi, E., et al., *Atomically resolved study of the unpinned GaN (10 1¯ 0) surface by cross-sectional scanning tunneling microscopy.* Physical Review B, 2023. **108**(8): p. 085304.
157. Liu, Z., et al., *Optimization and characterization of III–V surface cleaning.* Journal of Vacuum Science & Technology B: Microelectronics and Nanometer Structures Processing, Measurement, and Phenomena, 2003. **21**(4): p. 1953-1958.
158. Machuca, F., et al., *Simple method for cleaning gallium nitride (0001).* Journal of Vacuum Science & Technology A: Vacuum, Surfaces, and Films, 2002. **20**(5): p. 1784-1786.
159. Zajac, M., et al., *Basic ammonothermal growth of Gallium Nitride–State of the art, challenges, perspectives.* Progress in Crystal Growth and Characterization of Materials, 2018. **64**(3): p. 63-74.
160. Kucharski, R., et al., *Growth of bulk GaN crystals.* Journal of Applied Physics, 2020. **128**(5).
161. Grabianska, K., et al., *GaN single crystalline substrates by ammonothermal and HVPE methods for electronic devices.* Electronics, 2020. **9**(9): p. 1342.
162. Sochacki, T., et al., *Fundamental Studies on Crystallization and Reaching the Equilibrium Shape in Basic Ammonothermal Method: Growth on a Native Lenticular Seed.* Materials, 2022. **15**(13): p. 4621.
163. Scholz, F., M. Bockowski, and E. Grzanka, *GaN‐Based Materials: Substrates, Metalorganic Vapor‐Phase Epitaxy, and Quantum Well Properties.* Nitride Semiconductor Technology: Power Electronics and Optoelectronic Devices, 2020: p. 41-98.
164. Grabianska, K., et al., *Recent progress in basic ammonothermal GaN crystal growth.* Journal of Crystal Growth, 2020. **547**: p. 125804.
165. Boćkowski, M. and I. Grzegory, *Recent Progress in Crystal Growth of Bulk GaN.* Acta Physica Polonica, A., 2022. **141**(3).
166. Reshchikov, M., et al., *Defect-related photoluminescence from ammono GaN.* Journal of Applied Physics, 2021. **129**(9): p. 5703.
167. Reshchikov, M., et al., *The effect of annealing on photoluminescence from defects in ammonothermal GaN.* Journal of Applied Physics, 2022. **131**(3): p. 5704.
168. Kruszewski, P., et al., *Electrical properties of vertical GaN Schottky diodes on Ammono-GaN substrate.* Materials Science in Semiconductor Processing, 2019. **96**: p. 132-136.
169. Taube, A., et al., *High Breakdown Voltage and High Current Injection Vertical GaN-on-GaN pn Diodes With Extremely Low On-Resistance Fabricated on Ammonothermally Grown Bulk GaN Substrates.* IEEE Transactions on Electron Devices, 2022. **69**(11): p. 6255-6259.
170. Kirste, L., et al., *Large-Scale Defect Clusters with Hexagonal Honeycomb-like Arrangement in Ammonothermal GaN Crystals.* Materials, 2022. **15**(19): p. 6996.
171. Grabianska, K., et al., *On Stress-Induced Polarization Effect in Ammonothermally Grown GaN Crystals.* Crystals, 2022. **12**(4): p. 554.
172. Kirste, L., et al., *Structural analysis of low defect ammonothermally grown GaN wafers by Borrmann effect X-ray topography.* Materials, 2021. **14**(19): p. 5472.

173. Miller, D.J., *Gallium nitride epitaxy by a novel hybrid VPE technique*. 2011: Stanford University.
174. Ehrentraut, D., E. Meissner, and M. Bockowski, *Technology of gallium nitride crystal growth*. Vol. 133. (2010): Springer Science & Business Media.
175. Ashraf, H., et al., *Reduction of the dislocation density in HVPE-grown GaN epi-layers by an in situ SiNx treatment.* Journal of Crystal Growth, 2010. **312**(4): p. 595-600.
176. Łucznik, B., et al., *Deposition of thick GaN layers by HVPE on the pressure grown GaN substrates.* Journal of crystal growth, 2005. **281**(1): p. 38-46.
177. Fujito, K., et al., *Bulk GaN crystals grown by HVPE.* Journal of Crystal Growth, 2009. **311**(10): p. 3011-3014.
178. Liu, Y., et al., *Synchrotron X-ray topography characterization of high quality ammonothermal-grown gallium nitride substrates.* Journal of Crystal Growth, 2020. **551**: p. 125903.
179. Liu, Y., et al. *Synchrotron X-Ray Topography Characterization of Power Electronic GaN Materials*. in *Materials Science Forum*. 2022. Trans Tech Publ.
180. Ambacher, O., et al., *Two-dimensional electron gases induced by spontaneous and piezoelectric polarization charges in N-and Ga-face AlGaN/GaN heterostructures.* Journal of Applied Physics, 1999. **85**(6): p. 3222-3233.
181. Syed, N., et al., *Wafer-sized ultrathin gallium and indium nitride nanosheets through the ammonolysis of liquid metal derived oxides.* Journal of the American Chemical Society, 2018. **141**(1): p. 104-108.
182. Sanjay, S. and K. Baskar, *Fabrication of Schottky barrier diodes on clump of gallium nitride nanowires grown by chemical vapour deposition.* Applied Surface Science, 2018. **456**: p. 526-531.
183. Nečas, D. and P. Klapetek, *Gwyddion: an open-source software for SPM data analysis.* Open Physics, 2012. **10**(1): p. 181-188.
184. Yeh, J. and I. Lindau, *Atomic subshell photoionization cross sections and asymmetry parameters: $1 \leqslant Z \leqslant 103$.* Atomic Data and Nuclear Data Tables, 1985. **32**(1): p. 1-155.
185. Krawczyk, M., et al., *Energy dependence of electron inelastic mean free paths in bulk GaN crystals.* Surface Science, 2004. **566**: p. 1234-1239.
186. Martínez, P.D., et al., *VAMAS Inter-laboratory study on intensity calibration for XPS instruments using low-density polyethylene.* Journal of Vacuum Science Technology A, 2020. **38**(6): p. 063208-1-063208-15.
187. Alvarado-Leal, L., et al., *Formaldehyde adsorption on a hydrogenated gallium nitride monolayer: A density functional theory study.* Applied Surface Science, 2020. **506**: p. 144944.
188. Bieri, M., et al., *Two-dimensional polymer formation on surfaces: insight into the roles of precursor mobility and reactivity.* Journal of the American Chemical Society, 2010. **132**(46): p. 16669-16676.
189. Mitchell, S., et al., *Reactions of gallium atoms.* The Journal of Physical Chemistry, 1986. **90**(23): p. 6148-6154.
190. Linstorm, P., *NIST chemistry webbook, NIST standard reference database number 69.* Journal of Physical and Chemical Reference Data Monographs, 1998. **9**: p. 1-1951.
191. Miescher, E. and M. Wehrli, *Die Spektren der Galliumhalogenide.* Helvetica Physica Acta, 1934. **6**: p. 458.
192. Barrett, A. and M. Mandel, *Microwave spectra of the Tl, In, and Ga monohalides.* Physical Review, 1958. **109**(5): p. 1572.
193. Dutta, A., J. Bhattacharjee, and K.K. Das, *$A^3\Pi 0^+ – X^1\Sigma^+_{0^+}$ and $B^3\Pi_1 – X^1\Sigma^+_{0^+}$ transitions of GaI: an MRDCI study.* Chemical Physics Letters, 1999. **314**(3-4): p. 347-352.
194. Barrow, R., *Dissociation energies of the gaseous mono-halides of boron, aluminium, gallium, indium and thallium.* Transactions of the Faraday Society, 1960. **56**: p. 952-958.
195. Bulewicz, E., L. Phillips, and T. Sugden, *Determination of dissociation constants and heats of formation of simple molecules by flame photometry. Part 8.—Stabilities of the*

gaseous diatomic halides of certain metals. Transactions of the Faraday Society, 1961. **57**: p. 921-931.
196. Nair, K.R., H.-U. Schütze-Pahlmann, and J. Hoeft, *Millimeter-wave rotational spectrum and molecular constants of diatomic gallium bromide.* Chemical Physics Letters, 1981. **80**(1): p. 149-152.
197. Brunetti, B., V. Piacente, and P. Scardala, *A study on the sublimation of gallium tribromide.* Journal of Chemical & Engineering Data, 2009. **54**(8): p. 2273-2276.
198. Dehmer, J.L., et al., *Photoelectron spectroscopy of high temperature vapors. V. HeI spectra of GaX_3 and InX_3 (X= Cl, Br, I).* The Journal of Chemical Physics, 1974. **61**(2): p. 594-599.
199. Barker, G.K., et al., *Bonding studies of boron and the Group 3–5 elements. Part XV. He (I) photoelectron spectra of monomeric Group 3 trihalide, trimethyl, and mixed halogenomethyl species.* Journal of the Chemical Society, Dalton Transactions, 1975(18): p. 1765-1771.
200. Lappert, M., et al., *Bonding studies of compounds of boron and the Group III and IV elements.: XII. Variable temperature He I photoelectron spectra of Group III halides, $2MX3 \rightleftharpoons M2X6$ (M= Al or Ga, X= Cl, Br, or I).* Journal of Electron Spectroscopy and Related Phenomena, 1974. **3**(3): p. 237-239.
201. Hönle, W., et al., *Preparation, crystal structure, and ionic conductivity of digallium tribromide, Ga2Br3.* Journal of Solid State Chemistry, 1986. **61**(2): p. 171-180.
202. Cottrell, T.L., *The strengths of chemical bonds*. (1954): Butterworths Scientific, Academic Press, 2nd edition.
203. Gaston, N. and A. Parker, *On the bonding of Ga2, structures of Gan clusters and the relation to the bulk structure of gallium.* Chemical Physics Letters, 2011. **501**(4-6): p. 375-378.
204. Zhao, Y., et al., *Gallium clusters Ga n (n= 1− 6): Structures, thermochemistry, and electron affinities.* The Journal of Physical Chemistry A, 2004. **108**(36): p. 7448-7459.
205. James, G.S., *Lange's handbook of chemistry.* CD & W Inc, Wyoming, 2005.
206. Greenwood, N. and T. Srivastava, *Relative acceptor strengths of the gallium trihalides towards pyridine and triethylamine as donors.* Journal of the Chemical Society A: Inorganic, Physical, Theoretical, 1966. **A**: p. 267-270.
207. Denis, P.A. and K. Balasubramanian, *Spectroscopic constants and potential energy curves of gallium nitride (GaN) and ions: GaN^+ and GaN^-*. Chemical Physics Letters, 2006. **423**(1-3): p. 247-253.
208. Tzeli, D., G. Theodorakopoulos, and I.D. Petsalakis, *Theoretical Study of Gallium Nitride Molecules, GaN2 and GaN4.* The Journal of Physical Chemistry A, 2008. **112**(37): p. 8858-8867.
209. Gulo, F., et al., *Li–Cu Exchange in Intercalated Cu3N—With a Remark on Cu4N.* Angewandte Chemie International Edition, 2004. **43**(15): p. 2032-2034.
210. Goedken, A., et al., *STM studies of the N/Cu (111) system: surface structure, electron confinement and tip-induced modification.* The European Physical Journal Applied Physics, 2002. **19**(2): p. 77-82.
211. Su, C.-Y., et al., *Carbon nanotube-supported Cu 3 N nanocrystals as a highly active catalyst for oxygen reduction reaction.* Journal of Materials Chemistry A, 2015. **3**(37): p. 18983-18990.
212. Silva, S. and F. Leibsle, *Room temperature quantum corrals.* Surface science, 1999. **441**(1): p. L904-L909.
213. Child, T., et al., *An Introduction to the Kondo Effect.* Notas de PHYS, 2018.
214. Fiete, G.A. and E.J. Heller, *Colloquium: Theory of quantum corrals and quantum mirages.* Reviews of Modern Physics, 2003. **75**(3): p. 933.
215. Fallberg, A., M. Ottosson, and J.O. Carlsson, *CVD of copper (I) nitride.* Chemical Vapor Deposition, 2009. **15**(10‐12): p. 300-305.
216. Dinca, V. and M. Suchea, *Functional nanostructured interfaces for environmental and biomedical applications*. Vol. A volume in Micro and Nano Technologies. 2019, Amsterdam: Elsevier. 398.

217. Liu, Z., et al., *Thermal stability of copper nitride films prepared by rf magnetron sputtering.* Thin Solid Films, 1998. **325**(1-2): p. 55-59.
218. Terada, S., H. Tanaka, and K. Kubota, *Heteroepitaxial growth of Cu3N thin films.* Journal of crystal growth, 1989. **94**(2): p. 567-568.
219. Ruggiero, C.D., T. Choi, and J.A. Gupta, *Tunneling spectroscopy of ultrathin insulating films: CuN on Cu (100).* Applied Physics Letters, 2007. **91**(25): p. 253106.
220. Baek, H., et al., *Geometric and electronic structure of passive CuN monolayer on Cu (111): a scanning tunneling microscopy and spectroscopy study.* Journal of the Korean Physical Society, 2010. **56**(2): p. 620-624.
221. Higgs, V., et al., *Formation of a Surface Nitride on Copper (111) and its Influence on Carbon Monoxide Adsorption: Investigation by Leed, RAIRS and EELS*, in *Studies in Surface Science and Catalysis*. 1986, Elsevier. p. 137-144.
222. Heskett, D., A. Baddorf, and E. Plummer, *Nitrogen-induced reconstruction of Cu (110): Formation of a surface nitride.* Surface Science, 1988. **195**(1-2): p. 94-102.
223. Burkstrand, J., et al., *Study of the N–Cu (100) system.* Journal of Vacuum Science and Technology, 1976. **13**(1): p. 291-295.
224. Hirjibehedin, C.F., C.P. Lutz, and A.J. Heinrich, *Spin coupling in engineered atomic structures.* Science, 2006. **312**(5776): p. 1021-1024.
225. Detrattanawichai, P., et al., *Exploring the impact of the nitrogen layer on a Cu (001) substrate on the spin crossover properties of [Fe (SalEen-I) 2] Br: A DFT study.* Journal of Physics and Chemistry of Solids, 2023. **173**: p. 111111.
226. Niehus, H., et al., *N-induced (2× 3) reconstruction of Cu (110): Evidence for long-range, highly directional interaction between Cu-N-Cu bonds.* Physical Review B, 1991. **43**(15): p. 12619.
227. Leibsle, F., C. Flipse, and A. Robinson, *Structure of the Cu {100}-c (2× 2) N surface: a scanning-tunneling-microscopy study.* Physical Review B, 1993. **47**(23): p. 15865.
228. Driver, S. and D. Woodruff, *Nitrogen-induced pseudo-(100) reconstruction of the Cu (111) surface identified by STM.* Surface science, 1999. **442**(1): p. 1-8.
229. Skelly, J., et al., *Nitrogen induced restructuring of Cu (111) and explosive desorption of N2.* Surface science, 1998. **415**(1-2): p. 48-61.
230. Zoldan, V.C., et al., *Coupling of cobalt–tetraphenylporphyrin molecules to a copper nitride layer.* The Journal of Physical Chemistry C, 2013. **117**(31): p. 15984-15990.
231. Bhattacharjee, K., et al., *Electronic structure of the corrugated Cu3N network on Cu (110): Tunneling spectroscopy investigations.* Surface science, 2012. **606**(5-6): p. 652-658.
232. Depla, D., J. Haemers, and R. De Gryse, *Target surface condition during reactive glow discharge sputtering of copper.* Plasma Sources Science and Technology, 2002. **11**(1): p. 91.
233. Warren, H.N., The chemical news, 1887. **55**: p. 156.
234. Beilby, G.T. and G.G. Henderson, *CXXXII.—The action of ammonia on metals at high temperatures.* Journal of the Chemical Society, Transactions, 1901. **79**: p. 1245-1256.
235. Matignon, C., Trannoy, R., *Catalyseurs oxydants et generalisation de la lampe sans flamme.* Comptes rendus hebdomadaires des séances de l'Académie des sciences, 1906. **142**: p. 1210-1211.
236. Zervos, M., et al., *Observation of the direct energy band gaps of defect-tolerant Cu3N by ultrafast pump-probe spectroscopy.* The Journal of Physical Chemistry C, 2020. **124**(6): p. 3459-3469.
237. Juza, R., *Remarks on the crystal structure of Cu3N.* Z. Anorg. Allg. Chem, 1941. **248**: p. 118-120.
238. Winiarski, M., *Band gap evolution of bulk Cu3N and monolayer Cu2N under nonhydrostatic strain.* Journal of Solid State Chemistry, 2018. **266**: p. 161-165.
239. Johnson, N.W., D.I. Muir, and A. Moewes, *Oxidized monolayers of epitaxial silicene on Ag (111).* Scientific Reports, 2016. **6**(1): p. 22510.
240. Gottfried, J.M., *Surface chemistry of porphyrins and phthalocyanines.* Surface Science Reports, 2015. **70**(3): p. 259-379.

241. Choi, T., C. Ruggiero, and J. Gupta, *Incommensurability and atomic structure of c (2× 2) N/Cu (100): A scanning tunneling microscopy study.* Physical Review B, 2008. **78**(3): p. 035430.
242. Gloystein, A. and N. Nilius, *Empty Valence‐Band Pocket in p‐Type Cu2O (111) Probed with Scanning Tunneling Spectroscopy.* physica status solidi (b), 2021. **258**(11): p. 2100337.
243. Monig, H., et al., *Understanding scanning tunneling microscopy contrast mechanisms on metal oxides: a case study.* ACS nano, 2013. **7**(11): p. 10233-10244.
244. Tjung, S.J., et al., *STM and DFT studies of CO2 adsorption on O-Cu (100) surface.* Surface Science, 2019. **679**: p. 50-55.
245. Li, Z., et al., *Personal experience with four kinds of chemical structure drawing software: review on ChemDraw, ChemWindow, ISIS/Draw, and ChemSketch.* Journal of chemical information and computer sciences, 2004. **44**(5): p. 1886-1890.
246. Li, Y., et al., *Crystal-plane-dependent redox reaction on Cu surfaces.* Nano Research, 2020. **13**(6): p. 1677-1685.
247. Wiame, F., V. Maurice, and P. Marcus, *Initial stages of oxidation of Cu (1 1 1).* Surface Science, 2007. **601**(5): p. 1193-1204.
248. Önsten, A., M. Göthelid, and U.O. Karlsson, *Atomic structure of Cu2O (1 1 1).* Surface Science, 2009. **603**(2): p. 257-264.
249. Lawton, T., et al., *Initial oxidation of Cu (hkl) surfaces vicinal to Cu (111): A high-throughput study of structure sensitivity.* The Journal of Physical Chemistry C, 2012. **116**(30): p. 16054-16062.
250. Ullmann, F. and J. Bielecki, *Ueber synthesen in der biphenylreihe.* Berichte der deutschen chemischen Gesellschaft, 1901. **34**(2): p. 2174-2185.
251. Lackinger, M., *On-surface synthesis–there will be light.* Trends in Chemistry, 2022. **4**(6): p. 471-474.
252. He, Y., et al., *On-surface photo-induced dechlorination.* Chinese Chemical Letters, 2024: p. 109807.
253. Lackinger, M., *Synthesis on inert surfaces.* Dalton Transactions, 2021. **50**(29): p. 10020-10027.
254. Zimmermann, M., D. Domke, and M. Schween, *Photobromination (SR) and Corresp. SN1 Reactions–Key Reactions for the Development and the Application of the Concept of Hyperconjugation.* World, 2021. **9**(4): p. 175-184.
255. Katayanagi, H., N. Yonekuira, and T. Suzuki, *C–Br bond rupture in 193 nm photodissociation of vinyl bromide*. Chemical physics, 1998. **231**(2-3): p. 345-353.
256. Zhang, F., W.-J. Ding, and W.-H. Fang, *Combined nonadiabatic transition-state theory and ab initio molecular dynamics study on selectivity of the α and β bond fissions in photodissociation of bromoacetyl chloride.* The Journal of chemical physics, 2006. **125**(18).
257. Abadia, M., et al., *Enhancing Haloarene Coupling Reaction Efficiency on an Oxide Surface by Metal Atom Addition.* Nano Letters, 2024.
258. Grill, L., et al., *Nano-architectures by covalent assembly of molecular building blocks.* Nature nanotechnology, 2007. **2**(11): p. 687-691.
259. Lafferentz, L., et al., *Controlling on-surface polymerization by hierarchical and substrate-directed growth.* Nature chemistry, 2012. **4**(3): p. 215-220.
260. Zhang, H., et al., *On-surface synthesis of rylene-type graphene nanoribbons.* Journal of the American Chemical Society, 2015. **137**(12): p. 4022-4025.
261. Zhou, X., et al., *On-surface synthesis approach to preparing one-dimensional organometallic and poly-p-phenylene chains.* Materials Chemistry Frontiers, 2017. **1**(1): p. 119-127.
262. Wang, S., W. Wang, and N. Lin, *Resolving band-structure evolution and defect-induced states of single conjugated oligomers by scanning tunneling microscopy and tight-binding calculations.* Physical Review Letters, 2011. **106**(20): p. 206803.

263. Sun, K., et al., *On‐Surface Synthesis of 8‐and 10‐Armchair Graphene Nanoribbons.* Small, 2019. **15**(15): p. 1804526.
264. Ivanovskaya, V.V., et al., *On-Surface Synthesis and Evolution of Self-Assembled Poly (p-phenylene) Chains on Ag (111): A Joint Experimental and Theoretical Study.* The Journal of Physical Chemistry C, 2022. **127**(1): p. 393-402.
265. Zhang, Y.-Q., et al., *Synthesizing highly regular single-layer alkynyl–silver networks at the micrometer scale via gas-mediated surface reaction.* Journal of the American Chemical Society, 2019. **141**(13): p. 5087-5091.
266. Kolmer, M., et al., *Rational synthesis of atomically precise graphene nanoribbons directly on metal oxide surfaces.* Science, 2020. **369**(6503): p. 571-575.
267. Baklanov, A., et al., *On-Surface Synthesis of Nonmetal Porphyrins.* Journal of the American Chemical Society, 2020. **142**(4): p. 1871-1881.
268. Wang, Z., et al., *Layer-by-Layer Epitaxy of Porphyrin− Ligand Fe (II)-Fe (III) Nanoarchitectures for Advanced Metal–Organic Framework Growth.* ACS Applied Nano Materials, 2020.
269. Bhanu, U., et al., *Photoluminescence quenching in gold-MoS_2 hybrid nanoflakes.* Scientific reports, 2014. **4**(1): p. 5575.
270. Langlais, V., K. Schneider, and H. Tang, *Light assisted synthesis of poly-para-phenylene on Ag (001).* Journal of Physics: Condensed Matter, 2021. **34**(5): p. 055001.
271. Borsa, D. and D. Boerma, *Growth, structural and optical properties of Cu3N films.* Surface science, 2004. **548**(1-3): p. 95-105.
272. Butrymowicz, D.B., J.R. Manning, and M.E. Read, *Diffusion in copper and copper alloys part V. diffusion in systems involving elements of group VA.* Journal of Physical and Chemical Reference Data, 1977. **6**(1): p. 1-50.
273. Zhou, J., et al., *Probing Plexciton Emission from 2D Materials on Gold Nanotrenches.* arXiv preprint arXiv:2404.05161, 2024.
274. Thomas, J.C., et al., *A substitutional quantum defect in WS2 discovered by high-throughput computational screening and fabricated by site-selective STM manipulation.* Nature communications, 2024. **15**(1): p. 3556.
275. Thomas, J.C., et al., *Autonomous scanning probe microscopy investigations over WS2 and Au {111}.* npj Computational Materials, 2022. **8**(1): p. 99.
276. Zhou, J., et al., *Near-field coupling with a nanoimprinted probe for dark exciton nanoimaging in monolayer WSe2.* Nano letters, 2023. **23**(11): p. 4901-4907.
277. Selig, M., et al., *Dark and bright exciton formation, thermalization, and photoluminescence in monolayer transition metal dichalcogenides.* 2D Materials, 2018. **5**(3): p. 035017.
278. Tanaka, K.-i., *Surface nano-structuring by adsorption and chemical reactions.* Materials, 2010. **3**(9): p. 4518-4549.
279. Sotto, M., *Oxygen induced reconstruction of (h11) and (100) faces of copper.* Surface science, 1992. **260**(1-3): p. 235-244.
280. Braithwaite, M.J., R.W. Joyner, and M.W. Roberts, *Interaction of oxygen with Cu (100) studied by low energy electron diffraction (LEED) and X-ray photoelectron spectroscopy (XPS).* Faraday Discussions of the Chemical Society, 1975. **60**: p. 89-101.
281. Abadia, M., et al., *Enhancing Haloarene Coupling Reaction Efficiency on an Oxide Surface by Metal Atom Addition.* Nano Letters, 2024. **24**(6): p. 1923-1930.
282. Barth, J.V., *Molecular architectonic on metal surfaces.* Annual Review of Physical Chemistry, 2007. **58**(1): p. 375-407.
283. Kraushofer, F., et al., *Atomic-scale structure of the hematite α-Fe2O3 ($1\bar{1}02$)"R-Cut" Surface.* The Journal of Physical Chemistry C, 2018. **122**(3): p. 1657-1669.
284. Uphoff, M., *Atomistic Investigations and Control of Novel Quantum Materials: Lanthanide-Organic Nano-Architectures at Well-Defined substrates and the Iron Silicide (110) Facet*. 2019, Technische Universität München.
285. Zheng, H., J. Kröger, and R. Berndt, *Spectroscopy of single donors at ZnO (0001) surfaces.* Physical review letters, 2012. **108**(7): p. 076801.

286. Li, Y., et al., *Crystal-plane-dependent redox reaction on Cu surfaces.* Nano Research, 2020. **13**: p. 1677-1685.
287. Repp, J., et al., *Controlling the charge state of individual gold adatoms.* Science, 2004. **305**(5683): p. 493-495.
288. Hollerer, M., et al., *Charge transfer and orbital level alignment at inorganic/organic interfaces: The role of dielectric interlayers.* ACS nano, 2017. **11**(6): p. 6252-6260.
289. Pörtner, M., et al., *Charge State Control of F16CoPc on h‐BN/Cu (111).* Advanced Materials Interfaces, 2020. **7**(15): p. 2000080.
290. Wieghold, S., et al., *Photoresponse of supramolecular self-assembled networks on graphene–diamond interfaces.* Nature communications, 2016. **7**(1): p. 10700.
291. Waser, R. and M. Aono, *Nanoionics-based resistive switching memories.* Nature materials, 2007. **6**(11): p. 833-840.
292. He, Y., et al., *On-surface photo-induced dechlorination.* Chinese Chemical Letters, 2024. **35**(9): p. 109807.
293. Zimmermann, M., D. Domke, and M. Schween, *Photobromination (SR) and Corresp. SN1 Reactions–Key Reactions for the Development and the Application of the Concept of Hyperconjugation.* World Journal of Chemical Education, 2021. **9**(4): p. 175-184.
294. Dong, S.-h., et al., *Interaction of CO and O_2 with supported Pt single-atoms on TiO_2 (110).* Chinese Journal of Chemical Physics, 2020. **33**(3): p. 349-356.
295. Cui, X., et al., *Formation and diffusion of oxygen-vacancy pairs on TiO_2 (110)-(1× 1).* The Journal of chemical physics, 2008. **129**(4).
296. Wang, Z., et al., *Topologically Localized Vibronic Excitations in Second-Layer Graphene Nanoribbons.* Physical Review Letters, 2024. **133**(3): p. 036401.
297. Yin, R., et al., *Step-assisted on-surface synthesis of graphene nanoribbons embedded with periodic divacancies.* Journal of the American Chemical Society, 2022. **144**(32): p. 14798-14808.
298. Li, Z., et al., *Personal experience with four kinds of chemical structure drawing software: review on ChemDraw, ChemWindow, ISIS/Draw, and ChemSketch.* Journal of Chemical Information and Computer Science, 2004. **44**(5): p. 1886-1890.
299. Haag, F., *Spectroscopic Study of On–Surface Reactions on Model Metal and Metal Oxide Surfaces*, in *Physics*. 2017, Technische Universität München.
300. Møller, P.J. and M.-C. Wu, *Surface geometrical structure and incommensurate growth: ultrathin Cu films on TiO2 (110).* Surface Science, 1989. **224**(1-3): p. 265-276.
301. Onishi, H. and Y. Iwasawa, *Reconstruction of TiO2 (110) surface: STM study with atomic-scale resolution.* Surface science, 1994. **313**(1-2): p. L783-L789.
302. Sander, M. and T. Engel, *Atomic level structure of TiO2 (110) as a function of surface oxygen coverage.* Surface science, 1994. **302**(1-2): p. L263-L268.
303. Guo, Q., I. Cocks, and E. Williams, *Surface Structure of (1× 2) Reconstructed Ti O 2 (110) Studied Using Electron Stimulated Desorption Ion Angular Distribution.* Physical review letters, 1996. **77**(18): p. 3851.
304. Berkó, A. and F. Solymosi, *Study of clean TiO2 (110) surface by scanning tunneling microscopy and spectroscopy.* Langmuir, 1996. **12**(5): p. 1257-1261.
305. Halpegamage, S., et al., *An ordered mixed oxide monolayer formed by Iron segregation on rutile-TiO2 (011): Structural determination by X-ray photoelectron diffraction.* The Journal of Physical Chemistry C, 2016. **120**(46): p. 26414-26424.
306. Rønnau, A., *A closer look at the TiO2 (110) surface with STM.* University of Aarhus, Denmark, 2003.
307. Miyazaki, M., Y. Sugawara, and Y.J. Li, *Charge behavior of terminal hydroxyl on rutile TiO2 (110).* Langmuir, 2021. **37**(35): p. 10588-10593.
308. Langevoort, J., et al., *On the oxide formation on stainless steels AISI 304 and incoloy 800H investigated with XPS.* Applied surface science, 1987. **28**(2): p. 167-179.
309. Tan, B.J., K.J. Klabunde, and P.M. Sherwood, *X-ray photoelectron spectroscopy studies of solvated metal atom dispersed catalysts. Monometallic iron and bimetallic iron-cobalt particles on alumina.* Chemistry of Materials, 1990. **2**(2): p. 186-191.

310. Kim, Y.I. and W.E. Hatfield, *Electrical, magnetic and spectroscopic properties of tetrathiafulvalene charge transfer compounds with iron, ruthenium, rhodium and iridium halides.* Inorganica chimica acta, 1991. **188**(1): p. 15-24.
311. Carver, J., G. Schweitzer, and T.A. Carlson, *Use of X‐ray photoelectron spectroscopy to study bonding in Cr, Mn, Fe, and Co compounds.* The Journal of Chemical Physics, 1972. **57**(2): p. 973-982.
312. Shabanova, I. and V. Trapeznikov, *A study of the electronic structure of Fe_3C, Fe_3Al and Fe_3Si by x-ray photoelectron spectroscopy.* Journal of Electron Spectroscopy and Related Phenomena, 1975. **6**(4): p. 297-307.
313. Barber, M., et al., *High energy photoelectron spectroscopy of transition metal complexes. Part 2.—Metallocenes.* Journal of the Chemical Society, Faraday Transactions 2: Molecular and Chemical Physics, 1973. **69**: p. 559-562.
314. Fischer, A.B., et al., *An x-ray photoelectron spectroscopic study of multilayers of an electroactive ferrocene derivative attached to platinum and gold electrodes.* Journal of the American Chemical Society, 1979. **101**(13): p. 3442-3446.
315. Andersson, S.L.T. and R.F. Howe, *An X-ray photoelectron study of metal clusters in zeolites.* The Journal of Physical Chemistry, 1989. **93**(12): p. 4913-4920.
316. Yim, C.M., C.L. Pang, and G. Thornton, *Probing the local electronic structure of the cross-linked (1× 2) reconstruction of rutile TiO2 (110).* Surface Science, 2016. **650**: p. 71-75.
317. Abad, J., et al., *Characterization of thin silicon overlayers on rutile TiO 2 (110)-(1× 1).* Physical Review B—Condensed Matter and Materials Physics, 2010. **82**(16): p. 165420.
318. Ohashi, Y., et al., *Hydrogen distribution and electronic structure of TiO2 (110) hydrogenated with low-energy hydrogen ions.* The Journal of Physical Chemistry C, 2019. **123**(16): p. 10319-10324.
319. Schierbaum, K., et al., *The interaction of Pt with TiO2 (110) surfaces: a comparative XPS, UPS, ISS, and ESD study.* Surface science, 1996. **345**(3): p. 261-273.
320. Chung, Y., W. Lo, and G. Somorjai, *Low energy electron diffraction and electron spectroscopy studies of the clean (110) and (100) titanium dioxide (rutile) crystal surfaces.* Surface Science, 1977. **64**(2): p. 588-602.
321. Basagni, A., et al., *Tunable band alignment with unperturbed carrier mobility of on-surface synthesized organic semiconducting wires.* Acs Nano, 2016. **10**(2): p. 2644-2651.
322. Merino-Díez, N., et al., *Width-dependent band gap in armchair graphene nanoribbons reveals Fermi level pinning on Au (111).* ACS nano, 2017. **11**(11): p. 11661-11668.
323. Merino-Díez, N., et al., *Switching from reactant to substrate engineering in the selective synthesis of graphene nanoribbons.* The journal of physical chemistry letters, 2018. **9**(10): p. 2510-2517.
324. Vasseur, G., et al., *Quasi one-dimensional band dispersion and surface metallization in long-range ordered polymeric wires.* Nature Communications, 2016. **7**(1): p. 10235.
325. Talirz, L. and C.A. Pignedoli, *Electronic Structure of Atomically Precise Graphene Nanoribbons.* Handbook of Materials Modeling: Applications: Current and Emerging Materials, 2020: p. 685-719.
326. Ruffieux, P., et al., *Electronic structure of atomically precise graphene nanoribbons.* ACS nano, 2012. **6**(8): p. 6930-6935.
327. Mohanty, N., et al., *Nanotomy-based production of transferable and dispersible graphene nanostructures of controlled shape and size.* Nature communications, 2012. **3**(1): p. 844.
328. Johnson, A.P., H. Gangadharappa, and K. Pramod, *Graphene nanoribbons: A promising nanomaterial for biomedical applications.* Journal of controlled release, 2020. **325**: p. 141-162.
329. Kraushofer, F., et al., *Atomic-Scale Structure of the Hematite α-Fe2O3 ($1\bar{1}02$)"R-Cut" Surface.* The Journal of Physical Chemistry C, 2018. **122**(3): p. 1657-1669.

330. Huang, H., et al., *Spatially resolved electronic structures of atomically precise armchair graphene nanoribbons.* Scientific reports, 2012. **2**(1): p. 983.
331. Sun, K., et al., *A new on-surface synthetic pathway to 5-armchair graphene nanoribbons on Cu (111) surfaces.* Faraday Discussions, 2017. **204**: p. 297-305.
332. Zuzak, R., et al., *On-surface synthesis of nanographenes and graphene nanoribbons on titanium dioxide.* ACS nano, 2023. **17**(3): p. 2580-2587.
333. Sehon, A. and M. Szwarc, *The C—Br bond dissociation energy in halogenated bromomethanes.* Proceedings of the Royal Society of London. Series A. Mathematical and Physical Sciences, 1951. **209**(1096): p. 110-131.
334. Reticcioli, M., et al., *Polaron-driven surface reconstructions.* Physical Review X, 2017. **7**(3): p. 031053.
335. Henderson, M.A., S. Otero-Tapia, and M.E. Castro, *The chemistry of methanol on the TiO 2 (110) surface: the influence of vacancies and coadsorbed species.* Faraday Discussions, 1999. **114**: p. 313-329.
336. Baer, D.R., et al., *XPS guide: Charge neutralization and binding energy referencing for insulating samples.* Journal of Vacuum Science & Technology A, 2020. **38**(3).
337. Berberich, L. and M. Bell, *The dielectric properties of the rutile form of TiO2.* Journal of Applied Physics, 1940. **11**(10): p. 681-692.
338. Yang, B., et al., *Atomistic investigation of surface characteristics and electronic features at high-purity FeSi (110) presenting interfacial metallicity.* Proceedings of the National Academy of Sciences, 2021. **118**(17).
339. Zou, Z.-Q., et al., *Thermal stability of iron silicide nanowires epitaxially grown on Si (110) substrates.* Applied Surface Science, 2017. **399**: p. 200-204.
340. Neubauer, A., et al., *Ultra-high vacuum compatible image furnace.* Review of Scientific Instruments, 2011. **82**(1): p. 013902.
341. Raunau, W., et al., *Scanning tunneling microscopy and spectroscopy of iron suicide epitaxially grown on Si (111).* Surface science, 1993. **286**(3): p. 203-211.
342. Gallego, J. and R. Miranda, *The Fe/Si (100) interface.* Journal of applied physics, 1991. **69**(3): p. 1377-1383.
343. Fu, C. and S. Doniach, *Model for a strongly correlated insulator: FeSi.* Physical Review B, 1995. **51**(24): p. 17439.
344. De Parga, A.V., et al., *A new metastable epitaxial silicide: FeSi2/Si (111).* Ultramicroscopy, 1992. **42**: p. 845-850.
345. Hanaor, D.A. and C.C. Sorrell, *Review of the anatase to rutile phase transformation.* Journal of Materials science, 2011. **46**: p. 855-874.
346. Gallardo Amores, J.M., V. Sanchez Escribano, and G. Busca, *Anatase crystal growth and phase transformation to rutile in high-area TiO_2, MoO_3–TiO_2 and other TiO_2-supported oxide catalytic systems.* Journal of Materials Chemistry, 1995. **5**(8): p. 1245-1249.
347. Fairley, N., *CasaXPS manual 2.3. 15. Spectroscopy*. 2009: Casa Software Ltd.
348. Carin, R., J. Deville, and J. Werckmann, *An XPS study of GaN thin films on GaAs.* Surface and Interface Analysis, 1990. **16**(1‐12): p. 65-69.
349. Hedman, J. and N. Mårtensson, *Gallium nitride studied by electron spectroscopy.* Physica Scripta, 1980. **22**(2): p. 176.
350. Vitanov, S., *Simulation of high electron mobility transistors*, in *E360 - Institut für Mikroelektronik*. 2010, Technische Universität Wien. p. 155.
351. Ridley, B., O. Ambacher, and L.F. Eastman, *The polarization-induced electron gas in a heterostructure.* Semiconductor Science and Technology, 2000. **15**(3): p. 270.
352. Smorchkova, I., et al., *AlN/GaN and (Al, Ga) N/AlN/GaN two-dimensional electron gas structures grown by plasma-assisted molecular-beam epitaxy.* Journal of Applied Physics, 2001. **90**(10): p. 5196-5201.
353. Ahn, J., et al., *Surface composition and structure of GaN epilayers on sapphire.* The Journal of Chemical Physics, 1997. **107**(22): p. 9577-9584.
354. Sung, M., et al., *Composition and structure of the GaN {0001}-(1× 1) surface.* Physical Review B, 1996. **54**(20): p. 14652.

355. Messina, D.C., et al., *Challenges in atomic layer etching of gallium nitride using surface oxidation and ligand-exchange.* Journal of Vacuum Science & Technology A, 2023. **41**(2).
356. Weyher, J., et al., *Chemical etching of GaN in KOH solution: role of surface polarity and prior photoetching.* The Journal of Physical Chemistry C, 2022. **126**(2): p. 1115-1124.
357. Zhu, Y., et al., *Effect and mechanism of oxidant on alkaline chemical mechanical polishing of gallium nitride thin films.* Materials Science in Semiconductor Processing, 2022. **138**: p. 106272.
358. Lament, K., et al., *Growth and Properties of Ultra-Thin PTCDI-C8 Films on GaN (0001).* Crystals, 2024. **14**(3): p. 201.
359. Ma, Y., et al., *A two-dimensional manganese gallium nitride surface structure showing ferromagnetism at room temperature.* Nano Letters, 2018. **18**(1): p. 158-166.
360. Chiu, Y.-P., et al., *Scanning tunneling microscopy and spectroscopy of the electronic structure of dislocations in GaN/Si (111) grown by molecular-beam epitaxy.* Applied Physics Letters, 2010. **96**(8).
361. Horna, J., et al., *Scanning tunneling microscopy characterization of metalorganic chemical vapor deposition grown GaN.* Materials Science and Engineering: B, 1997. **44**(1-3): p. 414-418.
362. Dong, Y., R.M. Feenstra, and J. Northrup, *Oxidized GaN (0001) surfaces studied by scanning tunneling microscopy and spectroscopy and by first-principles theory.* Journal of Vacuum Science & Technology B: Microelectronics and Nanometer Structures Processing, Measurement, and Phenomena, 2006. **24**(4): p. 2080-2086.
363. Eisele, H., et al., *Cross-sectional scanning tunneling microscopy and spectroscopy of nonpolar GaN (11¯00) surfaces.* Journal of Vacuum Science & Technology B, 2010. **28**(4): p. C5G11-C5G18.
364. Wang, Y., *Quantitative investigation of group III-nitride interfaces by a combination of scanning tunneling microscopy and off-axis electron holography*. 2021, Dissertation, RWTH Aachen University, 2021.
365. Kumar, N., A. Kumar, and F. Chand, *Surface states passivation in GaN single crystal by ruthenium solution.* Applied Physics Letters, 2023. **122**(1).
366. Ivanova, L., *Nitrogen Containing III-V Semiconductor Surfaces and Nanostructures Studied by Scanning Tunneling Microscopy and Spectroscopy*, in *Inst. Festkörperphysik*. 2009, Thecnical University of Berlin.
367. Mazur, P., et al., *Obtaining Niobium Nitride on n-GaN by Surface Mediated Nitridation Technique.* Crystals, 2022. **12**(12): p. 1847.
368. Della Casa, P., *Two-step MOVPE, in-situ etching and buried implantation: applications to the realization of GaAs laser diodes*, in *Mathematik und Naturwissenschaften*. 2021, Technischen Universität Berlin.
369. Peczonczyk, S.L., *Heterogeneous Organic Reactions on Gallium-Rich Gallium Arsenide, Gallium Phosphide, and Gallium Nitride Surfaces,* in *Chemistry*. 2014, The University of Michigan.
370. Nagai, K., T. Shibanuma, and M. Hashimoto, *Zero-order desorption kinetics based on phase equilibrium.* Surface Science Letters, 1984. **145**(1): p. L459-L464.
371. Asada, H., *A model for the zero order desorption kinetics.* Journal of the Research Institute for Catalysis Hokkaido University, 1983. **30**(2): p. 55-59.
372. Smith, R.S., J. Matthiesen, and B.D. Kay, *Desorption kinetics of methanol, ethanol, and water from graphene.* The Journal of Physical Chemistry A, 2014. **118**(37): p. 8242-8250.
373. Bennett, R.A., et al., *Spectroscopy of ultrathin epitaxial rutile TiO2 (110) films grown on W (100).* The Journal of chemical physics, 2007. **127**(8).
374. Fukada, K., et al., *Effects of hydrogen on the electronic state and electric conductivity of the rutile TiO2 (110) surface.* Journal of the Physical Society of Japan, 2015. **84**(6): p. 064716.

375. Xiong, G., et al., *Photoemission electron microscopy of TiO2 anatase films embedded with rutile nanocrystals.* Advanced Functional Materials, 2007. **17**(13): p. 2133-2138.
376. Mansfeldova, V., et al., *Work function of TiO2 (anatase, rutile, and brookite) single crystals: effects of the environment.* The Journal of Physical Chemistry C, 2021. **125**(3): p. 1902-1912.
377. Maheu, C., et al., *UPS and UV spectroscopies combined to position the energy levels of TiO 2 anatase and rutile nanopowders.* Physical Chemistry Chemical Physics, 2018. **20**(40): p. 25629-25637.